

From Holography to Nanoimprint Lithography:
Investigation of Photo-Induced Effects
in Azobenzene-Functionalized
Molecular Glasses and Polymers

Von der Universität Bayreuth
zur Erlangung des Grades eines
Doktors der Naturwissenschaften (Dr. rer. nat)
genehmigte Abhandlung

von

Christoph Meichner

geboren in

Marktredwitz

Erstgutachter: apl. Prof. Dr. Lothar Kador
Zweitgutachter: Prof. Dr. Ernst Rössler
Drittgutachter: Prof. Dr. Christopher K. Ober,
Cornell University

Tag der Einreichung: 30.05.2017
Tag des Kolloquiums: 27.10.2017

Abstract

The rich photophysics of azobenzene-functionalized molecular glasses and polymers makes them a fascinating material class with a large scope of applications. When exposed to UV or blue light, the covalently attached azobenzene moieties perform repeated *trans-cis-trans* isomerization cycles. Depending on the polarization of the light and the molecular structure of the functionalized compounds, the azobenzene chromophores can either reorient at a fixed location or, in addition, migrate over macroscopic distances. Molecular orientation is useful for the storage of holographic volume gratings since it causes the refractive index to become anisotropic. To observe migration, the material must become photofluidic. This state is a peculiarity of azobenzene-functionalized glass formers and denotes their capability to flow like a viscous liquid without raising their macroscopic temperature when exposed to light. By means of external forces, such as optical gradients or adhesive forces, shaping of the material surface is possible. As a consequence, azobenzene-functionalized molecular glasses and polymers are suitable for different fields of application, which are discussed in this thesis. They comprise the holographic storage of data, the lithographic manufacturing of micrometer- and nanometer-sized structures, and the optical generation of surface relief patterns. In addition, a new method for the determination of refractive indices is presented and characterized.

The first part of this thesis constitutes a guide on how to improve the holographic performance of azobenzene-functionalized block copolymers. These compounds consist of a microphase-separated azobenzene-functionalized minority and a polystyrene majority block. They can be prepared with a low optical density, which is required for holographic data storage. Different homo- and block copolymers were blended with an azobenzene-functionalized molecular glass and holographic gratings were inscribed into them. From their diffraction behavior it could be concluded that cooperative interactions exist between the chromophores of the molecular glass as well as those of the molecular glass and the photo-addressable polymers. Thus, the molecular glass acts as a plasticizer and speeds up the alignment of the chromophores of the surrounding polymer matrix. Moreover, the addition of molecular glass allows for the storage of holograms of higher quality. In block copolymers, the molecular glass mainly accumulates in the photo-orientable minority phase. This concentration is further enhanced by annealing. Adding an amount of 15 wt% molecular glass to a block copolymer with stabilizing mesogenic units in its photo-addressable block results in a long-term-stable refractive-index modulation. Furthermore, the inscription time is reduced by a factor of more than 15 as compared to the neat block copolymer.

In the second part, a new method for the determination of the refractive index of solids based on diffraction gratings is developed, characterized, and tested. More specifically, two different criteria are derived from the grating equation. They allow for the calculation of the refractive index from first- and second-order critical diffraction angles. Both approaches apply in the Raman-Nath regime to arbitrarily shaped surface-relief, refractive-index, or absorption gratings. Moreover, no information about the thickness of the material below the grating is required. To study the applicability of the method, the refractive-index dispersion of polydimethylsiloxane was measured and compared to that determined with an Abbe refractometer. The results of the combined experiments show that the refractive index can be calculated with an accuracy of about three decimal digits. Possible error sources include the spectral width of the laser and the angular resolution of sample orientation. They can be eliminated either by correcting the wavelength accordingly or by using an approach that involves the determination of two critical diffraction angles. Finally, the new technique is applied to determine the refractive indices of different azobenzene-functionalized molecular glass formers.

The third part discusses a novel lithographic method which allows for the precise replication of micrometer- and nanometer-sized structures. It is dubbed “azobenzene-based nanoimprint lithography” (Azo-NIL) and uses the well-known concept of transferring patterns from a rigid master to a resist with a flexible mold. Unlike other imprint methods, the resist material is an azobenzene-functionalized molecular glass or homopolymer which can be switched to the photofluidic state with visible or UV light. The method has the advantage that it can be performed without thermal treatment or crosslinking reactions, so it is not affected by issues associated with material shrinkage. Coherent and incoherent light sources in the UV and blue spectral range can be used to photofluidize the azobenzene-functionalized resists. The filling speed depends on both the intensity of the light and the initial thickness of the resist. More precisely, it is proportional to the fluence at short illumination times. As soon as the cavities of the mold are completely filled, the material transport is terminated. For film thicknesses above 500 nm, complete filling is achieved at a constant rate. If the photofluidizable resist is thinner, both the filling rate and the filling height decrease. Capillary flow occurs in cavities smaller than 300 nm, which causes the imprinting time to increase for molds with finer features. Different azobenzene-functionalized low-molecular-weight compounds and a homopolymer were investigated for their suitability for Azo-NIL. Molecular glasses based on a spirobichromane core turned out to be the most efficient resist materials. The introduction of perfluorinated substituents at the azobenzene chromophores reduces both the filling speed and the imprint quality, whereas for methoxy groups the imprinting speed increases. In preheated films, the thermal barriers for azobenzene isomerization attempts are lowered, so the imprinting speed increases, but so does also the number of release-induced defects.

In part four, the surface-relief patterns formed by two different spirobichromane-based molecular glasses upon prolonged illumination with a *p*-polarized optical grating are analyzed and characterized. As long as the fluence stays below a critical value, the developing surface relief resembles the interference pattern, so its profile is essentially sinusoidal. For higher fluences, i. e., after the first-order diffraction efficiency has reached its maximum, the sinusoidal surface relief grating decays and rounded cones develop. The latter finally fuse into complex superstructures. They consist of irregular zigzag-shaped lines which run perpendicular to the interference fringes of the optical grating. The zigzag-shaped lines reach heights up to several micrometers and the resulting final pattern resembles a grating with a periodicity of $\sim 4\mu\text{m}$. Surprisingly, at high fluences the material transport occurs predominantly in a direction with negligible optical gradients. If the azobenzene moieties feature methoxy substituents, the formation of gratings or complex superstructures is accelerated.

Kurzdarstellung

Aufgrund ihrer reichen Fotophysik stellen azobenzolfunktionalisierte molekulare Gläser und Polymere eine faszinierende Materialklasse mit einem großen Anwendungsbereich dar. Wenn die kovalent gebundenen Azobenzoleinheiten UV- oder blauem Licht ausgesetzt sind, führen sie wiederholt *trans-cis-trans*-Isomerisierungszyklen durch. Je nach der Polarisation des Lichts und der Molekülstruktur der funktionalisierten Verbindungen können die Azobenzolchromophore entweder an einem festen Ort umorientiert werden oder darüber hinaus über makroskopische Distanzen wandern. Die molekulare Orientierung ist für die Speicherung von holographischen Volumengittern nützlich, da sie bewirkt, daß der Brechungsindex anisotrop wird. Um Migration zu beobachten, muss das Material fotofluidisch werden. Dieser Zustand ist eine Besonderheit von azobenzolfunktionalisierten Glasbildnern und bezeichnet ihre Fähigkeit, wie eine viskose Flüssigkeit zu fließen sobald sie Licht ausgesetzt sind, ohne dabei ihre makroskopische Temperatur zu erhöhen. Durch äußere Kräfte, wie optische Gradienten oder Adhäsionskräfte, ist eine Formgebung der Materialoberfläche möglich. Aufgrund dessen sind azobenzolfunktionalisierte molekulare Gläser und Polymere für verschiedene Anwendungsgebiete geeignet, welche in dieser Arbeit diskutiert werden. Sie umfassen die holographische Speicherung von Daten, die lithografische Herstellung von mikrometer- und nanometergroßen Strukturen sowie die optische Erzeugung von Oberflächenreliefmustern. Des Weiteren wird ein neues Verfahren zur Bestimmung von Brechungsindizes vorgestellt und charakterisiert.

Der erste Teil dieser Arbeit stellt einen Leitfaden dar, wie die holographische Leistungsfähigkeit von azobenzolfunktionalisierten Blockcopolymeren verbessert werden kann. Diese Verbindungen bestehen aus einem mikrophasenseparierten azobenzolfunktionalisierten Minoritäts- und einem Polystyrolmajoritätsblock. Sie können mit einer geringen optischen Dichte hergestellt werden, welche für die holographische Datenspeicherung erforderlich ist. Verschiedene Homo- und Blockcopolymere wurden mit einem azobenzolfunktionalisierten molekularen Glas gemischt und holographische Gitter wurden darin eingeschrieben. Aus deren Beugungsverhalten konnte geschlossen werden, dass kooperative Wechselwirkungen zwischen den Chromophoren des molekularen Glases sowie denen des molekularen Glases und der fotoadressierbaren Polymere bestehen. Somit wirkt das molekulare Glas als Weichmacher und beschleunigt die Ausrichtung der Chromophore der umgebenden Polymermatrix. Darüber hinaus ermöglicht die Zugabe von molekularem Glas die Speicherung von Hologrammen höherer Qualität. In Blockcopolymeren akkumuliert sich das molekulare Glas hauptsächlich in der fotoorientierbaren Minoritätsphase. Diese Konzentrierung wird durch Tempern weiter gefördert. Die Zugabe einer Menge von 15 wt% molekularem Glas

zu einem Blockcopolymer mit stabilisierenden mesogenen Einheiten innerhalb des fotoadressierbaren Blocks führt zu einer langzeitstabilen Brechungsindexmodulation. Weiterhin verringert sich die Einschreibzeit gegenüber dem reinen Blockcopolymer um einen Faktor von mehr als 15.

Im zweiten Teil wird ein neues Verfahren zur Bestimmung des Brechungsindex von Feststoffen auf Basis von Beugungsgittern entwickelt, charakterisiert und getestet. Insbesondere werden zwei verschiedene Kriterien aus der Gittergleichung abgeleitet. Sie erlauben die Berechnung des Brechungsindex aus den kritischen Beugungswinkeln erster und zweiter Ordnung. Beide Ansätze gelten im Raman-Nath Regime für beliebig geformte Oberflächenrelief-, Brechungsindex- oder Absorptionsgitter. Darüber hinaus ist keine Information über die Dicke des Materials unter dem Gitter erforderlich. Um die Anwendungsmöglichkeiten des Verfahrens zu untersuchen, wurde die Brechungsindexdispersion von Polydimethylsiloxan gemessen und mit derjenigen verglichen, die mit einem Abbe-Refraktometer bestimmt wurde. Die Ergebnisse der kombinierten Experimente zeigen, dass der Brechungsindex mit einer Genauigkeit von etwa drei Dezimalstellen berechnet werden kann. Mögliche Fehlerquellen sind die spektrale Breite des Lasers und die Winkelauflösung bezüglich der Probenorientierung. Diese können eliminiert werden, indem entweder die Wellenlänge entsprechend korrigiert wird oder durch die Verwendung eines Ansatzes, bei dem zwei kritische Beugungswinkel bestimmt werden. Schließlich wird die neue Technik angewendet um die Brechungsindizes verschiedener azobenzolfunktionalisierter molekularer Glasbildner zu bestimmen.

Der dritte Teil diskutiert ein neuartiges lithographisches Verfahren, das die genaue Replikation von mikrometer- und nanometergroßen Strukturen ermöglicht. Es wird als „Azobenzolbasierte Nanoimprintlithographie“ (Azo-NIL) bezeichnet und verwendet das bekannte Konzept der Übertragung von Mustern von einem starren Master auf einen Resist mit Hilfe einer flexiblen Gußform. Im Gegensatz zu anderen Prägeverfahren ist das Resistmaterial ein azobenzolfunktionalisiertes molekulares Glas oder Homopolymer, das mit sichtbarem oder UV-Licht in den fotofluidischen Zustand geschaltet werden kann. Das Verfahren hat den Vorteil, dass es ohne thermische Behandlung oder Vernetzungsreaktionen durchgeführt werden kann, so dass es nicht von Problemen betroffen ist, die mit Material schrumpfung verbunden sind. Für die Fotofluidisierung der azobenzolfunktionalisierten Resiste können kohärente und inkohärente Lichtquellen im UV- und im blauen Spektralbereich eingesetzt werden. Die Füllgeschwindigkeit hängt sowohl von der Intensität des Lichts als auch von der ursprünglichen Dicke des Resists ab. Genauer gesagt ist sie bei kurzen Belichtungszeiten proportional zur Fluenz. Sobald die Hohlräume der Gußform vollständig gefüllt sind, endet der Materialtransport. Bei Schichtdicken über 500 nm wird eine vollständige Füllung mit konstanter Geschwindigkeit erreicht. Wenn der fotofluidisierbare Resist dünner ist, nehmen sowohl die Füllrate als auch die Füllhöhe ab. In Hohlräumen kleiner als 300 nm tritt Kapillarströmung auf, was bewirkt, daß die Prägezeit für Gußformen mit feineren Strukturen zunimmt. Verschiedene azobenzolfunktionalisierte niedermolekulare Verbindungen und ein Homopolymer wurden auf ihre Eignung für Azo-NIL untersucht. Molekulare Gläser auf der Basis eines Spirobichromankerns erwiesen sich als die effizientesten Resistmaterialien. Die Einführung perfluorierter Substituenten an den Azobenzolchromophoren reduziert sowohl die Füllgeschwindigkeit als auch die Prägequalität, wohingegen die Prägegeschwindigkeit für Methoxygruppen zunimmt. In vorgeheizten Filmen verringern sich die thermischen Barrieren für Azobenzol-Isomerisierungsversuche, so dass sich die Prägegeschwindigkeit, aber auch die Anzahl ablöseinduzierter Defekte, erhöht.

In Teil vier werden die Oberflächenreliefmuster, die von zwei verschiedenen spirobichromanbasierten Molekulargläsern bei längerer Beleuchtung mit einem p-polarisierten optischen Gitter gebildet werden, analysiert und charakterisiert. Solange die Fluenz unter einem kritischen Wert bleibt, ähnelt das sich entwickelnde Oberflächenrelief dem Interferenzmuster, so dass dessen Profil im Wesentlichen sinusförmig ist. Für höhere Fluenzen, d. h. nachdem die Beugungseffizienz der ersten Beugungsordnung ihr Maximum erreicht hat, zerfällt das sinusförmige Oberflächenreliefgitter und es bilden sich abgerundete Kegel. Diese verschmelzen schließlich zu komplexen Superstrukturen. Sie bestehen aus unregelmäßigen, zickzackförmigen Linien, die senkrecht zu den Interferenzstreifen des optischen Gitters verlaufen. Die zickzackförmigen Linien erreichen Höhen bis zu einigen Mikrometern und das resultierende Endmuster ähnelt einem Gitter mit einer Periodizität von $4\ \mu\text{m}$. Überraschenderweise erfolgt der Materialtransport bei hohen Fluenzen überwiegend entlang einer Richtung mit vernachlässigbaren optischen Gradienten. Wenn die Azobenzoleinheiten Methoxysubstituenten aufweisen, wird die Bildung von Gittern oder komplexen Superstrukturen beschleunigt.

Contents

Abstract	I
Kurzdarstellung	III
1 Introduction	1
2 Theory and Basic Concepts of Holography	9
2.1 Plane-Wave Holography	9
2.1.1 Field Distribution of Interfering Plane Waves	10
2.1.2 Grating Diffraction	12
2.2 Diffraction Regimes of Gratings	14
2.3 Raman-Nath Diffraction off Thin Scalar Gratings	15
2.4 Raman-Nath Diffraction off Thin Polarization Gratings	17
2.4.1 Diffraction off a Grating Generated by <i>ss</i> Illumination	18
2.4.2 Diffraction off a Grating Generated by <i>sp</i> Illumination	18
2.4.3 Diffraction off a Grating Generated by <i>rlcp</i> Illumination	19
2.5 Bragg Diffraction off Thick Scalar Gratings	19
3 Azobenzene Physics	23
3.1 Molecular Motion — Rotational Effects	23
3.2 Macroscopic Motion — Translational Effects	26
3.3 Athermal Photofluidization	27
4 From Photofluidization to Lithography — Concept and Theory	29
4.1 Introduction to Nanoimprint Lithography	29
4.2 Athermal Azobenzene-Based Nanoimprint Lithography	31
4.3 Filling Characteristics of Cavities — A Comparison of Two Models	32
5 Materials	37
5.1 Azobenzene-Functionalized Molecular Glasses	37
5.1.1 Synthesis of Azobenzene-Substituted Molecular Glass Formers	40
5.1.2 Thermal and Optical Properties of Azobenzene Molecular Glasses	41
5.2 Azobenzene-Functionalized Polymers	43
5.3 Preparation of Amorphous Thin Films	46

6	Fabrication and Properties of Molds	47
6.1	Fabrication of Flexible Molds	47
6.1.1	Molds with Features on the Micrometer Scale	47
6.1.2	Molds with Features on the Nanometer Scale	49
6.1.3	Sinusoidal PDMS Surface Relief Gratings	51
6.2	Properties of Flexible Molds	52
6.2.1	Roof Collapse of PDMS Molds	52
6.2.2	Lateral Stability of PDMS Molds	53
7	Experimental Section	57
7.1	Holographic Setup	57
7.2	Imprinting Setup for Azo-NIL	59
7.3	Atomic Force Microscopy	60
7.4	Scanning Electron Microscopy	61
8	Holographic Writing Performance of Azobenzene-Functionalized Polymer and Molecular-Glass Blends	63
8.1	Holographic Inscription Speed in Polymer Blends	65
8.2	Photoinduced Anisotropy in Polymer Blends	67
8.3	Influence of Annealing	70
8.4	Long-Term Stability of Holographic Gratings	72
9	Refractive-Index Determination from First- and Second-Order Critical Diffraction Angles	75
9.1	Principle	76
9.2	Dispersion of Polydimethylsiloxane	78
9.3	Refractive Indices of Azobenzene-Functionalized Molecular Glasses	81
10	Azobenzene-Based Nanoimprint Lithography	85
10.1	Imprinting Properties of Photofluidizable Resists	86
10.1.1	Fluence Dependence of the Imprinting Speed	86
10.1.2	Filling Characteristics of Micrometer Cavities	88
10.1.3	Influence of the Light Source on the Imprinting Speed	89
10.1.4	Influence of the Initial Film Thickness on the Imprinting Speed	92
10.2	Influence of the Resist Material on the Imprinting Performance	94
10.2.1	Azobenzene-Functionalized Triphenylamine-Based Compounds	95
10.2.2	Azobenzene-Functionalized Trisamide-Based Compounds	96
10.2.3	Azobenzene-Functionalized Spirobichromane-Based Compounds	98
10.2.4	Azobenzene-Functionalized Homopolymer	101
10.3	Nanostructuring of Azobenzene-Functionalized Spirobichromane-Based Molecular Glasses	103
10.3.1	Influence of Mold Material and External Pressure	103
10.3.2	Influence of the Size of the Mold Cavities on the Filling Speed	108
10.3.3	Influence of the Substituent of the Azobenzene Chromophores on the Imprint Quality	109
10.4	Imprinting at Elevated Temperatures	112
11	Formation of Complex Superstructures in Spirobichromane-Based Molecular Glasses	115
11.1	Fluence Dependence of the Diffraction Efficiency	116
11.2	Formation of Sinusoidal Surface Relief Gratings at Low Fluence	117

11.3 Formation of Complex Superstructures at High Fluence	120
11.4 Complex Superstructures in Methoxyazobenzene-Functionalized Spirobichromane-Based Molecular Glasses	122
12 Conclusion	125
Appendices	129
A NIL-Technology Master Data Sheet	131
B List of Publications	133
List of References	135
Danksagung	150
Eidesstattliche Versicherung	152

The era in which we live is the information or digital age. Its beginning can roughly be traced back to the advent of the first personal computers in the 1970s and it continues until today. Similar to the preceding industrial age, the digital age is characterized by rapid scientific and technological progress. The industrial age, however, required almost 150 years to evolve its associated technological achievements, such as chemical fertilizers, radio, television, jet planes, cars, or modern medicine. Nowadays, this progress occurs on a much shorter timescale. Modern daily-life technologies such as the internet, e-mail, mobile communication, or computers have been developed and brought to market within less than a few decades.

The main reason for the accelerated technological progress in the past half century is the steadily increasing capability of humankind to store, communicate, and process information. According to Hilbert and López,^[1] the world population stored about 300 exabytes (300×10^{18} bytes) of digital and analog information in the year 2007. This is equivalent to the storage capacity of more than 400 billion CD-ROMs, enough to pile up a stack that is higher than the distance between the earth and the moon. For comparison, the globally stored information in 1986 was only 16 exabytes, which is about 20 times less. Simultaneously, the digital revolution led to the replacement of analog technology, and digital data processing began to dominate the consumer electronics market near the turn of the millennium. Storage media changed from vinyl long-play records, audio cassettes, and video tapes to compact discs (CD), digital versatile discs (DVD), Blu-ray discs (BD), hard-disk drives (HDD), and flash drives. In 1986, an amount of about 430 exabytes was transferred to the most common technological receivers used at that time, which were mainly analog devices such as mobile and fixed-line phones. This number increased to about 2 zettabytes (2×10^{21} bytes) in 2007, where 97% of the communicated information was transmitted by the internet. The global computational power increased from approximately 3×10^{15} instructions per second in 1986 to about 6.4×10^{18} instructions per second in 2007 and it shifted from stationary computers to mobile devices such as smart phones, tablets, cars, or even watches. The important statement is that the demand for higher storage capacity, data transmission rates, and computational power is immense and that it increases until today, one decade later in the year 2017. Moreover, this trend will persist during the next decades. Cisco, a developer and manufacturer of networking hardware and telecommunication equipment, for example, states that the global IP traffic in 2016 was 1 zettabyte and predicts that it will more than double to 2.3 zettabytes in 2020.^[2] Another forecast is made by the International Data Corporation (IDC). They state that the amount of digital data created worldwide will increase by a factor of ten from 4.4 zettabytes in 2013 to 44 zettabytes in 2020.^[3]

The key process which drives the above technological development is miniaturization. For example, continuous downsizing of digital circuits allowed engineers to preserve Moore's law during the last decades. The latter states that the density and, thus, the performance of transistors in an integrated circuit increases exponentially over time.^[4] Since 1970, the areal density of electronic components on a chip has been doubling roughly every two years. As a consequence, the semiconductor market and its associated technologies have been growing exponentially as well. The economical effect of this development is a deflationary drop in prices for electronic components. In 1954, the price per transistor was 5.52 \$, whereas in 2005 the cost per bit of dynamic random access memory decreased to a marginal one nanodollar.^[5] In addition to reducing costs, the miniaturization of logical circuits and their denser arrangement caused the chip size to stay within practical limits and enhanced both computational speed and power efficiency.^[6,7] Today, the field-effect transistors in Intel's latest i5 and i7 chips have a size of about 50 nm and feature 14 nm wide fins as conducting channels (Fin-FET technology).^[8] Samsung pushes this technology further to its limits and announced the mass production of a new mobile processor that comprises structures as small as 10 nm.^[7]

To enable the fabrication of such fine patterns, large technological effort is required. State-of-the-art chip manufacturing is based on photolithography. With this method, circuit patterns can be imaged from a transmission photomask to a silicon wafer by projection optics. The wafer is coated with a photoresist that reacts upon illumination and the resulting resist pattern is transferred during further processing steps to the substrate below. Deep-ultraviolet light sources at a wavelength of 193 nm are used to image the patterns. To inscribe structures significantly smaller than this wavelength, a number of sophisticated techniques have to be applied. They include, for example, immersion lithography, optical phase control, exotic photochemistry, and multiple patterning. A further aspect is that the conventional concept of two-dimensional transistor design has already reached its limits. To prevent current leakage effects, the gates of nanometer-sized transistors must have a certain height, so the fabrication of an operational circuit requires a three-dimensional patterning approach.^[9,10] For the above reasons, the costs entailing chip design and fabrication become excessive for transistor sizes below 50 nm and the validity of Moore's law may run into serious danger during the next years.

In order to prevent this from happening, the semiconductor industry focuses on new patterning concepts. The status of the most promising lithographic techniques is specified in the International Technology Roadmap for Semiconductors (ITRS).^[11] It lists four potential candidates which are expected to meet the resolution and patterning requirements within the years between 2014 and 2028. One technique currently under development is extreme ultraviolet light lithography (EUVL). It largely corresponds to photolithography, but uses a light source with a shorter wavelength of 13.5 nm. Therefore, EUVL has a much higher resolution. The drawback of existing EUVL systems is that up to now they lack stable high-power ultraviolet light sources, which limits their throughput. Furthermore, resist chemistry and resist post processing have to be improved and the availability of defect-free masks and higher-numerical-aperture optics has to be increased. E-beam lithography (or maskless lithography) offers a high resolution, but common devices are rather slow since they use a single electron beam to pattern an electron-sensitive resist. To increase throughput, parallel writing with a large number of electron beams is required. Respective devices are currently under development. Directed self-assembly (DSA) is a conceptually different patterning technique. It enables patterning by making use of the micro-phase separation of block copolymers. Block copolymers consist of two or more covalently connected polymers each made of a different monomer. Due to the chemical equality of the monomer units within each block and due to the spatial constraints of the polymer backbone, block copoly-

mers are capable of forming different morphologies with nanometer-sized domains. These domains can be arranged on a wafer such that they form the intended pattern. To achieve this, the wafer has to be pretreated with demanding epitaxial processes. Moreover, this technique faces different challenges, which include a low number of defects, the increase of pattern complexity, and the accurate pattern placement.

Probably the most promising alternative to photolithography is nanoimprint lithography (NIL). The principal idea behind NIL is to prepare a master with a high-resolution relief pattern first and to transfer it via imprinting. For this purpose, a casting mold is prepared from the master. Subsequently, this mold is immersed into a suitable resist that is coated onto a wafer. Depending on the resist, the pattern can either be fixed by curing with UV light or by cooling. When the mold is released, the resist assumes the shape of the master and the pattern can be transferred to the wafer in a further etching step. The advantage of this technique is that it is significantly cheaper as compared to other methods. After preparing the master once, multiple copies of the relief pattern can easily be transferred. Since the mold is in direct physical contact with the resist, release-induced defects constitute a major issue. A straightforward approach is to optimize the resist properties such that the defects can be reduced. This concept is also proposed by the ITRS, which states: “Historically, patterning has made as much resolution progress through the introduction of new materials and processes as it has through the introduction of new tools. We expect this trend to continue.”^[11] A fascinating class of materials which come into question as patterning resists are azobenzene-functionalized compounds.

Before going into detail about the potential applications of azobenzene-based materials in photolithography and NIL, another aspect emphasizing the impact of miniaturization on present technologies shall be discussed. With increasing ability to modify matter on the nanometer scale, mass storage devices have made a huge progress during the last half century. The most successful techniques developed for non-volatile data storage can roughly be divided into three categories. They comprise optical, magnetic, and, more recently, solid-state storage systems.

Non-volatile solid-state storage technology is mainly used in solid-state drives (SSDs), memory cards, and USB flash drives. In these devices, digital information is stored electrostatically by trillions of floating-gate metal-oxide-semiconductor field-effect transistors (FG-MOSFETs). A MOSFET is a voltage-controlled switch that consists of a source, a drain, and a gate electrode. The electric current between the source and the drain can be turned on or off by means of the applied gate voltage to represent the binary states “0” and “1”. FG-MOSFETs have a second, insulated gate which stores the electric field permanently, so the data is not lost when the device is turned off. As mentioned before, the market maturity and competitiveness of solid-state storage devices is a consequence of the growth of the semiconductor market. Downsizing and cost reduction of logical circuits were the prerequisite for the feasibility of this storage type. Solid-state storage devices have many advantages. First, they are very power-efficient. Second, SSDs have no moving parts and, thus, data can be written to, or accessed from, them very fast with rates up to several Gbit s^{-1} .^[12] Third, the data capacity of SSDs is very high, similar to that of the magnetic hard-disk drives discussed below. Nevertheless, solid-state storage devices are more expensive than magnetic ones, so both types share the market almost equally with each other.

The most common magnetic storage device used today is the hard-disk drive (HDD). It stores digital data in a magnetic medium along concentric tracks on a spinning disk. More precisely, a HDD consists of multiple aluminum or glass disks sputtered with magnetic layers. The disks are stacked above each other and are sealed in a protective atmosphere. To store digital data, an inductive write element locally modifies the magnetization within a small area on one of the magnetic disks. The magnetization direction of such a cell repre-

sents the two possible states of a digital bit. Read-out of the magnetization and conversion back to digital data is realized with a giant magnetoresistive sensor. Both the inductive element and the magnetoresistive sensor are mounted in a row on a slider and form the read and write head. To access or write data, the magnetic disk is rotated and the slider moves the head in radial direction. The technological innovations during the last 60 years enabled downsizing and denser arrangement of the magnetic domains, so the storage capacity of HDDs has increased by almost nine orders of magnitude during this time. The first HDD presented by IBM in 1956 allowed for the storage of only 2×10^{-3} Mbit in⁻²,^[13] whereas the storage density of modern HDDs is over 1 Tbit in⁻².^[14] Although heat assisted techniques promise slightly higher data densities, the limits of magnetic storage devices are almost exhausted. The reason for this is that thermal instabilities may cause a random flip of the magnetization if the grain size in the magnetic layer becomes too small. This effect is also known as superparamagnetism and inhibits the reduction of the size of a bit cell. Yet, HDDs constitute a cheap way to store large amounts of information and to access them with transfer rates as high as 1.5 Gbit s⁻¹.^[15]

The most successful representatives of optical storage media brought to market are CD, DVD, and BD. All three formats store digital information as a single spiral track of pits and lands on a polycarbonate disc. In pre-recorded discs, the pits are stamped with a master via imprint lithography. To enable optical readout, a reflecting metal layer is deposited on the generated pattern. A final lacquer layer protects the stored information from environmental impacts. Access to the stored information is gained by focusing a laser beam onto the data track and converting the reflected light back into digital bits. Also, optically recordable (write once) and rewritable (re-recordable) discs exist. They comprise an additional layer that consists of a light-sensitive organic dye (write-once discs) or a metal alloy (re-recordable discs).^[16] Depending on the format, different laser sources are used for inscription and readout. In CD systems, the wavelength is 780 nm, in DVD systems it is 650 and 635 nm, and in BD systems it is 405 nm. The shortening of the wavelength allows for a better focusing of the laser beam, which enhances the optical resolution. This allows for a denser arrangement of the data-representing pits and lands. For example, on a CD the pits have a width of 830 nm and the track distance is 1.6 μ m, whereas on a BD the corresponding values are 150 nm for the pit width and 320 nm for the track distance.^[17-19] Hence, the storage density and the data transfer rates of modern BD systems are significantly higher than those reached in CD devices. A single layer of a BD can store up to 33.4 GB of data, which corresponds to an approximate data density of 20 Gbit in⁻² and the data can be accessed with almost 600 Mbit s⁻¹. For comparison, a CD has a storage capacity of about 0.7 GB, its data density is below 1 Gbit in⁻², and the data transfer rates are on the order of 11 Mbit s⁻¹. Obviously, the above optical storage systems cannot compete with the high data densities of magnetic or solid-state storage devices. Yet, they are widely used, since they are cheap and allow for an easy exchange of the storage medium.

The capacity of optical storage media can be further increased by stacking multiple recordable layers within a single disc. For more than two superimposed layers, however, the signal-to-noise ratio becomes very low and this approach becomes impracticable.^[20] A conceptually different optical storage technique is holographic data storage (HDS). In a HDS system, a spatial light modulator (SLM) is illuminated with the light of a coherent laser. The SLM basically is a liquid-crystal display with a resolution up to several megapixels. Each of these pixels acts as a microscopic shutter for the incident laser light. Thus, the SLM translates a data array of logical bits into a two-dimensional light pattern consisting of bright and dark spots. The data page displayed by the SLM is projected onto a CCD camera. At the focus of the optical path, a holographic storage medium is placed. A second beam, referred to as the reference beam, passes through the storage medium at a different angle

and interferes with the first beam bearing the digital information. The latter is denoted the object or the signal beam. The holographic storage medium is photosensitive and changes its optical properties in the areas exposed to the laser light, so a hologram of the SLM image is recorded. To read-out the hologram, the storage medium is illuminated with the reference beam and the reconstructed object wave is processed by the CCD camera.

If the medium is much thicker than the writing wavelength, a Bragg or thick hologram develops. This type of hologram can be reconstructed only when the reference beam satisfies the Bragg condition, i. e., its wavelength, direction, and wavefront profile must be the same as during the inscription process. In this way, multiple holograms can be stored within the same volume of the storage medium and accessed individually by simply varying the angle of incidence of the reference beam. This technique is dubbed “angular multiplexing” and allows for the three-dimensional storage of digital information. Therefore, HDS systems reach significantly higher storage capacities and transfer rates than the currently available optical storage devices.^[20,21] Since millions of bits of digital information are stored or reconstructed simultaneously with a single flash of light, data transfer rates up to 1 Gbit s^{-1} are possible.^[22] For a 1.5 mm thick medium, which corresponds approximately to the thickness of a BD, the theoretical limit for the holographic storage density is as high as 40 Tbit in^{-2} .^[20] So far, data densities up to 663 Gbit in^{-2} have been demonstrated.^[23] Furthermore, an experimental consumer HDS drive with BD downward compatibility has been developed by the company InPhase. It allows for the storage of up to 2 TB on a disc with the same size as a BD and features transfer rates up to 400 Mbit s^{-1} .^[20] However, this device has not yet attained marketability. A reason for this is that the individual components such as the SLM, the CCD camera, or the imaging optics are very expensive. In addition, the materials requirements for holographic storage media are highly demanding. They include volumetric stability (i. e., absence of material shrinkage or thermal expansion), low scatter, easy manufacturability, high photosensitivity for recording, long-term stability of the inscribed holograms, and, ideally, rewritability.

A materials class which can be used for the inscription of holograms are photorefractive materials such as inorganic ferroelectric crystals (e. g., iron-doped LiNbO_3) or organic photoconductors. In these compounds, the holographic interference pattern is converted into a modulation of the refractive index due to the electro-optic effect.^[24-26] The latter occurs when the incident light excites the electrons of donor impurities into the conduction band. These electrons diffuse into areas of low light intensity and create a space-charge field which leads to the formation of a refractive-index grating. Although photorefractive storage media feature volumetric stability, reasonable refractive-index contrast, and rewritability, they do not meet important other requirements for HDS. Their main drawback is that without thermal aftertreatment the inscribed holograms are erased when exposed to light again. Since thermal fixing requires the medium to be heated to a temperature over $150 \text{ }^\circ\text{C}$,^[27] photorefractive materials become impracticable for consumer HDS drives. Another materials class suitable for HDS are photopolymer systems which consist of a photoreactive, polymerizable system dispersed in a polymer host.^[28,29] During inscription of a hologram, polymerization takes place in the bright areas of the interference pattern, whereas the monomer units remain unaffected in the dark areas. This leads to a concentration gradient, whereby the unreacted species diffuses into regions of higher intensity. With ongoing polymerization, the refractive index is modulated according to the holographic interference pattern. Since the polymerization is not reversible, photopolymer systems are most suitable for write-once-read-many (WORM) applications. The disadvantage of photopolymer systems is, however, that they rarely meet the criterion of volumetric stability.^[28,30] A promising alternative are photoaddressable systems such as azobenzene-functionalized polymers. Their suitability as holographic storage medium will be discussed below.

The previous discussion revealed that azobenzene-functionalized materials have a huge area of application including both lithography and holography. The different possibilities of use originate from the rich photophysics of the azobenzene chromophore, which constitutes the functional group of all compounds investigated in this thesis. As will be described in detail in Chapter 3, azobenzene exists either in the rodlike *trans* configuration or in the bent *cis* form. Both states can be converted into one another by the irradiation of visible light. These photoinduced isomerization cycles can either lead to a purely rotational motion or, in addition, to a translational movement of the azobenzene moieties. While the former is relevant for holography, the latter allows for the use of azobenzene-functionalized compounds as resist materials in lithographic applications.

The most widely used approach for the molecular design of a photoaddressable holographic storage medium is to functionalize a suitable polymer with azobenzene-containing side chains. When exposed to linearly polarized light, the azobenzene moieties begin to orientate and eventually align perpendicular to the electric light field due to a statistical selection process. This results in an optical anisotropy of the medium and, therefore, in the desired refractive-index modulation. For HDS applications, the translational motion must be suppressed since, otherwise, surface-relief patterns emerge which superimpose the hologram stored in the volume. First experiments were conducted on liquid-crystal side chain polymers by Wendorff and Ringsdorf in 1987.^[31,32] In the following years, various other liquid-crystalline polymers were the subject of intense research.^[33] In these compounds, the light-induced orientation of the azobenzene chromophores is stabilized by non-photoactive mesogenic units attached to the polymer backbone. Although this allows for the storage of long-term-stable holograms with a high refractive-index contrast, the possible applications of liquid-crystalline polymers in HDS are limited. The reason is that they tend to form a polydomain texture, which causes light scattering.^[17] Furthermore, in order to be rewritten, the inscribed holograms have to be erased through heating first.^[33] Photoinduced birefringence in amorphous azobenzene-functionalized homopolymers was first reported in 1992.^[34,35] These pioneering experiments demonstrated that anisotropy can be induced by light without the necessity of liquid-crystallinity. Moreover, the generated birefringence could be erased optically. Since the optical density of amorphous homopolymers is very high, the incident light is completely absorbed within a layer of less than a few hundred nanometers.^[36] Therefore, the inscription of thick holograms is not possible. Blending with photoinert polymers does not provide a satisfactory solution, since this would result in macrophase separation and, thus, in strong light scattering. To reach the optical density required for HDS, block copolymers represent a promising alternative.^[37-39] They typically consist of a photoinert majority and an azobenzene-functionalized minority block. In such block copolymers, the azobenzene phase forms nanometer-sized domains embedded in the inert phase. Thus, both the optical density and the light scattering remain low. In addition, the formation of surface patterns is efficiently suppressed^[40] and the spatial proximity of the chromophores is maintained, which allows for the storage of long-term-stable holograms.^[41] Finally, the azobenzene chromophores can be reorientated repeatedly by light, so optical erasure and frequent rewriting is possible. As a drawback, fairly long writing times are required to inscribe holograms into block copolymers, so their sensitivity is lower than that of inorganic ferroelectric crystals.^[37] This issue is addressed in one of the main sections of this thesis. It will be shown that the holographic performance of block copolymers can be significantly improved by blending them with azobenzene-functionalized molecular glasses. The latter are a class of organic, low-molecular-weight compounds capable of forming a stable amorphous phase (cf. Chapter 5).

As stated earlier, the second important scope of application for azobenzene-functionalized materials is photo- and nanoimprint lithography. This possibility of use arises from the fact that a large number of azobenzene-functionalized amorphous glass formers turn into the so-called photofluidic state when exposed to light.^[42–46] Simply speaking, photofluidization denotes the light-induced softening of amorphous azobenzene compounds that results from the repeated isomerization of the chromophores. In particular, photofluidizable materials have the ability to flow like a liquid without raising their macroscopic temperature. Chapter 3.3 is devoted to a detailed explanation of the underlying mechanism. A second important peculiarity of azobenzene-functionalized glass formers is that they migrate over macroscopic distances when exposed to an intensity or a polarization gradient. This effect was first described by the groups of Natansohn and Kumar in 1995.^[47,48] They found that the surface of azobenzene polymers can be reshaped by holographic exposure and that the resulting height profile resembles the intensity distribution of the interference pattern. Later experiments revealed the high sensitivity of this process to the polarization of the incident light.^[49–52] Despite large experimental and theoretical efforts, details of the driving force of the pattern formation remain unresolved until today.^[42,53] Although numerous models exist,^[54–60] none of them covers all the reported observations. In any case, photofluidization is required to enable the flow of the material below its glass transition temperature.

Surface structuring by means of optical gradients is most efficient in azobenzene-functionalized homopolymers^[33,40,61,62] and molecular glasses.^[50,63–67] Since surface-relief gratings (SRGs) can be generated easily with holographic methods, their formation has been investigated most widely so far. Different parameters such as the grating periodicity and the modulation height can be controlled simply by the polarization, the light intensity, or the irradiation time. For this reason, SRGs can be used for multiple applications, which include, e. g., diffractive elements,^[68] structural motifs for integrated electronic^[69] and energy devices,^[70–72] or etching masks for substrate patterning.^[73,74] The use of light-structurable azobenzene-functionalized compounds as resist materials in photolithography has also been demonstrated^[75] and promises different advantages as compared to micro- or nanopatterning methods based on conventional chemical etching. On the one hand, the surface deformation is completely reversible, i. e., relief patterns can be erased either by heating or light. Hence, multiple gratings can be superimposed to generate complex regular patterns.^[62,64,76] On the other hand, no cleaning step is required to remove unreacted agents after the exposure.

As discussed previously, the drawback of optical patterning methods is that the minimum structure size is limited by the wavelength of the light source. This restriction can be partially circumvented by using demanding methods that involve either the fabrication of proximity-field masks^[77] or the pre patterning of the resist.^[42] A different concept is to use azobenzene-functionalized compounds as resist materials in NIL instead.^[78,79] Since the former can flow like a liquid without considerable heating when exposed to light, they do not suffer from issues associated with thermal expansion. Furthermore, due to the intrinsic hydrophobicity of the azobenzene moieties, azobenzene materials are well suited for the fabrication of molding templates^[67,76,80] or, vice versa, for patterning by elastic polydimethylsiloxane stamps.^[78,79] Therefore, photofluidizable materials promise to be efficient patterning resists in NIL. The quantification of their suitability for imprinting is the subject of a main section of this work.

In the present thesis, both the holographic properties and the light-driven surface shaping of azobenzene-functionalized molecular glasses and polymers are investigated. The previous discussion illustrates the high demand for these applications and emphasizes the important role azobenzene-based compounds play for them. To understand the photophysics and to emphasize the application scope of azobenzene materials, the outline of this thesis is as follows.

Since holography and imprint lithography relate to different contents, the theoretical part is divided into three chapters. The relevant aspects of the theory of holography are described in Chapter 2. The properties and physics of azobenzene-functionalized materials and the associated phenomena such as SRG formation and photofluidization are discussed in Chapter 3. The concept of azobenzene-based NIL is developed in Chapter 4, which also includes theoretical considerations about the liquid transport in confined channels. A detailed characterization of the azobenzene polymers and molecular glasses used in the experiments is given in Chapter 5. Imprinting of micro- and nanometer-sized features is performed with flexible, adhesive stamps. Hence, Chapter 6 is devoted to their fabrication and their physical properties. The setups used for the holographic and NIL experiments are the subject of Chapter 7.

The experimental findings are thematically divided into four different parts. Chapter 8 provides a guide on how to improve the holographic performance of photoaddressable block copolymers by blending them with an azobenzene-functionalized molecular glass. The latter acts as a photoplasticizer and accumulates mainly in the minority phase of the block copolymers, so only molecular reorientation occurs during light exposure. A significant improvement of the holographic performance is achieved already at low molecular-glass content and the important characteristics of the block copolymer such as low optical density and long-term stability can be retained. A new method for the determination of refractive indices is developed and characterized in Chapter 9. It is based on measuring the critical diffraction angles of the different orders that emerge behind a grating. As compared to other methods, its advantage is that no information about the thickness of the medium is required. This topic relates to both holography and lithography, since the investigated surface relief gratings are first generated optically on an azobenzene-functionalized resist and then transferred to a transparent polymer film by molding. The usability of azobenzene-functionalized molecular glasses and homopolymers for imprinting nanometer-sized structures is investigated in Chapter 10. After preparing films of these compounds and generating their photofluidic state by light exposure, adhesive stamps are imprinted into them. The influence of the light wavelength, the external pressure, the temperature, and the molecular substituent of the azobenzene moieties on the imprinting process is analyzed in detail. From these basic experiments, the optimum experimental parameters and materials properties for high imprinting speed and quality are derived. Finally, Chapter 11 discusses important aspects of the optically induced mass migration in azobenzene-functionalized molecular glasses upon holographic illumination. Whereas the material is transported in the direction of the optical gradient for low light exposure, migration also occurs in the perpendicular direction for higher doses.

Theory and Basic Concepts of Holography

The concept of holography involves a two-step procedure, the recording and reconstruction of optical wave fronts. Recording a hologram denotes the process of storing the electric-field distribution of at least two interfering electromagnetic waves inside a photo-active medium. Unlike conventional photography, the stored pattern has no similarity to the object from which the light is emitted. The reason is that the interference pattern does not only contain information about the amplitude of the light wave, but also about its phase. The spatial information can be restored in a subsequent reconstruction step, generating a spatial impression identical to the one of the original image.

It was D. Gabor who invented the technique in 1948^[81] and suggested the term “holography”, which originates from Greek and means writing the complete information. His idea was to improve the resolution of transmission electron microscopy, but different problems arose, e. g., the missing of coherent light sources with sufficient intensity. It took until the invention of the laser in the 1960s when holography was revived by E. N. Leith and J. Upatnieks.^[82] Although Gabor did not solve the problem he originally intended, he finally was awarded the Nobel Prize in 1971 “for his invention and development of the holographic method”.^[83]

Half a century later, holography has developed to an extensive area of research. Different techniques have evolved, starting from Gabor’s inline holograms to the now common off-axis method. Theories have been developed to describe the diffraction off volume and surface-relief gratings. Depending on the physical properties of the storage medium, either the Raman-Nath or Bragg diffraction regime applies. A summary of important aspects is given in the following.

2.1 Plane-Wave Holography

In general, the interference of a plane wave and the coherent light emitted from an extended, three-dimensional object yields a complicated field distribution in the hologram plane. In the special case of the superposition of two coherent plane waves of equal wavelength, a simple sinusoidal interference pattern results. The latter is used for the inscription of volume or surface relief gratings. Both grating types contain all essential information about the suitability of a material as a holographic storage medium. Holographic reconstruction with a plane wave corresponds to grating diffraction in this case.

2.1.1 Field Distribution of Interfering Plane Waves

Superimposing an object and a reference plane wave \vec{E}_{obj} and \vec{E}_{ref} with equal frequency ω yields the total field

$$\vec{E}_{\text{tot}}(x, z, t) = \vec{E}_{\text{obj}} + \vec{E}_{\text{ref}} = \vec{E}_{0,\text{obj}} e^{i(\vec{k}_{\text{obj}}\vec{r} - \omega t)} + \vec{E}_{0,\text{ref}} e^{i(\vec{k}_{\text{ref}}\vec{r} - \omega t + \Delta\phi)}. \quad (2.1)$$

If both waves are coherent, they have a fixed phase relationship and the common time-dependent phase factor $\exp(-i\omega t)$ can be dropped for simplicity. The phase shift $\Delta\phi$ in Eq. (2.1) corresponds to the difference in travel time in this case. In the coordinate system depicted in Fig. 2.1 the wave vectors become

$$\vec{k}_{\text{ref}} = \frac{2\pi n_0}{\lambda_w} \begin{pmatrix} -\sin \theta_{\text{ref}} \\ 0 \\ \cos \theta_{\text{ref}} \end{pmatrix}, \quad \vec{k}_{\text{obj}} = \frac{2\pi n_0}{\lambda_w} \begin{pmatrix} \sin \theta_{\text{obj}} \\ 0 \\ \cos \theta_{\text{obj}} \end{pmatrix} \quad \text{and} \quad \vec{K} = \vec{k}_{\text{ref}} - \vec{k}_{\text{obj}}$$

with λ_w being the vacuum wavelength of the incident writing waves and n_0 the refractive index of the medium. The vector sum of the object and reference wave vector results in the grating vector \vec{K} . The above assumptions imply that the waves already propagate inside the medium ($n = n_0$ for $z < 0$). The boundaries can simply be taken into account by calculating the angles of the plane waves inside the medium according to Snellius' law.

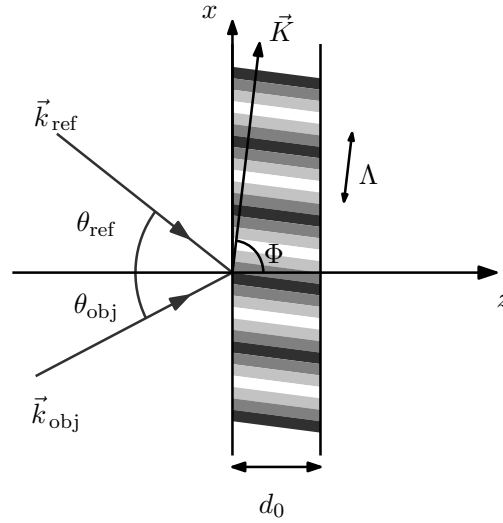


Figure 2.1: Schematic diagram of the sinusoidal interference pattern generated by two interfering plane waves in a medium of thickness d_0 . The y -axis is perpendicular to the x - z -plane. Λ : Grating period, \vec{K} : grating vector, Φ : slant angle.

If the angles of incidence are equal ($\theta_{\text{ref}} = \theta_{\text{obj}} = \theta$), the grating is unslanted, i. e., $\Phi = 90^\circ$ (cf. Fig. 2.1). In this case the total electric field becomes

$$\vec{E}_{\text{tot}}(x, z) = \begin{pmatrix} E_{0x,\text{obj}} e^{i\pi x/\Lambda} + E_{0x,\text{ref}} e^{-i\pi x/\Lambda} \cdot e^{i\Delta\phi} \\ E_{0y,\text{obj}} e^{i\pi x/\Lambda} + E_{0y,\text{ref}} e^{-i\pi x/\Lambda} \cdot e^{i\Delta\phi} \\ E_{0z,\text{obj}} e^{i\pi x/\Lambda} + E_{0z,\text{ref}} e^{-i\pi x/\Lambda} \cdot e^{i\Delta\phi} \end{pmatrix} \cdot e^{i2\pi n_0 \cos \theta z / \lambda_w} \quad (2.2)$$

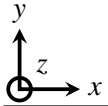
with

$$\Lambda = \frac{\lambda_w}{2n_0 \sin \theta}. \quad (2.3)$$

Without specification of the polarization state of object and reference wave, the total field is an unknown function of x and z . It can be seen, however, that the z dependency just describes the propagation of the wave, while the x dependency is responsible for the formation of a grating with grating period Λ .

Basically a large number of polarization states is conceivable, but only few of them are of practical importance. Without loss of generality, the phase difference can be chosen to be $\Delta\varphi = 0$. For equal amplitudes $|\vec{E}_{\text{obj}}| = |\vec{E}_{\text{ref}}| = E_0$ and some selected polarization states of the reference and object wave, the electric field in the x - y -plane at $z = 0$ takes the form shown in Table 2.1. The oscillation of \vec{E}_{tot} perpendicular to the plane of incidence is denoted as *ss* polarization, while the single letters indicate the polarization states of the individual waves. Accordingly, the oscillation of \vec{E}_{tot} in the x - z -plane is the *pp*-polarization state. The $\pm 45^\circ$ -state is generated by using waves with polarizations rotated to an angle of $\pm 45^\circ$ with respect to this plane. The term *rlcp* describes the interference of a left and a right circularly polarized wave also denoted as ‘‘orthogonal’’ polarization. Further polarization configurations can be found in the literature.^[62,84,85]

Table 2.1: Electric field of two interfering plane waves of equal amplitude and angle of incidence in the x - y -plane at $z = 0$. The arrows indicate the direction and time-dependent amplitude of the field for small angles of incidence, i. e., $\theta \rightarrow 0$. Red dots indicate the direction of \vec{E}_{tot} at $t = 0$, while black dots mean zero intensity. The coordinate system corresponds to the one shown in Fig. 2.1. A prefactor i denotes an optical phase shift by $\pi/2$.

	Field $\vec{E}_{\text{tot}}(x, z = 0)$	$x = 0$	$\Lambda/4$	$\Lambda/2$	$3\Lambda/4$	Λ
<i>ss</i>	$2E_0 \begin{pmatrix} 0 \\ \cos(\pi x/\Lambda) \\ 0 \end{pmatrix}$					
<i>pp</i>	$2E_0 \begin{pmatrix} \cos\theta \cos(\pi x/\Lambda) \\ 0 \\ i \sin\theta \sin(\pi x/\Lambda) \end{pmatrix}$					
<i>sp</i>	$E_0 \begin{pmatrix} \cos\theta e^{-i\pi x/\Lambda} \\ e^{i\pi x/\Lambda} \\ \sin\theta e^{-i\pi x/\Lambda} \end{pmatrix}$					
$\pm 45^\circ$	$\sqrt{2}E_0 \begin{pmatrix} \cos\theta \cos(\pi x/\Lambda) \\ i \sin(\pi x/\Lambda) \\ -i \sin\theta \sin(\pi x/\Lambda) \end{pmatrix}$					
<i>rlcp</i>	$\sqrt{2}E_0 \begin{pmatrix} \cos\theta \cos(\pi x/\Lambda) \\ -\sin(\pi x/\Lambda) \\ -i \sin\theta \sin(\pi x/\Lambda) \end{pmatrix}$					

The superposition of two waves with equal linear polarization, i. e., *ss* or *pp*, results in a sinusoidal variation of the intensity with the same polarization. Pure polarization gratings with constant intensity are obtained by mixing different states of polarization, such as in the *sp*, $\pm 45^\circ$, and *rlcp* configuration. It is worth to mention that only *rlcp* illumination generates a completely linearly polarized electric field with a rotating polarization vector. Other polarization gratings change from linearly to circularly polarization and, therefore, the transition areas are exposed to elliptical polarized light. The formulas listed in Table 2.1

for the total field are exact expressions. They imply, that except for the ss -polarized field, the plotted arrows become tilted if θ strongly deviates from zero.^[86] The black arrows also indicate an oscillation of \vec{E}_{tot} as time proceeds, while the red dots represent its initial direction. As the interaction of a photo-active material with the electric field only depends on the field amplitude but not on its sign, the periodicity of the inscribed grating is given by Λ .

2.1.2 Grating Diffraction

As mentioned above, a photo-active medium placed at the plane of interference interacts with the electric field distribution. This interaction changes the optical parameters (refractive index, absorption or sample thickness) in the illuminated areas and, ideally, results in a permanent storage of the interference pattern. An off-axis hologram is generated, if reference and object beam have different propagation directions while they enter the medium from the same side. If the object beam contains information about a three-dimensional object its reconstruction would appear on the other side of the sample, suggesting the term “transmission hologram”. Since there is no object present in the case of plane-wave holography, the storage of the interference pattern of object and reference beam results in a very simple hologram, i. e., a diffraction grating.

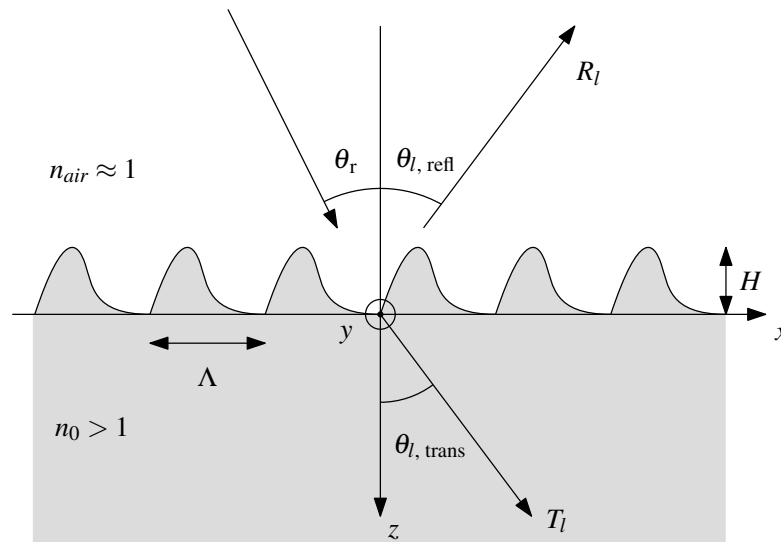


Figure 2.2: Diffraction of a plane wave off a grating with arbitrary periodic shape. Reflected orders appear under angles $\theta_{l, \text{refl}}$, transmitted ones under $\theta_{l, \text{trans}}$. The maximum height of the grating is H .

Three types of diffraction gratings may be distinguished, i. e., absorption, refractive-index and surface-modulated gratings. A schematic diagram of the latter is shown in Fig. 2.2. To provide access to the theory of grating diffraction in a more general manner, the surface of the depicted grating is assumed to be modulated periodically but the shape may, for the time being, be given by any function that fulfills $d(x) = d(x + m\Lambda)$ with $m \in \mathbb{N}$. Analogous expressions shall be valid for absorption or refractive-index gratings. Here the surface stays flat and the grating constitutes a periodic modulation of the respective parameter in the volume of the material. Figure 2.1 of the preceding chapter provides an illustration of the situation in this case. From the assumption that refractive index n , absorption α , or

thickness d of the material are periodic, it follows that they can be represented as Fourier series:

$$\begin{aligned} n(x) &= n_0 + \Delta n(x) = n_0 + \sum_{m=1}^{\infty} \left[n_{cm} \cos\left(\frac{2\pi mx}{\Lambda}\right) + n_{sm} \sin\left(\frac{2\pi mx}{\Lambda}\right) \right] \\ \alpha(x) &= \alpha_0 + \Delta\alpha(x) = \alpha_0 + \sum_{m=1}^{\infty} \left[\alpha_{cm} \cos\left(\frac{2\pi mx}{\Lambda}\right) + \alpha_{sm} \sin\left(\frac{2\pi mx}{\Lambda}\right) \right] \\ d(x) &= d_0 + \Delta d(x) = d_0 + \sum_{m=1}^{\infty} \left[d_{cm} \cos\left(\frac{2\pi mx}{\Lambda}\right) + d_{sm} \sin\left(\frac{2\pi mx}{\Lambda}\right) \right] \end{aligned} \quad (2.4)$$

The diffraction off the grating can be measured either by illumination with one of the writing beams or a plane wave at a different wavelength λ_r . The latter has the advantage that λ_r can be chosen such that it does not influence the process of grating formation. If any of the three material parameters α , n , or d satisfies Eq. (2.4), the diffracted field $E'_{\text{tot}}(x, z)$ becomes pseudo periodic,^[87,88] i. e., $E'_{\text{tot}}(x + \Lambda, z) = E'_{\text{tot}}(x, z) \exp(ik_r \Lambda \sin \theta_r)$ with $k_r = 2\pi n_{\text{air}}/\lambda_r$ and θ_r being the angle of incidence of the reading wave. Based on this assumption it can be shown,^[88] that for the situation depicted in Fig. 2.2 the diffracted electric field of an incident s -polarized plane wave takes the form

$$E'_{\text{tot}}(x, z) = \begin{cases} \exp(i\beta_0 x + i\gamma_0 z) + \sum_{l=-\infty}^{+\infty} R_l \exp(i\beta_l x - i\gamma_l z) & \text{if } z < -H \\ \sum_{l=-\infty}^{+\infty} T_l \exp(i\beta_l x + i\delta_l z) & \text{if } z > 0 \end{cases} \quad (2.5)$$

$$\text{with } \beta_l = k_r \sin(\theta_r) + 2\pi l/\Lambda, \quad \gamma_l = \sqrt{(k_r^2 - \beta_l^2)} \quad \text{and} \quad \delta_l = \sqrt{(4\pi^2 n_0^2/\lambda_r^2 - \beta_l^2)}.$$

To simplify matters, the amplitude of the incident field has been set to one in Eq. (2.5). The diffracted and the incident beam have the same polarization, therefore $\vec{E}'_{\text{tot}}(x, z)$ is s -polarized ($\vec{E}'_{\text{tot}}(x, z) = E'_{\text{tot}}(x, z)\hat{e}_y$). As can easily be seen, the diffracted field before and behind the grating resembles a plane-wave expansion and various diffracted orders can emerge. For the sake of clarity, only the l^{th} transmitted and reflected order have been plotted in Fig. 2.2. It is an important result that arbitrary grating types (surface relief or volume gratings) of arbitrary shape (sinusoidal, rectangular, etc.) follow Eq. (2.5) as long as they do not meet the requirements of the Bragg regime, which are discussed later. The reason for this is the assumption of the pseudo-periodicity of the diffracted wave, which is affected by Λ only and not by the exact grating geometry. However, the grating type and shape will affect the amplitudes R_l and T_l , which need to be derived for the special physical situation.

Additionally, the famous grating equation results from Eq. (2.5) in a more general way than in the case of a geometrical consideration of the optical paths. From $\beta_l = k_r \sin(\theta_{l, \text{refl}}) = 2\pi n_{\text{air}} \sin(\theta_{l, \text{refl}})/\lambda_r$ for $z < -H$ and $\beta_l = 2\pi n_0 \sin(\theta_{l, \text{trans}})/\lambda_r$ for $z > 0$ it follows that

$$n_{\text{air}} \sin \theta_{l, \text{refl}} = n_{\text{air}} \sin \theta_r + l\lambda_r/\Lambda \quad \text{if } z < -H \quad (2.6)$$

$$n_0 \sin \theta_{l, \text{trans}} = n_{\text{air}} \sin \theta_r + l\lambda_r/\Lambda \quad \text{if } z > 0. \quad (2.7)$$

For simplicity, the above results were derived from the assumption that an s -polarized plane wave is diffracted. The analysis for p -polarized light is similar.

The surface relief gratings discussed in this thesis emerge due to the unique photo-physical properties of the azobenzene functionalization of the storage medium. As discussed later, these materials allow for a macroscopic, photo-induced material transport if they are exposed to an intensity or polarization gradient. The modulation of the thickness of SRG

forming materials can, in the simplest case, be approximated by $d(x) = d_0 + d_1 \cos(2\pi x/\Lambda)$ with d_0 being the initial sample thickness before the illumination. Here, the modulation amplitude d_1 is related to the grating height by $H = 2d_1$. SRGs inevitably feature an in-phase absorption modulation, since the writing waves are absorbed more strongly in the hills than in the valleys of the grating. The contribution of the absorption grating to the diffracted field becomes negligible if λ_r of the readout beam is chosen to be outside the absorption of the photo-active medium.

Volume gratings, on the other side, are based on a local, molecular reorientation, which results in a periodic modulation of the refractive index. As long as the material response is linear, the refractive index reads $n(x) = n_0 + n_1 \sin(2\pi x/\Lambda)$ with all other Fourier components being zero. Again, the absorption stays unmodulated for the readout beam and $\alpha(x)$ in Eq. (2.4) reduces to $\alpha(x) = \alpha_0$, being the absorption of the material at the readout wavelength. The interpretation of Δn in photo-orientable materials is slightly different for gratings generated with intensity or polarization modulated fields. In the former case, Δn simply corresponds to the difference of the refractive index between illuminated and dark regions. For the polarization gratings, however, the whole medium is homogeneously illuminated with constant intensity. Hence, Δn is a measure of the optically induced anisotropy, which is defined as the difference between the ordinary and the extra-ordinary refractive index. Unlike in uniaxial crystals, the optical axis is not predefined here; instead it is photo-induced with its orientation depending on the polarization azimuth of the incident light. This distinction is important, since the theoretical description differs for the various grating types.

To characterize the holographic performance of the investigated materials, the intensities of the diffracted orders need to be analyzed. A suitable quantity for this purpose is the diffraction efficiency

$$\eta_l = \frac{I_l}{I_{\text{tot}}}, \quad (2.8)$$

defined as the ratio of the light intensity diffracted into the l^{th} order and the total incident intensity I_{tot} . The theoretical description in the next chapters will focus on the determination of the diffraction into the 1st order. Two diffraction regimes are introduced and the difference between scalar, polarization and surface relief gratings is discussed in detail.

2.2 Diffraction Regimes of Gratings

The diffraction behavior of a holographic volume grating depends on the physical properties of the storage medium. Depending on whether the grating is of the Raman-Nath or Bragg type, the theoretical description of the diffraction differs strongly. To assign a grating to one of the two diffraction regimes, the parameter

$$Q' = \frac{2\pi\lambda_r d_0}{n_0 \Lambda^2 \cos \theta_r} \quad (2.9)$$

and the modulation

$$\gamma = \frac{\pi n_1 d_0}{\lambda_r \cos \theta_r} \quad (2.10)$$

are decisive.

The requirements of the Raman-Nath or multi-wave diffraction regime are met if $Q' \ll 1$ or $Q'\gamma \leq 1$.^[89] In this case, light incident at arbitrary angles is diffracted into several different orders, which emerge behind the grating. Their diffraction efficiency is given by the Fourier coefficients of the refractive-index modulation.^[90] If $\rho = Q'/2\gamma \geq 10$, the grating

shows Bragg diffraction.^[91] A Bragg grating can diffract light solely into the 0th and 1st order, the intensity of the other orders being negligibly small. The light has to be incident at a certain angle, i. e., the Bragg angle; otherwise no diffraction can be observed at all. If the modulation decreases to values $\gamma \ll 1$ the diffraction efficiency of the 1st order is described equivalently in both regimes.^[89]

It should be noted that ρ is independent of the thickness of the grating. Earlier definitions of the Bragg regime only claim that Q' needs to be larger than 10, and Q' is a thickness-dependent parameter.^[92,93] Therefore, the term “Bragg diffraction” usually is taken as being a synonym for the diffraction off “thick” gratings. In the context of holographic data storage the equivalent use of both terms is correct, since high angular selectivity is achieved only by increasing the sample thickness to at least hundredfold of the grating period (see Chapter 2.5). However, one should keep in mind that Bragg-like behavior can be observed if both parameters Q' and γ are sufficiently small at the same time.^[91] Gratings of the Raman-Nath type are “thin” by definition.

The above definitions are easily applicable to volume gratings but need to be modified for the characterization of SRGs. To estimate values for Q' and γ one needs to replace d_0 , n_0 and n_1 by their corresponding parameters. The film thickness d_0 corresponds to the SRG amplitude d_1 , which is typically on the order of a few 100 nm. The refractive index modulation n_1 becomes the difference between the refractive index of the SRG former and air ($\Delta n \approx 0.5$), while n_0 has to be substituted by an average value which is on the order of 1 to 1.5. Substitution of the experimental parameters yields Q' and γ values slightly below 1, which assigns the investigated SRGs to the Raman-Nath regime.^[89] As will be discussed later, the diffraction behavior of the SRGs yields further evidence for this. An exception are lithographically prepared subwavelength SRGs fulfilling $\Lambda < \lambda_r$, which actually show Bragg-diffractive behavior.^[43,94]

2.3 Raman-Nath Diffraction off Thin Scalar Gratings

The theoretical description of scalar refractive-index and surface-modulated phase gratings is almost identical in the Raman-Nath regime. In both cases a transmittance function is defined for the reading wave, which is only sensitive to differences in the phase. The diffraction efficiency of many different shapes of thin refractive-index gratings (sinusoidal, rectangular, sawtooth, etc.) can be calculated analytically.^[90] The 1st order diffraction efficiency of a sinusoidal, scalar refractive-index grating has been calculated by Magnusson and Gaylord.^[89] For an *s*-polarized incident wave they derive the expression

$$\eta_1 = J_1^2(2\gamma) \cdot e^{-2\alpha_0 d_0 / \cos \theta_r} \approx J_1^2 \left(\frac{2\pi n_1 d_0}{\lambda_r \cos \theta_r} \right), \quad (2.11)$$

with J_1 being the Bessel function of the first kind of first order. If the reading wavelength is chosen such that the absorption in the medium is negligibly small, the exponential term can be omitted. The theoretical model assumes that the grating is already present in the sample. Thus, it neglects the influence of the vector character of the electric field of the writing beams on the photo-orientable medium. The latter is subject to the theory of polarization holography, which is briefly discussed in Chapter 2.4.

For Raman-Nath SRGs, the analogous expression to Eq. (2.11) reads:^[70,84,95]

$$\eta_1 = J_1^2 \left(\frac{2\pi \Delta n d_1}{\lambda_r \cos \theta_r} \right) \quad (2.12)$$

The surface of the medium is assumed to be sinusoidally modulated, the grating height being $2d_1$. The difference between the refractive indices of the material and air is denoted by $\Delta n = n_0 - n_{\text{air}}$.

In the Raman-Nath regime, a sinusoidal phase grating diffracts an incident plane wave into multiple orders. For the first order, Eq. (2.11) and (2.12) predict a maximum achievable diffraction efficiency of 33.8%. The diffraction efficiencies of orders with $|l| \geq 2$ are calculated from Bessel functions of higher orders and have negligible intensities as long as γ is sufficiently small.^[90] In this case, J_1 can be Taylor-expanded and replaced by

$$\eta_1 = J_1^2(2\gamma) \approx \gamma^2 = \left(\frac{\pi n_1 d_0}{\lambda_r \cos \theta_r} \right)^2. \quad (2.13)$$

The error of this approximation is less than 1% for $\gamma < 0.3$ or $\eta_1 < 0.1$, respectively. Usually this limit is valid for refractive-index modulated phase gratings with small n_1 . For SRGs, the value of γ can become quite high and significant power is diffracted into higher orders.^[96] The exact determination of the argument of the Bessel function is accomplished in this case by applying Newton's method for finding roots.

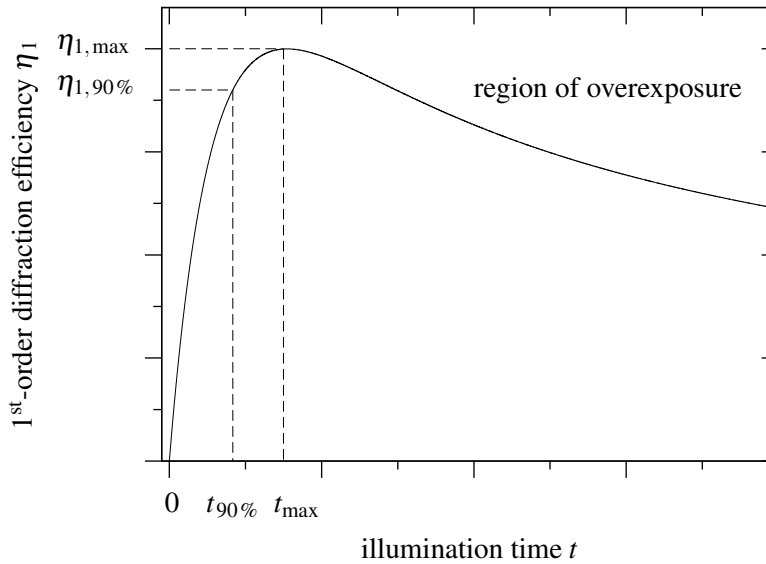


Figure 2.3: Diffraction efficiency of the first order as a function of the writing time for a volume grating.

An idealized curve for the temporal evolution of the diffraction efficiency of a thin volume grating is shown in Fig. 2.3. Due to the spatially varying electric-field distribution of the writing beams, a sinusoidal phase grating develops in the volume of the photo-active medium. After an initial steep increase, η_1 passes through a maximum denoted by $\eta_{1,\text{max}}$ and decreases afterward. For scalar gratings stored in the volume of the storage medium, the decay of η_1 at long illumination times usually can be attributed to the overexposure of the hologram. While the induced anisotropy in the bright areas reaches its maximum value first, the less exposed areas become oriented after longer illumination times. It should be noted that Eq. (2.11) and (2.12) are not valid in the region of overexposure, since the additional Fourier coefficients in Eq. (2.4) cause the diffraction behavior of the grating to be altered.

To characterize the holographic suitability of a material, the maximum achieved refractive-index modulation and the writing time can be specified. The former can be calculated from $\eta_{1,\text{max}}$ and is, therefore, denoted by $n_{1,\text{max}}$. It is important to realize, that for exceed-

ingly high values of γ the maximum of the Bessel function and the maximum caused by overexposure may overlap. The exact position of $\eta_{1,\max}$ is difficult to determine because the maximum is usually much broader than in the idealized case depicted in Fig. 2.3. To reduce the uncertainty of measurement, $t_{90\%}$ is introduced, which is the time required to reach 90 % of the maximum diffraction efficiency. Because the slope of $\eta_1(t)$ has a value significantly different from zero there, $t_{90\%}$ is well defined.

As a final remark, it should be noted that refractive-index and surface relief gratings can develop in the medium at the same time. Both gratings are not necessarily in phase. A deeper analysis is required to describe their overall diffraction efficiency.^[84,97–99] The largest contribution, however, usually originates from the SRG, while the diffraction off the refractive-index grating is negligibly small, except for very short writing times. Thus, Eq. (2.12) can also be applied for superimposed gratings.

2.4 Raman-Nath Diffraction off Thin Polarization Gratings

The holographic storage media investigated in this thesis are functionalized with photo-orientable azobenzene moieties (cf. Chapter 3.1). Upon illumination with polarized light they preferably align perpendicular to the electric field, whereby the refractive index of the material becomes anisotropic. The diffraction behavior of gratings stored in such materials can strongly deviate from that of the scalar type. For their theoretical description, the concept of polarization holography has to be applied, which is based on the Jones-matrix formalism.^[100] Within this approach the polarization state of a plane light wave is represented by a two-dimensional vector, the Jones vector. Hence, the electric field of a polarization or an intensity grating has a Jones-vector representation with spatially varying entries, resembling the polarization states depicted in Table 2.1 in Chapter 2.1. Assuming that the medium is photo-orientable, its refractive index becomes spatially modulated when illuminated with the optical grating. Therefore, the transmission function of the holographic medium turns into a Jones matrix, which can be applied to the Jones vector of the readout wave. The intensities of the diffracted orders and, moreover, the polarization state of the wave behind the grating can then be calculated easily. A more detailed description of the Jones formalism is given in the book of Azzam and Bashara.^[101]

The situation is illustrated in Fig. 2.4 for the example of an *ss*-polarized intensity grating, illuminating a photo-orientable medium. The molecules are assumed to orient perpendicular to the polarization direction of the light, while the degree of orientation changes proportionally to the spatially varying intensity. A polarized readout wave propagating along the z axis will see two different refractive-index modulations $n_{1,\parallel}$ and $n_{1,\perp}$ depending on whether its polarization is parallel or perpendicular to the light-induced optical axis in the illuminated areas. A variation of the diffracted intensity is expected if the polarization of the incident light is rotated by an angle ϑ in the xy plane.

The results presented in the following are a summary of theoretical considerations found in the literature.^[84,96,102] It is assumed that the writing beams have equal intensity and that the angle between them is small. Furthermore, no absorption shall be present in the sample. For the sake of simplicity, the readout wave is incident perpendicular to the surface normal of the medium, i. e., $\theta_r = 0$.

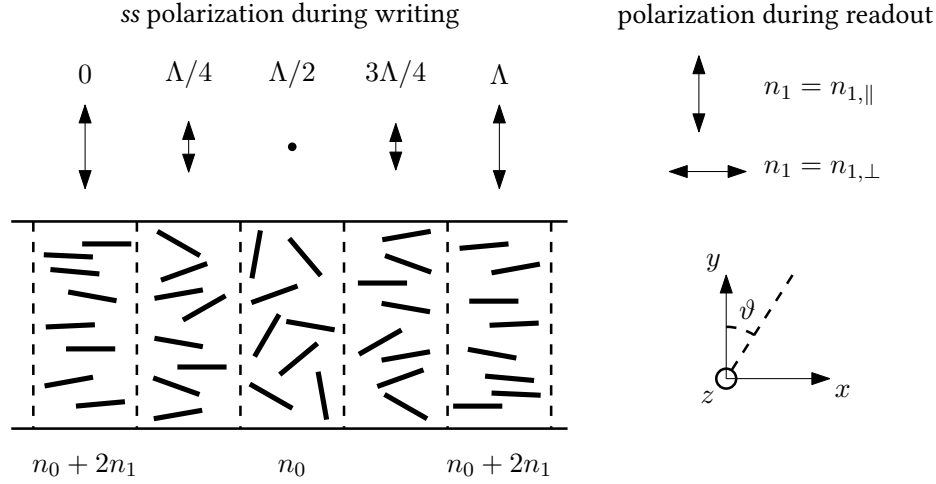


Figure 2.4: Sketch of the molecular alignment in a photo-orientable material upon illumination with an *ss*-polarized grating. Light waves of different polarization see different refractive-index modulations n_1 . The rotation of the polarization direction of the readout wave in the xy plane is denoted by ϑ .

2.4.1 Diffraction off a Grating Generated by *ss* Illumination

The 1st order diffraction efficiency of an anisotropic grating generated by an *ss*-polarized intensity grating is

$$\eta_1 = J_1^2 \left(\frac{2\pi n_{1,\parallel} d_0}{\lambda_r} \right) \cos^2 \vartheta + J_1^2 \left(\frac{2\pi n_{1,\perp} d_0}{\lambda_r} \right) \sin^2 \vartheta, \quad (2.14)$$

if it is illuminated with a linearly-polarized plane wave. Equation (2.14) and the formula for the diffraction efficiency of a scalar grating (Eq. (2.11)) become equivalent if $n_{1,\parallel} = n_{1,\perp} = n_1$. The dependence on ϑ vanishes in this case, which is the expected behavior for a scalar grating. If such a grating is illuminated with *s*-polarized light, the diffraction efficiency looks similar to the one of a scalar grating because the second term in Eq. (2.14) becomes zero ($\vartheta = 0$). However, the refractive-index modulation is $n_{1,\parallel}$ in this case, while one would measure $n_{1,\perp}$ if the hologram were illuminated with a *p*-polarized wave. This detail is often ignored in the literature and gratings generated with *s*-polarized writing beams are frequently referred to as being scalar. In general, the polarization of the reconstructed wave is a complicated function of $n_{1,\parallel}$ and $n_{1,\perp}$ for this grating type. For the special case of a scalar grating it can be shown that incident beam and diffracted orders have the same polarization.

2.4.2 Diffraction off a Grating Generated by *sp* Illumination

If an *sp* polarization grating is stored in the photo-orientable medium, the 1st order diffraction efficiency of a linearly-polarized plane wave reads

$$\eta_1 = J_1^2 \left(\frac{2\pi n_1 d_0}{\lambda_r} \right) \quad (2.15)$$

with $n_1 = n_{1,\perp} - n_{1,\parallel}$. Obviously, there is no dependence on the polarization angle ϑ of the incident wave. The diffraction behavior of the grating is the same as the one of an ordinary scalar grating, provided that n_1 is interpreted as discussed in Chapter 2.1. The polarization

of the diffracted wave shows an interesting behavior. For the odd orders it is rotated by an angle of 2ϑ in the xy plane and the grating acts as a $\lambda/2$ plate. The even orders, on the other hand, have the same polarization as the incident light.

2.4.3 Diffraction off a Grating Generated by *rlcp* Illumination

The *rlcp* polarization grating has the special characteristic to be polarized linearly throughout the whole interference plane. This results in remarkable properties of the grating stored in a photo-orientable medium. Light of arbitrary polarization is diffracted into maximally three orders, namely the orders 0 and ± 1 . As a consequence, the diffraction efficiency into the $\pm 1^{\text{st}}$ orders becomes higher than in the previous cases. For a linearly-polarized readout wave it can be shown that

$$\eta_1 = \eta_{-1} = \frac{1}{2} \sin^2 \left(\frac{2\pi n_1 d_0}{\lambda_r} \right). \quad (2.16)$$

Irrespective of the polarization direction, the $+1^{\text{st}}$ order is right-handed and the -1^{st} order is left-handed circularly polarized. The maximum diffraction efficiency is as high as 50%. This value can be increased even further if the readout wave is circularly polarized. In this case, Eq. (2.16) becomes $\eta_1 = \sin^2(2\pi n_1 d_0 / \lambda_r)$ and the diffraction into the -1^{st} order completely vanishes. Hence, the first-order diffraction can be as high as 100% even for a thin Raman-Nath grating. The diffracted orders switch their role depending on whether the incident light is left- or right-handed circularly polarized. This finding impressively illustrates the potential of photo-orientable materials as holographic writing media as compared to conventional scalar storage media.

2.5 Bragg Diffraction off Thick Scalar Gratings

The 1^{st} -order diffraction off a thick Bragg grating is discussed based on the theory of Kogelnik.^[92] In his model a homogeneous, scalar grating with straight fringes is already present in the volume of the sample. Hence, the dynamics of grating formation are not taken into account. If photo-orientable materials are used, their capability of real-time recording usually results in self-diffraction.^[84,86,103] Both the phase difference between the writing beams and their intensities become a function of the coordinate z along the depth of the material in this case. Thus, the writing beams transfer energy between each other if a thick sample is placed in the plane of interference (two-beam coupling). This is a typical indicator for the dynamic formation of curved grating fringes.^[84] Still, Kogelnik's theory represents a well-established model for the description of the Bragg diffraction off thick samples.

As stated in Chapter 2.2, diffraction occurs only if the light is incident at a certain angle, i. e., the Bragg angle θ_B . It is defined by the Bragg condition, which reads

$$2\Lambda n_0 \cos(\Phi - \theta_B) = \lambda_r. \quad (2.17)$$

Here θ_B refers to the angle inside the medium. As a consequence of Eq. (2.17), all diffracted orders except the 1^{st} one vanish behind the grating. For small deviations from the Bragg angle, and under the assumptions that an unslanted phase grating ($\Phi = \pi/2$) with homogeneous absorption ($\alpha = \alpha_0$) and small amplitude ($n_1 \ll n_0$) is present in the volume of the sample, the first-order diffraction efficiency is calculated as

$$\eta_1 = \frac{\sin^2 \sqrt{(v^2 + \xi^2)}}{1 + \xi^2/v^2} \cdot e^{-2\alpha_0 d_0 / \cos \theta_r} \quad (2.18)$$

with

$$v = \frac{\pi n_1 d_0}{\lambda_r \cos \theta_r} \quad (2.19)$$

and

$$\xi = \frac{\pi d_0 \cos \theta_B \Delta \theta}{\Lambda \cos \theta_r}. \quad (2.20)$$

The angle $\Delta \theta$ is the deviation from the exact Bragg angle. They are related to each other by the angle of incidence θ_r :

$$\Delta \theta = \theta_r - \theta_B \quad (2.21)$$

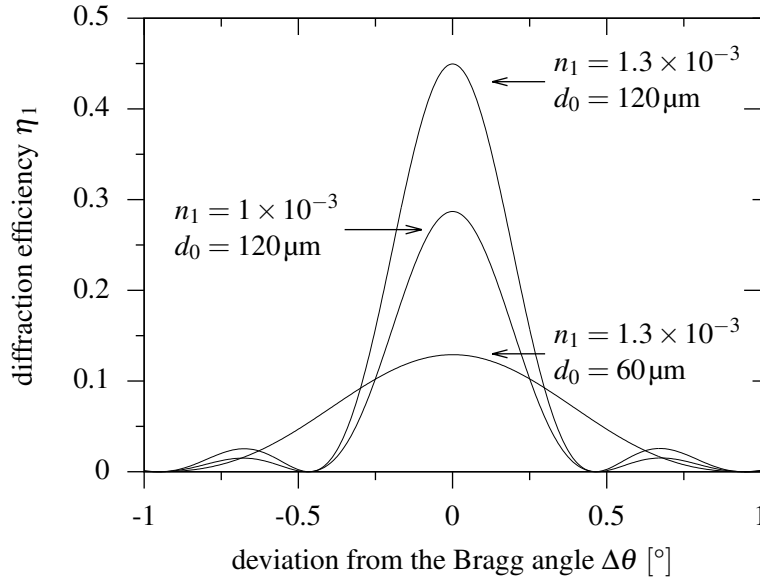


Figure 2.5: Angular dependence of the diffraction efficiency in the Bragg regime for different sample thicknesses d_0 and refractive-index modulations n_1 . The values $\Phi = \pi/2$, $\lambda_r = 685 \text{ nm}$, $\Lambda = 1 \mu\text{m}$ and $n_0 = 1.5$ apply to all curves.

Eq. (2.18) is plotted in Fig. 2.5 for three different combinations of the parameters d_0 and n_1 . For the sake of simplicity, it has been assumed that the exponential term is one, i. e., no absorption is present in the sample ($\alpha_0 = 0$). Increasing the value of n_1 results in an increased maximum diffraction efficiency. Note that diffraction into higher orders may recur in thick gratings if the refractive-index modulation n_1 exceeds a certain value.^[104] If the grating thickness is decreased, the width at half-maximum of the peak becomes significantly broader until the restrictions of the Bragg equation do not apply anymore. Hence, thick volume holograms diffract light only if it is incident exactly under the Bragg angle. This allows for a technique denoted by “angular multiplexing”. Multiple holograms can be stored in the same spot of the medium, if the sample is rotated between each writing cycle. Upon illumination with the readout beam, the Bragg condition cannot be fulfilled for two holograms at the same time. By simply rotating the medium, the holograms are reconstructed individually.

The principle of angular selectivity can be applied to more complex gratings as well. In holographic data storage applications, the expanded object wave is spatially modulated with bright and dark areas, representing the information of a binary data field. As the intensity

distribution of the object beam can be decomposed into plane waves, the stored data fields show angular selectivity as well. The number of separately accessible holograms is proportional to the thickness of the medium. Therefore, angular multiplexing is the only technique known so far which realizes true three-dimensional data storage.^[20]

If the readout beam is incident under the Bragg angle ($\Delta\theta = 0$), the diffraction efficiency becomes

$$\eta_1 = \sin^2 v \cdot e^{-2\alpha_0 d_0 / \cos \theta_r} \approx \left(\frac{\pi n_1 d_0}{\lambda_r \cos \theta_r} \right)^2. \quad (2.22)$$

The approximations made in the last term of Eq. (2.22) are valid if the argument of the sine function is sufficiently small and if the absorption term can be neglected. From Eq. (2.22) one can see that the diffraction efficiency of a thick, scalar phase grating can reach values as high as 100 %.

The materials used for the holographic and imprint experiments in this thesis are photoanisotropic polymers and photofluidizable amorphous glass formers. They have in common, that their photophysical behavior arises from azobenzene-functionalized moieties with different substitution patterns. Photoinduced motion of azobenzenes and azobenzene-functionalized materials occurs at different length scales. Depending on their interaction with the optical field, their motion can be divided into two classes. Molecular reorientation upon absorption of a photon is a mainly rotational effect. It involves the motion of a single molecule and its nearest neighbors at the nanometer scale. On the other hand, mass transport can occur over macroscopic distances up to several micrometers, which is a translational rearrangement of the chromophores in the bulk. The latter requires a photoplastification or photofluidization of the solid matrix. This chapter addresses these effects and illustrates the significance of azobenzene-functionalization in holographic and mass migration experiments.

3.1 Molecular Motion — Rotational Effects

The behavior of azobenzene-functionalized materials upon illumination with visible light can best be understood by means of the basic azobenzene molecule depicted in Fig. 3.1. It is composed of two phenyl rings separated by an azo group and exists in either the *trans* or the *cis* form. In contrast to the *trans* isomer, which has a planar structure,^[105] the phenyl rings in *cis* azobenzene are twisted symmetrically relative to the C–N=N–C plane.^[106] The permanent electric dipole moment of the *trans* isomer is zero, whereas it is approximately 3 D in the *cis* state.^[107] The *trans* isomer is thermodynamically more stable by about 50 kJ mol⁻¹ ^[108,109] and, therefore, is the preferential state if stored in the dark. Isomerization can occur after the absorption of a photon or, in the case of the *cis* form, by thermal activation. The energy barrier for the latter process is on the order of 90 to 100 kJ mol⁻¹.^[110,111] Optically induced isomerization takes place on a picosecond timescale, whereas thermal back relaxation usually occurs within days.^[110] The isomerization is completely reversible and free from any side reactions.^[53]

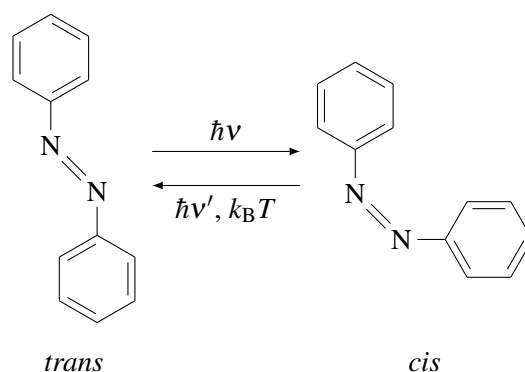


Figure 3.1: The *trans* and *cis* isomerization states of azobenzene. The isomerization is reversible and can be induced by UV light, visible light, or thermal activation.

The absorption spectra of the azobenzene isomers differ strongly, but both of them show two well separated bands in the UV and in the visible region due to a $\pi \rightarrow \pi^*$ and a $n \rightarrow \pi^*$ transition, respectively.^[112] For *trans* azobenzene, the $\pi \rightarrow \pi^*$ transition is found to cause a strong absorption band with a maximum near 320 nm.^[113] The second band has its maximum near 440 nm and is much weaker because the $n \rightarrow \pi^*$ transition is symmetry-forbidden.^[114] For *cis* azobenzene, the $n \rightarrow \pi^*$ transition is allowed. Thus, its absorption is higher in the visible region than that of the *trans* isomer. The UV absorption decreases at the same time and shifts to shorter wavelengths ($\lambda_{\max} \approx 260$ nm).^[110] As a result, azobenzene is a photochromic material, i. e., its absorption changes during illumination. This is illustrated by the schematic azobenzene absorption spectra in Fig. 3.2 a) and b). The solid black lines indicate the azobenzene absorption in the photo-stationary state upon illumination with different light sources. If illuminated with UV light, a *cis*-rich state is formed, whereas a *trans*-rich state develops from illumination with visible light. The dashed line in Fig. 3.2 a) with the highest $\pi \rightarrow \pi^*$ absorption peak corresponds to *trans* azobenzene stored in the dark. All other curves are superpositions of *cis* and *trans* azobenzene absorption spectra. After UV illumination, the initial shape of the *trans* absorption spectrum can only be restored by thermal relaxation in the absence of light. In Fig. 3.2 b) it has been assumed that the sample is prepared in a *cis*-rich state initially.

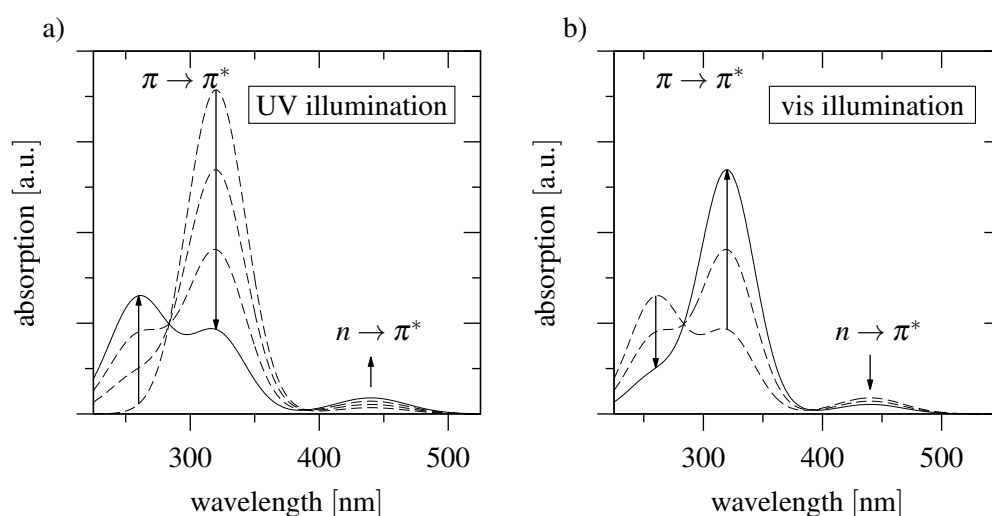


Figure 3.2: Schematic azobenzene absorption spectra upon illumination with a) UV and b) visible light. The illumination time increases along the arrows. The solid lines represent the absorption in the photo-stationary states.

The exact dynamics of the isomerization mechanism have been discussed controversially for more than half a century.^[110,115–118] Isomerization is believed to predominantly follow one of two possible reaction pathways. The first one is rotation, which requires that the N=N double bond be ruptured such that the phenyl rings can move freely around the remaining single bond. The other mechanism is inversion. It denotes the planar change of one of the C–N=N angles. In this case, the double bond stays intact during the whole isomerization process. Thermal or photochemical relaxation from the *cis* to the *trans* state is accepted to occur via rotation.^[53,110,119] Different opinions exist about the isomerization pathway from the *trans* to the *cis* state. This is aggravated by the fact that the inner-molecular dynamics can be altered by both the environment^[120,121] and the substitution pattern.^[110] Most results indicate, however, that either inversion^[120,122] or concerted inversion occurs.^[110,119] The latter involves a simultaneous planar increase of both C–N=N angles.

Azobenzene can be used as a doping material to create photochromic “guest-host” systems.^[121,123] Both rotation and inversion require a small free volume below 0.4 nm³,^[117,124] which explains why the isomerization of azobenzene molecules can take place even in rigid matrices. Azobenzene moieties are often covalently attached to other materials such as molecular glasses or polymers to obtain materials with customized photophysical properties.^[53,125] A large variety of azobenzene-functionalized materials has been developed in the past decades, comprising liquid-crystalline^[117,126] or amorphous polymers^[33] and molecular glasses,^[50,127] to mention but a few. Azobenzene derivatives can be categorized into three spectroscopic classes, denoted as azobenzenes, aminoazobenzenes and pseudo-stilbenes.^[128] Depending on the substitution pattern of the phenyl rings, their absorption behavior differs strongly. The materials investigated in this thesis belong to the first class, the azobenzenes. Their characteristics are similar to those of the basic azobenzene molecule.

Azobenzene-functionalized materials are suitable holographic storage media because they become birefringent if exposed to polarized light with a wavelength that excites both the $n \rightarrow \pi^*$ and the $\pi \rightarrow \pi^*$ transition. Since the electronic transition dipole moment of azobenzene is parallel to the long axis of the molecule, the probability of absorbing a photon is higher for chromophores which are aligned parallel to the polarization of the incident light. Excitation occurs less frequently for chromophores with a different orientation. In a material with an initially isotropic angular distribution of chromophores about one third of the azobenzenes are aligned such that they can absorb. These chromophores repeatedly perform *trans-cis-trans* isomerization cycles until they eventually revert from the *cis* to the *trans* form with an orientation perpendicular to the direction of the electric field. In this case, the chromophores stop absorbing and, thus, cannot participate in the isomerization process anymore. The underlying statistical selection process causes the molecular order to increase in the illuminated areas, whereby the refractive index of the material becomes anisotropic. As a further consequence, azobenzene-based media are capable of storing both intensity and polarization gratings. Moreover, they are rewritable, because the molecular order can be erased thermally or with circularly polarized light. An important parameter for holographic storage applications is the good long-term stability of the generated grating. Illumination with UV light increases the isomerization rate, but a large number of randomly relaxing *cis* isomers remains in the storage medium after the inscription. To convert them back to the *trans* state and inscribe stable gratings, the wavelength of the interfering writing beams has to be close to the $n \rightarrow \pi^*$ absorption band.

3.2 Macroscopic Motion — Translational Effects

In 1995, the groups of Rochon/Natansohn and Tripathy/Kumar independently observed an unexpected effect, which occurred during the illumination of azobenzene-functionalized homopolymers with different interference patterns.^[47,48] Surprisingly, the surface profile of the polymers changed in such a way that it reproduced the spatial modulation of the incident light field. A non-contact patterning technique with great potential for the fabrication of micrometer- or nanometer-sized structures was discovered. Since then, photo-generated patterns in azobenzene-functionalized materials have been subject to intense fundamental and applied research.^[33,42,43,49,53,129]

Upon holographic illumination with two plane waves, the resulting pattern is a sinusoidal surface relief grating (SRG). An example of such a grating is shown in Fig. 3.3. It was inscribed into an azobenzene-functionalized molecular glass based on a spirobichromane core, which is described in detail in Chapter 5. SRG formation is profoundly inter-related with the ability of a material to perform repeated isomerization cycles.^[125,130] Non-isomerizable absorbing materials do not show this effect. Experiments with amorphous azobenzene-functionalized polymers and molecular glasses demonstrate that macroscopic mass transport occurs already at room temperature, significantly below the glass transition temperature T_g .^[43,50,51] The gratings reach a height of several 100 nm and, depending on the intensity and the polarization of the incident light, usually require only a few minutes to reach their maximum modulation.^[50,51,67] Even low intensities on the order of 1 to 10 mW cm^{-2} are sufficient to initiate the SRG formation.^[53,131] The grating formation is usually reversible and the initial film surface can be restored either by heating the material above T_g or illuminating it homogeneously.^[132,133] This is an important finding since it proves that the formation of SRGs is not due to material ablation.

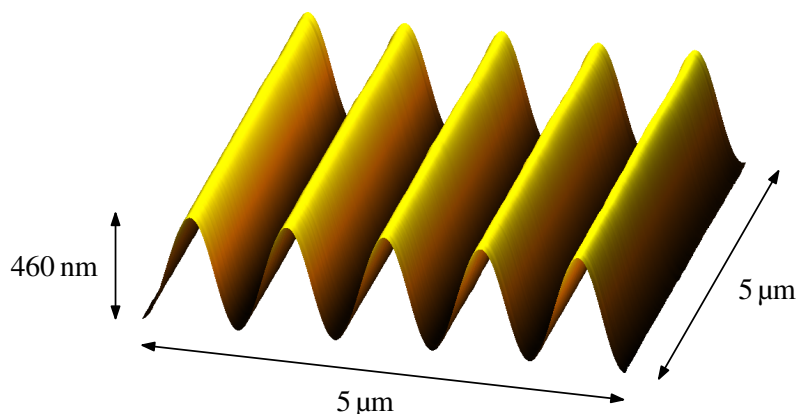


Figure 3.3: Section of the surface profile of a sinusoidal SRG inscribed into an azobenzene-functionalized molecular glass based on a spirobichromane core as determined by AFM. The grating was formed by holographic pp illumination for 90 s at a total intensity of 2 W cm^{-2} .

The direction of the material transport strongly depends on the polarization and the intensity gradients of the optical field. In amorphous azobenzene-functionalized materials the SRGs are usually 180° out of phase with the intensity grating.^[52,56,134] Thus, the material accumulates in the dark areas. Interestingly, this behavior is inverted at very high intensities ($\sim 300 \text{ W cm}^{-2}$).^[135] In-situ atomic force microscopy experiments of Yadavalli et al. demonstrated that sp illumination causes the material to be transported into areas where the light is polarized linearly.^[51,52] As a consequence, SRGs with half the spatial periodicity of the optical grating develop (cf. Tab. 2.1). For $\pm 45^\circ$ illumination, the material migrates

from *p*-polarized regions to those with *s* polarization, whereas the opposite is true for *rcpl* illumination. The maximum amplitude and the formation speed of SRGs strongly depend on the polarization of the writing beams. Usually, SRGs of weak amplitude are formed upon *ss* or *sp* illumination, whereas *pp*, *rlcp*, and $\pm 45^\circ$ illumination leads to the formation of pronounced gratings.^[50,62,131] If the illumination time is sufficiently long, some materials develop SRGs for all discussed illumination types.^[51]

The underlying mechanism leading to SRG formation remains unresolved until today.^[42,53] Various models have been suggested to explain the origin of the driving force, involving thermal considerations,^[54] models of gradient forces induced by isomerization pressure^[55] or optical fields,^[56,57] mean-field theory,^[58] and diffusion-based approaches.^[59,60] None of them explains all the experimental findings of SRG formation. In the thermal model, SRGs result from gradients in temperature, which turn out to be negligibly small for the applied optical fields ($\sim 10^{-4}$ K). Moreover, part of the theoretical considerations apply to any absorbing material and do not require the isomerization of azobenzene. Pressure gradients may arise during the isomerization process because the *cis* and *trans* form occupy a different amount of free volume. The polarization dependence is not predicted correctly in such a model for all the optical fields of the various grating types. The optical-field gradient force model seems to solve this problem, since it reproduces experimentally found polarization features. Based on the assumption that the photoisomerization induces a spatially varying electric polarization, it suggests that the optical field exerts a force onto the medium. Saphiannikova et al. pointed out that the optically induced force density at a typical writing intensity of 100 mW cm^{-2} is about two orders of magnitude smaller than that of gravity.^[136] Moreover, arguments exist that the forces exerted on polarizable media should depend on gradients in the light intensity and not on polarization.^[33] Attractive forces between the dipoles of aligned chromophores are taken into account in the mean-field approach. Because it predicts an accumulation of the material in bright areas, it does not describe the phase shift of the optical and the surface relief grating observed in amorphous systems. Instead, the model can be applied to certain liquid-crystalline side chain polymers in which the interaction between chromophores is so strong that they form an in-phase relief grating.^[137,138] Diffusion models are based on the assumption that the azobenzene chromophores perform an inchworm-like motion along their long axis. This describes the polarization dependency correctly and predicts a higher formation speed for systems with smaller molecules. SRG formation in polymers is excluded from these models, since the random motion of the backbone-connected moieties is not expected to allow for any net transport. Eventually, it is conceivable that more than one of the models applies, adding even more complexity to the mechanism of SRG formation.

Without further specification of the origin of the molecular force leading to SRG formation, the material transport can be described successfully with fluid-mechanics models.^[139,140] One has to assume, however, that the material is in a liquid or liquid-like state.

3.3 Athermal Photofluidization

A prerequisite for SRG formation or any other photo-induced macroscopic motion is the ability of an amorphous azobenzene-functionalized glass to flow like a liquid. A temperature increase of the material caused by optical heating can be excluded as a source of such a phase transition. Even at intensities as high as 2 W cm^{-2} , the photothermal temperature increase in azobenzene glass formers has been found not to exceed 15 K.^[54,67,141] This is negligibly small as compared to the high T_g of many glass formers. Instead, the liquid-like flow behavior can be attributed to another peculiarity of azobenzene-functionalized materi-

als, denoted by “photoplasticizing effect” or “athermal photofluidization”. The latter term has entered the discussion about the flow mechanism of azobenzene-functionalized glass formers very recently.^[79,142,143] Its existence was debated controversially in the early time, which can mainly be attributed to the discrepancy between the physical and the descriptive definition of the term “fluid”.^[45] A reasonable definition of a photofluid will be given after briefly summarizing the underlying physics according to the current state of knowledge.

Upon absorption of a photon, an excitation energy of 2 to 3 eV is stored in an azobenzene moiety. In an isolated azobenzene molecule (in vacuum), most of this energy is dissipated into its low-frequency vibration modes upon electronic relaxation and isomerization within ~ 0.4 ps,^[142] raising its internal temperature to ~ 1150 K.^[112] In solution, the isomerization is hindered by intermolecular forces and the conversion takes place on a much longer timescale ($\gtrsim 10$ ps).^[144] Here, the process is too slow to excite molecular vibrations and the energy can be transferred into cooperative motion of the adjacent molecules. Fang et al. showed that in an azobenzene-based tethered self assembled monolayer a similar interaction allows for the activation of 30 degrees of freedom at 800 K, which are distributed over the nearest neighbors of the absorbing molecule.^[142] Even though the situation changes in bulk materials, such high temperatures clearly exceed the T_g of polymers or molecular glasses. At the same time, the above temperature value does not correspond to an average temperature increase because the absorption events of single photons are separated in space and time even for high intensities. However, local barriers hindering the reorientation of the molecule can be overcome, resulting in a local glass transition. At ambient light conditions the efficiency of local fluidization stays below a critical value. Thus, the viscosity remains that of a solid.

The photofluidization of azobenzene-functionalized homopolymers and molecular glasses in the bulk has been investigated by Vapaavuori et al.^[45] They found that illumination with visible light leads to a strong band shift of the vibrational modes of the azobenzene moieties without affecting the T_g of the material. The changes in the molecular environment of the azobenzene moieties upon illumination are similar to those measured during conventional heating of the material above T_g in the absence of light. However, the optically induced motions and, therefore, the generation of free volume is very heterogeneous, occurring predominantly close to the azobenzene moieties. Consequently, the amorphous phase is maintained by the polymer backbone or the core of the molecular glass former, whereas the azobenzene-functionalized part experiences an effective temperature of up to 530 K.^[45] This temperature is derived by means of comparing vibrational modes and does not correspond to the actual temperature of the material, which is essentially that of the photo-inactive bulk. It is an effective quantity to indicate that the mobility of the photo-active groups is increased to such a degree that the amorphous glass former behaves like a liquid.

In summary, athermal photofluidization denotes the light-induced process of turning an azobenzene-functionalized material into a photomobile state, in which it has the properties of both a glass and a fluid. Although the macroscopic change in temperature is negligibly small, the viscosity decreases by many orders of magnitude.^[44,142] Depending on the intensity of the incident light and the molecular structure of the material, amorphous azobenzene systems show either viscoelastic^[44,143] or viscous^[46] flow behavior. The interaction of the azobenzene moieties with the optical field is so efficient that even crystalline systems can be converted into photofluidic melts.^[145] The capability of azobenzene materials to form SRGs at room temperature impressively proves the existence of the photofluidic state. In contrast to thermal melting, photofluidization occurs quasi-instantaneously throughout the whole illuminated volume.

From Photofluidization to Lithography — Concept and Theory

Switching azobenzene systems into the photofluidic state grants access to unexpected areas of application. The fabrication of coatings or resists with patterns of high complexity is of great importance for the lithographic manufacturing process of various devices. Optical, contact-free patterning of azobenzene-based resists, also denoted by “directional photofluidization lithography” (DPL), may even become an alternative to common optical lithographic techniques.^[42] A new and different concept is introduced here, following the concept of well-established imprint techniques. It utilizes photofluidizable systems and the adhesive properties of flexible molds to replicate predefined structures from a master. The theoretical background discussed in this chapter addresses the flow characteristics of viscous fluids in confined geometries.

4.1 Introduction to Nanoimprint Lithography

Nanoimprint lithography (NIL) is a replication technique developed to overcome the drawbacks of high-resolution patterning methods.^[146] For instance, e-beam lithography is capable of generating structures with features as small as 5 nm, but its throughput is rather low. Photolithography is fast, but its resolution is limited to ~ 30 nm and high facility costs arise from circumventing the optical diffraction limit.^[147–149] The idea of NIL is to transfer a pattern from a rigid master — e. g., prepared from one of the techniques mentioned above — to a resist by molding. For this purpose, a resist material, which either cures upon UV-light irradiation or softens upon heating, is coated onto a suitable substrate.^[150] Subsequently, the master is brought into contact with the resist and the pattern of the master is imprinted in the resist. In a final step, the master is removed and the imprinted structures are etched into the substrate. High costs are avoided because neither an expensive equipment nor a great amount of time is needed. These advantages in combination with the high resolution of more costly techniques makes NIL a good candidate for nanoscale mass production.^[151]

In the early stages, NIL was also referred to as the “mold mask method”.^[152] This is due to the fact that often a less rigid polymer mold is prepared from the master, which is used for the imprinting process instead. The advantage of this approach is that the master suffers less stress and that a larger number of materials becomes available for the imprinting process. Despite the fact that the mold carries the inverse pattern, the principle does not differ from imprinting the master.

Because NIL is a direct contact method, problems can emerge from the interaction of the mold or the master with the resist, e. g., partial mold filling or breaking, sticking of the resist layer, or material shrinkage. To minimize such defects, various techniques have been developed in the past.^[42] Three of the most important ones are discussed in the following.

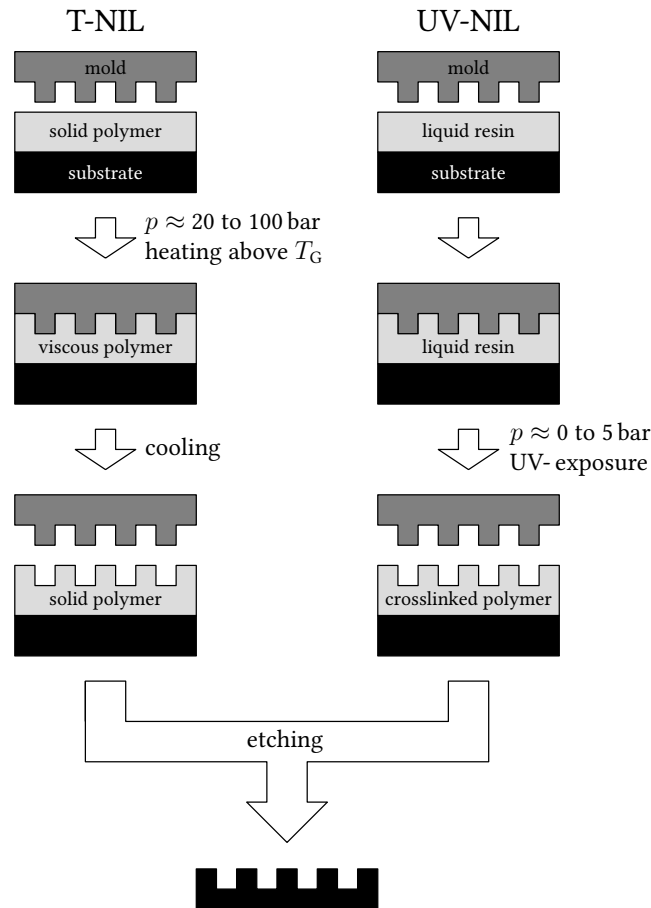


Figure 4.1: Scheme of the T-NIL (left) and UV-NIL (right) process. Both techniques transfer the profile of a mold to a thin polymer film on top of a substrate. Etching transfers the structure to the substrate below.

Thermal Nanoimprint Lithography (T-NIL) is based on the characteristic of thermoplastic materials to have a significantly decreased viscosity when heated above T_g . Initially, a thermoplastic is prepared as a thin, homogeneous film on a substrate, to which the relief pattern of the mold needs to be transferred (cf. Fig. 4.1). After placing the mold on top of the solid film, the resist is heated above T_g and the thermoplastic begins to fill the cavities of the mold. Typical values for the resist viscosity during this step are 10^3 to 10^7 Pa s.^[153] The mold is removed as soon as the resist layer has cooled down sufficiently to maintain the imprinted surface profile.

A clear advantage of this method is that a large number of polymers can be used. This is important, e. g., for the fabrication of optical elements.^[154] However, the cooling step takes a crucial amount of time, which can be partially compensated by decreasing the processing temperature. Robust, rigid molds withstanding high pressures have to be used in this case. The imprints are prone to mold-sticking defects due to the differing thermal expansion coefficients of mold and resist. Yet, T-NIL has made a lot of progress, starting from the initial work of Chou et al.^[155] in 1995 to now being capable of producing high-quality micro- and

nanostructures.^[156–160] High throughput can be realized with sophisticated techniques such as roll-to-roll imprint lithography.^[161]

Ultra-Violet Nanoimprint Lithography (UV-NIL) is a process similar to T-NIL. Apart from usually being carried out at ambient temperature, a photo-curable resin is used instead of a thermoplastic. As illustrated on the right side of Fig. 4.1, the mold is placed on top of a resin-wetted substrate. Due to the low viscosity of the resin (10^{-2} to 10^{-3} Pa s),^[153] the mold cavities fill even under moderate pressure. After crosslinking the resin with UV light, the mold can be removed and a structured, solid polymer layer remains on top of the substrate. As in the case of T-NIL, pattern transfer to the substrate is realized by etching.

UV-NIL has many advantages compared to T-NIL. Because neither heating nor cooling is required, the imprinting speed is significantly higher and the polymer shrinkage during curing is much smaller. The low viscosity of the resin improves the quality of the imprint and the absence of high pressures results in a more homogeneous filling of larger areas.^[162] Furthermore, the release can be facilitated by using flexible molds with low surface energy (e. g., polydimethylsiloxan (PDMS), perfluoropolyether (PFPE) derivatives, or thiol-ene functionalized systems).^[163] Because the crosslinking reaction is initiated by UV-irradiation, either the mold or the substrate must be transparent.

Capillary Force Lithography (CFL) can be considered an extension of T-NIL. From capillary-flow theory it is known that a wetting liquid tends to fill micrometer- or nanometer-sized pores or channels even in the absence of externally applied pressure.^[164,165] The reason is that the hydrostatic pressure drop across the curved surface of the liquid pushes the resist into the mold cavities. Usually thermoplastic polymers are used for CFL, which must be heated above T_g until they become liquid.^[166,167] The principle is also applicable to UV-curable resins, but the difference to UV-NIL is marginal. The molds for this process are prepared from polymers of low Young's modulus and low surface energy.^[48,153,166]

Due to the absence of high pressures, imprints prepared by CFL have high quality.^[166] A major drawback of this method is the large thermal expansion and shrinkage of both the mold and the resist during processing. Moreover, the imprinting speed of CFL is quite low due to the high viscosity of the liquefied thermoplastics. For example, Suh et al. reported that a void of 600 nm height and 400 nm width takes as long as 30 min to be filled with an styrene-butadiene-styrene (SBS) block copolymer at a process temperature of 100 °C.^[167]

4.2 Athermal Azobenzene-Based Nanoimprint Lithography

Athermal azobenzene-based nanoimprint lithography (Azo-NIL) is a new method, which adopts the basic concepts of CFL without suffering from thermally induced shrinkage defects. Like the NIL techniques discussed before, it can be applied to replicate the micro- and nanometer-sized features of a mold, which preferably consists of a low-surface-energy material of low Young's modulus (e. g., PDMS). In this case, the mold adheres to the substrate without externally applied pressure and the number of defects upon release is significantly reduced. As depicted in Fig. 4.2, the mold is brought into contact with a thin, solid film of an azobenzene-functionalized, amorphous glass former coated onto a substrate. If stored under ambient light conditions, the isolated isomerization events of the azobenzene moieties cannot photofluidize the resist and no material transport is observed. This situation changes as soon as the resist is irradiated through the mold or the substrate with UV or visible light of sufficiently high intensity. Once in the photofluidic state, capillary forces pull the resist into the cavities. At the same time, the macroscopic optical heating of the resist is negligibly small (cf. Chapter 3.3). When the irradiation source is turned off, the resist becomes solid again. Subsequently, the mold is removed while its profile remains imprinted in the azobenzene-functionalized resist.

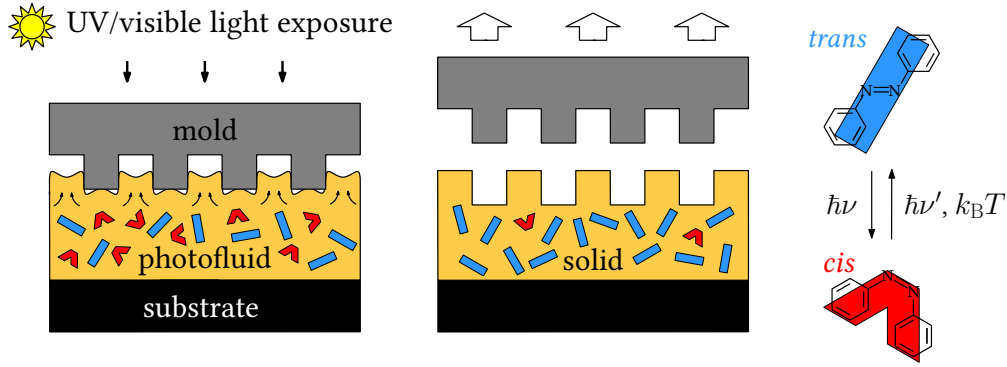


Figure 4.2: Scheme of the Azo-NIL process. Upon irradiation with UV or visible light the azobenzene-functionalized resist becomes photofluidic and fills the cavities of the mold due to capillary forces.

Experiments with photofluidizable azobenzene materials concentrated on migrating mass by intensity or polarization gradients in the past.^[42,43,77] The DPL concept is a promising approach since it is a contact-free, single-step patterning method.^[42] However, as in the case of photolithography, the spatial resolution of optically generated patterns is limited by diffraction and their preparation is highly demanding. Azo-NIL has the advantage that it is a cheap method and combines the non-diffraction-limited replication of arbitrary structures with the absence of material shrinkage. The latter is expected to significantly reduce defects caused by mold sticking. Photofluidization takes place immediately upon light irradiation and, therefore, the processing is faster than with CFL. Azo-NIL can also be used to study the flow behavior of photofluids under the influence of externally applied forces in confined geometries. The latter is relevant, e. g., to understand the formation process of SRGs.

4.3 Filling Characteristics of Cavities — A Comparison of Two Models

An idealized model of a mold used for NIL is the periodic arrangement of infinitely extended rectangular protrusions of height h_m and width s separated by the distance w as shown in Fig. 4.3. A vertical shift of the mold caused by an externally applied pressure p results in a squeezed flow of the viscous or fluid resist into the cavities of the mold. The external pressure is assumed to be constant during the whole imprinting process with no air being trapped between the protrusions and the resist. During this process the initial thickness d_0 of the resist decreases and a residual layer of thickness d_f remains below the protrusions. By solving the Navier-Stokes equation for an ideal incompressible, viscous liquid with no-slip boundary conditions at the protrusion and substrate surfaces, one can derive an expression for the imprinting time

$$t_f = \frac{\eta_0 s^2}{2p} \left(\frac{1}{d_f^2} - \frac{1}{d_0^2} \right), \quad (4.1)$$

also known as the Stefan equation.^[153,165] The imprinting time depends on the viscosity η_0 of the resist. Hence, t_f can vary by many orders of magnitude if the temperature of the resist material is changed or, in the case of azobenzene-functionalized glass formers, if the photofluidizable film is exposed to light. It should be noted that the assumptions made to derive Eq. (4.1) are quite restrictive. Not all of them are necessarily fulfilled in real

systems.^[168] Yet, the Stefan equation has successfully been used to explain the imprinting characteristics of viscous, polymeric liquids.^[153,169,170]

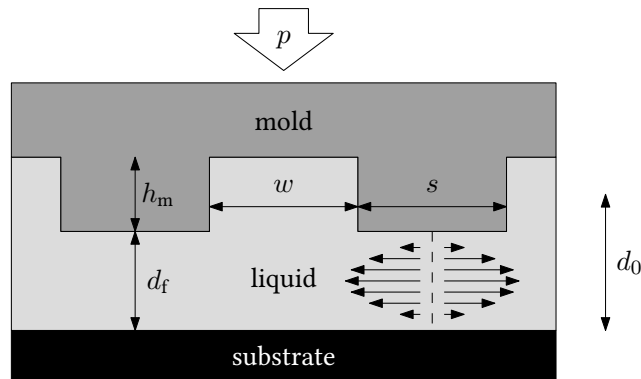


Figure 4.3: Schematic diagram of a mold with rectangular protrusions, being completely inserted into a resist. The arrows indicate the flow profile during imprinting.

The parabolic flow profile indicated by the black arrows in Fig. 4.3 shows that the mass transports occurs mainly in the lateral direction in this model. Sinking of the mold virtually stops as soon as it is completely inserted into the resist, since afterward the material transport has to occur over large distances towards the outer borders. The flow rate of transported fluid is higher for thicker films and the imprinting time decreases with increasing d_0 . Improving the imprinting speed by increasing the thickness of the resist comes at the cost of a thick residual layer, which deteriorates the quality of the pattern transferred to the substrate after etching. Provided that the volume of the resist is conserved, the residual film thickness becomes $d_f = d_0 - \nu h_m$ for a completely inserted mold. For the simple rectangular mold geometry discussed above, the fill factor ν can easily be calculated according to $\nu = w/(w + s)$. A consequence of the Stefan equation is that narrow protrusions sink faster than wide ones if the same pressure is applied to them. This has to be considered when complex patterns with features of varying size are imprinted. To accomplish homogeneous sinking of the mold, it is advantageous to keep the fill factor constant over the whole imprint area.

Eq. (4.1) requires a pressure to be applied to the mold, otherwise it predicts an infinite imprinting time. Most of the imprint experiments discussed in this thesis, however, have been conducted without externally applied pressure. Instead, the pressure arises from the adhesion of the elastic mold as soon as it comes into contact with the resist. The spatial distribution of the adhesion-induced pressure below the mold protrusions is rather complex but can be calculated analytically for certain periodic surfaces.^[171,172] Without going into further detail, one can easily understand that the mold protrusions encounter an average pressure even if no additional load is applied to them. In this case, the Stefan equation is applicable without the requirement of externally acting pressure.

An interesting result is obtained if the liquid transport is assumed to be caused by Poiseuille flow inside the small capillaries of the mold. In a narrow, circular tube capillary action causes a perfectly (contact angle $\theta = 0^\circ$) or partially ($0^\circ < \theta < 90^\circ$) wetting liquid to form a hemispherical meniscus with radius R as depicted in Fig. 4.4 a). The liquid is pulled into the capillary without externally applied pressure due to the Laplace pressure drop p_L across the curved liquid-air interface. The latter can be calculated as

$$p_L = \frac{2\gamma \cos \theta}{R}, \quad (4.2)$$

with γ being the surface tension between liquid and air.

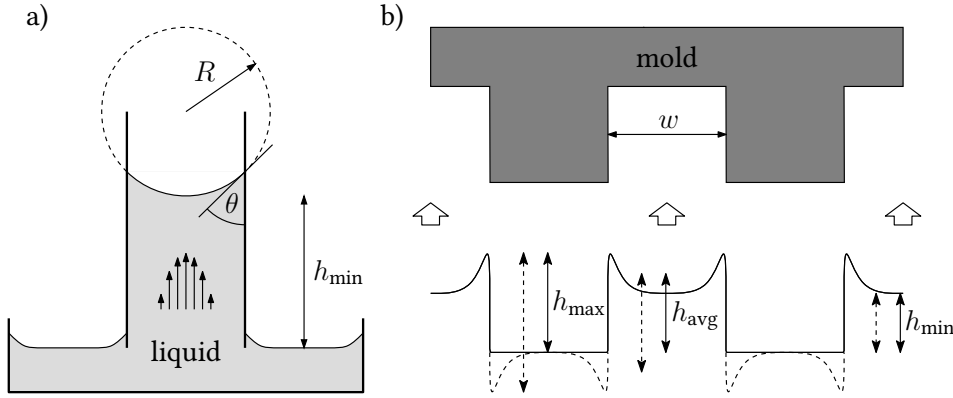


Figure 4.4: Liquid transport in confined geometries caused by the Laplace pressure drop under capillary action. A similar situation arises for a liquid confined by either a) two parallel plates or b) a mold with rectangular protrusions. For the sake of clarity, the mold is drawn lifted above its real position in part b).

Washburn demonstrated in 1929 that the rise time of the meniscus of a wetting liquid in a vertically or horizontally aligned cylindrical capillary can be calculated analytically.^[173] His theory has been proven to be valid for capillaries as small as 100 nm^[174] and was expanded to the arrangement of two parallel plates by Oliva and Joye.^[175] Their findings can simply be adapted to the periodic, rectangular mold geometry discussed before because the liquid transport inside each cavity occurs independently of its neighbors. If gravity is neglected and no external pressure is present, the time t_{CF} required to rise the menisci in the mold cavities to the height h_{\min} is

$$t_{\text{CF}} = \frac{3\eta_0}{w\gamma\cos\theta} h_{\min}^2. \quad (4.3)$$

In contrast to the squeezed flow-model discussed before, Eq. (4.3) assumes that the flow profile develops inside each cavity, i. e., the mass transport occurs predominantly into the vertical direction (cf. Fig. 4.4 a)). Consequently, the filling time is quite different from the one predicted by the Stefan equation. One can see this by solving Eq. (4.2) for γ and substituting it into Eq. (4.3). The cavity width is on the order of R , which allows the approximation $R \approx w$. Equation (4.3) then reads

$$t_{\text{CF}} = 6 \frac{\eta_0}{p_L} \frac{h_{\min}^2}{w^2}, \quad (4.4)$$

which has some common features with Eq. (4.1). Despite the fact that p and p_L are different quantities, Eq. (4.1) and (4.4) imply that both a lower viscosity and a higher pressure speed up imprinting. The filling time, however, now increases with decreasing feature size of the mold (without loss of generality, one can assume that the cavities and protrusions of the mold have equal size, i. e., $w = s$). This behavior originates from the strong dependency of the volume flow on the cavity diameter in the Poiseuille flow model.

Depending on the mold geometry, either of the two models, squeezed or capillary flow, predicts the formation speed of line patterns during imprinting. For $w = s$ and if $h_m < w$ or s , liquid transport occurs mainly in lateral direction and squeezed flow becomes the dominant mechanism. As a consequence, the imprinting time decreases for larger mold features. On the other hand, the capillary-flow model applies for very high cavities ($h_m \gg w$), resulting in increased imprinting times for smaller structures. The transition to the capillary-flow regime

already occurs if h_m and w are on the same order of magnitude.^[168] A detailed classification into squeezed, Poiseuille, or mixed flow for other ratios of w and s can be found in the review of Cross.^[168]

In contrast to long, open capillaries, the liquid flow is terminated early inside mold cavities of finite height and, therefore, effects of gravity can be neglected. Figure 4.4 b) shows a generalized scheme of a resist profile as it can be obtained from imprinting a flexible or rigid mold with rectangular protrusions with Azo-NIL. If the light is switched off before the mold is filled completely, the rising menisci “freeze” inside the cavities. Their profiles can be measured with AFM after removing the mold. For molds of moderate elasticity, an ordinary meniscus profile evolves. This means that the resist surface stays flat below the protrusions, whereas a meniscus rises in each of the mold cavities (solid line). If both Young’s modulus and aspect ratio of the mold are rather low ($h_m \ll w + s$), one observes that the profile below the protrusions resembles the one inside the cavities for short imprinting times (dashed line). This material displacement does not correspond to a snapshot of the flow profile. Instead, it is caused by the adhesion-induced deformation of the mold, which occurs when it comes into contact with the photofluidic resist (see Chapter 6.2.1). In both cases, a maximum, a minimum, and an average imprint height, h_{\max} , h_{\min} , and h_{avg} , can be defined to characterize the meniscus-shaped surface. As depicted in Fig. 4.4 b) by the solid and dashed arrows, their definition slightly changes depending on the exact form of the resist profile. Owing to the rectangular geometry of the mold, h_{avg} is a direct measure for the overall transported resist volume.

The material requirements for holographic data storage, SRG formation, and Azo-NIL differ strongly. Even though all three concepts are based on the photophysics of the azobenzene molecule, neither of them is feasible in the neat, crystalline state. Consequently, the materials used for the experiments in this thesis are azobenzene-functionalized molecular glass formers and amorphous polymers. Depending on their chemical design, they are capable of both storing optically induced anisotropy or material transport over large distances. Their chemical structures and preparation, as well as their thermal and optical properties are the subject of the following discussion.

All materials presented in this chapter have been synthesized and prepared at the chair of Macromolecular Chemistry I (Prof. H.-W. Schmidt) at the University of Bayreuth.

5.1 Azobenzene-Functionalized Molecular Glasses

The term “molecular glass” was introduced by Shirota^[176] and denotes a class of organic, low-molecular-weight materials capable of forming a stable, amorphous phase. A prerequisite for this is a molecular design which inhibits the crystallization of the small molecules in the bulk. According to Shirota et al.,^[131,177] a non-planar molecular structure with a large number of conformers impedes the easy packing of the molecules and, therefore, is essential for the formation of an amorphous phase. Linear, branched, X-shaped, or star-shaped molecular topologies constitute successful concepts.^[178] The introduction of bulky or heavy groups in general reduces translational and rotational motions and increases the T_g of the molecular glass. Strong intermolecular interactions caused by van der Waals forces or hydrogen-bonds have similar effects, but may also promote crystallization.

The azobenzene functionalization of such molecular glass cores enables their application in various fields, e. g., storage of holographic volume gratings,^[179,180] inscription of SRGs,^[50,67,181,182] or photolithographic^[42] and nanoimprint^[79] processes. Apart from their easy preparation as homogenous, thin films, azobenzene-substituted molecular glasses show excellent optical properties, including absence of light scattering and high stability against photobleaching. In contrast to photoactive, amorphous polymers, they have the advantage that they feature a uniform molecular structure without ill-defined side groups. Stable holographic gratings can be stored in the volume of a neat molecular glass if the azobenzene-functionalized moieties are decoupled from the rigid core such that they have a mesogenic character.^[127,180] Molecular glasses show good miscibility with photoinactive polymers,^[127,179] and act as photoplasticizing additives in azobenzene homo- or block-copolymer systems to improve their overall holographic performance.^[183] Depending on

the polarization of the illumination source, molecular glasses have a strong tendency to form SRGs even if they are confined by a rigid polymer matrix.^[181,184] SRG formation in neat molecular glasses is faster than in polymers, which can be attributed to the absence of entanglements. With all the above features combined, this class of materials constitutes the ideal candidate for Azo-NIL as well.

The feasibility of the above-mentioned applications depends on the chemical structure of the molecular core, the attached azobenzene moieties, and their linkage.^[64,67,127,180] The molecular glasses used in this thesis feature star-shaped topology with three or four identical azobenzene moieties connected to a central core unit. As depicted in Fig. 5.1, both types comprise the same basic components, i. e., a central core (open circle) and a photoactive part, consisting of azobenzene (gray boxes) and an optional terminal substituent (filled black circles). Linkage group (open ellipses) and substituent are located opposite to each other at the para positions of the azobenzene (cf. inset in Fig. 5.1). Whereas characteristic values of the amorphous phase such as its T_g are predominantly determined by the central core, optical properties and wetting behavior are adjusted by proper substituents of the azobenzene chromophores.

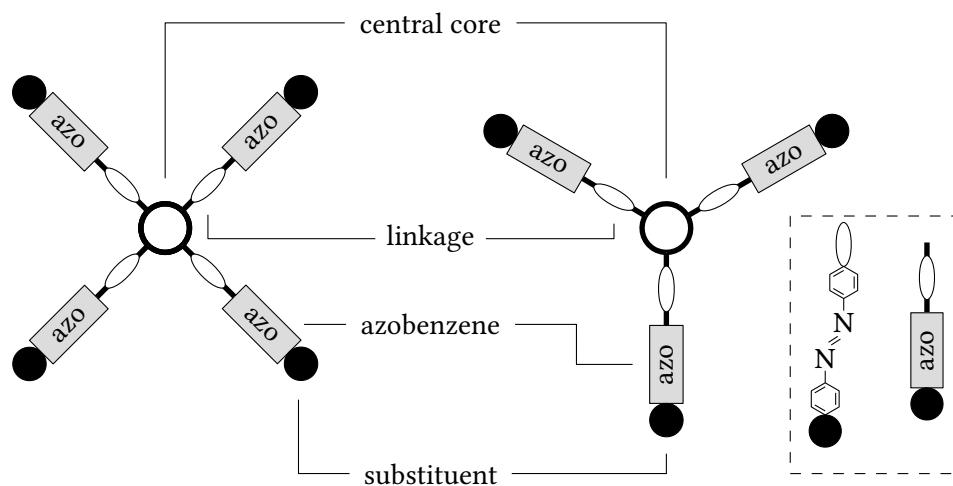


Figure 5.1: Schematic diagram of the molecular glass structure. They are star-shaped with four or three azobenzene-functionalized moieties attached to the core.

A total number of twelve different molecular glasses were investigated in this thesis, i. e., compounds **1a-e** (four arms) and **2a-d**, **3a-b**, and **4e** (three arms). The chemical structure of the cores (**1-4**) and their azobenzene-functionalized substituents (**a-e**) are shown in Fig. 5.2 and Fig. 5.3, respectively. Glass formers based on cores **1**, **2**, and **3** efficiently form SRGs and have been used for mass migration experiments and patterning methods based on photofluidization. Due to its good miscibility with polymers, compound **4e** served as a photoplasticizer for volume holography. In contrast to the threefold-branched molecular cores, compounds based on core **1** are intrinsically non-planar due to their central spiro linkage. In addition, spirochromane-based molecular glasses (**1a-e**) have a more rigid core as compared to triphenylamine-based compounds (**3a-b**). In trisamide compounds (**2a-d**) the central core features amide moieties, which stabilize the amorphous phase by intermolecular H-bond formation.^[185]

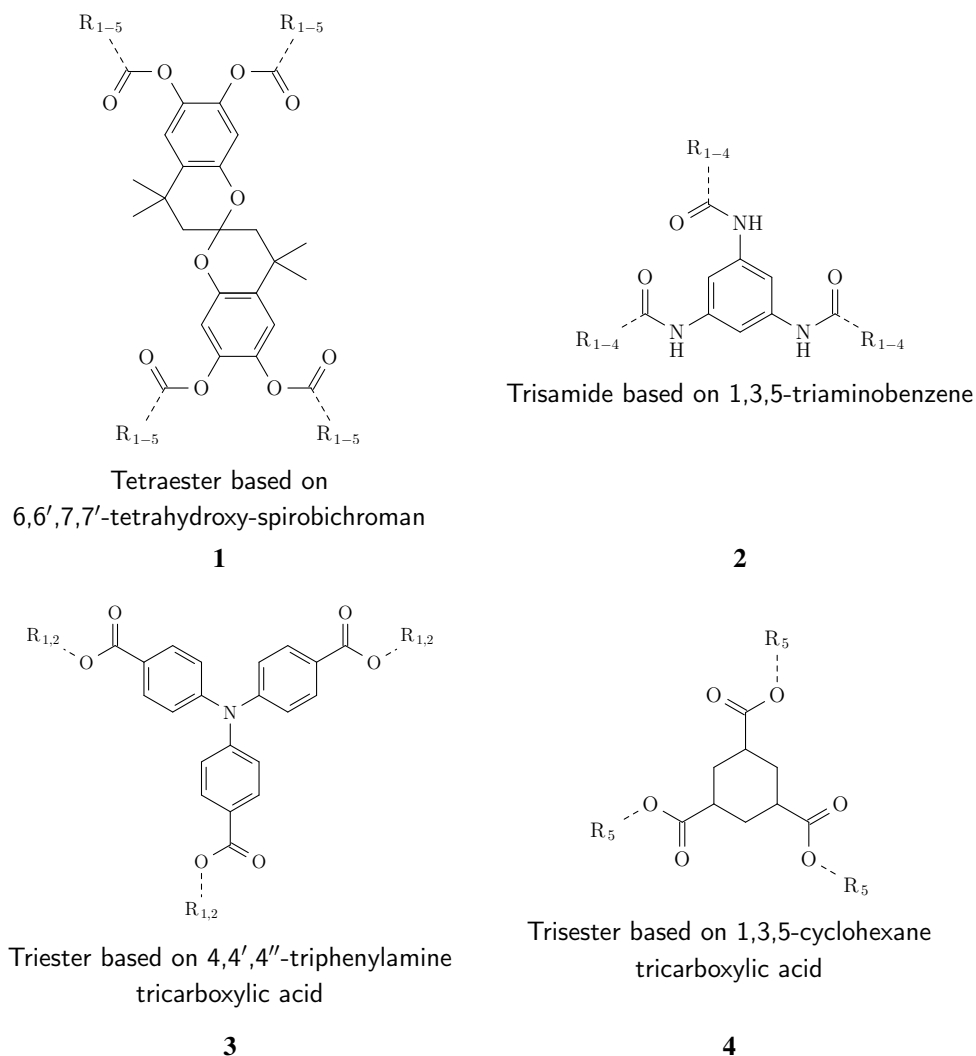


Figure 5.2: Chemical structure of the central building blocks of the functionalized molecular glasses.

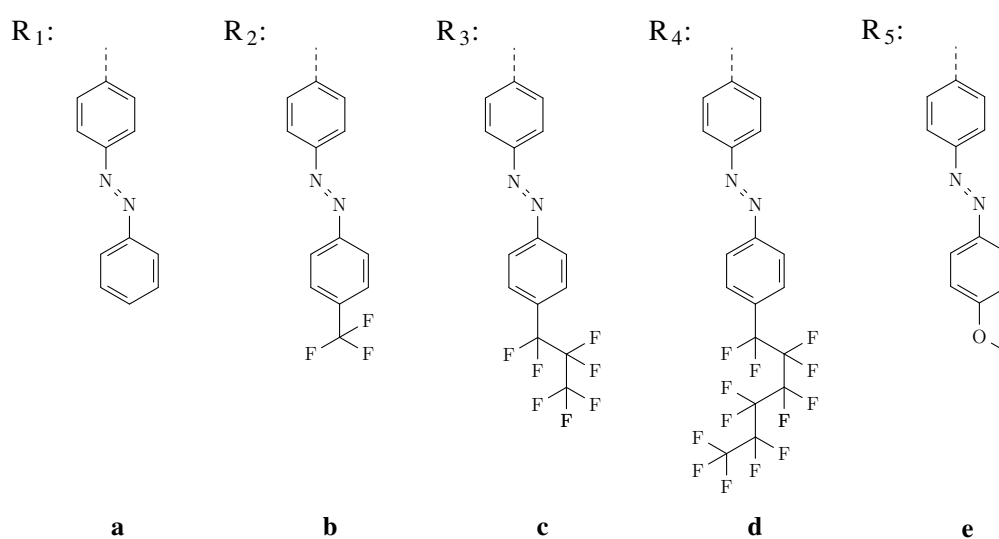


Figure 5.3: Side groups attached to the central building block. They comprise the azobenzene chromophore **a** and its para-substituted derivatives **b-e**.

The optical properties of a molecular glass in the visible and near-UV spectral range are mainly determined by the para-substituted azobenzene chromophores and can be discussed independently of the central core. As compared to unsubstituted azobenzene, the $\pi \rightarrow \pi^*$ absorption peak of a methoxy-functionalized chromophore is shifted towards longer wavelengths. Thus, it overlaps more strongly with the $n \rightarrow \pi^*$ absorption band and the light sources used in the experiments, which leads to an enhanced efficiency of the *cis-trans* interconversion. Since the viscosity of the photofluid is expected to decrease more strongly in this case, shorter processing times should result for SRG and Azo-NIL experiments. The introduction of the perfluoroalkyl substituents addresses the mold release problem in NIL.^[153] When the structures are very small, hydrogen bonds or van der Waals interactions may cause sticking of the mold, which damages the imprint upon release. Fluorination of the molecular-glass chromophores increases the hydrophobicity of the resist and does not require additional anti-adhesive coatings of the mold. Although the perfluoroalkyl substitution has minor influence on the chromophore absorption, it affects the film and SRG formation properties of the molecular glass.^[61]

5.1.1 Synthesis of Azobenzene-Substituted Molecular Glass Formers

Azobenzene-functionalized molecular glasses were synthesized by C. Probst^[186] (molecular glasses based on cores **1** and **2**) and R. Walker^[187] (molecular glasses based on cores **3** and **4**). Their preparation comprises three important steps, viz., synthesis of the azobenzene side groups, synthesis of the molecular core, and the covalent assembly of both. This modular system has the advantage that a large variety of compounds becomes easily accessible. The main focus of this chapter is on the synthesis of the side groups, since the other processing steps have largely been discussed in the literature.^[67,85,127,187] To give only a basic overview about the reaction products, specific details such as processing temperature, surrounding atmosphere, or purification steps are omitted.

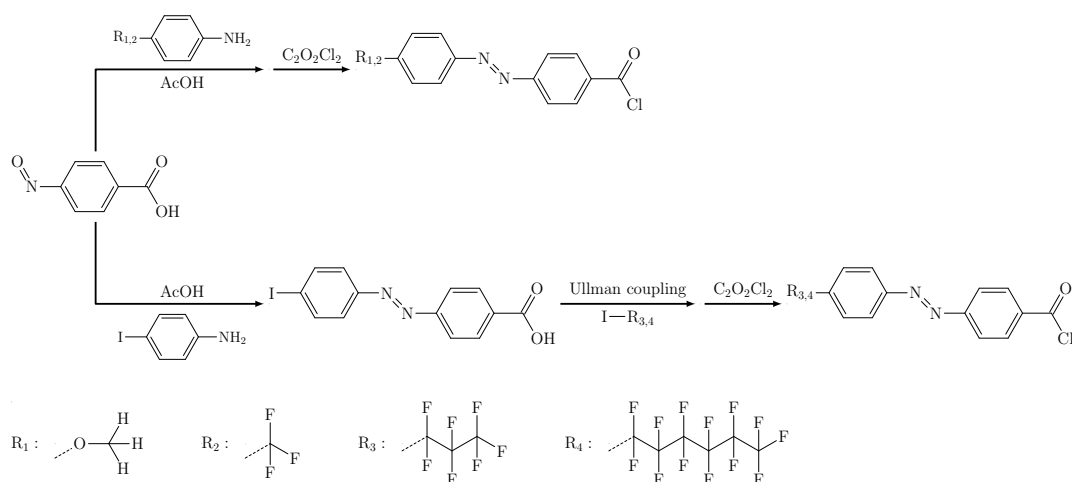


Figure 5.4: Reaction scheme of the synthesis of the azobenzene moieties used for the functionalization of the molecular glass cores.

The synthesis of the azobenzene side groups is based on the so-called Mills reaction, which involves the condensation of a nitrosobenzoic acid with an aniline derivative. Figure 5.4 shows that the reaction routes differ depending on the para substituent of the final azobenzene derivative. Para-methoxy- or para-trifluoromethyl-substituted (phenylazo)-benzoic acids were obtained from the Mills reaction directly, since the O-CH₃ and CF₃ moieties are the para substituents of commercially available aniline derivatives. Function-

alization with the perfluorinated moieties C_3F_7 and C_6F_{13} required a separate coupling reaction. Reacting an 4-iodoaniline during the Mills reaction step instead, resulted in a para-iodine-substituted azobenzene derivative. In a second step, the respective perfluoroalkyl iodide derivative was coupled to the product by a copper-catalyzed Ullmann reaction. It also involved an acid to ester conversion of the benzoic acid molecular part as well as the inverse process, which is not shown in Fig. 5.4. For further processing, the products of both reaction routes were subjected to chlorination.

To obtain molecular glasses **1a-e**, the azobenzoic derivatives were attached to a commercially available 6,6',7,7'-tetrahydroxy-4,4,4',4'-tetramethylbis-2,2'-spirobichroman core via an esterification reaction.^[127,179] The synthesis of the azobenzene-derivative reactants for the preparation of molecular glasses **2a-d** was equivalent to the one of the spirobichromane derivatives. Core and azobenzene moieties were linked by amidation of the 1,3,5-benzenetrisamine core in this case.^[127] A similar synthetic route was chosen for the molecular glasses **3a** and **3b** based on the triphenylamine core and **4e** based on the cyclohexane core.^[67,187]

5.1.2 Thermal and Optical Properties of Azobenzene Molecular Glasses

Differential scanning calorimetry (DSC) measurements were performed on a Perkin-Elmer DSC DIAMOND or METTLER DSC II under constant flow of liquid nitrogen (50 mL min^{-1}) at a scan rate of 10 K min^{-1} . Crucibles of $40 \mu\text{L}$ (Perkin Elmer) or $50 \mu\text{L}$ (METTLER) volumetric capacity were filled with 3 to 12 mg of the respective compound and the phase transitions were determined from the first and second heating and cooling thermograms. The first thermogram was taken from initially crystalline molecular glass as obtained from purification during synthesis. After erasing its thermal history during first heating, the crystallization temperature T_c was determined from first cooling. Glass transition temperature T_g , melting temperature T_m , and recrystallization temperature T_{recr} were measured during the second heating step. Molecular glasses with strong crystallization tendency, such as compounds **1b-c** and **2a-d**, did not show a glass transition in the second DSC thermogram. Therefore, materials **1b** and **2a** were prepared in the amorphous state by quenching them with liquid nitrogen from melt prior to DSC measurements. In this case, the T_g was determined from the first heating run. Glass transition temperatures of the remaining materials **1c-d** and **2b-d** could not be resolved by this procedure. For compound **2b**, however, it could be estimated from polarization optical microscopy (POM). A summary of the characteristic thermal and optical properties and the molar weights of the materials is given in Table 5.1.

Materials based on cores **1-3** feature high glass transition temperatures ranging from 90 to 140°C . As expected, the glass transition temperature depends on the molecular design of the core. While molecular glasses **3a-b** feature the lowest T_g , it increases for the spirobichromane compounds with the more rigid core and exhibits its highest value for the trisamide derivatives due to the formation of intermolecular H-bonds. The core unit of compound **4e** is similar to that of the trisamides, but due to the absence of H-bonds in the ester sequence, its T_g is as low as 58°C . Whereas a high T_g is ideal to protect imprints at high processing temperatures during etching, the low value of material **4e** is advantageous to enhance photoplastification in blend systems. As compared to the influence of the intermolecular interactions, the dependence of the glass transition temperature on the molecular weight (ranging from approximately 750 to 2500 g mol^{-1}) is small. All materials except for the neat molecular glass **3a** show a tendency to crystallize at the moderate scanning rate of the DSC. A polymorphic phase arises for the methoxy and some of the perfluoroalkyl-substituted compounds, as evidenced by the presence of multiple crystallization peaks in the DSC thermograms (cf. Table 5.1). In general, the introduction or lengthening of the perflu-

oroalkyl chains promotes crystallization. Despite increasing T_g , the formation of H-bonds between the molecular glasses based on core **2** has the same effect. However, all materials can be quenched into the amorphous phase by spin coating from solution or rapid cooling, which is confirmed by POM investigations. The decomposition temperatures of all materials are between 350 and 400 °C as determined by thermogravimetric analysis. CF₃- and C₃F₇-substituted molecular glasses have a characteristic melting temperature close to this temperature range, while the other compounds melt at temperatures below 275 °C. Additionally, compound **1d** shows polymorphic melting.

Table 5.1: Thermal and optical parameters of the molecular glasses. M : molar weight, T_g : glass transition temperature, T_m : melting temperature, T_c : crystallization temperature, $T_{\text{recr.}}$: recrystallization temperature, –: not existing. Estimated values are shown in parentheses.

compound	M [g mol ⁻¹]	T_g [°C]	T_m [°C]	T_c [°C]	$T_{\text{recr.}}$ [°C]	max. of $\pi \rightarrow \pi^*$ transition [nm]	max. of $n \rightarrow \pi^*$ transition [nm]
1a	1205	108 ^{b)}	249	–	215	327	(460)
1b	1477	126 ^{a)}	314	329	326	315	(457)
1c	1877	–	322	240	–	312	(456)
1d	2492	–	227, 260, 270	210, 222, 269	–	311	(458)
1e	1325	107 ^{b)}	239	–	170, 190	347	(475)
2a	748	136 ^{a)}	252	214	–	326	(438)
2b	952	128 ^{c)}	315	343	–	322	(465)
2c	1252	–	–	–	–	323	(467)
2d	1702	–	275	250	–	324	(468)
3a	918	92 ^{b)}	174	–	–	see text	(449)
3b	1122	100 ^{b)}	146	119, 143	–	see text	(444)
4e	847	58 ^{b)}	180	–	108, 150	346	(435)

^{a)} determined from first heating DSC ^{b)} determined from second heating DSC ^{c)} determined with POM

Optical properties of the molecular glasses were determined from thin solid films of 20 to 50 nm thickness after measuring their absorption spectra with a standard spectrometer (JASCO V-670). Either ester or amide linkages largely decouple the functionalized moieties from the core, reducing the π conjugation of the electronic system over the entire molecule. Therefore, the optical properties of all molecular glasses are mainly defined by the individual azobenzene chromophores and the absorption spectra of all compounds show a strong $\pi \rightarrow \pi^*$ transition in the UV and a much weaker $n \rightarrow \pi^*$ transition in the visible region. The influence of the para substituent of the chromophores can be discussed by means of the absorption spectra of compounds **1a**, **1b**, and **1e**, as depicted in Fig. 5.5. All spectra have been normalized to the optical density (OD) at the $\pi \rightarrow \pi^*$ transition maximum. The methoxy substituent as an electron-donating group shifts the spectral position of both transitions significantly to the red (cf. compound **1a** with the unsubstituted azobenzene chromophore). The trifluoromethyl substituent on the contrary, causes a blue shift of the $\pi \rightarrow \pi^*$ transition without strongly affecting the $n \rightarrow \pi^*$ band. Because of the decoupling of core and chromophore, the above statements apply to the other molecular glasses as well, even though the absolute shifts in absorption are much smaller (cf. Table 5.1). Molecular glasses based on C₃F₇- or C₆F₁₃-substituted chromophores have a similar absorption as their trifluoromethyl-substituted counterparts. The $\pi \rightarrow \pi^*$ transition of the azobenzene side groups in materials **3a** and **3b** strongly overlaps with the absorption of the molecular core, resulting in an ab-

sorption maximum at a wavelength of ~ 365 nm. By fitting two superimposed Gaussians, the $\pi \rightarrow \pi^*$ transition of the compounds based on the triphenylcore turns out to be in a similar spectral range as in molecular glasses with the same substituent.

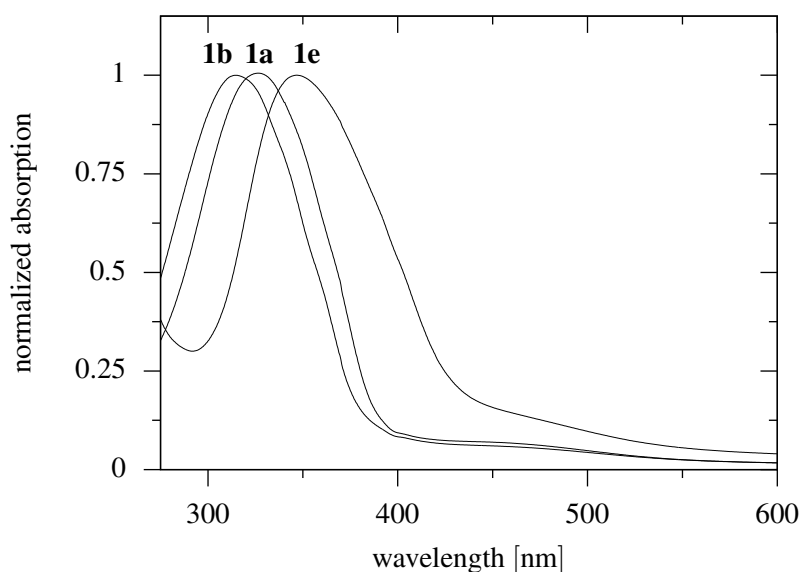


Figure 5.5: Normalized absorption spectra of thin films of molecular glasses **1a**, **1b** and **1e**.

In all materials, the $n \rightarrow \pi^*$ transition is weak and overlaps strongly with the $\pi \rightarrow \pi^*$ transition, such that the position of its maximum is difficult to determine. Fitting two Gaussians yields the approximate positions of the $n \rightarrow \pi^*$ transition listed in Table 5.1. Closer inspection reveals that the absorption comprises more than two components, however.

5.2 Azobenzene-Functionalized Polymers

Azobenzene-functionalized homopolymers and block copolymers have been shown to be suitable materials for the storage of long-term-stable holographic Raman-Nath or Bragg-selective gratings.^[37,40,41] In contrast to molecular glasses, the azobenzene side chains are connected via a spacer to a polymer backbone and the amorphous phase is further stabilized by the presence of entanglements. In azobenzene-functionalized homopolymer films, *trans-cis-trans* isomerization can take place in a cooperative manner, since the azobenzene chromophores are in spatial proximity. As a result, the holographic volume gratings show increased writing speed and enhanced stability.^[33,181] On the other hand, the high optical density of functionalized homopolymers prevents their use for the inscription of Bragg-selective volume holograms. Blending of these polymers usually causes macro-phase separation and, therefore, scattering increases, which is detrimental to holographic applications. Instead of homopolymers, statistical copolymers with much lower optical density can be used. Yet, the cooperative effect between the azobenzene chromophores is lost in these materials and the inscribed gratings lack long-term stability.^[181]

A different material class are block copolymers, which are composed of an azobenzene-containing minority and a photo-inactive majority block. In these systems uniform micro-phase separation occurs, leading to the formation of different morphologies (e. g., lamellae, cylinders, or spheres) with the photo-active domains typically below 50 nm in size.^[40] Consequently, the optical density is significantly reduced and scattering of visible light is

avoided. At the same time, the spatial proximity of the photo-orientable azobenzene moieties is preserved. The majority block usually shows a good miscibility with a homopolymer of the same kind, allowing further dilution of the minority phase without changing the morphology.^[37,188] Although most block copolymers are found to meet the stability criterion, the azobenzene moieties in the confined domains usually lack high reorientation rates.^[41] SRG formation is prevented in block copolymers but can occur in homopolymers and statistical copolymers, where the azobenzene moieties are not confined by an amorphous, optically inert majority block.^[40,42,43]

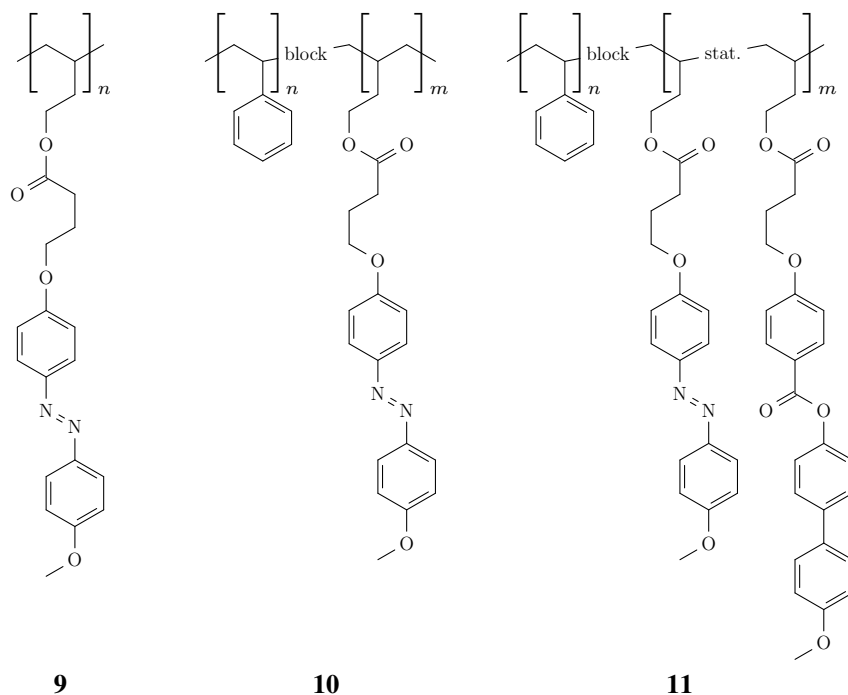


Figure 5.6: Chemical structures of methoxyazobenzene-functionalized homopolymer **9** and block copolymers **10** and **11**.

The chemical structures of the polymers used for holographic grating inscription or Azo-NIL experiments are depicted in Fig. 5.6. Homopolymer **9** and block copolymers **10** and **11** show good miscibility with molecular glass **4e** as they share the same (methoxy-substituted) azobenzene moieties. DSC measurements revealed a glass transition for each polymer (cf. Table 5.2), meaning that they can easily be prepared as amorphous thin films or thick samples. In block copolymers, glass transitions exist for both minority and majority block. Often, DSC is not sensitive enough to detect the former but previous holographic measurements have shown that the T_g of the minority block of block copolymer **10** is around 34 °C.^[38] Polydispersity index (PDI) and number-average molecular weight M_n further characterize the polymers. The PDI is defined as the weight-average molecular weight divided by the number-average molecular weight. It is a measure for the length distribution of polymer chains, whereby values close to one indicate a narrow molecular-weight distribution.

In addition to photoactive, azobenzene-functionalized polymers, polystyrene (BASF 165 H) was used as an optically inert blending material as received from BASF SE. Its important characteristics are listed in Table 5.2.

Table 5.2: Polymer specification. M_n : number-average molar weight, PDI: polydispersity index, w_{PS} , w_{azo} , and $w_{mesogen}$: weight fractions of the polymer blocks, n. d.: not determined, –: not present.

compound	T_g [°C]	M_n [g mol ⁻¹]	PDI	w_{PS} [wt%]	w_{azo} [wt%]	$w_{mesogen}$ [wt%]	max. of $\pi \rightarrow \pi^*$ transition [nm]
PS	97	124 000	1.9	100	–	–	–
9 (i)	47	200 000	1.4	–	100	–	327 ^{a)}
9 (ii)	74	375 000	n. d.	–	100	–	333
10	34 ^{b)} ;103	59 000	1.04	82.5	17.5	–	346 ^{a)}
11	n. d.;106	127 000	1.05	72	11	17	361 ^{a)}

^{a)} from ref. [85] ^{b)} from ref. [38]

Homopolymer **9** is a methoxy-azobenzene-based side chain polymer with a poly(1,2-butadiene) backbone and was synthesized as described in literature.^[40] It exists in two types **9 (i)** and **9 (ii)**, which differ in their degree of polymerization and, hence, their T_g . For the sake of comparability to previous results, homopolymer **9 (i)** was used for volume holography. The higher molecular weight of homopolymer **9 (ii)** is expected to have significant influence on the photo-induced mass transport; hence, it was used for Azo-NIL. As compared to the methoxyazobenzene-substituted molecular glasses, the $\pi \rightarrow \pi^*$ absorption of the homopolymers is blue-shifted, which can be attributed to the formation of H-aggregates between the chromophores. Obviously, the mechanical constraints of the polymer backbone increase the spatial proximity of the azobenzene moieties.

Materials **10** and **11** are AB-type block copolymers with a poly(1,2-butadiene) backbone. Detailed information about their synthesis can be found in the literature.^[40,41] Both block copolymers have a polystyrene majority block but differ in the percentage and the composition of their minority block. Whereas the minority block consists solely of methoxyazobenzene-functionalized side chains in **10**, it is functionalized statistically with methoxyazobenzene and non-photoactive mesogenic side chains (46 mol % : 54 mol %) in **11**. The introduction of photoinactive, rigid mesogenes results in a long-term stable refractive-index modulation, which is not the case for gratings stored in block copolymer **10**.^[41] Yet, block copolymer **10** is an interesting system because its blocks correspond to either the PS (polystyrene) or the azobenzene-functionalized homopolymer discussed above. It is known from literature, that block copolymer **10** has a cylindrical morphology.^[40] For block copolymer **11**, data are available only for similar compounds with comparable block weight ratios but different molecular weights.^[41] Since the latter has minor influence on the polymer morphology, compound **11** is expected to have a cylindrical morphology as well. The spectral position of the $\pi \rightarrow \pi^*$ transition of **10** does not significantly deviate from that of the methoxyazobenzene moiety in the molecular glasses. In **11**, however, it is shifted to the red, which may be attributed to the presence of the mesogenic units.

5.3 Preparation of Amorphous Thin Films

The method used for the preparation of the above materials as thin, photoactive films is crucial for the formation of the amorphous phase and for their behavior during holographic and Azo-NIL experiments. If prepared from solution in a volatile solvent, molecular glasses or polymer blends are frozen in a glassy state due to the quick evaporation process. Unless otherwise stated, amorphous, homogeneous films of high optical quality free from light scattering were obtained for all materials by applying the techniques discussed below.

Thin films for the inscription of holographic volume gratings were prepared on commercial microscope slides by spin coating or doctor blading. For spin coating, a small amount of filtered THF solution, comprising a total amount of 4 wt% of a blend of polymer and molecular glass, was dropped onto the glass substrate. The mixing ratio of polymer and molecular glass was chosen according to the intended total composition. By rotating the substrate at a speed of 1000 rpm, the solution homogeneously spread under the influence of the centrifugal force. Since the solvent quickly evaporated during the coating process, a uniform, amorphous film formed within a spinning time of 60 s. For doctor blading, a blade was positioned with a predefined gap above a glass slide. While constantly adding the same 4 wt% THF solution as used for spin coating, a blade moved at a fixed speed of 20 mm s⁻¹ over the substrate and distributed the material homogeneously. After evaporation of the solvent, a solid film remained. Subsequent to the above coating techniques, residual solvent was removed by annealing the freshly prepared films for 3 h at a temperature of 70 °C. The final films had thicknesses between 0.3 and 2.0 μm, as measured with a profilometer (Dektak Veeco 3300ST auto remote control stage profiler).

Neat molecular glass or homopolymer films used for SRG formation or Azo-NIL were prepared by spin coating a filtered solution of 7 to 11 wt% of the respective compound in the following solvents, cyclopentanol for compounds **1a** and **1e**, N-methyl-2-pyrrolidone for compound **2a**, and tetrahydrofuran (THF) for the remaining materials. Prior to coating, the glass substrates were cleaned with THF and compressed argon. After coating at a rotational speed of 700 to 1000 rpm for 60 s, the films had an approximate thickness of ~500 nm. For the preparation of films with thicknesses ranging from 50 to 1000 nm, the rotational speed was adjusted accordingly (500 to 1500 rpm), while the coating time stayed constant. To remove any residual solvent, all films were annealed for 1 h at temperatures between 70 and 110 °C.

Compounds **1d** and **2d** crystallized directly after spin coating. Films of these materials have poor optical quality due to light scattering and their inhomogeneous surface.

Fabrication and Properties of Molds

6.1 Fabrication of Flexible Molds

Rigid quartz or chromium masters are expensive to produce and, due to their size, difficult to handle. To avoid damage to the master, direct use as a mold is not recommended. Furthermore, rigid masters lack sufficient adhesion for Azo-NIL. Hence, prior to imprinting, flexible molds should be prepared from the master by common UV-curing techniques. For holographically prepared SRGs, molding is a convenient concept to obtain optically stable gratings.

6.1.1 Molds with Features on the Micrometer Scale

A standard lithographic photo mask for an EVG[®] 620 automated alignment system (company EVG) was used as a master for the preparation of molds with micrometer-sized features. It is made of transparent fused silica covered with a chromium layer of 100 nm thickness featuring grooves of varying width. A small section of the master containing a field with L-shaped grooves is shown in the microscope image on the left side of Fig. 6.1. The grooves have a rectangular profile and are arranged such that line patterns of different periodicity result. The width and spacing of the lines of each pattern are 1, 1.5, 2, 2.5, 5, and 10 μm , respectively. Thus, their periodicity corresponds to twice these values. Because cavities and protrusions have equal size, the filling factor remains constant over the whole field, viz., $\nu = 0.5$. The length of the structures in horizontal and vertical direction is large as compared to their width.

To obtain a transparent, flexible PDMS replica, the whole master was cast from a temperature-curable two-component system (Elastosil[®] 601). A Hausschild SpeedMixer[™] DAC 150 SP was used to mix prepolymer and thermal initiator in a ratio of 9:1. After casting the mixture onto the master, crosslinking took place first at room temperature for 12 h and, subsequently, at 150 °C for another two hours. When the cured PDMS mold was removed it had a thickness of approximately 5 mm with the inverse structures of the master on its top.

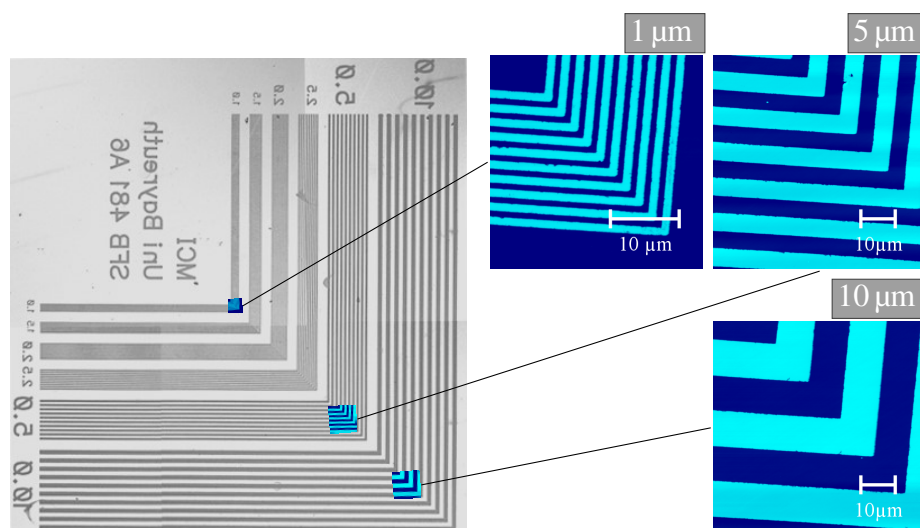


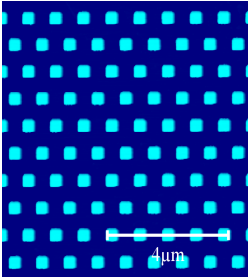
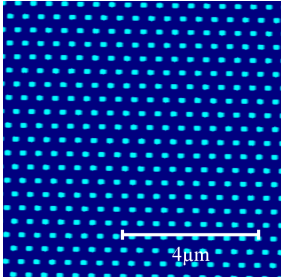
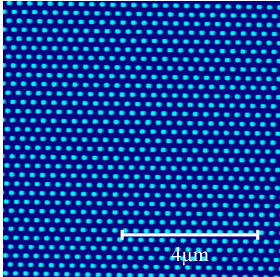
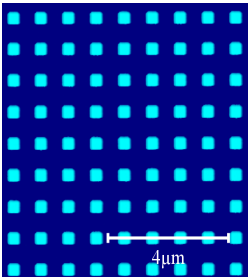
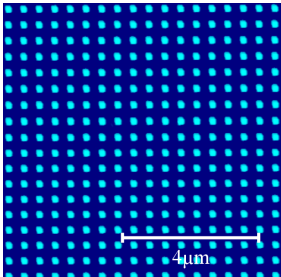
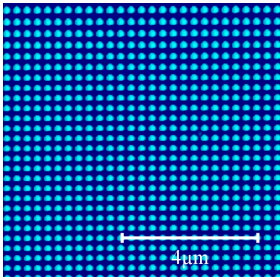
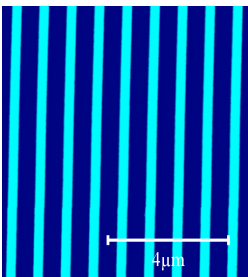
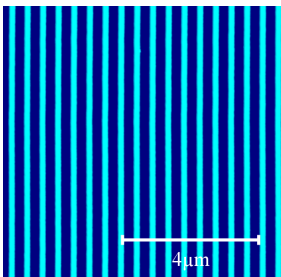
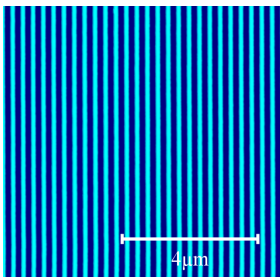
Figure 6.1: A PDMS mold with various L-shaped line patterns of different sizes was obtained from casting the master shown on the left. Available line widths are 1, 1.5, 2, 2.5, 5, and 10 μm . Replica perfectly match the inverse profile of the master as shown by the AFM images on the right side. Differences in height between bright and dark areas are 100 nm and 99 ± 1 nm for master and mold, respectively.

The master has a diameter of ~ 10 cm and contains several hundred of the fields shown in Fig. 6.1, as well as an inverse version of the pattern. The final PDMS molds were obtained from the large replica by cutting it into the separate fields. Hence, a large number of molds were simultaneously prepared from casting the master once. Each of them has a quadratic shape with dimensions $2.5 \times 2.5 \text{ mm}^2$ and contains all the L-shaped line patterns discussed above. The molds feature depth profiles with the same height as the master, which was verified by AFM measurements as shown on the right side of Fig. 6.1. The height difference between bright and dark regions is 99 ± 1 nm, which is close to that of the master of 100 nm. The AFM data were measured at different spots on one of the PDMS molds. Their positions are indicated by the highlighted areas in the left panel of Fig. 6.1.

6.1.2 Molds with Features on the Nanometer Scale

Molds for imprinting structures with features on the nanometer scale were prepared by casting a so-called 65 standard fused-silica master (Stamp ID: 65SS_V1) from NIL Technology ApS. As illustrated in the AFM images in Table 6.1, the master features different pattern types of pillars or lines (top to bottom) with protrusion sizes 300, 150, and 100 nm (left to right). These numbers represent target values for the manufacturing process of the master. The actual values for all pattern types are listed in Appendix A. For clarity, the protrusion sizes are categorized according to the three numbers presented above, disregarding small deviations of less than 15%. Detailed information about the arrangement of the patterns and the available types is given within the discussion of the mold properties. The height difference between bright and dark regions in the AFM images of Table 6.1 is 105 ± 1 nm for all patterns, which is in good agreement with the specification of the manufacturer of 103 nm.

Table 6.1: AFM images of nine different pattern types present on the NIL-Technology ApS master. It features three different geometries (lines, rectangular and hexagonal arrangement of pillars) with protrusion widths of 300, 150, and 100 nm. Dark areas indicate lower regions, while bright areas represent elevated regions of 105 nm height. The distance between the protrusions is twice their width (type II pattern).

pillar or line width/spacing			pattern
300 nm / 600 nm	150 nm / 300 nm	100 nm / 200 nm	
			hexagonal arrangement of pillars
			rectangular arrangement of pillars
			lines

Prior to molding, approximately 10 ml hexamethyldisilazane were heated up to reflux (160 °C, 2 h) and condensed at the surface of the master to reduce adhesion (silanization). A UV-curable fluorinated polymer kit distributed by EVG[®] was used for casting. First, the EVG[®] prepolymer and 2 wt% UV initiator were mixed for 30 min at ambient conditions in the dark. Subsequently, this mixture was poured over the silanized master and exposed to UV light at a wavelength of 365 nm for 100 s. The light was provided by the mercury lamp of an EVG[®] 620 mask aligner, ensuring uniform illumination at an intensity of 20 mW cm⁻² and homogeneous crosslinking of the resin. Casts were also prepared from Elastosil[®] 601 resin under different curing conditions. Detailed information about their preparation and properties is given in Chapter 6.2.2.

After release, the EVG[®] cast has an approximate thickness of 1 mm with eight spatially separated fields on top of it as schematically depicted in Fig. 6.2 (top left). In a final step these fields were cut apart. Thus, eight EVG[®] molds were fabricated from casting the master once. Each of them has a size of 2.5 × 2.5 mm² and is subdivided into nine individually patterned quadratic sections of 200 × 200 μm² area. The enlarged section of Fig. 6.2 illustrates the different geometries, comprising hexagonal and rectangular patterns of punches (inverse pillars) and lines (top to bottom) with cavity sizes $w = 300, 150, \text{ and } 100 \text{ nm}$ (left to right). The definition of the protrusion and cavity width s and w , respectively, depends on the pattern type as indicated by the white arrows. Two spacings are available on the different fields of the uncut mold. For type I the ratio of s and w is 1 : 1, whereas for type II it is 2 : 1. Within one of the fields, the spacing does not change; thus, four identical molds, each of type I or II, are prepared from a single cast. The above procedure was repeated accordingly to obtain the number of molds required for the Azo-NIL experiments.

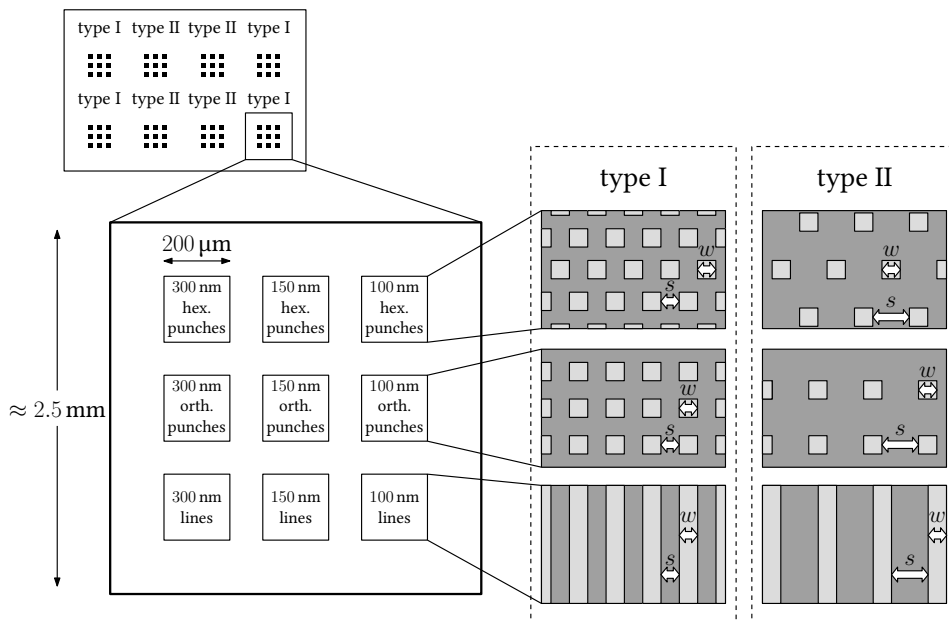


Figure 6.2: The enlarged section shows the schematic diagram of an EVG[®] mold used for nanopatterning. It contains nine fields with different patterns (lines, rectangularly and hexagonally arranged punches) and feature sizes of 300, 150, and 100 nm. Dark areas indicate elevated regions, while bright areas represent cavities. The master features two different spacings such that the molds can be of type I or II with $w : s$ being 1 : 1 and 1 : 2, respectively.

6.1.3 Sinusoidal PDMS Surface Relief Gratings

Sinusoidal gratings in PDMS were prepared by casting SRGs, which have been generated holographically on a thin film of molecular glass **1a**. A homogeneous, flat film was obtained by spin coating a 7 wt% THF solution of **1a** on a glass substrate similar to the procedure described in Chapter 5.3. The solvent THF, however, resulted in a film thickness of approximately 1 μm after spinning the glass slide at a rotational speed of 700 rpm for 60 s. Residual solvent was removed in this case by annealing the film at 80 $^{\circ}\text{C}$ for 1 h under nitrogen atmosphere.

The holographic setup was used to inscribe SRGs with a diameter of ~ 2 mm at different spots on the film. For efficient grating generation, the polarization of the writing beams was adjusted to *pp*. The intensity of each beam was 1.0 W cm^{-2} . After illumination for 100 s, a SRG of ~ 250 nm amplitude with a grating period of 1000.6 ± 1.7 nm developed. The latter was calculated from the wavelength and the angle of incidence of the writing beams outside the medium according to Eq. (2.3).

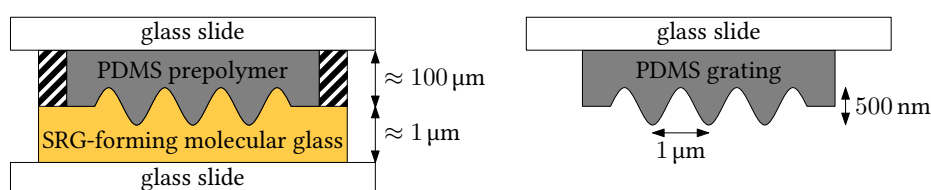


Figure 6.3: Preparation of a sinusoidal PDMS grating by casting a holographically written SRG. Left side: Assembly during curing. Right side: PDMS grating after removal of the SRG master.

To transfer the grating, 1 g of Sylgard[®] 184 cast resin (siloxane/curing agent = 10:1 (w/w)) was placed on top of the holographically processed film. Subsequently, a glass slide was positioned approximately 100 μm above it, the distance being determined by Scotch tape spacers which were attached to both sides of the molecular glass master (see Fig. 6.3). During this procedure the resin spread homogeneously over the entire film surface and filled the voids between molecular glass and upper substrate. Thermal curing was performed by first storing the assembly at ambient conditions overnight and, in a second step, at 80 $^{\circ}\text{C}$ for 2 h. After this procedure, the glass slides were separated from each other and a homogeneous, transparent PDMS layer on top of a glass substrate with the negative SRG patterns transferred to its surface was obtained. Because PDMS and molecular glass **1a** are easily separable, no cleaning was required. Height and periodicity of the imprinted PDMS gratings matched the values of the holographically generated SRG master.

6.2 Properties of Flexible Molds

Unlike rigid masters, adhesive molds which are prepared from polymers of low Young's modulus deform upon interaction with the resist material or with themselves. Depending on the mold geometry, collapse of the mold roofs or lateral deformation can occur. The description of these effects is important to understand the behavior of the flexible molds when applied in Azo-NIL experiments. In particular, the instructions given below constitute a guideline for the preparation of defect-free molds.

6.2.1 Roof Collapse of PDMS Molds

Roof collapse denotes an effect which is observed when an elastic mold with a low Young's modulus and critical profile dimensions comes into contact with a solid substrate. This situation is illustrated in Fig. 6.4 for a mold with protrusion and cavity width s and w and height h_m . The initial profile of the PDMS mold is assumed to be rectangular in shape as indicated by the dashed lines. Obviously, the cavity roofs of a flexible material bend if external pressure is applied or if gravitational forces act on the mold.^[189] Moreover, if adhesive forces exist between PDMS polymer and substrate, neither gravity nor pressure is required to induce lowering of the roofs.^[190,191] For sufficiently strong adhesion, the roofs either jump into contact with the substrate below spontaneously or stay collapsed after the mold is pressed against the substrate initially. In both cases, roof collapse is stable even if gravitational forces act in a direction away from the substrate.

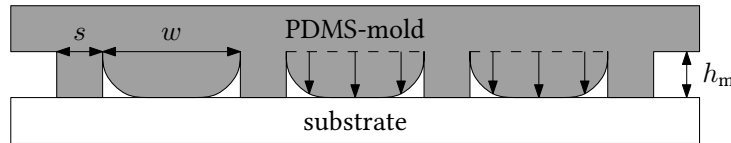


Figure 6.4: Schematic diagram of the roof collapse of a soft PDMS mold caused by adhesion.

It is easy to see that the presence of large cavities with $w/s \gg 1$ favors sagging. Furthermore, the roofs are able to touch the substrate more easily if w is significantly larger than h_m . Analytical solutions for the adhesion-induced pressure distribution below arbitrary, soft periodic structures in contact with a substrate can be found in the literature.^[171] A more specific solution for the exact deformation of a rectangular PDMS mold was derived by Zhou et al.^[192] The criterion for the stable roof collapse of a periodic rectangular structure derived by Huang et al.,^[191] however, is of more practical use. It reads

$$w_{\text{crit}} = \frac{0.29}{\ln 2} \cdot \frac{E h_m^2}{W_{\text{adh}}} \quad (6.1)$$

if s and w are assumed to be equal. For s or $w > w_{\text{crit}}$, the PDMS roofs are predicted to collapse towards the substrate.

The Young's modulus E of PDMS is usually in the range of 1 to 5 MPa and depends on the curing conditions.^[193,194] In the case of the Elastosil[®] 601 molds discussed in Chapter 6.1.1, Young's modulus is expected to be approximately $E = 1.4$ MPa.^[194,195] The work of adhesion W_{adh} can only be estimated roughly, since it is calculated from different surface energy terms, which depend on the interaction with the substrate. A value of $W_{\text{adh}} \approx 50.6 \text{ mJ m}^{-2}$ is available from a roof collapse experiment conducted with the more common Sylgard[®] 184 PDMS polymer on a native silica glass layer by the group of Huang.^[191] This

value is reasonable since it is approximately twice the critical surface tension γ_c of PDMS, which is in the range of 22 to 24 mJ m⁻².^[196] From the above values and a mold height of 100 nm, the critical protrusion width is calculated to be $w_{\text{crit}} = 0.12 \mu\text{m}$.

To investigate the deformation behavior of PDMS molds with features on the micrometer scale, their diffraction was monitored with a 489 nm laser (cf. Chapter 7.1) before and after bringing them into contact with different solid surfaces. Roof collapse occurred for all L-shaped line patterns, as soon as the molds came into contact with any of the photo-active films or a fused-silica substrate even without applying any external pressure. This finding is in good agreement with Eq. (6.1) because all patterns present on the molds fulfill the criterion $w > w_{\text{crit}}$ (width of the smallest cavity: $w = 1 \mu\text{m}$). Obviously, sagging is facilitated by the low aspect ratio ($10 \leq w/h_m \leq 100$).

Even though the voids below a roof-collapsed mold are quite small, the feasibility of Azo-NIL is not impaired. As will be shown in Chapter 10, imprints with the inverse profile of an uncollapsed mold can easily be prepared. It is known from literature that roof collapse can be reversed if the voids between mold and sample are filled with a liquid.^[191] In this case W_{adh} decreases up to an order of magnitude. With azobenzene-functionalized systems, a similar behavior may arise from the interaction with the resist, once it is in the photofluidic state. If, for example, W_{adh} decreases by a factor of ten, w_{crit} assumes a value of 1.2 μm . In this case, roofs of smaller cavities are expected to rise, while bigger structures stay collapsed.

6.2.2 Lateral Stability of PDMS Molds

In contrast to roof collapse, the deformation mechanism discussed here is not based on the interaction of the mold with the surface of a substrate. Instead, the elastic behavior of the mold material in combination with the adhesive forces between the protrusions causes the imprinted profile to differ from the one of the rigid master. The lateral collapse of the mold protrusions is depicted schematically in Fig. 6.5. As soon as their strain energy is sufficiently low to be overcome by adhesion, neighboring protrusions spontaneously jump into contact. For this to happen, the lateral collapse requires that h_m be at least on the order of w . Therefore, this effect is not observed on the molds with indentations on the micrometer scale (cf. Chapter 6.1.1).

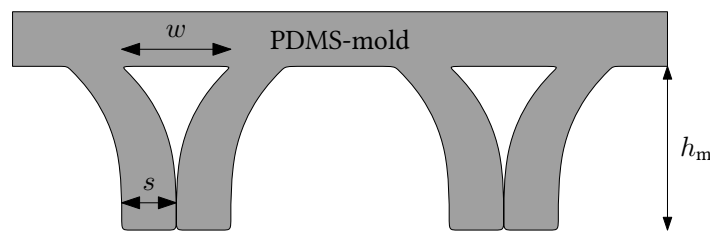


Figure 6.5: Schematic diagram of laterally collapsed line patterns of an elastic mold (cross-sectional view). The collapse is induced by the adhesive interaction of neighboring protrusions.

A quantitative stability criterion has been derived by Hui et al. based on a model of two isolated plates clamped at one end.^[197] According to their theory, lateral collapse of line patterns occurs for cavity widths $w < \tilde{w}_{\text{crit}}$, with

$$\tilde{w}_{\text{crit}} = \sqrt[5]{\frac{\gamma_s h_m^4}{E \zeta^3}} \quad (6.2)$$

and $\zeta = s/w$.

Due to their good adhesive properties, first attempts to produce molds with features on the nanometer scale from the NIL-Technology master were carried out with the PDMS polymers Elastosil[®] 601 and Sylgard[®] 184. The surface energy γ_s of PDMS is on the order of 20 mJ m^{-2} .^[196,198] By inserting a typical modulus of $E_{\text{Elastosil}} = 1.4 \text{ MPa}$ and a height of $h_m = 100 \text{ nm}$ into Eq. (6.2), one obtains $\tilde{w}_{\text{crit}} = 68 \text{ nm}$ for $\zeta = 1$ (type I pattern) and $\tilde{w}_{\text{crit}} = 45 \text{ nm}$ for $\zeta = 2$ (type II pattern). Young's modulus is chosen to be the one of Elastosil[®] 601, which is lower than that of Sylgard[®] 184 ($E_{\text{Sylgard}} \approx 1.8 \text{ MPa}$).^[195,199] From the above results, lateral collapse is not expected to occur for any of the line patterns on the molds prepared from both PDMS polymers.

However, while the 150 and 300 nm line patterns kept their lateral line profile after release from the master, the 100 nm line patterns were found to collapse for both polymers. These values denote the cavity width w and are valid for both type I and II molds. The deformation caused by lateral collapse is illustrated in Fig. 6.6 a) and 6.6 b) for 100 and 300 nm line patterns of type I molds prepared from Elastosil[®] 601, respectively. For decreasing values of w , the periodic arrangement of parallel lines transforms into a complicated Y-branched pattern. Consequently, the true value of \tilde{w}_{crit} turns out to be in the range $100 \text{ nm} < \tilde{w}_{\text{crit}} < 150 \text{ nm}$.

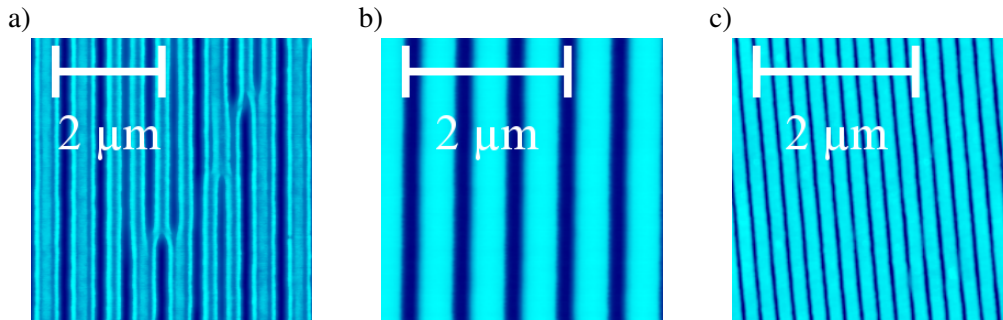


Figure 6.6: AFM pictures of line patterns of molds prepared from different UV-curable polymers. a) Laterally collapsed 100 nm line pattern prepared from Elastosil[®] 601 (type I). b) 300 nm line pattern prepared from Elastosil[®] 601 (type I). c) 100 nm line pattern prepared from EVG[®] (type II).

Deviations from theory can be attributed to the fact that the stability criterion in Eq. (6.2) is based on the assumption that two isolated plates protrude perpendicularly from a rigid substrate. Obviously, this applies here only partially, since the protrusions are located on a flexible underground which can bend itself. The derivation of Eq. (6.2) then overestimates the strain energy required to deform the structures and \tilde{w}_{crit} is predicted to be smaller than the measured value. Nevertheless, Eq. (6.2) yields valuable information about the influence of changes in specific mold parameters on the lateral stability.

The absence of Y branches for 150 nm line patterns suggests that even a slight increase in Young's modulus of the polymers may be sufficient to prevent lateral collapse. For PDMS polymers, E is known to be almost doubled if curing is performed at elevated temperatures.^[193] Thus, Elastosil[®] 601 and Sylgard[®] 184 molds were cast from the master under different curing conditions. In procedure 1 (**P1**), curing was performed overnight at room temperature and, subsequently, the polymer was stored at 80°C for 14 h. For molds prepared according to procedure 2 (**P2**), the resin was heated up to 150°C within 20 min immediately after it had wet the master and was kept at this temperature for 12 h. The latter preparation method is expected to increase Young's modulus of the PDMS polymers as a consequence of a higher degree of cross-linking caused by the higher curing temperature.

First, the profiles of line patterns of type I and II molds with $w = 300$ nm prepared from the two PDMS polymers under the above curing conditions were investigated. Three representative profiles measured with AFM are shown in Fig. 6.7. After release, the surface tension deforms the elastic PDMS molds, until an equilibrium state is reached. Thus, flexible molds generally develop rounded corners at their edges, even if cast from a perfectly rectangular shaped master. A lower limit for the radius of curvature is $R \approx \gamma_s/E$, which is on the order of 50 nm in PDMS.^[196] Since the Elastosil[®] 601 molds have the lowest Young's modulus, their profiles show the strongest deviations from the rectangular profile. The profile of an Elastosil[®] 601 mold with 1 : 1 spacing prepared with **P1** looks almost sinusoidal due to the spatial proximity of the protrusions (Fig. 6.7, bottom). The higher curing temperature of **P2** produces line patterns with slightly sharper edges although the profile of the investigated mold with 2 : 1 spacing reveals slanted sidewalls (Fig. 6.7, middle). Preparing Sylgard[®] 184 molds with **P2** results in a significantly improved reproduction of the edges (Fig. 6.7, top). As compared to Elastosil[®] 601 molds, however, the transferred cavities are clearly narrower. In sum, adjustment of the annealing procedure has a much smaller influence on the mold quality than varying the polymer type.

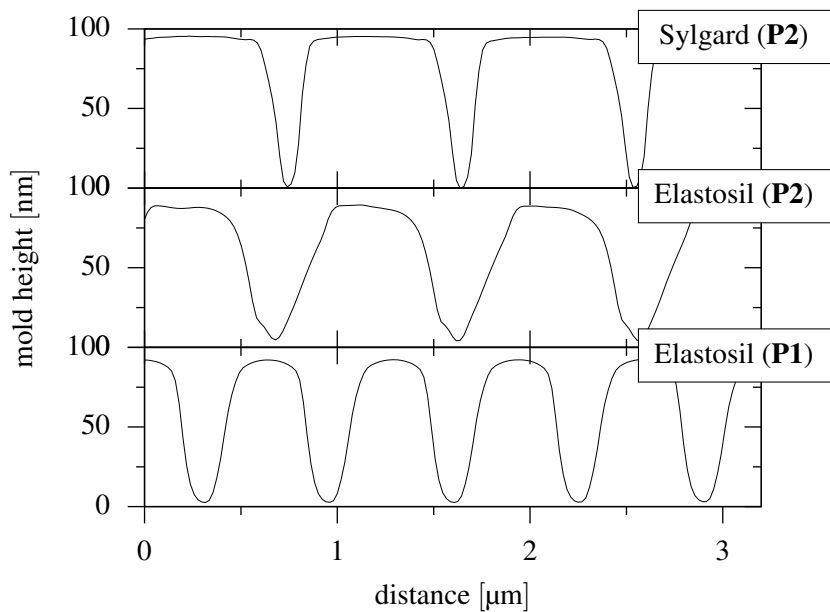


Figure 6.7: AFM profiles of 300 nm line patterns of PDMS molds prepared under different curing conditions. Bottom: Profile of an Elastosil[®] 601 mold (type I) prepared from **P1**. Middle: Profile of an Elastosil[®] 601 mold (type II) prepared from **P2**. Top: Profile of a Sylgard[®] 184 mold (type II) prepared from **P2**.

The lateral collapse of the 100 nm structures could not be avoided, neither by curing the molds at higher temperatures nor by preparing them from Sylgard[®] 184. Unlike roof collapse, the shape of the mold does not change during imprinting. Instead, the Y-branched patterns are transferred to the azobenzene resist material. Laterally stable line patterns with $w = 100$ nm for type I and II molds were obtained only after changing the mold material to the EVG[®] polymer and applying the preparation method discussed in Chapter 6.1.2. The reason is that the cured EVG[®] polymer features an increased Young's modulus. In addition it is functionalized with fluorine, whereby its surface energy is significantly lower than that of PDMS. The profile of a 100 nm EVG[®] line pattern (type II) is shown in the AFM image of Fig. 6.6 c), revealing homogenous, uncollapsed lines. As a drawback, adhesion of an EVG[®] mold to an arbitrary substrate decreases as well, which affects the imprinting speed.

For comparability of imprinting times, molds used for the fabrication of micrometer- or nanometer-sized structures should preferably consist of the same material. Hence, using Elastosil[®] 601 molds is reasonable for imprinting uncollapsed 150 and 300 nm line patterns as well as for rectangular and hexagonal arrangements of punches.

7.1 Holographic Setup

Inscription of holographic gratings was performed with the setup shown in Fig. 7.1. It has been built and improved during several PhD works.^[85,184,200,201]

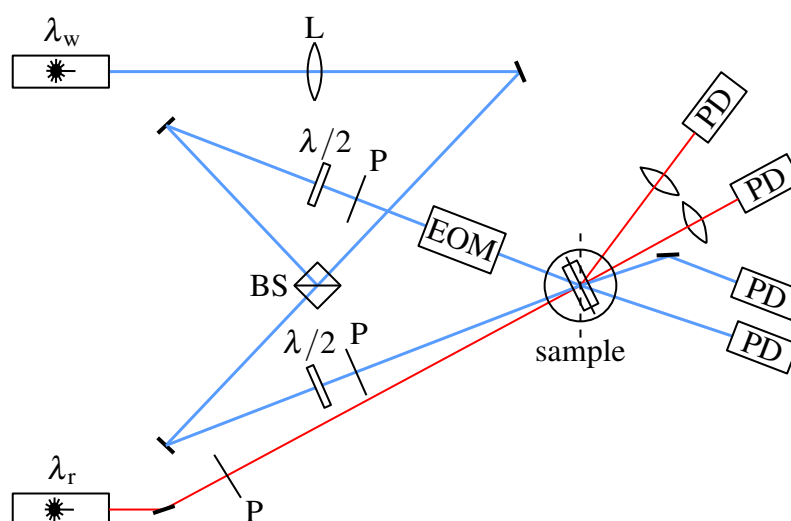


Figure 7.1: Setup for the inscription of plane-wave holographic gratings. BS: beam splitter, $\lambda/2$: half-wave plate, P: polarizer, PD: photodiode, EOM: electro-optical modulator, L: lens.

Coherent light for the inscription of the holographic gratings is provided by an argon-ion laser (Coherent Innova 307) at a wavelength of $\lambda_w = 488$ nm or by an optically pumped semiconductor laser (Coherent Genesis™ MX SLM Series) at $\lambda_w = 489.2$ nm. Owing to the system change during the PhD work, the wavelengths of the two laser systems differ slightly. The influence on the efficiency of the azobenzene isomerization, however, is negligible. In both cases, the $n \rightarrow \pi^*$ transition of the azobenzene-functionalized samples is excited, giving rise to a *trans*-rich state during illumination. Since this reduces the number of randomly relaxing *cis* isomers after the inscription process, the long-term stability of volume holograms is fostered. The writing beam first passes a lens (see discussion below). Subsequently, it is divided into two beams by a beam splitter. Either of them is deflected by a mirror, such that they interfere at the sample position. Their intensity and polarization can be adjusted individually by an arrangement of a half-wave plate and a polarizer. Unless

stated otherwise, the intensity of each beam was 1.0 W cm^{-2} . The polarization configuration was either *pp* or *ss*, depending on whether SRG formation was desired or not. In both cases, sinusoidal intensity gratings are generated at the interference region.

The temporal evolution of a grating is monitored with an *s*-polarized diode laser (Laser 2000 PMT24). Since its peak wavelength of $\lambda_r = 685 \text{ nm}$ is outside the azobenzene absorption band, it does not affect the development of the grating. The reading laser is adjusted to hit the center of the grating with an optical power of $87 \mu\text{W}$. The intensities of the 0th and 1st diffracted order emerging behind the sample are measured with photodiodes (Thorlabs PDA-55). Their signals are processed with lock-in amplifiers (Stanford Research Systems SR830) operating with an integration time of 10 ms. For this purpose, the intensity of the reading laser is modulated at a frequency of 10 kHz. This measurement method results in a high signal-to-noise ratio with the lower detection limit of the diffraction efficiency as low as 1×10^{-6} .

To generate gratings with constant periodicity throughout the entire interference region, the wave fronts of the writing beams have to be highly planar. For a laser with Gaussian intensity profile this requirement is best fulfilled near its beam waist. Hence, the writing beams are focused onto the sample surface by placing a lens ($f = 150 \text{ cm}$) between the laser head and the beam splitter. Depending on the laser system used for inscription, the resulting beam diameter at the sample position is 1.4 mm (488 nm) or 1.1 mm (489.2 nm). Grating diffraction theory further assumes that the probing light be a plane wave. Focusing of the reading beam onto the sample is achieved by adjusting a lens integrated in the laser module.

Samples are mounted on a rotational stage. It is used to vary the angle of incidence of the reading beam for either angular multiplexing or the determination of critical diffraction angles (cf. Chapter 9). The stage is driven by a stepper motor which provides an angular resolution of 1×10^{-2} degrees.

The angle between the writing beams is 28.30° in air, resulting in a grating period of approximately $1 \mu\text{m}$. During grating inscription, the angle of incidence of the reading wave is $\theta_r = 19.85^\circ$. It is adjusted such that the Bragg condition is fulfilled for thick holograms. To calculate the refractive-index or surface modulation from the diffraction efficiency of Raman-Nath and Bragg-selective gratings, the angle of incidence of the readout beam inside the medium has to be determined. It can be derived from Snellius's law if the refractive index of the photo-active material is known. Assuming that n_0 is about 1.5, the angle of the reading beam inside the medium becomes 13.2° .

An extension of the plane-wave setup has been implemented by installing an electro-optic modulator (EOM, Gsänger LM0202) in the object beam path. The EOM is oriented such that the phase of the object beam shifts proportionally to an externally applied DC voltage. Thus, it can be used to spatially shift the intensity grating relative to a previously inscribed grating. In standard holographic experiments, the EOM is switched off and has no effect. The phase shift between the light intensity and the refractive-index grating manifests itself in a difference of the intensities of the writing beams behind the sample, also referred to as "photo-refractive effect" or "asymmetric two-beam coupling".^[202,203] In thick azobenzene-based polymer samples, this energy transfer can be observed even without the EOM. To measure the intensities of the writing beams behind the sample, two additional preamplified photodiodes (Thorlabs PDA-55) are used. Conversion to a digital voltage signal is achieved by processing their output with a DAQ computer card (Keithley DAS-1700 Series).

Holography requires interferometric stability to warrant a constant phase relationship between object and reference beam. To protect the experimental setup from external vibrations or air draft, it is mounted on an optical table with air suspension and is surrounded

by a closed box. Holographic experiments were conducted at room temperature, which is regulated by an air-conditioning system.

Some of the results presented in Chapter 8 are based on data measured by H. Audorff in a slightly modified version of the setup.^[85] It does not have an EOM installed, which allows for a more compact arrangement of the optical components. Furthermore, the writing beams have a diameter of 1.9 mm at the sample position and the overall optical power of the reading laser is 130 μ W. All other experimental parameters remain the same. Since the measured diffraction efficiencies are not affected by the modifications, both setups yield identical results.

7.2 Imprinting Setup for Azo-NIL

The profiles of the molds discussed in Chapter 6.1 were transferred to the azobenzene-functionalized films with two different setups. In a first step, the PDMS or EVG mold was placed on top of a glass slide coated with the azobenzene-functionalized material. Both sticking of the mold and filling of the cavities (during UV or visible light irradiation) is caused by adhesion. Thus, no further preparation steps were required for standard imprint experiments. Yet, the influence of pressure acting onto the mold is of great interest. For this reason, experiments have also been conducted with a small magnet placed behind the mold. It is attracted by a ring washer positioned on the opposite side of the glass substrate. The resulting external pressure p_{mag} is about 0.34 bar.

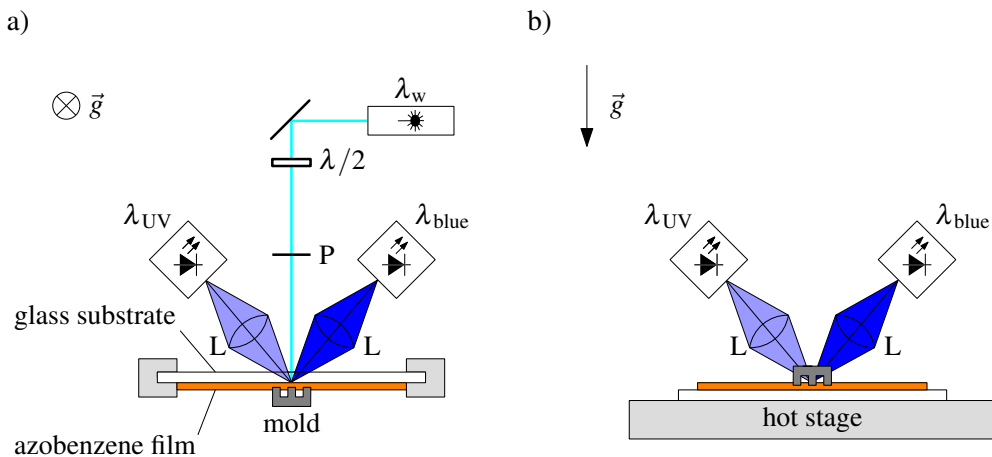


Figure 7.2: Two different configurations of the Azo-NIL setup. a) The azobenzene film is aligned vertically and illuminated through the glass substrate. b) The azobenzene film is placed on a hot stage and illuminated from the opposite direction (horizontal alignment). Illumination is realized by either two focused high power LEDs ($\lambda_{\text{UV}} = 365 \text{ nm}$ and $\lambda_{\text{blue}} = 455 \text{ nm}$) or a laser at $\lambda_w = 489.2 \text{ nm}$. P: polarizer, $\lambda/2$: half-wave plate, L: lens, \vec{g} : direction of the gravitational force.

In the first setup shown in Fig. 7.2 a), the substrate with the film and mold on top of it is fixed in a vertical position such that its surface normal is perpendicular to the direction of the gravitational force and sinking of the mold due to its weight cannot contribute to the imprinting speed. Different illumination sources are used to irradiate the film below the mold. An UV LED (Thorlabs High-Power LED M365L2) with a peak wavelength of 365 nm (FWHM: 7.5 nm) provides light near the $\pi \rightarrow \pi^*$ transition of the azobenzene-functionalized materials. A blue LED (Thorlabs High-Power LED M455L3, FWHM: 18 nm) with a peak

wavelength of 455 nm excites the $n \rightarrow \pi^*$ transition. Both LEDs are focused with quartz lenses to a spot with the same size as the mold. Near the sample surface, the UV and the blue LED have an intensity of 0.30 W cm^{-2} and 0.42 W cm^{-2} , respectively. Furthermore, s -polarized light at a wavelength of 489.2 nm is generated by the optically pumped semiconductor laser (Coherent Genesis™ MX SLM Series) used in the holographic setup discussed before. After passing through a half-wave plate and a polarizer, the intensity of the laser light is 1.0 W cm^{-2} . All three light sources are arranged such that they illuminate the mold from the side of the glass substrate through the photoactive film. Each of them can be switched on individually with a computer-controlled shutter or LED driver. Experiments are conducted at room temperature in this setup.

In the configuration depicted in Fig. 7.2 b), only LED sources are used for illumination. The glass slide with the coated film and the mold on top of it is placed on a hot stage (Harry Gestigkeit GmbH Präzitherm PZ 28-2 SR) to keep the sample at a constant elevated temperature during illumination. Hence, the gravitational force acts parallel to the surface normal of the film. Imprinting has to be performed by illuminating the film through the transparent PDMS and EVG molds in this case, which also requires the optical components to be rearranged. They are positioned such that the LED intensities at the film surface are identical as above. If the hot stage is switched off, the filling speed of the mold cavities is identical in both experimental setups. This further indicates that the weight of the molds has negligible influence on the imprinting experiments.

7.3 Atomic Force Microscopy

Information about the surface profile of molds and imprinted or holographically prepared structures was obtained via atomic force microscopy (AFM). This technique is based on the determination of the vertical displacement of a flexible cantilever, which has a sharp tip at its end that interacts with the specimen placed below (cf. Fig. 7.3). In “contact mode”, the tip is in direct physical contact with the sample and the cantilever behaves like a spring. Due to the adhesive and repelling forces between tip and sample, the cantilever is bent. Simultaneously, the deflection of a laser beam focused onto the cantilever is detected with a four-quadrant photodiode. Its output is processed by a feedback control, driving a piezo actuator. To keep the pressing force constant, it readjusts the z position of the sample accordingly. Thus, the z displacement of the actuator directly corresponds to the actual sample height. To obtain a relief map of the sample surface, the sample has to be raster-scanned in horizontal direction. This is accomplished with an additional xy piezo stage mounted below the specimen.

Direct contact with the tip can permanently damage the investigated structures if the induced stress during scanning exceeds the yield point of the sample. For this reason, most atomic force microscopes can be operated in a “tapping” or “noncontact” mode. Here, the cantilever oscillates slightly above the sample with a frequency near its resonance. As a consequence, the tip approaches and retracts from the sample several times within one height measurement. The amplitude of the oscillation, which is affected by the tip-sample interaction, serves as a measure for the actual height. Additional information about the surface features is gained in this mode from the phase shift between the driving oscillator signal and the response of the tip. The basic operation of the feedback control is similar to that in contact mode. More information about the AFM working principle can be found in the textbook of G. Haugstad.^[204]

All profiles were measured with a commercial atomic force microscope (Digital Instruments NanoScope Dimension 3100) equipped with a Nanoscope IV Controller and a Closed Loop XY Dimension Head in noncontact mode. The tip is located on a silicon cantilever

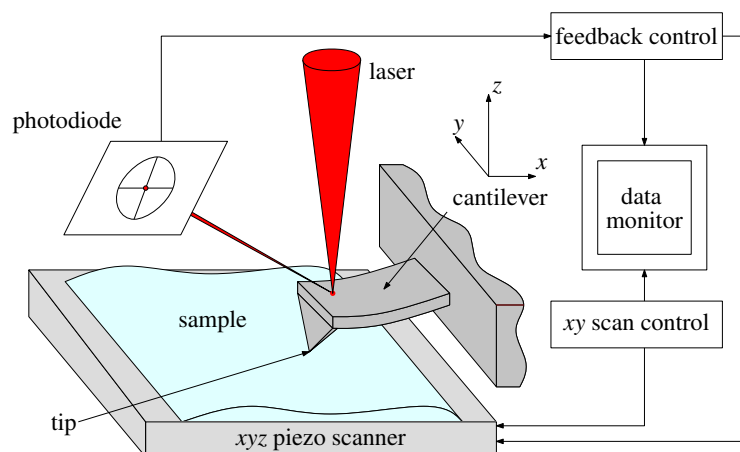


Figure 7.3: Schematic diagram of an atomic force microscope.

(type OTESPA-R3) with a typical spring constant of 26 N m^{-1} and a tip radius ranging from 7 nm (nominal value) to 10 nm (maximum value).

7.4 Scanning Electron Microscopy

Scanning Electron Microscopy (SEM) is an imaging technique with a high spatial resolution. Information about the specimen is obtained by focusing an electron beam onto its surface and counting the elastically scattered or emitted secondary electrons. Depending on the type of electron source and the objective coil, the electron beam diameter at the sample position is as small as a few nanometers. For field emission (FE) sources it can be reduced down to 1 nm, which defines the maximum spatial resolution of the SEM.^[205] The topography of the specimen is recorded by deflecting the electron beam into different directions. A highly enlarged raster scan is obtained by adjusting the size of the scanned area and counting the number of the detected electrons for each scattering center. To avoid blurring, the SEM components and the sample are placed in vacuum. Furthermore, the accumulation of electrostatic charges must be avoided, which is, in general, accomplished by grounding, provided that the sample or its surface is electrically conducting.

SEM measurements were carried out by C. Probst and M. Heider at the Bayreuth Institute of Macromolecular Research (BIMF) at the University of Bayreuth. Images were taken with a commercial Zeiss Ultra plus FE-SEM (Schottky-field-emission cathode; SE2 (45°) or in-lens (90°) detector) with an accelerating voltage of 2 to 3 kV. Prior to the SEM measurements, the patterned molecular glass films were sputtered with a conductive platinum layer of 1.3 to 2 nm thickness, using a Cressington 208HR sputter coater with an MTM20 thickness controller. After cutting the substrate into pieces of appropriate size, the fragments were mounted either on a 45° or a 90° sample holder and grounded by a conductive adhesion graphite-pad (Plano).

Holographic Writing Performance of Azobenzene-Functionalized Polymer and Molecular-Glass Blends

The results presented in this chapter are partially based on data measured by H. Audorff, which were also used in the discussion part of his thesis.^[85] Within this work, remaining questions could be settled by carrying out additional experiments. Analysis and interpretation of the combined data resulted in the substantial new insights leading to publication # 1 (cf. Appendix B).

A suitable medium for the storage of holographic volume gratings is capable of saving long-term-stable gratings within a small amount of time. In order to meet this demand, various azobenzene-functionalized materials have been synthesized and investigated in the past. Advantages and disadvantages of diverse polymer types have already been discussed in Chapter 5.2. Among them, azobenzene-functionalized block copolymers can be considered to be one of the most promising materials. They can be designed to have the low optical density required for holographic data storage and to fulfill the criterion of stable grating inscription.^[206–211] Yet, they lack sufficiently high orientation speed. Recently molecular glasses became the subject of intense research and their suitability as long-term-stable holographic medium was investigated (cf. Chapter 5.1). As a result, birefringence was found to build up faster than in polymers.^[131,179,212,213] In fully amorphous molecular glasses, however, the orientation of the azobenzene moieties is not stable and the gratings tend to decay.

The explanations below constitute a guide of how to combine the above material properties to create a new, improved storage medium for holographic applications. For this purpose, two different azobenzene-functionalized block copolymers, block copolymers **10** and **11**, were blended with molecular glass **4e**. Compound **4e** is an amorphous molecular glass former and, thus, holograms inscribed into the neat material are not long-term stable. However, **4e** can be used as a photo plasticizer, accelerating the reorientation of the azobenzene moieties of the polymers during illumination. Plastification immediately stops as soon as the writing beams are switched off, similar to the photofluidization in Azo-NIL experiments (cf. Chapter 10). As will be shown later, the long-term stability of the surrounding matrix may be retained in this case. This approach substantially differs from blending azobenzene polymers with non-photoactive low-molecular-weight plasticizers. Sasaki et al. showed that the latter method shortens the required inscription time by a factor of 3.^[214] Information about the long-term stability of their system, however, does not exist. Because the photophysical behavior of block copolymer blends is rather complex, blends of polystyrene and homopolymer **9 (i)** with **4e** were also analyzed. These homopolymers correspond to the

photoinactive and -active domains of block copolymer **10**, respectively. Figure 8.1 illustrates this for the different polymer blends. Owing to the similarity of the azobenzene moieties of **4e** and the minority phase of the block copolymers, accumulation of the molecular glass is expected to occur mainly in the photoactive block. To provide evidence for the above statements, build-up times, induced anisotropy, and long-term stability of the blends will be discussed.

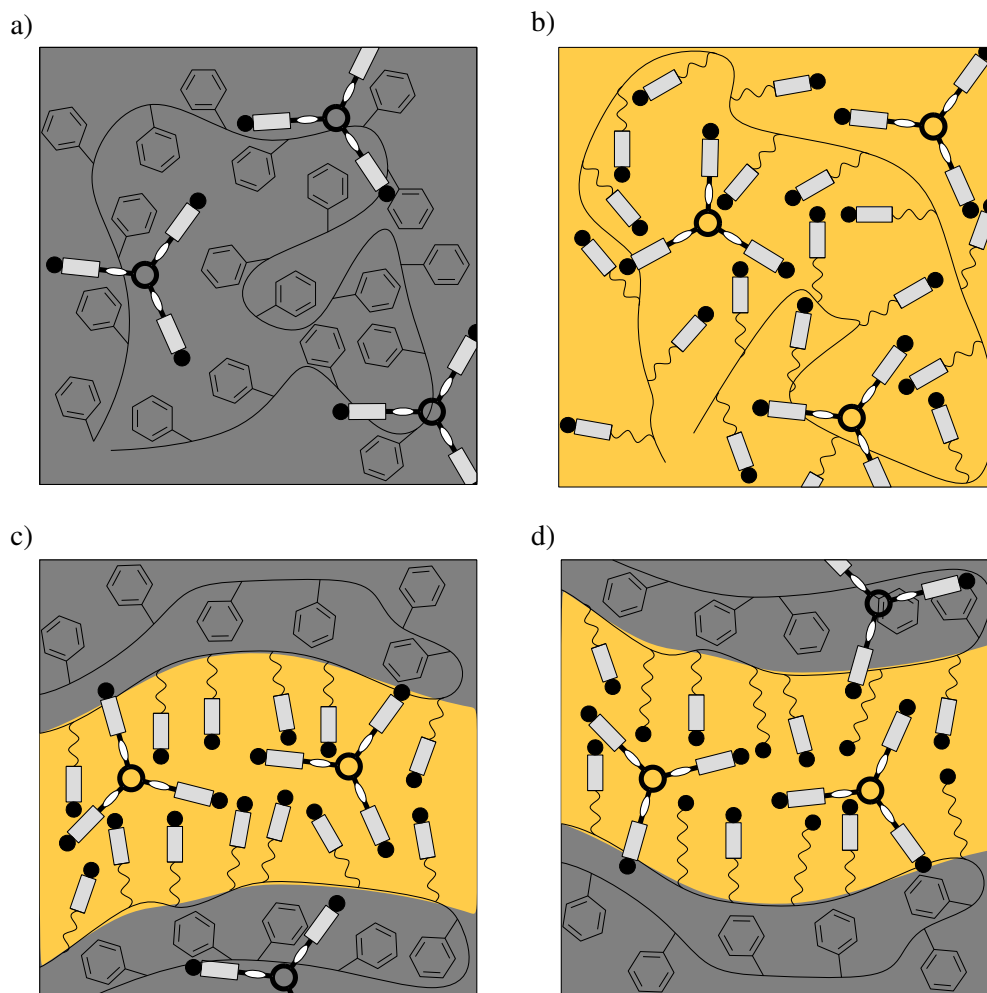


Figure 8.1: Blends of a) polystyrene, b) homopolymer **9(i)**, c) block copolymer **10**, and d) block copolymer **11** with molecular glass **4e**. Orientable domains are highlighted with orange color, photoinert domains are grey (molecular glass located in the polystyrene phase becomes immobilized). Note that block copolymers **10** and **11** show microphase separation.

A brief summary of the experimental conditions and the conventions applying for this chapter shall be provided. Volume phase gratings were inscribed in thin films of the blends or neat materials with the holographic setup presented in Chapter 7.1. For all experiments, *ss*-polarized writing beams with a total intensity of 2 W cm^{-2} (sum of both beams) were used. At this polarization configuration, the formation of surface relief gratings is efficiently suppressed.^[63,179] The maximum diffraction efficiency $\eta_{1,\text{max}}$ and the writing time $t_{90\%}$ to reach 90 % of it were determined as discussed in Chapter 2.3. Refractive-index modulations were calculated from the diffraction efficiencies according to Eq. (2.13). This requires the readout laser to be *s*-polarized such that the theoretical description for scalar and polarization gratings becomes equivalent (cf. Chapter 2.4). For the sake of clarity, the nomenclature of the scalar gratings is used in the discussion. Thus, $n_{1,\parallel}$ and $n_{1,\text{max},\parallel}$ are denoted by n_1 and

$n_{1,\max}$, respectively. All values, however, refer to the refractive-index modulations measured with *s*-polarized light. Prior to grating inscription, the films were annealed according to the procedure described in Chapter 5.3. Neat materials are indicated by open symbols and blends are indicated by filled symbols in the figures.

8.1 Holographic Inscription Speed in Polymer Blends

The writing times in blends of **4e** with non-photoactive and photoactive homopolymers are investigated first. As mentioned before, polystyrene and homopolymer **9(i)** correspond to the compounds, which form the majority and minority phase of block copolymer **10**, respectively. Analysis of the photophysical behavior of each individual homopolymer upon blending is a prerequisite to understand the experimental observations made in the more complex systems composed of block copolymer **10** or **11** and molecular glass **4e**.

Figure 8.2 a) shows $t_{90\%}$ as a function of the concentration of **4e** in PS and in the neat molecular glass. Films were spin-coated from solution and had a thickness of $\sim 1.5\ \mu\text{m}$ for the blends, whereas for the sample consisting of neat **4e** the thickness was 300 nm. All blends showed good optical quality, which indicates that the molecular glass is homogeneously distributed in the polystyrene matrix. The required inscription time remains below 1 s over the large concentration range of 20 to 100 wt% of **4e**, which is on the order of the value of the neat molecular glass indicated by the open square ($t_{90\%} = 0.35\ \text{s}$). At lower concentrations, $t_{90\%}$ increases by more than two orders of magnitude up to 211 s in the 6 wt% sample. This implies that cooperative interactions exist between the azobenzene chromophores. Upon dilution in the PS matrix they are significantly reduced, leading to a nonlinear decrease of the writing speed.

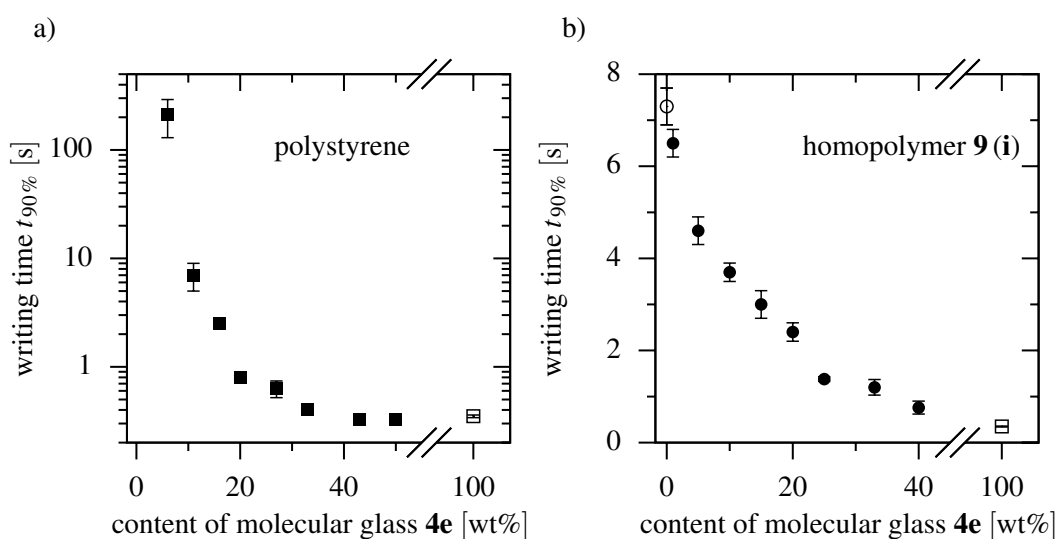


Figure 8.2: Time to reach 90 % of the maximum diffraction efficiency as a function of the concentration of molecular glass **4e** in a) polystyrene and b) azobenzene-functionalized homopolymer **9(i)**. The data of the neat materials are indicated by open symbols. Note the logarithmic ordinate scale in a).

In the next step, azobenzene-functionalized homopolymer **9(i)** was blended with weight fractions of **4e** ranging from 1 to 80 wt%. Films of the blends and the neat homopolymer **9(i)** were prepared by doctor blading. Their thicknesses varied between 250 and 650 nm. As in the case of PS, all blends were highly homogeneous and did not show light scattering. The

corresponding writing times are plotted in Fig. 8.2 b). Since this blend series contains two photoactive species, $t_{90\%}$ is a superposition of the inscription times of the individual neat materials, i. e., 0.35 s for neat molecular glass **4e** and 7.3 s for neat homopolymer **9(i)**. Similar to the polystyrene series, the writing times at concentrations above 40 wt% are largely dominated by the molecular glass. For the 10 wt% blend, $t_{90\%}$ is still as short as 3.6 s, which is half the writing time in PS. This strongly suggests that cooperative interactions are present between the azobenzene moieties of homopolymer **9(i)** and molecular glass **4e**. This finding is further supported by the work of Audorff,^[85] who showed that decreasing the concentration of **4e** in blends with either PS or homopolymer **9(i)** results in a red or blue shift of the azobenzene $\pi \rightarrow \pi^*$ transition, respectively. The first result was attributed to the disappearance of H-aggregates formed by the molecular glass, whereas the second one was explained by the increasing disorder caused by **4e** as it disturbs the light-induced liquid crystalline order in homopolymer **9(i)**. In both cases, the azobenzene moieties interact strongly with each other, resulting in a photoinduced plastification of their surrounding matrix during illumination. The faster molecular glass can be regarded as the plasticizer, while the polymer is the material to be plasticized. Upon dilution in PS, the spatial proximity of the azobenzene chromophores is gradually lost and the glass molecules become trapped in the photoinactive matrix. In homopolymer **9(i)**, however, a cooperative effect is obviously present for all concentrations of **4e**. Thus, the writing times of the blends with the photoinactive and the photoactive homopolymer at low concentrations of **4e** differ substantially from each other and from that of the neat molecular glass.

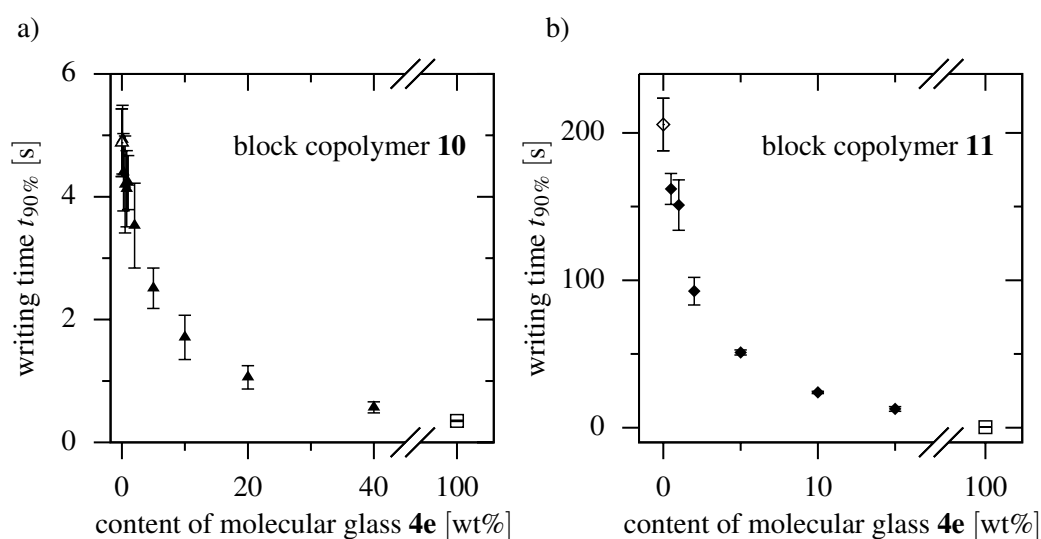


Figure 8.3: Time to reach 90% of the maximum diffraction efficiency as a function of the concentration of molecular glass **4e** in a) blockcopolymer **10** and b) blockcopolymer **11**. The data of the neat materials are indicated by open symbols.

As mentioned before, the homopolymers correspond to the minority and majority phase of block copolymer **10**. In contrast to homopolymer **9(i)**, holograms inscribed into neat block copolymer **10** are not long-term stable.^[38] This behavior is already known from a similar block copolymer in which the liquid-crystalline order of the photoactive minority phase has been found to be reduced as compared to that of the respective homopolymer.^[215] To investigate the photoplastification effect of the molecular glass on the block copolymer, blends of **10** with concentrations of **4e** ranging from 0.25 to 40 wt% were prepared as amorphous films of $1.5 \pm 0.3 \mu\text{m}$ thickness. A film of neat block copolymer **10** with a thickness

of 1.7 μm serves as a reference. Fig. 8.3 a) shows the respective writing times. All blends feature shorter writing times as compared to neat **10**, which has a $t_{90\%}$ value similar to neat homopolymer **9 (i)**. An amount of **4e** as small as 5 wt% causes $t_{90\%}$ to decrease by a factor of 2, which demonstrates that the concentration of the molecular glass cannot be high in the PS matrix of **10**. In this case, $t_{90\%}$ would be significantly longer like in the blends with the PS homopolymer (cf. Fig. 8.2 a)).

The concentration of **4e** in the minority phase appears to be significantly higher than one would expect for a homogenous distribution of the molecular glass in both blocks. This can be seen from a rough estimate of the amount of molecular glass located in the photoorientable minority block. The weight fraction of PS to azobenzene block in compound **10** is approximately 5 : 1. For a random distribution, only one sixth of the molecules of **4e** would sit in the functionalized minority block. At an overall content of 5 wt% molecular glass in **10**, for example, a writing time corresponding to below 1 wt% molecular glass in homopolymer **9 (i)** would be expected. Hence, the shortening of $t_{90\%}$ in block copolymer **10** should be significantly smaller than the observed factor of almost 2, which shows that the molecular glass preferably accumulates in the minority block. It should be stressed, however, that this argument applies only if the minority and majority block have similar densities and if the content of **4e** is small. At higher concentrations, the molecular glass located in the PS block will more and more contribute to the diffraction efficiency, since the cooperative effect between its molecules leads to a strong decrease of the writing time (cf. Fig. 8.2 a)).

Finally, molecular glass **4e** is added as a plasticizer to block copolymer **11**, which is the most promising candidate for holographic data storage. The content of molecular glass in the block copolymer ranges from 0.5 to 15 wt%. Films of the blends, as well as a film of neat **11**, were prepared by doctor blading and had an average thickness of 750 ± 100 nm. As before, all films showed good optical quality. A study of Häckel et al. demonstrated that the refractive-index modulation in thin films of neat block copolymer **11** is stable for more than one year.^[41] As compared to compound **10**, $t_{90\%}$ is significantly higher, however. Whereas it is only 5 s in neat **10**, it has a value of 206 s in neat **11** (cf. open triangle and open diamond in Fig. 8.3). The reason is that the orientation of the non-photoactive mesogens requires additional writing time. With increasing concentration of **4e**, the writing time shortens significantly. The gain in speed is even more pronounced than in block copolymer **10**. For an addition of only 15 wt% of **4e**, the writing time of **11** improves by a factor of over 15. Similar arguments as in the case of block copolymer **10** apply for the distribution of the molecular glass. Due to the chemical similarity of the azobenzene chromophores, **4e** is expected to migrate into the photoactive block of **11**. Furthermore, the maximum amount of **4e** in the investigated blends is only 15 wt%. Thus, due to the lack of spatial proximity of the molecular-glass chromophores located in the PS matrix, their contribution to the shortening of the writing time is negligible. Further evidence for the accumulation of the molecular glass in the photoactive block is provided in the following sections.

As indicated by the error bars in Fig. 8.3, blending with molecular glass **4e** improves the reproducibility of the writing times in both block copolymers. A possible explanation is that the accumulation of the molecular glass in the minority phase of the block copolymers improves micro phase separation. Also a complete change of the block copolymer morphology, e. g., from cylindrical to lamellar, is conceivable. This observation is advantageous for holographic applications.

8.2 Photoinduced Anisotropy in Polymer Blends

While short inscription times are important on the one hand, holographic applications also require n_1 to be sufficiently high. Apparently, the maximum achievable anisotropy depends

on the density of azobenzene chromophores. This is illustrated in Fig. 8.4 for the concentration series of PS blended with **4e**, in which only one photo-orientable species is present. As expected, the maximum refractive-index modulation $n_{1,\max}$ increases with the amount of **4e**. The ordinate scale is logarithmic and the increase of the generated anisotropy as a function of the concentration of **4e** is nonlinear. The maximum refractive-index modulation in neat **4e** is found to be $n_{1,\max} = 7.5 \times 10^{-3}$.

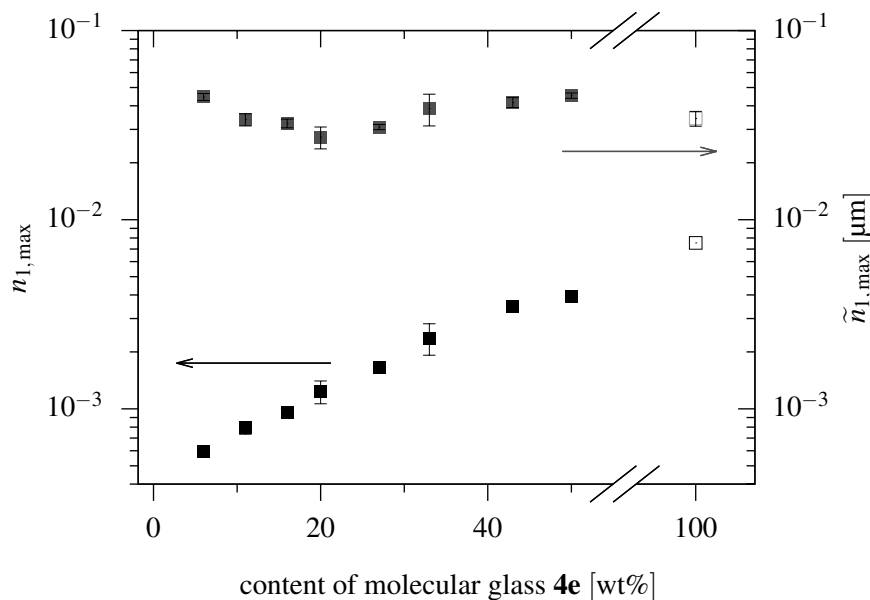


Figure 8.4: Maximum refractive-index modulation $n_{1,\max}$ (left ordinate) and its normalized value $\tilde{n}_{1,\max}$ (right ordinate) for different concentrations of molecular glass **4e** in polystyrene. The data of the neat material are indicated by the open symbols. Note the logarithmic ordinate scale.

To analyze the blends with azobenzene-functionalized polymers, it is reasonable to introduce the quantity $\tilde{n}_{1,\max}$, which is calculated as

$$\tilde{n}_{1,\max} = n_{1,\max} / (\text{OD}_{488} / d_0). \quad (8.1)$$

The denominator is the optical density at the inscription wavelength, OD_{488} , divided by the sample thickness d_0 . Thus, it is proportional to the concentration of azobenzene chromophores in the illuminated volume. Since no proportionality constant is introduced, the unit of $\tilde{n}_{1,\max}$ is micrometer. This normalized refractive-index modulation is a measure for the contribution of each individual chromophore to the maximum achieved refractive-index modulation. It is unaffected by the variable number of azobenzene moieties in the different blends and, therefore, better suited to compare the different concentration series. This is demonstrated for the example of the blends of PS with **4e** in Fig. 8.4. Unlike the maximum refractive-index modulation, $\tilde{n}_{1,\max}$ stays almost constant throughout the whole concentration series. The blends behave as one would expect for a purely amorphous molecular glass. Increasing its concentration gives neither rise to additional stabilization nor to higher order. Hence, the average contribution of each photo-orientable moiety to the induced anisotropy is the same for all concentrations. This finding slightly deviates from the conclusions drawn in the work of Audorff in which the data of the neat molecular glass was not taken into account.^[85]

The holographically induced anisotropy in blends of the photo-orientable polymers **9** (i), **10**, and **11** with **4e** is discussed in Fig. 8.5. At high concentrations of **4e**, both $n_{1,\max}$ and $\tilde{n}_{1,\max}$ approach the respective values of the neat molecular glass for all concentration series.

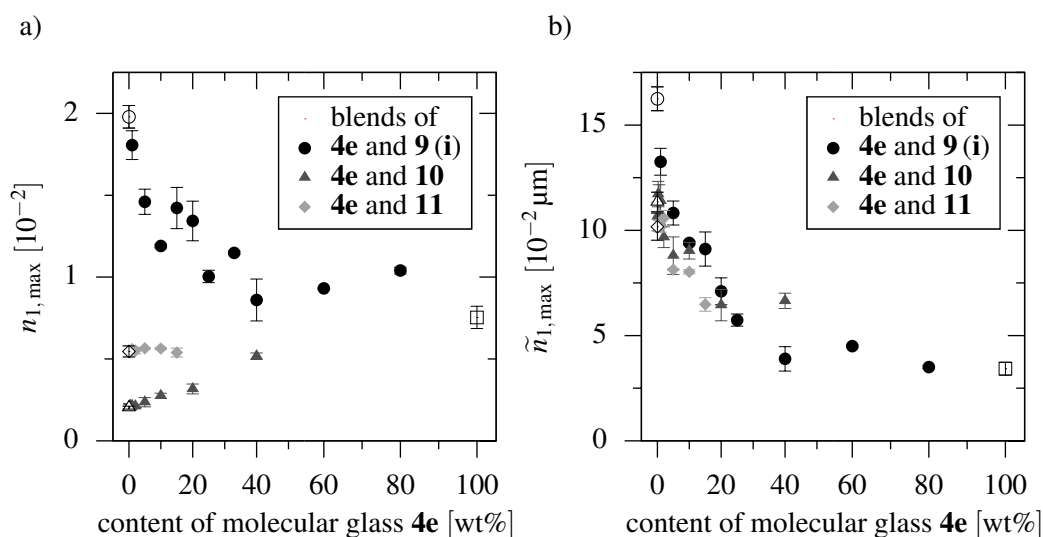


Figure 8.5: a) Maximum refractive-index modulation $n_{1,\max}$ for different concentrations of molecular glass **4e** in homopolymer **9(i)** (solid circles), block copolymer **10** (solid triangles), and block copolymer **11** (solid diamonds). b) Same as in a) but for the normalized refractive-index modulation $\tilde{n}_{1,\max}$. The data of the neat materials are indicated by open symbols.

Fig. 8.5 a) shows that $n_{1,\max}$ is basically a linear combination of the refractive-index modulations of neat **4e** and the respective photo-orientable polymer. Neat homopolymer **9(i)** features the highest $n_{1,\max}$ of all materials, approximately 2×10^{-2} . Hence, the maximum achieved refractive-index modulation decreases with increasing amount of **4e**. The opposite behavior is observed for block copolymers **10** and **11**. Here, the maximum refractive-index modulation of the neat compounds is below that of the neat molecular glass. It has a value of $n_{1,\max} = 2 \times 10^{-3}$ in neat block copolymer **10** and increases throughout the whole concentration series. In neat **11** it is about 5.5×10^{-3} , which is similar to the maximum refractive-index modulation of **4e**. Therefore, $n_{1,\max}$ depends only slightly on the amount of molecular glass present in the blends. The refractive-index modulations measured in the homopolymer blends are generally higher than in both block copolymers. This is plausible because the azobenzene chromophores are densely packed in the neat homopolymer. With respect to the maximum achievable anisotropy, the addition of molecular glass **4e** is beneficial for both block copolymers.

The normalized refractive-index modulation in Fig. 8.5 b) reveals that the photoinduced anisotropy in the photoactive polymers is significantly higher than in the molecular glass. For neat **4e** it has its smallest value of $3.4 \times 10^{-2} \mu\text{m}$. The highest $\tilde{n}_{1,\max}$ of $1.6 \times 10^{-1} \mu\text{m}$ is achieved in neat homopolymer **9(i)**, while in the neat block copolymers **10** and **11** it is 1.1×10^{-1} and $1.0 \times 10^{-1} \mu\text{m}$, respectively. The difference between the values measured in the homopolymer and the block copolymers further indicates that the confinement in the microphase-separated block copolymers impedes the alignment of the photo-orientable moieties. Since the optical density in Eq. (8.1) is only sensitive to absorbing chromophores, it does not take the alignment of the mesogenic moieties into account. In block copolymer **11**, however, they constitute over 50 mol % of the minority phase and, thus, their orientation contributes to $n_{1,\max}$. Nevertheless, blends of **10** and **11** with **4e** feature similar normalized refractive-index modulations. Apparently, the underestimation of the number of oriented moieties cancels out in the calculation of $\tilde{n}_{1,\max}$. The reason is that the maximum refractive-index modulation of neat **11** is approximately twice the one of neat **10**.

8.3 Influence of Annealing

The spatial distribution of the molecular glass in the microphase-separated block copolymer blends can be further improved. As shown before, the molecular glass tends to accumulate in the azobenzene-functionalized block. To remove residual solvent, all blends were annealed at a temperature of 70 °C for 3 h. This temperature is above the glass transition temperature of the molecular glass ($T_g = 58$ °C), but below that of the PS block of the block copolymers ($T_g \gtrsim 100$ °C). Hence, the accumulation takes place only during the formation of the amorphous phase in the short period before the annealing. Some of the molecular glass, however, remains trapped in the PS matrix. Because annealing at elevated temperatures allows the molecular glass to diffuse through the PS block, it is expected to further equilibrate the blend systems and to enhance their microphase separation.

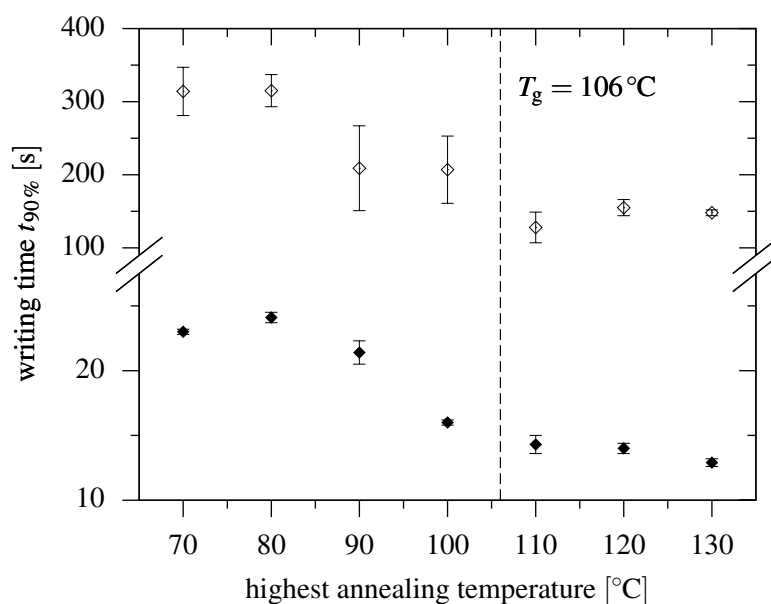


Figure 8.6: Writing time $t_{90\%}$ as a function of the highest annealing temperature for neat block copolymer **11** (open diamonds) and a blend of **11** with 10 wt% of molecular glass **4e** (filled diamonds). The glass transition temperature of the polystyrene block is indicated by the dashed line at 106 °C.

The influence of annealing is investigated by comparing films of neat block copolymer **11** and a blend of **11** with 10 wt% of molecular glass **4e**. As before, both films were annealed at 70 °C for 3 h. Afterward, they were cooled down to room temperature for the inscription of volume gratings. This procedure was repeated in 10 °C intervals of the annealing temperature between 70 and 130 °C. Each annealing step took 3 h and involved subsequent cooling to room temperature prior to the inscription of the next set of holographic gratings. The individual gratings were written at different spots on the samples. Finally, $t_{90\%}$ and $n_{1,\max}$ were determined as a function of the highest annealing temperature.

As indicated by the open diamonds in Fig. 8.6, the writing times in neat block copolymer **11** become gradually shorter at higher annealing temperatures and, at the highest temperatures, better reproducible. Both observations are ascribed to the homogenization of the film as a consequence of its improved micro phase separation. The writing time begins to decrease even before the annealing temperature exceeds the glass transition temperature of the PS block ($T_g = 106$ °C). As discussed in Chapter 8.1, the increase in speed is a clear indication of enhanced cooperative effects between the azobenzene moieties. Still,

the magnitude of the writing time reduction is unexpectedly high. Within the investigated temperature range, $t_{90\%}$ decreases from 315 to 150 s by more than a factor of 2.

In the blend with 10 wt% of **4e**, the reproducibility of the writing times is considerably better even at the lowest annealing temperatures (filled diamonds in Fig. 8.6). This indicates that the addition of molecular glass **4e** influences the micro phase separation already in freshly prepared films. The writing times decrease from 23 to 13 s, which is a factor of almost 2, similar to the case of neat block copolymer **11**. In this situation, $t_{90\%}$ does not provide enough information to clarify the mechanism of the homogenization. The gain of writing speed in the blend can either be a consequence of stronger cooperative effects between the azobenzene chromophores due to molecular glass accumulation in the minority block of **11** or a more favorable morphology of the block copolymer. To associate the improved writing times with the diffusion of **4e**, the information obtained from the refractive-index modulation needs to be taken into account as well.

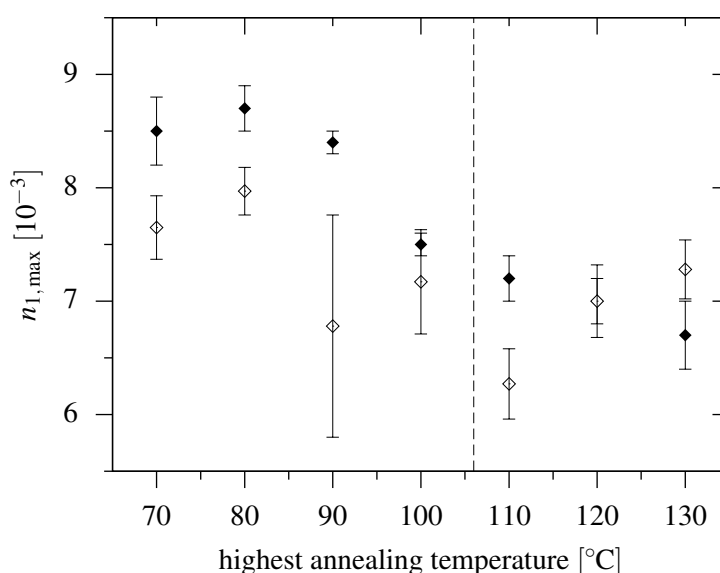


Figure 8.7: Maximum refractive-index modulation $n_{1,max}$ as a function of the highest annealing temperature for neat block copolymer **11** (open diamonds) and a blend of **11** with 10 wt% molecular glass **4e** (filled diamonds).

As for the writing times, the maximum refractive-index modulation of both samples is studied as a function of their highest annealing temperature. The results for neat **11** (open diamonds) and its blend with 10 wt% of **4e** (filled diamonds) are shown in Fig. 8.7. Since the average number of azobenzene moieties in the illuminated volume does not change during grating inscription, $n_{1,max}$ is roughly constant in the neat block copolymer. The error bars are quite large in this case. In contrast to the neat material, $n_{1,max}$ slightly decreases in the blend at temperatures above 90 °C and its overall behavior resembles that of the writing times (cf. Fig. 8.6). This is consistent with the results presented in Chapter 8.2 and can be attributed to the increasing disorder in the photo-orientable block caused by the diffusion of the molecular glass. Hence, the previously discussed decrease in writing time cannot be solely due to enhanced microphase separation of the block copolymer. Apparently, heating sufficiently softens the PS matrix to enhance the diffusion of the molecular glass even at a temperature 15 °C below the T_g of the PS majority block.

8.4 Long-Term Stability of Holographic Gratings

All materials discussed so far show a post-development of the inscribed volume gratings as soon as the writing beams are switched off.^[38,41,85,179] The slope of the refractive-index modulation as a function of the readout time of the purely amorphous materials glass formers, however, differs from that of the polymers with liquid-crystalline properties. Molecular glass **4e** and block copolymer **10** belong to the former class. Because the chromophore alignment is not stabilized by molecular interactions in these systems, the photoinduced anisotropy thermally decays in the neat compounds, which is detrimental to holographic data storage. The photo-orientable polymers **9(i)** and **11**, on the other hand, feature a positive slope of n_1 . For holographic data storage, this is favorable because their diffraction efficiency increases further. Blending compounds with a negative and a positive slope of n_1 represents a suitable approach to create real long-term-stable materials with no or largely reduced post-development.

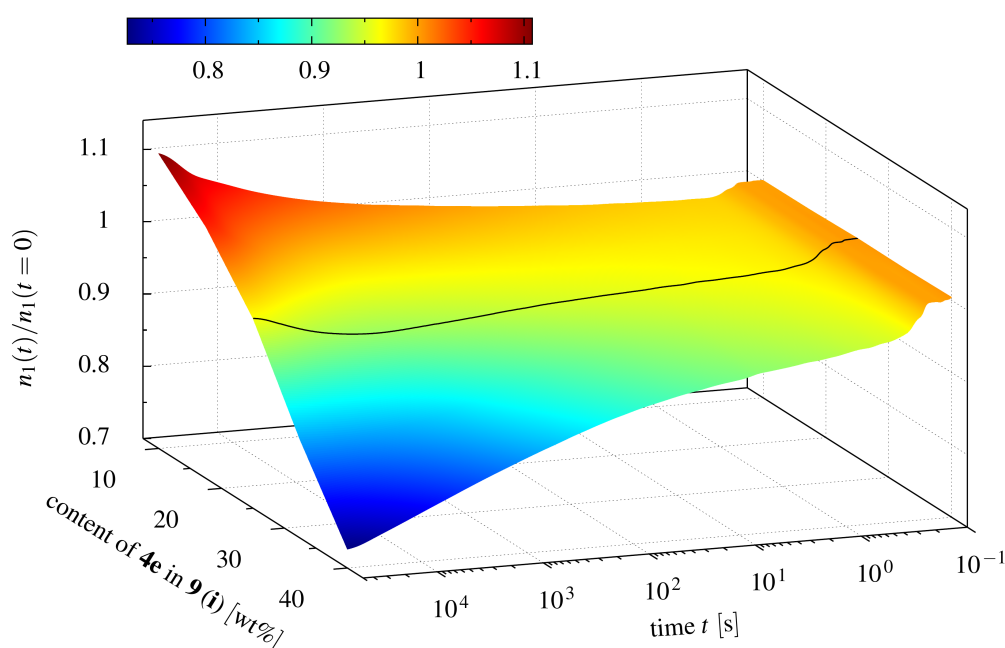


Figure 8.8: Temporal evolution of the normalized refractive-index modulation in blends of molecular glass **4e** with homopolymer **9(i)** as a function of the content of **4e** and the time after hologram inscription. The time axis is logarithmic. Each refractive-index modulation has been normalized to $n_1(t=0)$, its value immediately after switching the writing beams off. The black line indicates the blending ratio with the lowest post-development at 25 wt% molecular glass **4e**. The plot has been reproduced from previously reported data.^[85]

To illustrate this concept, Fig. 8.8 has been reproduced from the data presented in the thesis of Audorff.^[85] It depicts the temporal evolution of the refractive-index modulations measured in blends of homopolymer **9(i)** with molecular glass **4e**, normalized to their values directly after switching the writing beams off. The data covers a concentration range between 10 and 40 wt% of **4e** and the long-term stability is measured for a time period up to 12 h. All gratings were inscribed until their 1st order diffraction efficiency reached its maximum. The post-development was monitored with the readout laser. Due to the liquid-crystalline properties of homopolymer **9(i)**, n_1 increases in the blends with low content of **4e**. On the contrary, the amorphous characteristics of the molecular glass are found to dominate at higher concentrations of **4e**, which leads to a decay of n_1 . For the above definition

of long-term stability, the black line at 25 wt% of **4e** indicates the optimum molecular-glass concentration in the homopolymer. The refractive-index modulation resumes its initial value in this blend after approximately 12 h, whereas all other concentrations give rise to a stronger post-development. Furthermore, $t_{90\%}$ is as low as 1 s and the maximum refractive-index modulation is on the order of $n_{1,\max} \approx 1 \times 10^{-2}$. Although the optical density in a 25 wt% blend of **4e** in **9 (i)** is too high for holographic data storage, it constitutes a suitable medium for the inscription of long-term-stable, thin volume gratings in the Raman Nath regime.

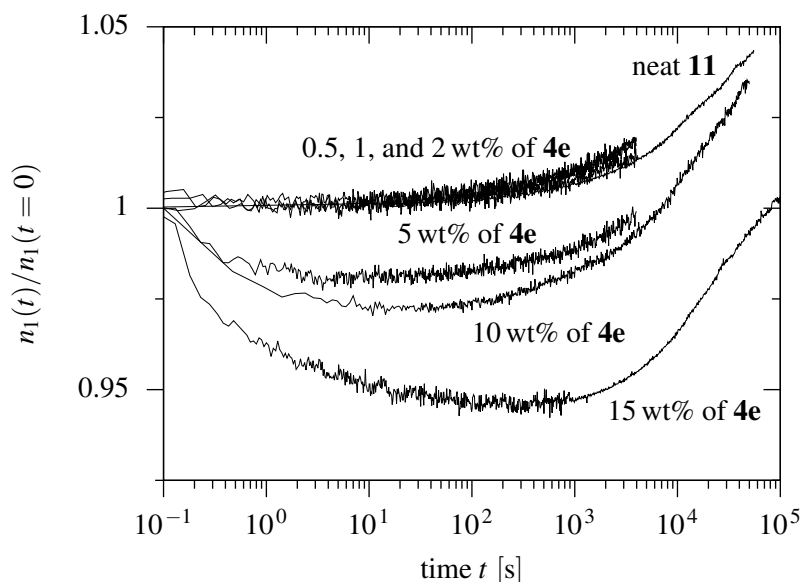


Figure 8.9: Temporal evolution of the normalized refractive-index modulation in neat block copolymer **11** and its blends with molecular glass **4e** after hologram inscription. Each refractive-index modulation has been normalized to $n_1(t=0)$, its value immediately after switching the writing beams off. The time axis is logarithmic.

To obtain a long-term-stable material for holographic data storage applications, one can blend block copolymer **11** with molecular glass **4e**. This is illustrated in Fig. 8.9, which shows the post-development of the refractive-index modulation in all investigated blends of **11** with **4e**. Here, n_1 is measured for times up to 28 h. The inscription and readout procedure are identical to that discussed for homopolymer **9 (i)**. Again, each data set is normalized to the maximum refractive-index modulation directly after switching the writing laser off. From literature it is known that n_1 shows a strong post-development in neat **11**.^[41] Hence, the normalized refractive-index modulation of the neat film shows the expected behavior (cf. Fig. 8.9). As compared to the homopolymer blends, however, the magnitude of the post-development is smaller. An amount of up to 2 wt% of **4e** does not significantly change the post-development. For higher concentrations of 5, 10, or 15 wt% of **4e**, however, the normalized refractive-index modulation initially decreases. The fast decay within the first second is similar to that in the homopolymer blends (cf. Fig. 8.8) and, therefore, seems to be characteristic for the relaxation of the molecular glass in the photoactive block. A slower decay following in the first hundred seconds is observed in the 15 wt% sample. It can be attributed to the molecular glass located in the PS segment of the block copolymer. At this concentration its orientation speed during inscription is sufficiently high to contribute to the overall refractive-index modulation (cf. Fig. 8.2). Gratings written in blends of PS and **4e**, however, are not long-term-stable.^[179] As time proceeds, the contribution of the decay decreases and becomes superimposed by the characteristic post-development of the block

copolymer. After a period of 28 h, the initial refractive-index modulation is restored in the 15 wt% blend.

In summary, the blend of 15 wt% of **4e** with **11** constitutes the most promising material for holographic data storage of all investigated systems. Although the addition of molecular glass increases the optical density of the block copolymer, it is still much lower than in homopolymer **9(i)**. The 15 wt% blend features a short, reproducible writing time on the order of 10 s, which is an improvement by a factor of more than 15 compared to the neat block copolymer. Furthermore, its maximum refractive-index modulation is similar to that of the neat molecular glass and it is a medium with a good long-term stability.

Refractive-Index Determination from First- and Second-Order Critical Diffraction Angles

The refractive index and its wavelength dispersion are among the most important optical parameters of transparent substances. Extensive lists of applications requiring the exact knowledge of n_0 can be found in the literature.^[216,217] In the case of solids, for instance, they include thin-film coatings, fiber optics, and optical elements. Holographically generated SRGs represent another good example. Since the refractive index enters in Eq. (2.12), the exact value of n_0 is required to calculate the modulation amplitude d_1 of the surface from the diffraction efficiency of the grating. In volume holography, one needs to apply Snellius's law in order to obtain the angle of incidence inside the medium. Because the solid films used for holographic inscription are prepared from novel, azobenzene-functionalized materials, their optical properties and, thus, n_0 are basically unknown.

Many techniques for the determination of n_0 have been developed in the past and also in recent years.^[218–220] While most of them are easily applicable to liquids, the determination of n_0 in solids becomes demanding. For example, if an Abbe refractometer is applied to measure the refractive index of an azobenzene-functionalized molecular glass or polymer film, a refractive-index matching fluid is required to couple film and prism. Usually, these contact liquids tend to be chemically or physically aggressive, which results in a deterioration of the film homogeneity. The scale of a common refractometer is calibrated for the sodium-D line at 589 nm and, therefore, the exact dispersion of the prism has to be known to calculate n_0 for other wavelengths. A method more suited for the investigation of thin, solid films is spectral ellipsometry. However, their dispersion is calculated from theoretical models, which require information about the thicknesses of all optical layers (including the substrate). The accuracy of the results depends on the model and the analysis becomes rather complex if absorption is involved or if the thickness in the illuminated area varies.^[221] Similar arguments apply to refractive indices determined from reflectance or transmittance spectra.

The method for the determination of the refractive index of solids or solid films presented in this chapter is novel and makes use of holographically or lithographically prepared SRGs. It requires no additional information besides the angle of incidence of the reading laser to calculate n_0 . Hence, the method is independent of the sample thickness and the determination of n_0 could easily be accomplished with the holographic setup. To demonstrate that it can be applied to any transparent solid, the sinusoidal profile of an SRG was transferred to a PDMS film. Its dispersion was measured and the precision of the predicted refractive indices was analyzed by comparing all data to Abbe refractometer measurements.

Finally, the method was applied to find the refractive indices of SRG-forming molecular glasses.

9.1 Principle

To determine the refractive index n_0 of a transparent, solid film, one can use the diffraction off a scalar, Raman-Nath type grating, which is assumed to be present at its surface (see Fig. 9.1). The surrounding medium is supposed to be air ($n_{\text{air}} \approx 1$). Without loss of generality, the spatial extension of the periodically patterned area is assumed to be large as compared to the grating constant Λ . For optical diffraction gratings, this is fulfilled already for spot sizes well below 1 mm. According to the grating equation, a monochromatic, plane light wave with wavelength λ_r is diffracted by the grating into various orders (cf. Chapter 2.1). They emerge at different angles $\theta_{l, \text{trans}}$ behind the grating, fulfilling the equation

$$n_0 \sin \theta_{l, \text{trans}} = n_{\text{air}} \sin \theta_{l, \text{in}} + l \frac{\lambda_r}{\Lambda}, \quad (9.1)$$

while θ_r in Eq. (2.7) has been replaced by $\theta_{l, \text{in}}$ to assign to each diffracted order its specific angle of incidence.

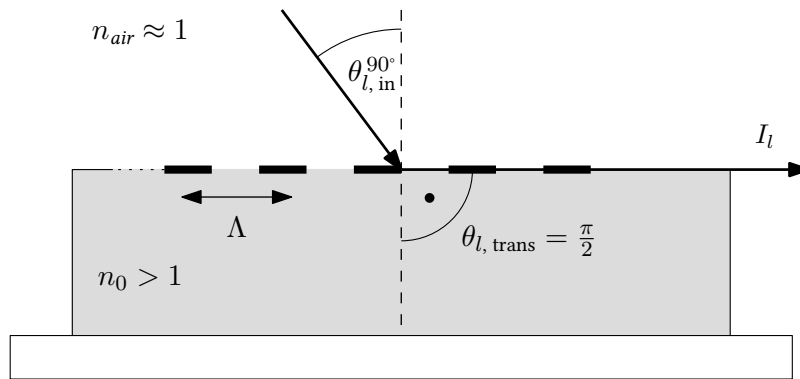


Figure 9.1: Schematic diagram of a light beam diffracted off a grating present near the surface of a film with refractive index n_0 . For the sake of clarity, only one diffracted order is drawn. If incident at an angle $\theta_{l, \text{in}}^{90}$, it emerges at $\theta_{l, \text{trans}} = \pi/2$ inside the medium.

Both the cross-sectional shape of the grating and its amplitude influence the intensity of the diffracted orders but not the diffraction angle. Hence, since the grating equation is derived from the only assumption that the electric field is pseudo-periodic inside the grating region, it is valid for all Raman-Nath grating types (absorption, refractive-index, and surface-relief gratings) and arbitrary shapes (sinusoidal, rectangular, etc.). For certain grating geometries^[90] or polarization gratings (cf. Chapter 2.4), however, some higher orders may completely vanish. A similar situation arises for Bragg-selective gratings, which do not only suppress all diffracted orders except the 0th and 1st, but also show angular selectivity. To avoid this situation, γ and Q' have to fulfill the requirements of the Raman-Nath regime discussed in Chapter 2.2. Periodic surface structures prepared with holographic or imprinting techniques usually meet this criterion while, at the same time, they provide sufficiently high diffraction efficiencies to enable the observation of several diffracted orders.

For the 0th order ($l = 0$) the angle of incidence is always larger than the angle inside the medium. It is diffracted according to Snellius's law as if only the medium without the grating were present. The diffraction angles of higher orders, on the other hand, depend on the ratio λ_r/Λ . Thus, they usually propagate inside the material at angles $\theta_{l, \text{trans}} > \theta_{l, \text{in}}$. Increasing the angle of incidence causes the individual diffracted orders to successively reach a point where they propagate parallel to the grating vector, i. e., $\theta_{l, \text{trans}} = \pi/2$. With n_{air} set to 1, Eq. (9.1) reads

$$n_0 = \sin \theta_{1, \text{in}}^{90^\circ} + \frac{\lambda_r}{\Lambda} \quad (9.2)$$

if the 1st diffracted order propagates at $\theta_{1, \text{trans}} = \pi/2$ inside the medium. The associated angle of incidence outside the medium is denoted by $\theta_{1, \text{in}}^{90^\circ}$. The calculation of n_0 from Eq. (9.2) is simple and does not require any additional information about the sample thickness or the substrate below. Moreover, the 1st order is easily detectable, because it usually has the highest intensity. To further reduce the required information, one can derive $n_0 = \sin \theta_{2, \text{in}}^{90^\circ} + 2\lambda_r/\Lambda$ for the 2nd order and substitute this expression into Eq. (9.2), yielding

$$\frac{\lambda_r}{\Lambda} = \sin \theta_{1, \text{in}}^{90^\circ} - \sin \theta_{2, \text{in}}^{90^\circ} \quad (9.3)$$

By inserting Eq. (9.3) into Eq. (9.2) one obtains

$$n_0 = 2 \sin \theta_{1, \text{in}}^{90^\circ} - \sin \theta_{2, \text{in}}^{90^\circ} \quad (9.4)$$

Depending on the accessibility of the experimental quantities, either Eq. (9.2) or Eq. (9.4) can be used for the calculation of n_0 . For holographically prepared SRGs, the grating period can easily be determined with Eq. (2.3) from the angle of incidence and the wavelength of the writing beams. If the grating is prepared lithographically, Λ is generally defined by the manufacturing process or can be measured with AFM or SEM. To apply Eq. (9.2), the exact wavelength of the probing light source must be known. Its knowledge, however, is a prerequisite for holographic experiments. It is provided by the manufacturer or can be obtained from spectroscopic analysis. Equation (9.4) on the other hand, is solely based on two angle measurements. With a holographic setup designed for angular multiplexing, they can be performed with high accuracy by simply rotating the grating relative to the reading laser on a rotational stage.

Since the first term in Eq. (9.2) contributes a maximum value of 1, the 1st-order approach is applicable only if the ratio λ_r/Λ is sufficiently high. This is not fulfilled for large grating periods, short probing wavelengths, or in materials with very high refractive indices. In the presence of higher diffracted orders, however, this does not restrict the applicability of the presented method. In general, the l^{th} diffracted order can be used for the calculation of the refractive index if it fulfills the condition $l\lambda_r/\Lambda < n_0 < 1 + l\lambda_r/\Lambda$, which follows from Eq. (9.1). Assuming, for example, that a probing beam with a wavelength $\lambda_r = 500\text{nm}$ is incident on a grating with period $\Lambda = 1000\text{nm}$, an angular measurement of the propagation of the 1st order allows for the determination of the refractive index of the material if it is below 1.5. For materials with refractive indices between 1 and 2 the 2nd diffracted order can be measured, while the 3rd order propagates inside materials with $1.5 < n_0 < 2.5$. If $\lambda_r < \Lambda$, the accessible refractive-index range of adjacent orders overlaps. Thus, at least two of them can propagate inside the medium (although they are not necessarily present at the same time). Expressions analogous to Eq. (9.2) and Eq. (9.4) can be formulated for higher orders, allowing one to measure arbitrary values of n_0 .

9.2 Dispersion of Polydimethylsiloxane

To study the applicability of the model developed in the previous chapter, Eq. (9.2) and Eq. (9.4) were used to determine the dispersion of a cast PDMS film (Sylgard[®] 184) in the visible range. PDMS constitutes a well suited material for this purpose, since it allows for easy molding of holographically written SRGs. Unlike azobenzene-based materials, it is colorless in the visible region and imprinted gratings are stable if exposed to light of arbitrary wavelength. Using a molded grating also demonstrates that the presented technique is not limited to the determination of refractive indices of SRG-forming materials but also applies to any solid with a grating near its surface.

To measure the dispersion of Sylgard[®] 184, a slightly modified version of the setup for the inscription of holographic gratings (cf. Chapter 7.1) was used. Instead of placing a photo-active medium into the sample holder on the rotational stage, a glass substrate covered with a PDMS layer was installed. The latter was cast from a molecular glass film with holographically generated SRGs according to the procedure described in Chapter 6.1.3. Thus, it featured several spatially separated sinusoidal SRGs with a periodicity of $\Lambda = 1000.6 \pm 1.7$ nm on its surface. AFM measurements further confirmed the presence of defect-free, uncollapsed gratings. The substrate was mounted with one of the gratings located exactly at the position where usually the hologram would develop. Since the grating was already present on the PDMS film, illumination with a holographic interference pattern was not required and the writing beams were switched off during the whole experiment.

Determination of n_0 as a function of the wavelength requires the use of diverse reading lasers. A multi-color He-Ne laser generated light at the wavelengths 593.932, 604.613, 611.802, and 632.816 nm. Further light sources were the laser at 489.20 nm, normally used for holographic grating inscription, and several diode lasers providing lines at 532.06, 660.3, 671.8, and 688.4 nm. In combination, a total number of nine different wavelengths were available. All laser beams were collimated and passed a polarizer to illuminate the PDMS grating with *s*-polarized light.

To measure the angles $\theta_{l, \text{in}}^{90^\circ}$, the sample was rotated. The pivot coincided with the center of the grating spot, so it was continuously hit by the reading laser. For normal incidence, the diffracted orders passed through the PDMS layer and the glass substrate behind it. With increasing rotation angle, the emerging orders became totally reflected at the air surfaces of glass substrate and PDMS film, acting as a waveguide. Further rotation of the sample caused a given diffracted order to propagate at an angle at which it did not reach the boundary between PDMS film and substrate anymore. The associated angle of incidence was $\theta_{l, \text{in}}^{90^\circ}$, which could be determined for the 1st and 2nd diffraction orders ($l = 1$ and 2). As a consequence of Eq. (9.2), higher orders were not observed.

The refractive indices determined with the above method were controlled by reference measurements performed with an Abbe refractometer (Zeiss Abbe-Refraktometer Modell A). To perfectly fit the size of the refracting prism, Sylgard[®] 184 resin was cured in a casting mold and prepared as a stripe with a size of 4×1 cm² and a thickness of 2.5 mm. Due to its low Young's modulus, it easily adhered to the prism and, thus, no contact liquid was required. The PDMS stripe on the refracting prism was successively illuminated with the monochromatic light of the laser sources, while the compensator of the refractometer was adjusted to its neutral position. To obtain the refractive index, the internal scale was recalculated for each wavelength as specified by the manufacturer.

The refractive indices of the PDMS elastomer determined by the different measurement procedures are plotted in Fig. 9.2 as a function of the wavelength. According to the data of the Abbe refractometer (solid squares), n_0 decreases from 1.421 in the blue to 1.412 in the red spectral region. An uncertainty of 5×10^{-4} arises from the reading accuracy of its

internal scale. The data of the refractometer show normal dispersion, which is the expected behavior for a transparent, colorless material. Similar values for the refractive indices were calculated from Eq. (9.2) (solid circles) and Eq. (9.4) (solid triangles). The deviations from the refractometer data are small but show a systematic trend. Refractive indices determined from Eq. (9.4) have an almost constant offset of about -2×10^{-3} , which is also present for wavelengths up to 650 nm if calculated from Eq. (9.2). For larger wavelengths, n_0 increases such that the last data point is located slightly above the refractometer data.

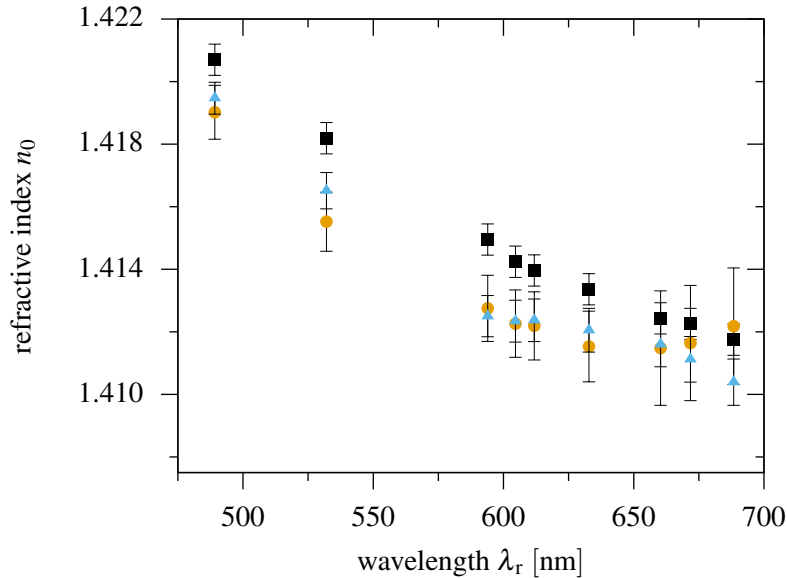


Figure 9.2: Refractive index of the Sylgard[®] 184 PDMS elastomer as a function of the wavelength. Its values are determined by Abbe refractometer measurements (solid squares) or calculated either from Eq. (9.2) (solid circles) or Eq. (9.4) (solid triangles).

As confirmed by the Abbe refractometer data, the increasing values of n_0 derived from Eq. (9.2) at longer wavelengths cannot be caused by anomalous dispersion in PDMS. To understand their origin, a closer inspection of the experimental error sources is required. The accuracy to which the refractive index can be determined from Eq. (9.4) depends only on two subsequent angular measurements. Equation (9.2), on the other hand, requires additional precise knowledge of the grating period and the wavelength of the reading beam. Thus, the error bars of the filled triangles in Fig. 9.2 are smaller than those of the filled circles. An error of the grating period would not only change n_0 at longer wavelengths but introduce an offset to the whole data set. Incorrect determination of the critical diffraction angles would influence the refractive indices determined from both Eq. (9.2) and Eq. (9.4). Thus, the wavelength λ_r remains the only parameter which can affect Eq. (9.2) exclusively in part of the data points.

Depending on the angular resolution, the 1st-order critical diffraction angle can be measured with almost arbitrary accuracy if the incident plane wave is monochromatic. For a light source of non-negligible spectral width, however, each spectral component is diffracted by the grating at its own angle, so the collimated beam splits up into its different colors. Equation (9.1) implies that light with shorter wavelength emerges at a smaller angle inside the medium. Upon rotation, the red part of the probing beam becomes evanescent first, followed by the light at its wavelength peak. Hence, for quasi- or non-monochromatic light, the criterion that the 1st order must not propagate into the substrate is fulfilled by the blue part of its spectrum. Specification of n_0 to the third decimal place requires the wavelength

of the light source to be known to an accuracy of better than 1 nm. Otherwise, the spectral splitting of the probing beam reduces the precision. Spectrometer measurements showed that this was actually the case for the diode lasers at the long wavelengths 660.3, 671.8, and 688.4 nm. They had a spectral width of 2.8 nm (full width at half-maximum). For all other laser sources it was below 0.1 nm.

The systematic error caused by the uncertainty of the peak wavelength λ_r in Eq. (9.2) can be compensated by replacing it with an adequately blue-shifted wavelength λ'_r . For diode lasers with a Gaussian spectral profile, it is reasonable to define λ'_r as the wavelength at which their intensity decreases to $1/e^2$ of its maximum. This yields 658.8, 669.9, and 686.9 nm as the corrected wavelengths λ'_r for the red diode lasers. The refractive indices calculated from these wavelengths are plotted in Fig. 9.3 together with the (unchanged) values determined before. Refractive indices calculated from both Eq. (9.2) and Eq. (9.4) now show normal dispersion and match each other. As a consequence of the broader spectral width of the laser sources above 650 nm, the error bars become quite large in this range. The constant offset to the Abbe refractometer data remains present in both data sets.

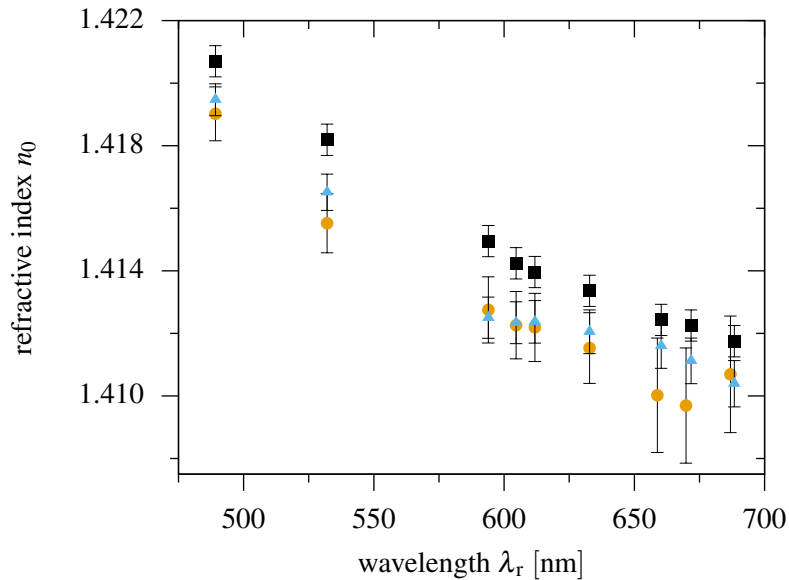


Figure 9.3: Data are identical to the one shown in Fig. 9.2 except for the refractive indices calculated from Eq. (9.2) for the red diode lasers. Instead of the peak wavelengths 660.3, 671.8, and 688.4 nm, the corrected wavelengths 658.8, 669.9, and 686.9 nm were inserted, respectively.

The grating period Λ enters only in Eq. (9.2) and cannot be responsible for both shifts. An independent reference value is the average grating period $\bar{\Lambda}$, which is the mean value of the grating periods determined from Eq. (9.3) for each individual laser source. It is calculated as $\bar{\Lambda} = 999.7 \pm 1.0$ nm, which agrees with the value of Λ within the error margins. Therefore, substitution of $\bar{\Lambda}$ into Eq. (9.2) only gives rise to minor changes of the refractive indices. This proves that Λ is calculated correctly from Eq. (2.3).

Several other error sources can also be excluded to cause the offset. The experiment was repeated with different laser polarizations. For both *s*- and *p*-polarized light, the critical diffraction angles were identical. Thus, no anisotropy or birefringence was introduced into the PDMS film during preparation. Also, switching to a different grating spot did not have any significant effect on the refractive-index data. The critical diffraction angles of the -1^{st} and -2^{nd} diffracted orders, $\theta_{-1, \text{in}}^{90^\circ}$ and $\theta_{-2, \text{in}}^{90^\circ}$, were determined by reversing the direction of rotation. Because negative and positive orders propagate at angles with opposite sign,

the values measured for the critical diffraction angles may become distorted if the grating vector is not parallel to the film surface. The refractive indices calculated from Eq. (9.2) and Eq. (9.4), however, are identical for orders with both signs, implying that the grating is unslanted. This also proves that the presented method is not affected by slight inhomogeneities of the sample surface.

The refractive indices calculated from Eq. (9.2) and Eq. (9.4) are both shifted to lower values. To match the refractive indices of the Abbe refractometer within the error bars, it is sufficient to increase each angle by as little as 0.05° . Thus, it is plausible to assume that the offset is caused by a systematic error in the determination of $\theta_{1, \text{in}}^{90^\circ}$. Diffracted orders do not vanish abruptly near their critical diffraction angle. Instead, their intensity decreases to zero within a narrow angular interval. This causes some uncertainty about the angular position of $\theta_{l, \text{in}}^{90^\circ}$. In the above experiments, $\theta_{l, \text{in}}^{90^\circ}$ was simply defined as the angle at which the diffracted order becomes invisible to the human eye. This may give rise to the small deviation.

9.3 Refractive Indices of Azobenzene-Functionalized Molecular Glasses

The above measurements show that n_0 can be determined from 1st- and 2nd-order critical diffraction angles with an accuracy of about three decimal digits. Thus, the method is applicable to the determination of the refractive indices of the SRG-forming molecular glasses discussed in Chapter 5.1.

For this purpose, films of molecular glasses **1a-e**, **2a-d**, and **3a-b** were prepared and placed on the sample holder of the holographic setup. Each sample was illuminated with a *pp*-type intensity grating at an overall intensity of 2 W cm^{-2} (1 W cm^{-2} per beam). The writing beams were switched off immediately after the 1st-order diffraction efficiency of the developing SRG reached its maximum. Both the maximum diffraction efficiency $\eta_{1, \text{max}}$ and the time t_{max} required to reach $\eta_{1, \text{max}}$ strongly depend on the molecular glass. A detailed list of all values is given in Table 9.1. In films of materials **1a-b**, **2a**, and **3a-b**, $\eta_{1, \text{max}}$ reaches a value of 25 to 29 % within a few minutes. Increasing the length of the perfluorinated moieties impedes SRG formation, as indicated by the reduced writing speed and the low diffraction efficiency of materials **1c** and **2c**. This behavior is similar to that reported for perfluoroalkyl-azobenzene polymers.^[61] In contrast, the introduction of methoxy-substituted azobenzene chromophores in molecular glass **1e** fosters SRG formation. Here, the diffraction efficiency reaches a value of 30.5 % within an illumination time as short as 34 s. The crystallized films of materials **1d** and **2d** (cf. Chapter 5.3) did not allow for the inscription of SRGs. Thus, no refractive indices could be calculated for these compounds. To precisely characterize the grating used for the determination of the refractive index, $\eta_{1, \text{max}}$ and t_{max} were determined from the respective single hologram measurement on each film. Repeated grating inscription at different spots on the films gives rise to deviations from the listed values, which are typically below 10 %.

Critical diffraction angles were measured by rotating the inscribed gratings with the rotational stage according to the procedure described in Chapter 9.2. Only wavelengths relevant for holographic grating inscription were used, i. e., the writing wavelength of 489.2 nm and the reading wavelength of 685 nm. Modification of the reading laser or the holographic setup was not required in this case. Irradiation of light at the writing wavelength causes the SRGs to decay. Thus, $\theta_{1, \text{in}}^{90^\circ}$ and $\theta_{2, \text{in}}^{90^\circ}$ were measured with the reading laser first. Afterward, one of the writing beams was turned on with its intensity reduced to 100 mW cm^{-2} . Since the mass transport during holographic illumination depends on the optical energy per unit area (cf. Chapter 11), the SRG decay process is expected to be slowed down by a factor

of ~ 10 . This is sufficient to determine the angular position of $\theta_{2, \text{in}}^{90^\circ}$. Critical diffraction angles of other orders were not measured with the writing laser (see discussion below). As mentioned earlier, the grating height does not affect the angle at which the diffracted orders propagate. Thus, neither the low diffraction efficiency of the molecular glasses with perfluorinated azobenzene moieties nor the grating decay during illumination with light at 489.2 nm cause errors of n_0 .

Table 9.1: Holographic and optical parameters of various azobenzene-functionalized molecular glasses. $\eta_{1, \text{max}}$: maximum diffraction efficiency, t_{max} : time required to reach $\eta_{1, \text{max}}$, $n_0(\lambda)$: refractive index at the wavelength λ , n. d.: not determined

Compound	$\eta_{1, \text{max}}$ [%]	t_{max} [s]	$n_0(489 \text{ nm})^{\text{a)}}$	$n_0(685 \text{ nm})^{\text{b)}}$	$n_0(685 \text{ nm})^{\text{c)}}$
1a	28.5	90	1.520	1.511	1.508
1b	28.1	328	1.521	1.513	1.510
1c	4.8	1112	1.521	1.512	1.508
1d	n. d.	n. d.	n. d.	n. d.	n. d.
1e	30.5	34	1.521	1.513	1.510
2a	25.3	630	1.524	1.515	1.511
2b	4.1	1488	1.523	1.516	1.515
2c	1.4	2591	1.520	1.513	1.512
2d	n. d.	n. d.	n. d.	n. d.	n. d.
3a	27.2	133	1.520	1.512	1.510
3b	28.6	91	1.520	1.513	1.509

^{a)} calculated as $n_0 = \sin \theta_{2, \text{in}}^{90^\circ} + 2\lambda_r/\Lambda$ ^{b)} calculated from Eq. (9.2) ^{c)} calculated from Eq. (9.4)

Depending on the wavelength of the probing beam, refractive indices have been calculated from different equations. For light at a wavelength of 489.2 nm, the values of n_0 become as large as 1.524 (cf. Table 9.1). A 1st-order critical diffraction angle does not exist in this case and the refractive indices must be determined from the 2nd order according to $n_0 = \sin \theta_{2, \text{in}}^{90^\circ} + 2\lambda_r/\Lambda$. The narrow spectral width of the writing laser allows for the use of the peak wavelength without corrections. From the obtained refractive indices, the 3rd-order critical diffraction angle $\theta_{3, \text{in}}^{90^\circ}$ at 489.2 nm can be estimated to be approximately 3° . At this small angle the relative error resulting from the angular resolution of the rotational stage is noticeable. The above calculation is more accurate in this case than applying a higher-order approach based on the diffraction angles of the 2nd and 3rd diffracted orders.

At a wavelength of 685 nm, both the 1st and the 2nd order can propagate parallel to the grating vector and the respective critical diffraction angles could easily be measured. To determine n_0 , Eq. (9.2) and Eq. (9.4) were applied, with the peak wavelength ($\lambda_r = 685 \text{ nm}$) substituted into the former. The spectral width of the reading laser was similar to that of the red diode laser used for the experiments on PDMS. This causes the refractive indices to deviate from their true values if calculated from Eq. (9.2). As in PDMS, they are slightly higher than those determined with Eq. (9.4) and the latter method of calculation is less sensitive to the spectral width of the probing beam. Hence, the higher accuracy of Eq. (9.4) for the diode lasers is independent of the film material.

A complete list of all values obtained for n_0 is given in Table 9.1. For their calculation, $\Lambda = 1000.6 \text{ nm}$ was inserted as the grating period. All molecular glasses have similar refractive indices for the reading and the writing wavelengths. Variations only affect the third decimal digit and are most pronounced in molecular glasses **2a** and **2b**, which have slightly higher values. On average, n_0 has a value of ~ 1.521 at 489.2 nm and either ~ 1.513

or ~ 1.510 at 685 nm if calculated from Eq. (9.2) or Eq. (9.4), respectively. Since the wavelength of the writing laser is located at the red edge of the weak $n \rightarrow \pi^*$ transition of the azobenzene chromophores, all molecular glasses show normal dispersion in the investigated spectral range.

Azobenzene-Based Nanoimprint Lithography

The fabrication of structures on the submicrometer (1000 to 100 nm) and nanometer (100 to 1 nm) scale received huge attention in the past decades.^[153] For example, increasing the transistor density is essential for circuit and processor development and constitutes the key to preserve Moore's law in computer technology.^[5] Also various other fields of application require objects to be miniaturized or surfaces to be structured on the nanoscale. These are, e. g., artificial tissues,^[222] carbon nanotube wires,^[223] high density memory devices,^[224] fuel cells,^[225–227] and 3D nanostructures.^[228,229] In addition, the structure size of a material influences its magnetic, mechanical, optical, and thermal properties, which are dominated by the quantum nature of matter at very small length scales. Advances in the fabrication of structures such as quantum wells, quantum wires, or quantum dots are a prerequisite for the feasibility of many fundamental experiments and, thus, are of great interest for scientific research. The high demand for cost-effective replication techniques of nanometer-sized structures is a valid argument for the development of new methods such as azobenzene-based nanoimprint lithography (Azo-NIL).

This chapter discusses the feasibility and applicability of Azo-NIL. For this reason, it covers exclusively the presentation and the analysis of results obtained from diverse imprinting experiments. The basic concept of Azo-NIL has already been explained in Chapter 4, where it was compared to well established imprint techniques. Moreover, the theoretical part discussed the flow behavior of a confined viscous liquid and the time dependence of the filling process on characteristic quantities of the mold (i. e., protrusion height h_m , protrusion width s , and cavity width w) and the resist (i. e., initial and residual film thickness d_0 and d_f , respectively, and viscosity η_0). To characterize the imprinted profiles, h_{\max} , h_{\min} and h_{avg} were introduced. They define the meniscus-shaped profile, which is formed when the resist material fills the cavities of the mold (cf. Chapter 4.3). The fabrication and the properties of the Elastosil[®] 601 or EVG[®] molds used for imprinting were discussed in Chapter 6.1. As photofluidizable resist material, either molecular glasses or a homopolymer with azobenzene-functionalized moieties are possible (cf. Chapter 5). Samples were illuminated with the setups presented in Chapter 7.2. Imprinted heights have been determined by AFM measurements as described in Chapter 7.3.

A short outline of this chapter is given in the following. Because Azo-NIL is a new technique, fundamental questions concerning the interaction of the photofluidizable resist with the incident light and the flexible molds are discussed first. The topics comprise the fluence dependence of the imprinting speed and the capability of a photofluid to completely fill the channels of a mold by adhesion. Furthermore, the influence of the wavelength and the polarization of the light source is investigated. The initial thickness of the resist is found to affect the cavity filling speed, which is compared with the predictions of the Stefan

equation. Subsequently, a systematic study of the suitability of different resist materials for Azo-NIL is conducted. For this purpose, azobenzene-functionalized SRG-forming materials are used, comprising homopolymer **9** (ii) and the molecular glasses **1a-e**, **2a-d**, and **3a-b**. In the homopolymer, the influence of entanglements on the flow behavior of the photofluid is investigated, while in the molecular glasses the effects of altering the core or the substituent of the azobenzene moieties are studied. The actual nanostructures with pattern sizes down to 100 nm are imprinted into the best materials, which are the spirochromane-based derivatives **1a** and **1e**. Here, the experiments focus on the analysis of the imprint quality and on the dependence of the imprinting speed on the pattern size. In a final step, the discussion is broadened to molecular glass films which are preheated to a temperature slightly below their T_g before the imprinting.

10.1 Imprinting Properties of Photofluidizable Resists

As emphasized in the outline, different questions concerning the feasibility of Azo-NIL have to be settled first. For this purpose, all experiments in this section were carried out on films of molecular glass **1a** at room temperature. Compound **1a** is an efficient SRG former (cf. Chapter 9.3) and, in a retrospective view, also one of the most suitable materials for Azo-NIL. Elastosil[®] 601 molds with L-shaped protrusions on the micrometer scale were used for imprinting due to their easy handling and good adhesive properties. The molecular glass films with the attached molds were placed in the Azo-NIL setup for vertical alignment without applying external pressure.

10.1.1 Fluence Dependence of the Imprinting Speed

The Gaussian profile of a laser beam was used to show that the filling of a mold can be controlled by the fluence F , which is the product of the intensity of the light source and the illumination time. For this purpose, molecular glass **1a** was prepared as a thin film of approximately 500 nm thickness and brought into contact with one of the Elastosil[®] 601 molds. Adhesion was sufficiently strong to keep the mold in contact with the molecular glass film. The molecular glass and the mold were illuminated through the substrate with the s -polarized light of the 489.2 nm laser for 15 s.

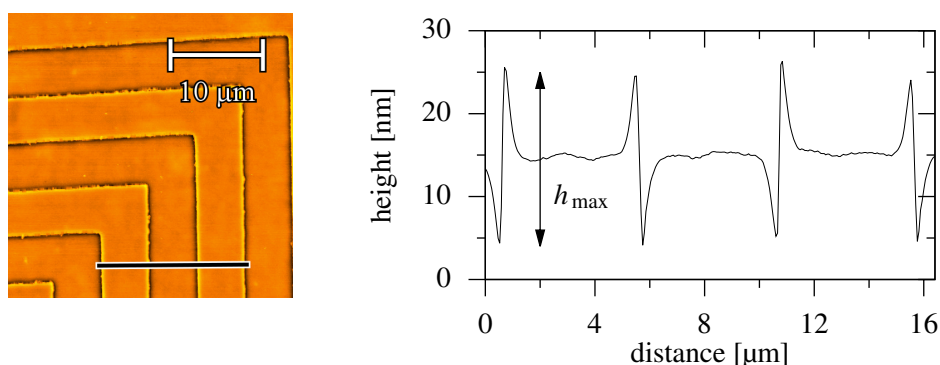


Figure 10.1: The left side shows a false-color AFM image of the L-shaped 5 μm pattern imprinted into a film of molecular glass **1a** after 15 s of illumination with an intensity of $\sim 0.87 \text{ W cm}^{-2}$. The light source was an s -polarized laser with a wavelength of 489.2 nm. The profile measured along the black line is plotted on the right.

Since the roofs of the mold are collapsed to the resist initially, only the remaining cavities at the protrusion edges fill during the short imprinting time. Thus, the molecular glass film features sharp lines with widths below $1\ \mu\text{m}$ after removing the mold. This is demonstrated in Fig. 10.1 for the example of the L-shaped line pattern with $w = s = 5\ \mu\text{m}$. The left side shows an AFM image of the imprint and the right side a plot of the cross section along the black line drawn in the image. Due to the adhesive interaction of the flexible mold with the photofluidic resist, the imprint features a symmetric profile with peaks directed upwards or downwards. Within the short illumination time, only h_{max} increases, whereas h_{avg} and h_{min} are zero. This applies to the imprinted line patterns of different periodicity in the same way.

The diameter of both the laser beam and the mold are on the same order of magnitude. Therefore, the irradiation intensity changes over the area of the mold. Since the laser provides a TEM_{00} Gaussian mode, its intensity distribution in a direction perpendicular to its propagation is given by

$$I(r) = I_{\text{max}} \cdot \exp(-2r^2/w_0^2), \quad (10.1)$$

with r being the distance from the optical axis and $2w_0$ the beam diameter. The sample was positioned such that the maximum intensity of $I_{\text{max}} = 1.0\ \text{W cm}^{-2}$ was reached near the bottom right edge of the mold between the 5 and $10\ \mu\text{m}$ structures. This is illustrated by the blue coloring in the inset of Fig. 10.2. According to Eq. (10.1), the intensity decreases to a value of $0.14\ \text{W cm}^{-2}$ at the $1\ \mu\text{m}$ protrusions near the mold center.

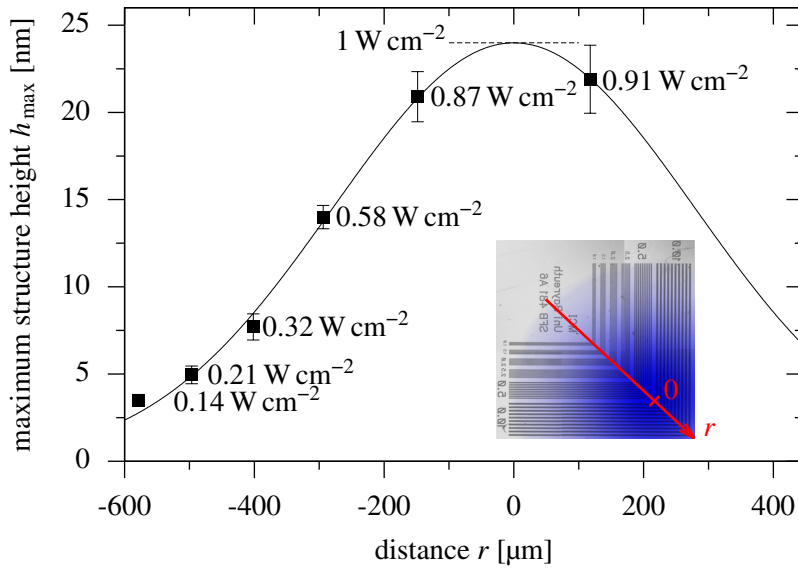


Figure 10.2: Maximum structure height h_{max} imprinted into a film of molecular glass **1a** after 15 s of illumination as a function of the position r . The black line indicates a fit to the data according to Eq. (10.2). The light source was a laser with a wavelength of $489.2\ \text{nm}$ and a maximum intensity of $1.0\ \text{W cm}^{-2}$. The inset indicates the position of the maximum of the Gaussian intensity profile relative to the mold and the coordinate r (red axis).

In Fig. 10.2 also the maximum structure heights h_{max} measured at different positions r along the red axis are plotted. As indicated by the black solid line, the heights imprinted into the molecular glass are well described by the fit function

$$h_{\text{max}}(r) = 24\ \text{nm} \cdot \exp\left[-2r^2/(557\ \mu\text{m})^2\right]. \quad (10.2)$$

From the above equation, $2w_0$ is calculated to be 1.1 mm, which matches the diameter of the laser beam exactly. This proves that the required imprinting time and, thus, the viscosity of the azobenzene-functionalized resist becomes smaller with increasing intensity. For small structure heights, the cavity filling rate turns out to be proportional to the intensity. In terms of the fluence, this implies that the maximum structure height obeys $h_{\max} \propto F = I \cdot t$. Even at the lowest intensity of 0.14 W cm^{-2} significant mass flow was observed. This is plausible, since the corresponding fluence is about 100 times higher than the minimum value of 20 mJ cm^{-2} required to athermally photofluidize a self-assembled tethered azobenzene monolayer.^[142]

The perpendicular arrangement of the cavities can be used to further investigate the influence of the polarization of the laser on the filling behavior of the mold. This is important, since the flow direction of azobenzene-functionalized homopolymers has been reported to be highly sensitive to the polarization of the incident light.^[44] It is conceivable that the filling speed of vertically and horizontally aligned cavities depends on their orientation relative to the laser polarization. Such a difference was not observed in the above experiments, however. The filling speed depends only on the laser intensity and the heights of vertical and horizontal lines are similar for each pattern type. Obviously, the mass transport is primarily driven by the adhesive forces of the mold.

10.1.2 Filling Characteristics of Micrometer Cavities

It is of great importance to find out whether the capillary forces acting on a photofluid are capable of filling the mold cavities completely. As in the previous section, an Elastosil[®] 601 mold was attached to a film of molecular glass **1a** and irradiated with the *s*-polarized laser at a maximum intensity of 1.0 W cm^{-2} . The illumination time, however, was increased to 4 h, by a factor of almost 1000. Thus, even in regions of low intensity the fluence was 100 times higher than in the previous experiment.

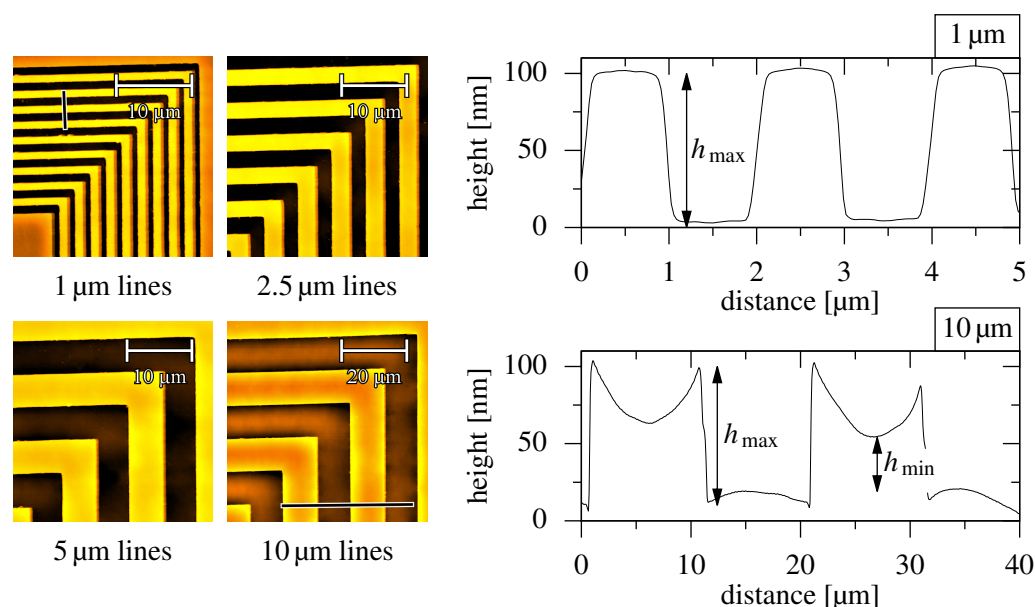


Figure 10.3: Structures imprinted into a film of molecular glass **1a** after 4 h of illumination with a 489.2 nm laser at $I_{\max} = 1.0 \text{ W cm}^{-2}$. Left: False-color AFM images of the imprinted 1, 2.5, 5, and 10 μm line patterns. Right: Profiles of the 1 and 10 μm line patterns along the black lines in the respective AFM picture.

A selection of the imprinted structures are presented in Fig. 10.3. It comprises AFM images of the 1, 2.5, 5, and 10 μm line patterns on the left and plots of the respective profiles of the 1 and 10 μm line patterns on the right. The latter were extracted from the AFM images and correspond to the data measured along the black lines. For reasons of clarity, the AFM images of the 1.5 and 2 μm line patterns are not shown. Apart from a scaling factor, their AFM data look similar to those of the 1 and 2.5 μm line patterns. For the 1, 1.5, 2, and 2.5 μm line patterns, the mold immerses completely into the molecular glass film. Therefore, all four pattern types feature heights of $h_{\text{max}} = h_{\text{min}} = h_{\text{avg}} = 100\text{nm}$ as illustrated for the example of the 1 μm patterns (cf. Fig. 10.3). The AFM pictures of the 1 and 2.5 μm patterns demonstrate that the small cavities fill homogeneously over a large area. Furthermore, no visible defects are caused by the detachment of the mold. In sum, the L-shaped structures of the mold are reproduced with high quality for $w \leq 2.5\mu\text{m}$. For the 5 and 10 μm patterns, the imprints feature a meniscus-shaped profile (cf. Fig. 10.3). The maximum values of the imprinted heights are $h_{\text{max}} = 96\text{nm}$ and $h_{\text{min}} = 73\text{nm}$ for the 5 μm structures and $h_{\text{max}} = 90\text{nm}$ and $h_{\text{min}} = 35\text{nm}$ for the 10 μm structures, respectively. Although h_{max} is close to the 100 nm depth of the master in both cases, the middle part of the cavities remains unfilled for the most part.

The complete filling of mold cavities with $w = 10\mu\text{m}$ requires a large amount of resist material to be transported. Equation (4.1) implies that the filling time varies with the square of the protrusion width of the mold. Hence, the imprinting of the 10 μm line patterns is expected to take 100 times longer than for the 1 μm line patterns. From the results discussed later in Chapter 10.1.4 it can be estimated that the complete filling of the 10 μm structures would require $\sim 50\text{h}$ of illumination at a laser intensity of 1.0W cm^{-2} . Moreover, even if the sample were irradiated for such a long time, sagging of the roofs of the flexible mold is expected to impede the replication of a rectangular profile. Obviously, this effect is most pronounced for mold patterns with a low aspect ratio ($h_{\text{m}}/(w+s) \ll 1$). The fact that the imprints of the 5 and 10 μm structures are not an exact copy of the original pattern does not constitute a major drawback for the applicability of Azo-NIL. Its main use will be the replication of patterns with sizes significantly below 1 μm .

The rectangular shape of the imprints with protrusion (or cavity) widths up to 2.5 μm indicates that the roof collapse of the mold is reversed upon illumination. This further implies that w_{crit} changes during imprinting (cf. Chapter 6.2.1). For patterns with $w \geq 5\mu\text{m}$, the roofs of the Elastosil[®] 601 mold rise only partially, which becomes apparent in the final shape of the imprint. As stated previously, illumination for 4 h is too short to completely fill the 5 and 10 μm cavities. Therefore, it cannot be clearly specified whether the roofs of the mold already reached their equilibrium state or not. Yet, $w_{\text{crit}}' = 2.5\mu\text{m}$ constitutes a lower estimate of the cavity width at which the roof collapse completely reverses upon illumination. By inserting this value into Eq. (6.1), one can estimate the work of adhesion that would be required to separate the Elastosil[®] 601 mold from the photofluidic film. It is on the order of 1mJ m^{-2} .

10.1.3 Influence of the Light Source on the Imprinting Speed

To analyze the temporal evolution of the fill height of the mold cavities, imprinting was performed at different spots on films of molecular glass **1a** for various illumination times. As in the previous chapters, the initial film thickness of the molecular glass films was $\sim 500\text{nm}$. Different light sources were used for imprinting. They comprise the laser at 489.2 nm and a UV or a blue LED at 365 or 455 nm, respectively. The mold was illuminated either with only one of the three light sources switched on or with both LEDs at the same time. The intensities of the individual light sources are listed in Table 10.1 and remained unchanged

during the whole experiment. For the LEDs, the values correspond to their maximum optical output. Their intensity is homogenous over the entire area of the mold. If illumination was performed with the laser, the sample was positioned such that the 1 μm pattern was hit by the maximum intensity. The exposure time and, thereby, the fluence was increased between each imprint. After completion of the imprinting process, the average filling height h_{avg} of the 1 μm line patterns was determined. It is plotted as a function of the imprinting time in Fig. 10.4 for each of the three individually operated illumination sources. For reasons of clarity, the data obtained with illumination with both LEDs is shown in the next section in Fig. 10.5.

Table 10.1: Parameters of the imprinting process. I : intensity, h_0 : imprint height of the 1 μm line patterns for $t \rightarrow \infty$, τ : filling time constant of the 1 μm cavities according to Eq. (10.3), τ' : filling time constant calculated from Eq. (10.4).

illumination source	wavelength [nm]	I [W cm^{-2}]	h_0 [nm]	τ [s]	$\tau'(0.72 \text{ W cm}^{-2})$ [s]
laser	489.2	1.0	92	301	418
blue LED	455	0.42	99	305	176
UV LED	365	0.30	89	301	127
both LEDs	365/455	0.30 + 0.42	96	112	112

The results discussed in Chapter 10.1.1 suggest that h_{avg} increases linearly for short imprinting times. Furthermore, h_{avg} must saturate quickly as soon as the cavities of the mold become completely filled or if adhesion is not sufficient anymore to further raise the photofluid. An exponential approach to the maximum imprint height h_0 according to

$$h_{\text{avg}}(t) = h_0(1 - \exp(-t/\tau)) \quad (10.3)$$

fulfills these requirements. An exponential law has also been applied to describe the growth of microlens arrays in T-NIL experiments^[230] and yields good fits to the data. h_0 denotes the average protrusion height of the imprinted 1 μm patterns after illuminating the mold for an infinitely long time ($t \rightarrow \infty$). It is different from h_{max} , which is the maximum filling height within each cavity at short imprinting times. If the mold is filled completely, h_0 is equal to the height of the mold protrusions h_{m} (cf. Fig. 6.4).

Homogeneous, L-shaped imprints, which reproduce the cavities of the mold in height and shape, can be imprinted with all four illumination schemes listed in Table 10.1. For sufficiently long imprinting times, the mold is filled completely and the AFM data of the 1 μm patterns looks similar to the one depicted in Fig. 10.3 in the previous section. Figure 10.4 shows that this process takes ~ 20 min for each of the three illumination sources. The maximum imprinted pattern heights determined from the fits are 94 ± 5 nm (cf. Table 10.1). Slight variations are due to the use of different molds for each light source. Although the intensities and wavelengths of the laser and the LEDs differ from each other, τ is on the order of 300 s for all three light sources. Illumination with both LEDs exposes the sample to an overall intensity of 0.72 W cm^{-2} . The build-up time constant decreases to $\tau = 112$ s in this case (cf. Table 10.1). This is almost three times faster than in the case of the single sources.

The intensity and the wavelength of the individual light sources are different. Hence, the built up constants determined for the four illumination schemes are not indicative of the influence of the wavelength on the filling speed. To allow for direct comparison of the data, τ' is introduced. It is defined as the build-up constant that would be measured if the patterns were imprinted at the intensity I' . Since the filling height is proportional to the fluence

for short illumination times, it follows from Eq. (10.3) that $h_{\text{avg}}(t) = h_0(1 - \exp(-t/\tau)) \approx h_0 t/\tau = CIt$. Because τ is inversely proportional to the intensity, one can calculate $\tau'(I')$ according to

$$\tau'(I') = I/I' \cdot \tau(I). \quad (10.4)$$

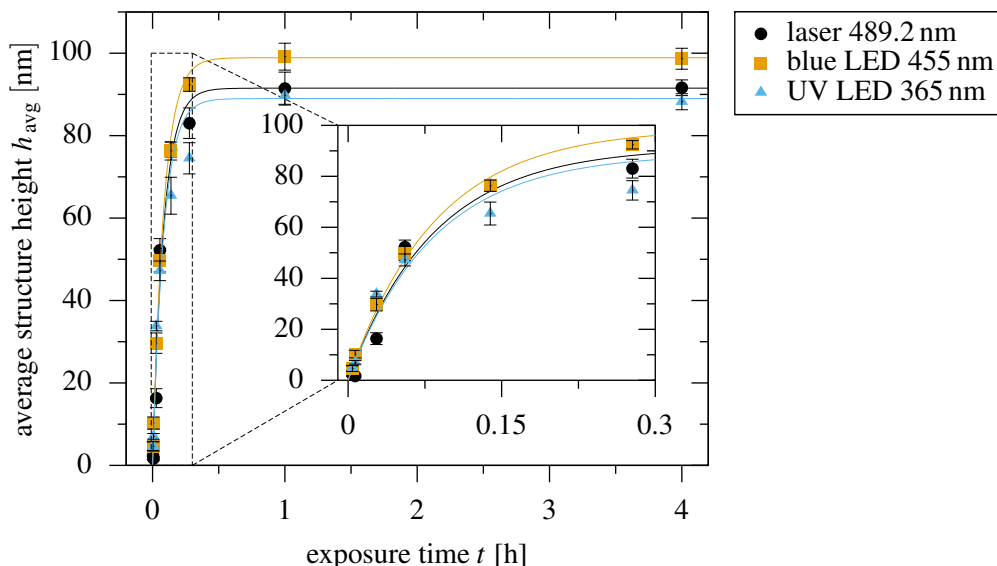


Figure 10.4: Average structure height h_{avg} as a function of the exposure time t for the different single light sources. Illumination was performed with a laser at 489.2 nm (black circles), a blue LED at 455 nm (brown squares), and a UV LED at 365 nm (blue triangles). The fitted lines indicate an exponential approach to the height of the mold protrusions according to Eq. (10.3).

Eq. (10.4) can be applied to determine τ' at an intensity of $I' = 0.72 \text{ W cm}^{-2}$ (the overall intensity of both LEDs) for each light source. The respective values are listed in Table 10.1. Obviously, τ' and, thus, the imprinting time decreases for shorter wavelengths of the illumination source. The wavelength of the laser is located at the red edge of the azobenzene $n \rightarrow \pi^*$ transition band. The low absorption of molecular glass **1a** does not allow for efficient isomerization of the azobenzene moieties in this case and, therefore, the imprinting speed is low. The wavelength of the blue LED at 455 nm corresponds almost exactly to the position of the maximum of the $n \rightarrow \pi^*$ transition. Although the absorption of molecular glass **1a** is still quite low (cf. Fig. 5.5 in Chapter 5.1.2), τ' decreases strongly as compared to the laser. With UV illumination the $\pi \rightarrow \pi^*$ transition is excited primarily. This does not only result in a *cis*-rich photo-stationary state, but it also increases the *trans-cis-trans* isomerization rate. Hence, the build-up constant τ' becomes as short as 127 s, which is about three times faster than in the case of the laser. The above results suggest that the imprinting speed can be further increased by adjusting the illumination wavelength to the $\pi \rightarrow \pi^*$ maximum at 327 nm. This is not surprising, since the viscosity of a photofluid correlates with the efficiency of the *trans-cis-trans* isomerization.^[142] Irradiation with both LEDs at the same time is expected to change the ratio of *cis* and *trans* isomers in the photo-stationary state. The differences between the absorption spectra of the photochromic molecular glass for either plain UV or combined LED illumination may therefore result in a more efficient photofluidization. As can be seen in Table 10.1, τ' is minimal when the sample is irradiated with both LEDs simultaneously. Although the build-up time is only about 10 % shorter than that determined for the UV LED, illumination with both LEDs constitutes the most efficient way to imprint patterns.

It is also an important result that incoherent light can be used for imprinting. This proves that the mass migration is not caused by an interference phenomenon as in holographic SRG experiments.

10.1.4 Influence of the Initial Film Thickness on the Imprinting Speed

The residual film thickness d_f below the imprint influences the quality of postprocessing steps like etching and, therefore, needs to be low. To analyze the capabilities of Azonil, films of **1a** were prepared with initial film thicknesses $d_0 = 55, 90, 180, 360, 505,$ and 790 nm. Exposure was performed with both LEDs switched on simultaneously. The temporal evolution of h_{avg} was determined from the height profiles of the $1\ \mu\text{m}$ structures according to the procedure described in the previous chapter.

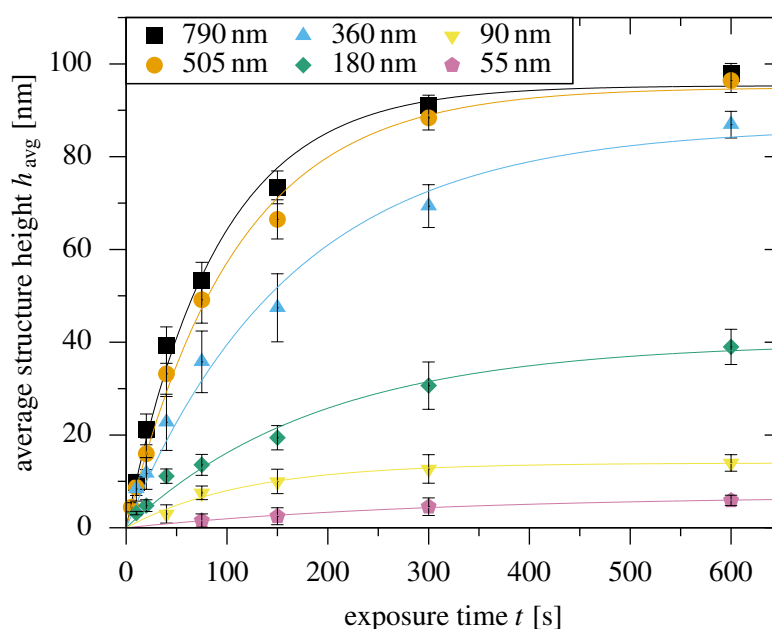


Figure 10.5: Average structure height h_{avg} as a function of the exposure time t for films of molecular glass **1a** with different initial thicknesses d_0 as indicated at the top.

Fig. 10.5 shows that h_{avg} tends exponentially to a maximum height in all films. As indicated by the solid lines, the data are well reproduced by inserting the parameters listed in Table 10.2 into Eq. (10.3). For the films of 790 and 505 nm thickness, the mold is filled completely after 5 to 10 min illumination. The imprinted pattern height is $h_0 = h_m = 95$ nm and the filling of the cavities is faster than for the other films. Increasing d_0 to values above 500 nm causes only small changes with respect to the imprinting speed or h_{avg} . If d_0 becomes smaller than this value, the required imprinting time increases strongly and complete filling of the the mold is not achieved anymore. The film with $d_0 = 55$ nm, for example, gives rise to the formation of structures as low as $h_0 = 7$ nm, although a pattern height of 100 nm with a 5 nm residual layer below would be conceivable. The pressure induced by adhesion seems not to be sufficient to overcome the resistance of the confined flow in this case.

This behavior can be understood by means of the Stefan equation, which reads

$$t_f = \frac{\eta_0 s^2}{2p} \left(\frac{1}{(d_0 - \nu h_m)^2} - \frac{1}{d_0^2} \right) \approx \frac{\nu \eta_0 s^2}{p} \cdot \frac{h_m}{d_0^3} \quad (10.5)$$

if a mold with fill factor ν is completely inserted into the resist (cf. Chapter 4.3). The mold height h_m enters as a parameter. The approximation applies if h_m is small compared to the initial film thickness ($h_m \ll d_0$). It indicates that t_f follows a power law, viz., $t_f \propto d_0^{-3}$. Therefore, the time required to fill a mold completely is expected to increase strongly with decreasing film thickness.

Table 10.2: Summary of the experimental data of films of molecular glass **1a**. d_0 : initial film thicknesses, h_0 : imprint height of the 1 μm line patterns for $t \rightarrow \infty$, τ : filling time constant of the 1 μm cavities according to Eq. (10.3).

d_0 [nm]	h_0 [nm]	τ [s]
790	95	89
505	95	112
360	86	164
180	40	193
90	14	118
55	7	304

To apply Eq. (10.5) to the measured data, one needs to determine the time after which the mold is completely immersed into the molecular glass film. This is not possible for the used mold since it fills only partially for the thinner films, even at long imprinting times ($h_0 < h_m$ for $t \rightarrow \infty$). For this reason, $t_{5\text{nm}}$ is calculated from the fit parameters listed in Table 10.2 for each film. It corresponds to the time required to imprint a step profile of 5 nm height. This height is chosen such that it is lower than the maximum pattern height imprinted into the thinnest film. The calculated times are identical to the ones that would be required to fill a fictitious mold of height $h_m = 5$ nm.

Fig. 10.6 depicts $t_{5\text{nm}}$ as a function of d_0 . To highlight deviations from the predictions made by Eq. (10.5), the data are also shown in log-log representation in the inset. The dotted line represents a fit of the form $t_{5\text{nm}}(d_0) = C \cdot d_0^{-3}$. Because h_m is only 5 nm, the approximation made in Eq. (10.5) is valid even for films as thin as 55 nm. At film thicknesses above 200 nm the data clearly deviate from the simple power law and approach a constant value of 4.8 s. In the derivation of the Stefan equation it is assumed that an infinite initial film thickness causes an infinite liquid flow below the mold and, therefore, the imprinting time becomes zero. In the experiment, however, it appears more realistic to assume that in the thicker films the lower resist layers do not contribute to the filling of the mold. This can be taken into account by adding a constant t_{min} to the right side of Eq. (10.5). The Stefan equation then becomes

$$t_f = \frac{\eta_0 s^2}{2p} \left(\frac{1}{(d_0 - \nu h_m)^2} - \frac{1}{d_0^2} \right) + t_{\text{min}} \quad (10.6)$$

such that films with high initial thickness still require a finite time to fill a mold. As indicated by the solid black line in Fig. 10.6, this modified equation with the parameters $t_{\text{min}} = 4.8$ s, $\nu h_m = 0.5 \cdot 5$ nm, and $\eta_0 s^2 / 2p = 1.17 \times 10^7$ nm² s reproduces the experimental data well. In

the above considerations, adhesion is assumed to exert a constant, average pressure p onto the mold protrusions.

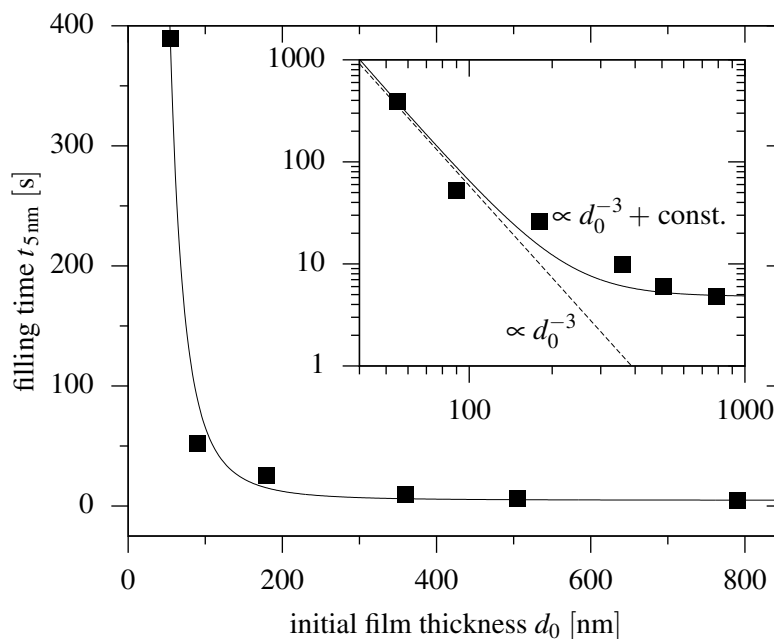


Figure 10.6: Time required to fill a fictitious mold of height $h_m = 5$ nm with molecular glass **1a** as a function of the initial film thickness d_0 . The inset shows the same data in double-logarithmic representation. The dashed straight line indicates a power law of the form $t_{5\text{nm}} \propto d_0^{-3}$. The solid line corresponds to Eq. (10.6).

10.2 Influence of the Resist Material on the Imprinting Performance

Various compounds have been discussed as potential candidates for Azo-NIL in Chapter 5. They comprise the molecular glasses based on cores **1**, **2**, and **3** and homopolymer **9(ii)**. The spirochromane-based derivatives **1a-e** feature a more rigid core than the triphenylamine-based derivatives **3a-b** and, therefore, have a higher glass transition temperature. The presence of additional amide moieties in the core of the trisamide-based derivatives **2a-d** fosters intermolecular H-bond formation, which increases the glass transition temperature even further. Depending on the molecular core, the performance of the different compounds is expected to vary strongly in Azo-NIL experiments. The imprinting experiments with homopolymer **9(ii)** focus on the influence of entanglements on the imprinting speed. They also serve as a reference to illustrate the advantages of molecular glasses as compared to homopolymers.

The modification of the substituents of the azobenzene moieties in the molecular glasses addresses different issues. A common method to avoid sticking of the resist in NIL techniques is to decrease the surface energy of the mold by coating it with a fluorinated alkylsilane layer.^[153] Alternatively, fluorine can be introduced into the resist or mold material directly. By linking perfluorinated alkyls of increasing length to the azobenzene moieties of the molecular glasses, their influence on the adhesive properties and the imprinting behavior can be investigated. Methoxy-substituted azobenzene moieties are present in molecular

glass **1e**. Their absorption is shifted towards the irradiation wavelength, which is expected to increase the imprinting speed.

Experiments were conducted at room temperature under the optimized conditions determined in the preceding chapters. Elastosil[®] 601 molds with L-shaped micrometer features were used for imprinting due to their easy handling. The molecular-glass films with the attached molds were placed in the Azo-NIL setup for vertical alignment without applying external pressure. Illumination was performed with both LEDs simultaneously. All discussed heights refer to the average imprint height h_{avg} of the 1 μm line patterns.

10.2.1 Azobenzene-Functionalized Triphenylamine-Based Compounds

First, the suitability of the triphenylamine-based molecular glasses **3a** and **3b** as photofluidizable resist materials was investigated. Both compounds are efficient SRG formers,^[50] which makes them promising candidates for Azo-NIL. Films of molecular glasses **3a** and **3b** were prepared with thicknesses of 500 and 750 nm, respectively, so the influence of the initial film thickness on the imprinting speed is expected to be negligible. Patterns were imprinted in both of the films by illuminating them through the substrate for 600 s.

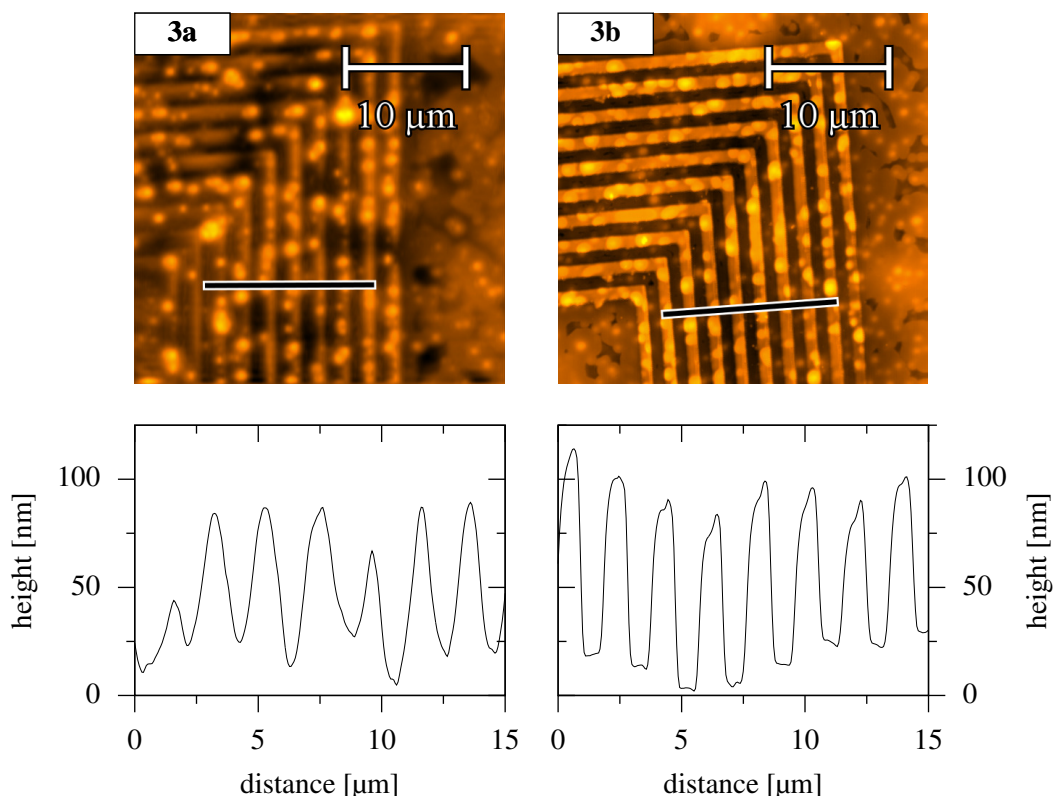


Figure 10.7: Structures imprinted into films of molecular glass **3a** (left) and **3b** (right) with an Elastosil[®] 601 mold after 600 s illumination with both LEDs. Top: False-color AFM images of the imprinted 1 μm line patterns. Bottom: Profiles of the 1 μm line patterns along the black lines in the respective AFM picture.

Figure 10.7 shows the AFM data of the structures imprinted into molecular glasses **3a** (left) and **3b** (right) after removing the mold. Although both materials fill the cavities of the mold to a certain height, various cone- and diamond-shaped protrusions are superimposed

on the imprints of the line pattern. The reason for the inhomogeneous pattern formation is that molecular glasses **3a** and **3b** crystallize upon illumination. This is confirmed by the observation that the films become opaque at the illuminated spot, even if no mold is attached to them. Interestingly, this effect is not observed during holographic SRG inscription (cf. Chapter 9.3). Due to the growth of the crystallites, both compounds are not suited for Azo-NIL.

10.2.2 Azobenzene-Functionalized Trisamide-Based Compounds

Azobenzene-functionalized molecular glasses based on the trisamide core **2** represent another potential resist material for Azo-NIL. Both the reduced flexibility of the core and the intermolecular interaction of the amide moieties appear to stabilize the amorphous phase (cf. Chapter 5.1). Therefore, the crystallization tendency is expected to be significantly reduced for trisamide-based derivatives when they return from the photofluidic to the solid state.

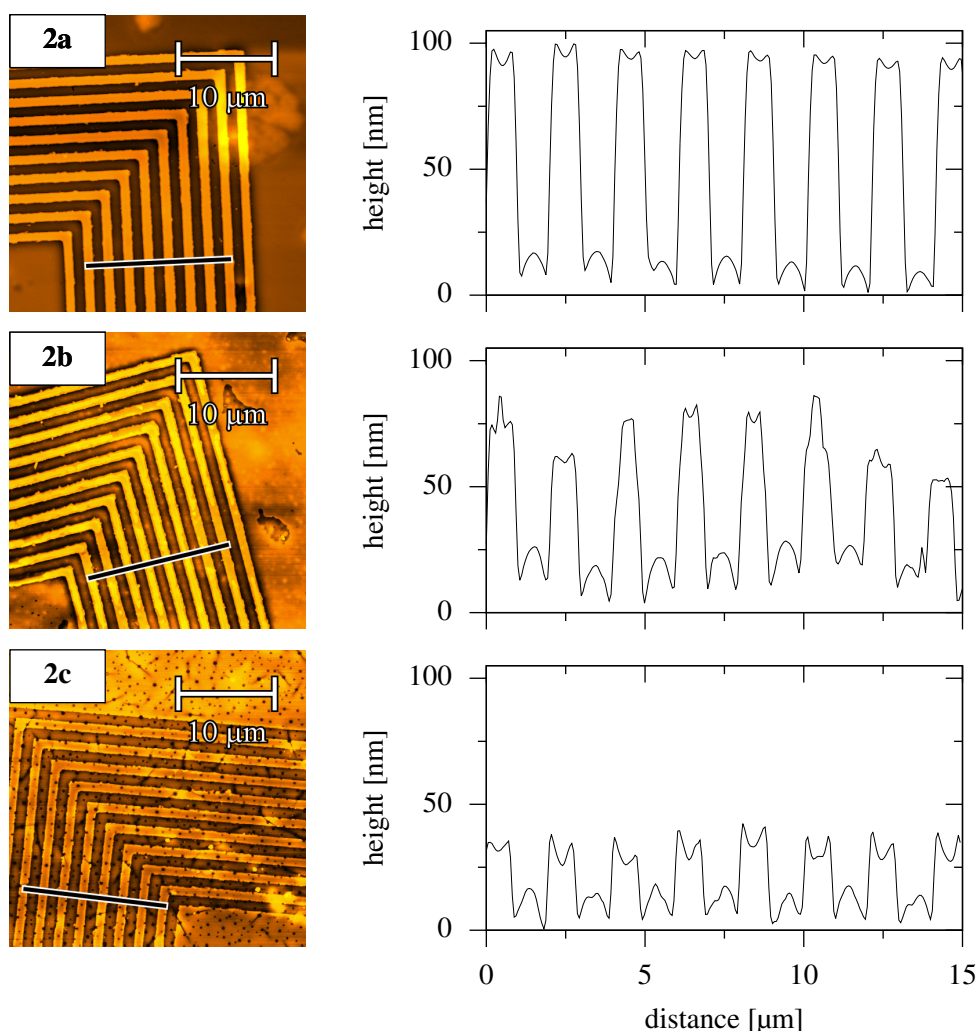


Figure 10.8: Structures imprinted into films of molecular glasses **2a** (top), **2b** (middle), and **2c** (bottom) with an Elastosil[®] 601 mold after 1200 s illumination with both LEDs. Left: False-color AFM images of the imprinted 1 μm line patterns. Right: Profiles of the 1 μm line patterns along the black lines in the respective AFM picture.

To test whether molecular glasses **2a-d** can be used for efficient, defect-free pattern transfer, molds were imprinted into films of each compound. The preparation of a 500 nm thick film was accomplished only with material **2b**, whereas the thicknesses of the films of **2a** and **2d** were 250 and 430 nm, respectively. In a first step, the attached molds were illuminated through the substrate with both LEDs for 1200 s. The functionalization of the azobenzene chromophores turns out to affect the quality of the imprints strongly. This is illustrated by the AFM images of the imprinted patterns (left) and the respective profile plots (right) in Fig. 10.8. The line patterns reach reasonable heights in compounds **2a** and **2b**. In the top right corner of the AFM image of molecular glass **2a**, a slight deformation is visible. It is attributed to inhomogeneities of the initial film surface. The overall quality of the imprint, however, is very high. For molecular glass **2b** the reproduction of the mold edges is less accurate than in **2a**. The profile plot of the imprinted pattern shows that the channels of the mold fill in an inhomogeneous manner. Furthermore, the meniscus shape of the rising photofluid is less pronounced in most cavities. This implies that the functionalization of the azobenzene moieties with CF_3 substituents changes the wetting behavior of the photofluid significantly. In molecular glass **2c**, the average imprint height is only about 25 nm. Moreover, several cracks and holes appear throughout the whole scanned area. AFM measurements show that the defects were present on the film surface already before imprinting. Since light scattering appears to be absent in films of molecular glass **2c** if viewed with the naked eye, this finding is rather unexpected. Homogenization of the film surface can probably be achieved by changing the substrate or adjusting spin-coating parameters such as the solvent type. However, both the imprinting speed and the maximum pattern height are too low to allow for efficient molding with molecular glass **2c**. Thus, no further effort has been put into the optimization of the film homogeneity. Molecular glass **2d** features C_7F_{13} -substituted azobenzene moieties. It could not be quenched into the amorphous state from solution, since it crystallized directly after spin coating (cf. Chapter 5.3). No structures could be imprinted into the crystallized film of compound **2d**.

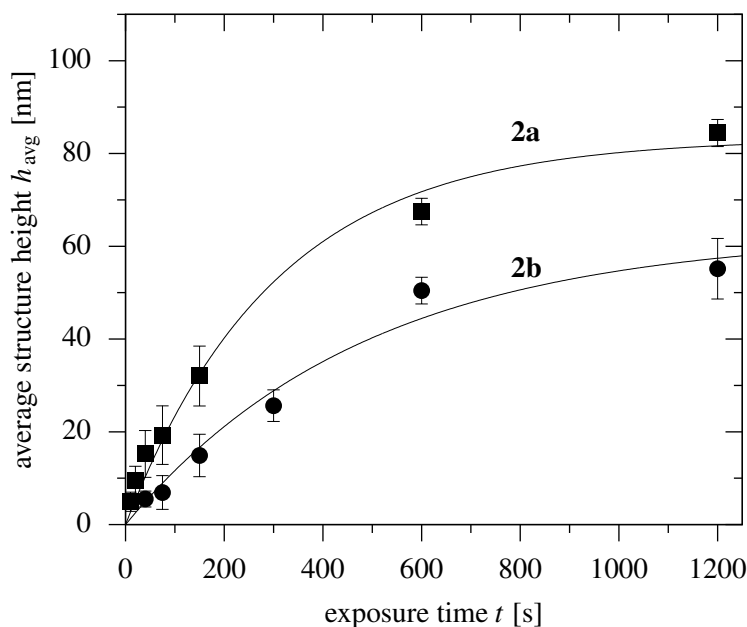


Figure 10.9: Average structure height h_{avg} as a function of the exposure time t for molecular glasses **2a** and **2b**. The azobenzene moieties in molecular glass **2b** have a trifluoromethyl substituent, whereas in **2a** the substituent is hydrogen.

Figure 10.9 shows the average structure height imprinted on the films of molecular glasses **2a** and **2b** as a function of the exposure time. As indicated by the black lines, h_{avg} follows an exponential function approaching the maximum height in both compounds. The fitted curves are obtained from inserting the values of h_0 and τ listed in Table 10.3 into Eq. (10.3). The results presented in Chapter 10.1.4 imply that the low thickness of compound **2a** affects both the build-up constant and the maximum imprint height. Yet, molecular glass **2a** is faster than **2b** and forms higher patterns. The build-up constants are 303 and 488 s, respectively. Both compounds do not reach the maximum possible pattern height of $h_{\text{m}} \approx 100$ nm determined by the mold (cf. Table 10.3). The maximum imprint height and the speed of pattern formation are expected to increase in molecular glass **2a** if it is prepared with higher initial thickness. The partial filling of the mold with molecular glass **2b** ($h_0 = 63$ nm), on the other hand, is attributed to the different wetting behavior of the resist material.

Table 10.3: Summary of the experimental data of the trisamide-based molecular glasses. d_0 : initial film thicknesses, h_0 : imprint height of the 1 μm line patterns for $t \rightarrow \infty$, τ : filling time constant of the 1 μm cavities according to Eq. (10.3).

material	d_0 [nm]	h_0 [nm]	τ [s]
2a	250	83	303
2b	500	63	488
2c	430	–	–

10.2.3 Azobenzene-Functionalized Spirobichromane-Based Compounds

Although crystallization is prevented successfully in the molecular glasses based on the trisamide core, their imprinting speed is rather low. Furthermore, the imprints lack high quality except for molecular glass **2a**. Azobenzene-functionalized spirobichromane-based derivatives do not feature additional amide moieties, but their core is more rigid than that of the triphenylamine-based compounds. Hence, molecular glasses **1a-e** are promising candidates for achieving faster patterning without photo-induced crystallization.

First, the effect of lengthening the perfluoroalkyl chains is investigated. Similar to the trisamide-based derivative **2d**, films of molecular glass **1d** with C_6F_{13} -substituted chromophores crystallized directly after spin coating. AFM measurements did not reveal any pattern formation for this compound, even after imprinting a mold for more than 1 h with both LEDs simultaneously. This implies that photofluidization is prevented in crystallized low-molecular-weight compounds.

To reduce the influence of small initial film thickness on the imprinting speed, films of molecular glass **1b** and **1c** were prepared with a thickness of at least 500 nm. For both compounds, the average structure height of the imprints increases with exposure time. It exponentially approaches a maximum height, similar as in the case of the films of molecular glass **1a** or the trisamide-based compounds. Figure 10.10 shows h_{avg} as a function of the exposure time (left side) and two AFM images of the L-shaped 1 μm patterns imprinted on films of molecular glasses **1b** and **1c** after 600 and 1200 s illumination, respectively. The red symbols in the left panel indicate the difference in height between the bright and dark areas. The dashed and solid lines correspond to the fit functions found for the data of the 505 nm thick film of **1a** (cf. Chapter 10.1.4) and the data of compounds **1b** and **1c**, respectively. The build-up constants and the maximum imprint heights determined by the fits as well as the exact values of the initial film thicknesses are summarized in Table 10.4.

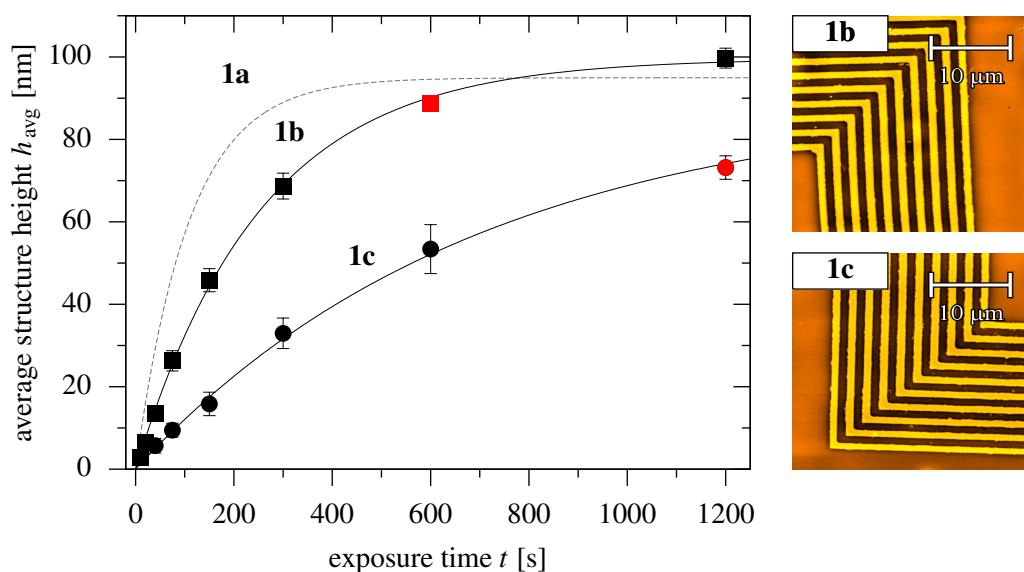


Figure 10.10: Left: Average structure height h_{avg} as a function of the exposure time t for molecular glasses **1b** and **1c**. For the sake of comparability, the fit function found for the 505 nm thick film of molecular glass **1a** is drawn as a dotted line (cf. Fig. 10.5). Right: False-color AFM images of two 1 μm line patterns imprinted into films of **1b** and **1c** after exposing them to both LEDs for 600 and 1200 s, respectively. The red symbols in the left panel indicate the imprint heights for these images.

The functionalization with perfluoroalkyl substituents affects the imprinting speed significantly. While τ has a value of 112 s in molecular glass **1a**, the build-up constant increases to 254 s for **1b**. Both materials differ from each other by the CF_3 substituent, which is linked to each azobenzene moiety of molecular glass **1b**. Lengthening of the perfluoroalkyl chains slows down the pattern formation even further. Thus, τ is as high as 696 s in compound **1c** with the C_3F_7 -substituted chromophores. In the Materials section in Chapter 5.1 it was shown that the $\pi \rightarrow \pi^*$ absorption of films of molecular glasses **1b-d** is shifted to the blue by about 15 nm with respect to compound **1a**. According to the results discussed in Chapter 10.1.3, a blue shift of the $\pi \rightarrow \pi^*$ absorption relative to the irradiation wavelength slows down the imprinting process. This explains the increase of τ in materials **1b** and **1c** only partially, however. No significant difference exists between the absorption spectra of molecular glass **1b** and **1c**. The decrease of the imprinting speed is most likely due to a different wetting behavior of the photofluidic molecular glasses in this case. For sufficiently long illumination times, the mold is filled completely with each of the materials **1a-c**. After one hour of exposure, 1 μm line patterns with $h_{\text{avg}} = 93 \text{ nm}$ were imprinted into the film of compound **1c** (data not shown in Fig. 10.10). For compound **1b**, complete filling of the mold took 1200 s. As illustrated by the AFM images on the right-hand side of Fig. 10.10, the patterns imprinted into molecular glasses **1b** and **1c** have the same quality as in **1a** (cf. Chapter 10.1.2).

To improve the imprinting speed, a possible approach is to change the resist material to an azobenzene-functionalized molecular glass with higher absorption near the peak emission wavelengths of the light sources. In molecular glass **1e**, the maximum of the $\pi \rightarrow \pi^*$ transition is shifted 20 nm to the red with respect to molecular glass **1a** (cf. Chapter 5.1.2). Other material properties such as molar weight or glass transition temperature are almost identical in both compounds, which is advantageous for direct comparison.

Table 10.4: Summary of the experimental data of the spirobichromane-based molecular glasses. d_0 : initial film thicknesses, h_0 : imprint height of the $1\ \mu\text{m}$ line patterns for $t \rightarrow \infty$, τ : filling time constant of the $1\ \mu\text{m}$ cavities according to Eq. (10.3).

material	d_0 [nm]	h_0 [nm]	τ [s]
1a	505	95	112
1b	625	100	254
1c	500	90	696
1e	560	102	62

The left-hand side of Fig. 10.11 depicts h_{avg} as a function of the exposure time for a film of molecular glass **1e** with an initial thickness of 560 nm. As indicated by the solid black line, the heights of the imprinted line patterns describe an exponential approach to $h_0 = 102\ \text{nm}$ according to Eq. (10.3). A list of the fit parameters is given in Table 10.4. The dashed line is the same as in Fig. 10.10 and illustrates the pattern growth in molecular glass **1a**. Complete filling of the mold with molecular glass **1e** requires approximately 300 s. The build-up time constant τ is 62 s, which is shorter by a factor of almost two as compared to **1a**. On the right-hand side of Fig. 10.11, the $1\ \mu\text{m}$ line pattern imprinted on the film of **1e** after 300 s is shown. The difference in height between the bright and dark areas in the AFM image is 102 nm. As in the previous cases, the line patterns transferred to the molecular glass film are free from defects.

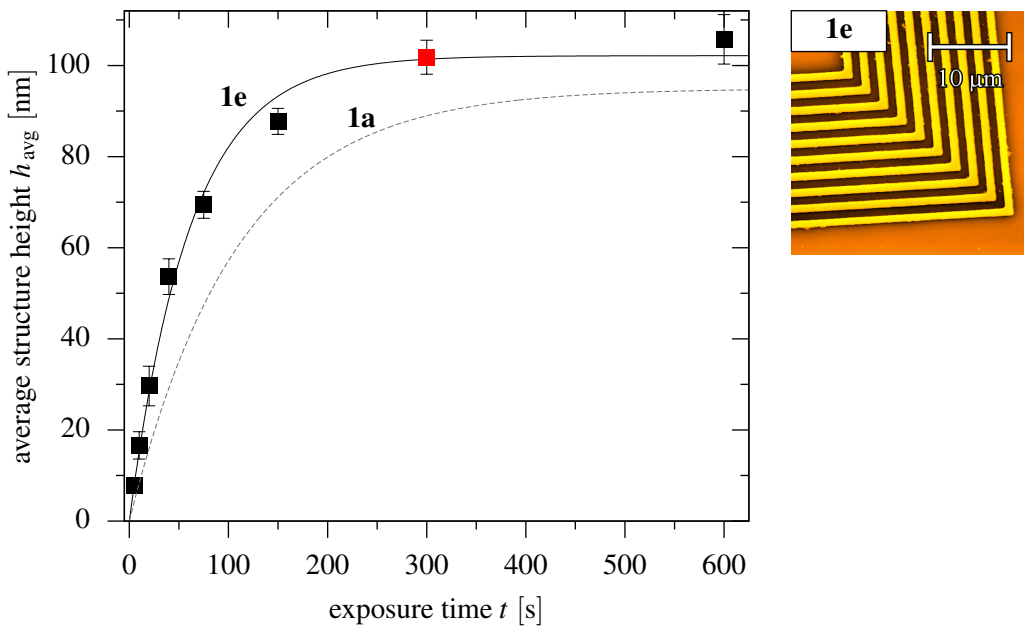


Figure 10.11: Left: Average structure height h_{avg} as a function of the exposure time t for molecular glass **1e**. For the sake of comparability, the fit function found for the 505 nm thick film of molecular glass **1a** is drawn as a dotted line (cf. Fig. 10.5). Right: False color AFM image of the $1\ \mu\text{m}$ line pattern imprinted into a film of molecular glass **1e** after exposing it to both LEDs for 300 s. The red filled square in the left panel indicates the average height of the depicted line pattern.

10.2.4 Azobenzene-Functionalized Homopolymer

In the past sections, the concept of Azo-NIL has been successfully applied to resists prepared from azobenzene-functionalized molecular glasses. A fundamentally different material is homopolymer **9 (ii)**. It is capable of forming SRGs of reasonable height during holographic illumination.^[40] In contrast to the molecular glasses, the photo-isomerizable units are covalently interconnected in the homopolymer by its backbone. The individual chains of homopolymer **9 (ii)** are expected to be entangled, given its rather high molar weight of $M = 3.75 \times 10^5 \text{ g mol}^{-1}$. Thus, it is possible that mass transport may be slowed down significantly. The purpose of the following experiments is to figure out, whether the capillary forces are sufficiently strong to overcome the restraints of the polymer network in the photofluidic state.

A film of homopolymer **9 (ii)** with 350 nm thickness was prepared on a glass slide by spin coating. Imprinting of the mold was performed with both LEDs simultaneously. The experimental procedure was identical to that applied to the molecular glasses. Figure 10.12 shows the AFM image of a 1 μm line pattern imprinted into homopolymer **9 (ii)** after 2400 s of illumination (left) and the respective profile plot (right) along the black marked line. Obviously, imprinting is possible in the homopolymer, similar as in the molecular glasses. The imprinted line pattern is defect-free and filling occurs homogeneously to a height of $h_{\text{avg}} \sim 75 \text{ nm}$.

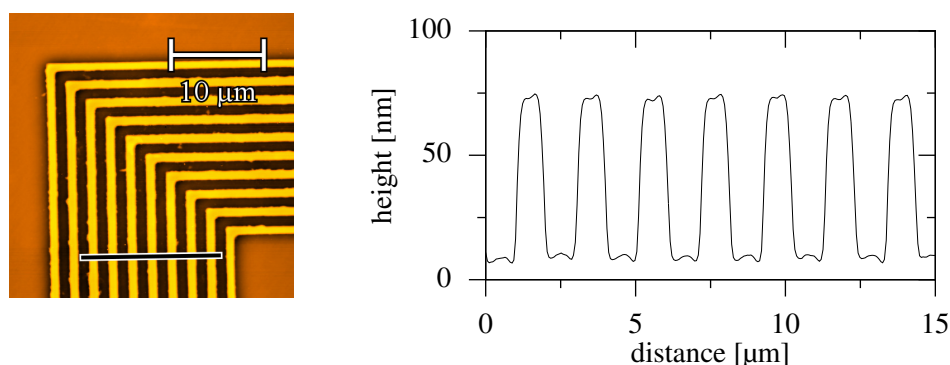


Figure 10.12: The left-hand panel shows a false-color AFM image of the 1 μm pattern imprinted into a film of homopolymer **9 (ii)** after 2400 s of illumination with both LEDs. The profile measured along the black line is plotted on the right.

The average structure height of the imprinted 1 μm patterns is plotted in Fig. 10.13 as a function of the exposure time. In contrast to the molecular glasses, a single-exponential function does not fit the data well. Instead, the empirical equation

$$h_{\text{avg}}(t) = h_0 \{1 - 0.5 \cdot [\exp(-t/\tau_1) + \exp(-t/\tau_2)]\} \quad (10.7)$$

can be applied to fit the data in Fig. 10.13. It comprises two equally weighted exponential terms. The fit yields the build-up time constants $\tau_1 = 56.7 \text{ s}$ and $\tau_2 = 851.3 \text{ s}$ and a maximum imprint height of $h_0 = 81 \text{ nm}$. It describes the temporal evolution of h_{avg} in homopolymer **9 (ii)** well. A possible interpretation of the origin of the second build-up constant is as follows. Due to the absence of entanglements in the molecular glasses, it is plausible that they show a simple viscous flow behavior in the photofluidic state. If the illuminated homopolymer **9 (ii)** is assumed to resemble a polymer melt, the presence of entanglements may result in a viscoelastic-flow behavior.^[56] Entangled, viscoelastic polymer melts can be described with the reptation model.^[231,232] Its key point is that the flow of polymers takes place

on two different time scales, since disentangling takes much longer than the deformation of the polymer chains. It must be stressed, however, that this model has not been tested for a complex system like a photofluidic homopolymer. Moreover, the information obtained from the imprint experiment is not sufficient to prove that reptation is the underlying mechanism which causes the existence of two build-up constants. Yet, this model provides a possible explanation for the difference between the imprinting behavior of homopolymer **9 (ii)** and the molecular glasses.

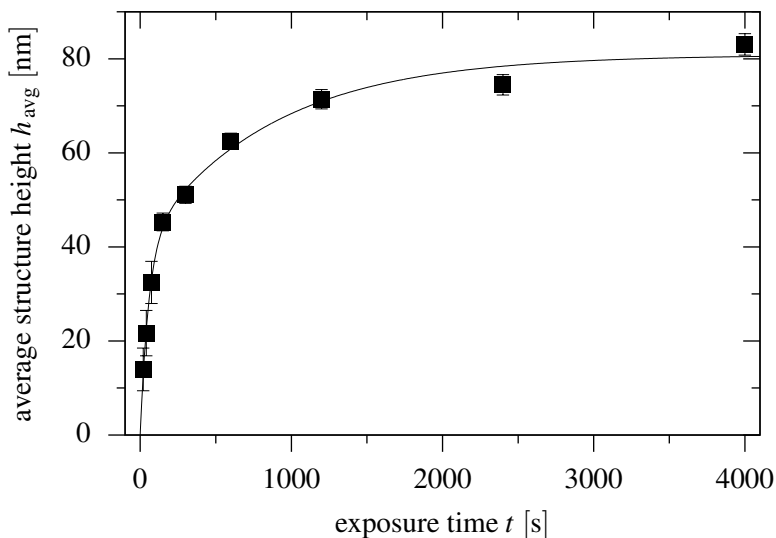


Figure 10.13: Average structure height h_{avg} as a function of the exposure time t for homopolymer **9 (ii)**. The solid line indicates a fit according to Eq. (10.7).

The initial resist thickness of the homopolymer film is very small, so both the filling speed and the maximum imprint height are expected to be reduced. In Chapter 10.1.4, a film of molecular glass **1a** with 360 nm thickness was investigated. The maximum imprint height of $h_0 = 86 \text{ nm}$ was reached after 600 s, the build-up constant being 1.5 times longer than that of a 505 nm thick film. Patterns imprinted into homopolymer **9 (ii)** reach a similar height, but require a significantly longer time ($\sim 1 \text{ h}$). Molecular glass **1e** is well suited for direct comparison with homopolymer **9 (ii)**, since both compounds have the same methoxy-functionalized azobenzene moieties. The build-up constant of the $1 \mu\text{m}$ line pattern in molecular glass **1e** is smaller than in **1a** by a factor of almost two (cf. Table 10.4 in Chapter 10.2.3). Thus, the reduced filling speed becomes even more pronounced in the homopolymer.

10.3 Nanostructuring of Azobenzene-Functionalized Spirobichromane-Based Molecular Glasses

The result of the preceding chapters are essential to efficiently imprint molds with features on the nanometer scale. Spirobichromane-based molecular glasses turned out to be the most promising resist materials for this purpose. Micrometer-sized line patterns imprinted into them are reproduced with high quality and the speed of pattern formation is reasonably high. Furthermore, they do not crystallize upon illumination.

Due to these advantages, spirobichromane-based molecular glasses were used as resist material in the following imprint experiments. Both Elastosil[®] 601 and EVG[®] molds with nanometer-sized punches and line cavities were imprinted into the molecular glass films. Elastosil[®] 601 molds were produced with curing procedure **P1** (cf. Chapter 6.2.2). Illumination of the attached molds was performed in the Azo-NIL setup for vertical sample alignment with both LEDs simultaneously. To avoid limitations of the imprinting speed by the initial film thickness, films were prepared with thicknesses of at least 500 nm. The experiments were conducted at room temperature.

10.3.1 Influence of Mold Material and External Pressure

The formation speed and the quality of nanopatterns imprinted into molecular glass **1a** with molds consisting of either Elastosil[®] 601 or EVG[®] polymer were investigated first. According to Chapter 6.2.2, the line protrusions of the molds prepared from Elastosil[®] 601 collapse laterally for cavity widths as small as 100 nm. For this reason, such molds cannot be used to imprint 100 nm line patterns without Y-branched defects. Yet, the flexible Elastosil[®] 601 polymer perfectly adapts to the molecular glass film due to its good adhesive properties and its low Young's modulus. The good conformal contact of the Elastosil[®] 601 molds with the photofluidizable resist is expected to allow for homogenous reproduction of any other pattern of the master.

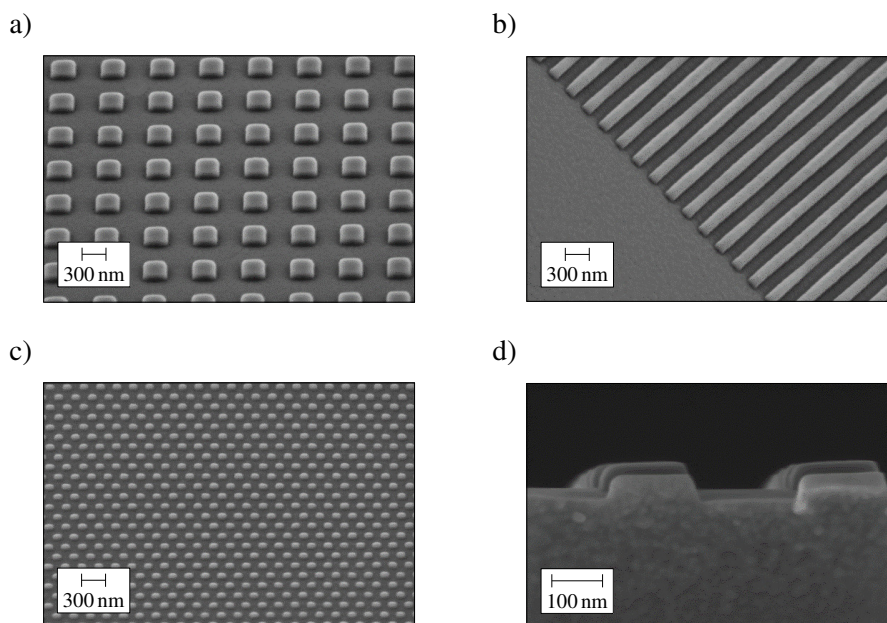


Figure 10.14: SEM images of diverse pattern types imprinted into molecular glass **1a** with an Elastosil[®] 601 mold. The depicted pattern types are a) 300 nm orthogonally arranged pillars, b) 150 nm lines, c) 100 nm hexagonally arranged pillars, and d) 150 nm orthogonally arranged pillars (cross-sectional image). The ratio between w and s is 1:1 for all pattern types (type I mold).

Figure 10.14 shows SEM images of different patterns imprinted on a film of molecular glass **1a** with an Elastosil[®] 601 mold after 600 s exposure with both LEDs. The initial film thickness was 500 nm. A type I mold was used for imprinting. Thus, the ratio between w and s is 1:1 for all pictures. Figure 10.14 a), b), and c) depict 300 nm orthogonally arranged pillars, 150 nm lines, and 100 nm hexagonally arranged pillars, respectively. The images show a representative subset of the nine pattern types present on the imprint. Homogeneous, defect-free pattern transfer is achieved for all three templates even without further functionalization of the mold or the resist material. The cross-sectional SEM image of Fig. 10.14 d) demonstrates that molecular glass **1a** is homogenous in the bulk below and inside the imprinted pillars. No signs of a boundary layer or crystallization are visible. As indicated by the scale bar, the pattern height is about 50 nm. The edges of the imprinted patterns are rounded because the Elastosil[®] 601 mold deforms as soon as it is released from the master (cf. Chapter 6.2.2).

The heights of the lines and pillars imprinted on molecular glass **1a** with an Elastosil[®] 601 mold were further measured as a function of the exposure time. For this purpose, a type II mold ($w : s = 1 : 2$) and a film with an initial thickness of 550 nm were used. The heights of the transferred structures were determined by AFM. Figure 10.15 shows the data of the 300 and 150 nm line patterns. Similar as in the case of the L-shaped micrometer patterns, h_{avg} exponentially approaches a maximum height. The black solid lines correspond to Eq. (10.3) with the fit parameters listed in Table 10.6. Since the imprinted lines are very regular and have a similar height, the error bars are small. Imprinting of laterally collapsed 100 nm line patterns is possible; then the patterns generated on the molecular glass film have the same Y-branched defects as the mold. The heights determined for this pattern type are not very informative, so they are not shown. Mold patterns with the same periodicity fill with almost identical speed. This applies only to the line and punch cavities with $w = 150$ and 300 nm, however. For structures as small as 100 nm, only orthogonally and hexagonally arranged punches fill with a similar speed, whereas the laterally collapsed line cavities fill faster.

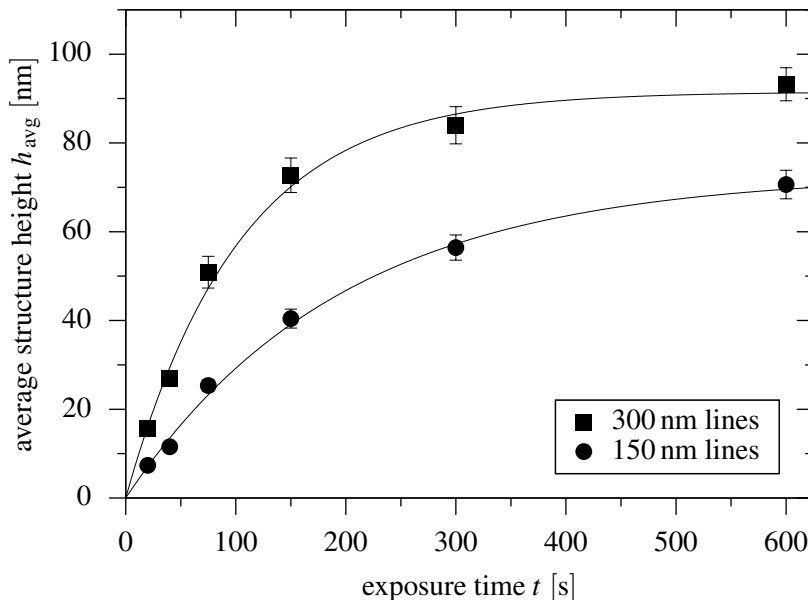
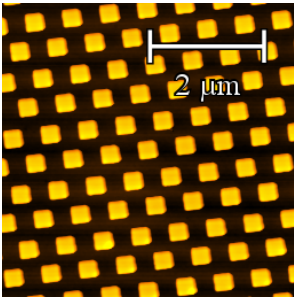
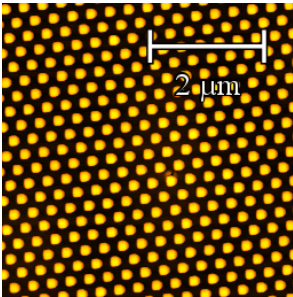
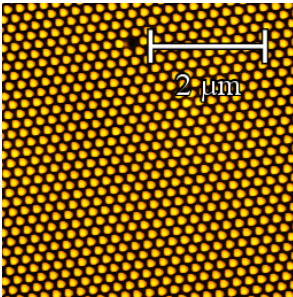
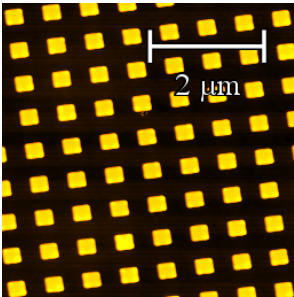
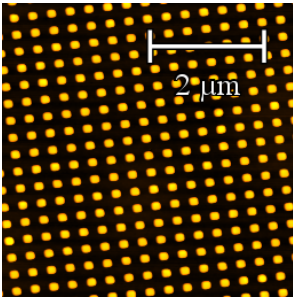
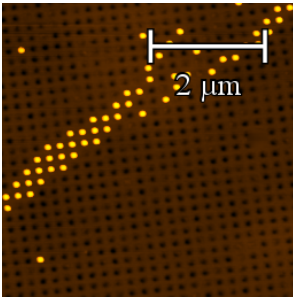
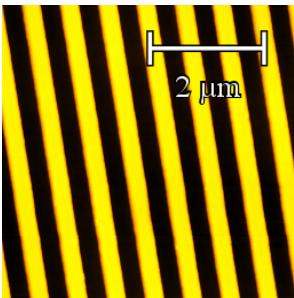
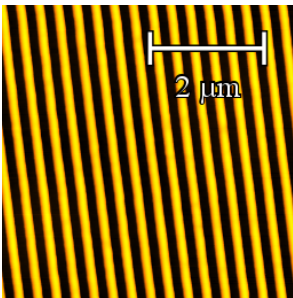
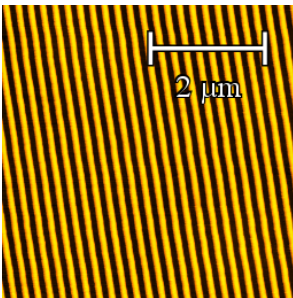


Figure 10.15: Average height h_{avg} of the 150 and 300 nm line patterns imprinted on a film of molecular glass **1a** as a function of the exposure time t . An Elastosil[®] 601 mold (type II) was used for imprinting. No external pressure was applied.

A build-up constant of 103 s and a maximum imprint height of 92 nm was determined for the 300 nm line patterns. In the case of the 150 nm line patterns τ increased to 195 s and a maximum height of 73 nm was reached. The height of the structures on the mold is approximately 100 nm in both cases. This implies that cavities with $w < 300$ nm do not fill completely, even for long exposure times. Hence, Elastosil[®] 601 molds are not suited to imprint patterns with significant aspect ratios ($h_m \gtrsim s + w$). This is not surprising, since they suffer from different deformation mechanisms (cf. Chapter 6.2). Furthermore, the build-up constants depend on the cavity width w , which is discussed in the next Chapter.

Table 10.5: False-color AFM images of nine different patterns imprinted on a film of molecular glass **1a** with an EVG[®] mold after 600 s illumination. The imprint features lines as well as orthogonally and hexagonally arranged pillars with $w = s = 300, 150,$ and 100 nm. Dark areas indicate lower regions, whereas the yellow, bright areas represent elevated regions. The average difference in height between them is given below each image. No external pressure was applied.

	w/s			
300 nm / 300 nm	150 nm / 150 nm	100 nm / 100 nm		pattern
				hexagonal pattern of pillars
				orthogonal pattern of pillars
				lines

The above results show that EVG[®] molds are required to imprint elongated structures if their width becomes as small as 100 nm. Due to the decreased surface energy and the high Young's modulus of the EVG[®] polymer, however, adhesion is barely sufficient to keep an EVG[®] mold and an azobenzene-functionalized resist in conformal contact. Yet, the capillary

forces are strong enough to partially fill the cavities of the mold with the molecular glass once it is in the photofluidic state. This is illustrated by the AFM images in Table 10.5. The patterns were imprinted into a film of molecular glass **1a** after illuminating an attached EVG[®] mold (type I) with both LEDs for 600 s through the substrate. The thickness of the film was 570 nm and no external pressure was applied to the mold. Except for the orthogonal 100 nm pillars, all patterns were reproduced homogeneously and without major defects over a large area. The pillars are prone to ripping, since they are completely surrounded by the stiff EVG[®] polymer during mold release. The images show that the orthogonal arrangement is affected more strongly than the hexagonal one. The missing conformal contact between mold and resist becomes apparent in the heights of the imprinted structures which range from 50 to 85 nm. As discussed below, cavities with constant w fill with similar speed if the mold is in conformal contact with the resist. This is only fulfilled for the 100 nm structures here.

A small external pressure can be applied to the EVG[®] mold to ensure that each of its nine different fields is in uniform contact with the molecular-glass film. To investigate the influence of externally applied pressure on the quality of the imprints and the speed of cavity filling, the following experiments were carried out. First, the above imprinting procedure was repeated for different exposure times, i. e., the EVG[®] mold was attached to the molecular glass film by adhesion without externally applied pressure ($p_{\text{mag}} = 0$). Both film and mold were identical to those discussed in the previous paragraph. The heights of the 100 nm lines and pillars imprinted into the molecular glass were determined by AFM. Subsequently, a fresh EVG[®] mold (type II) was imprinted into a different film of molecular glass **1a**. At the same time, a magnet exerted a pressure of $p_{\text{mag}} = 0.34$ bar onto the mold as described in Chapter 7.2. Here, the thickness of the molecular glass film was 560 nm. The heights of all nine pattern types imprinted into the azobenzene-functionalized resist after different exposure times were measured by AFM. To quantify the heights of the imprinted patterns, the parameter \tilde{h}_{avg} is used. It is defined as the average of the heights measured for each of the three different pattern types under the condition that w is constant. Thus, \tilde{h}_{avg} is calculated as $\tilde{h}_{\text{avg}} = \frac{1}{3}(h_{\text{avg, lines}} + h_{\text{avg, orth. pillars}} + h_{\text{avg, hex. pillars}})$ for $w = 300, 150,$ and 100 nm.

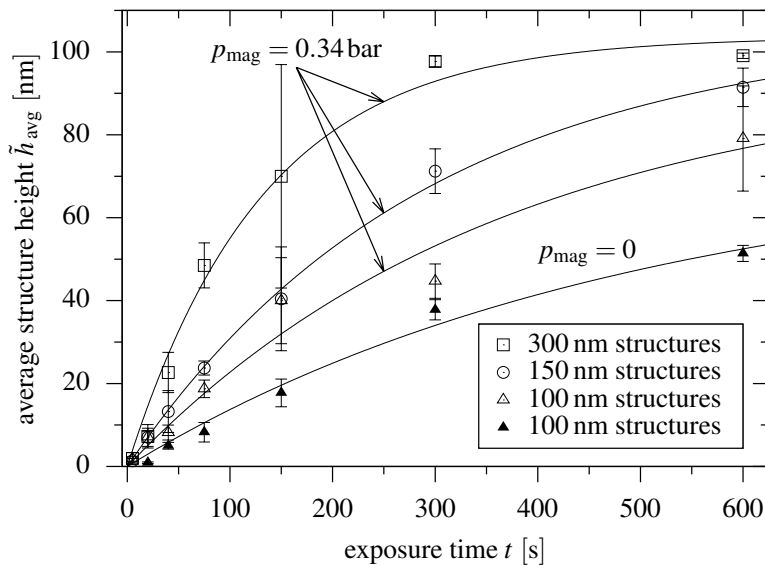


Figure 10.16: Average height \tilde{h}_{avg} of the 100, 150, and 300 nm structures imprinted on films of molecular glass **1a** as a function of the exposure time t . Imprinting was performed with either an EVG[®] mold (type I) and $p_{\text{mag}} = 0$ (filled triangles) or an EVG[®] mold (type II) and $p_{\text{mag}} = 0.34$ bar (open symbols). p_{mag} denotes the mechanical pressure exerted by a small magnet.

The heights of the structures imprinted with $p_{\text{mag}} = 0$ (filled triangles) and $p_{\text{mag}} = 0.34$ bar (open symbols) are plotted as a function of the exposure time in Fig. 10.16. Independent of the applied pressure, \tilde{h}_{avg} follows an exponential function tending to a maximum height for all data sets. The build-up time constant of the 100 nm structures imprinted without externally applied pressure is 491 s and the fitted black line predicts a maximum structure height of 74 nm (cf. Table 10.6). Here, the 100 nm cavities of the EVG[®] mold do not fill completely, even for exposure times significantly longer than 600 s. The build-up time constants of the 300, 150, and 100 nm structures imprinted with $p_{\text{mag}} = 0.34$ bar are 132, 290, and 368 s, respectively. τ increases with decreasing w if the EVG[®] mold is in conformal contact with the molecular-glass resist. Furthermore, the fits predict all cavities of the mold to fill completely (cf. Table 10.6). Imprinting with externally applied pressure also slightly increases the filling speed of the mold cavities. Since the time constants of the 100 nm structures with and without applied pressure differ only by a factor of 0.75, the average pressure exerted solely by adhesion must be comparable to the value of the externally applied pressure.

Table 10.6: Summary of the experimental data of the nanostructures imprinted into molecular glass **1a** with Elastosil[®] 601 and EVG[®] molds. d_0 : initial film thickness, p_{mag} : externally applied pressure, w : width of the mold cavities, s : spacing between the mold cavities, h_0 : imprint height of the patterns for $t \rightarrow \infty$, τ : filling time constant of the cavities according to Eq. (10.3).

mold material	d_0 [nm]	p_{mag} [bar]	w [nm]	s [nm]	h_0 [nm]	τ [s]
Elastosil [®] 601	550	0	300	600	92	103
Elastosil [®] 601	550	0	150	300	73	195
EVG [®]	570	0	100	100	74	491
EVG [®]	560	0.34	300	600	104	132
EVG [®]	560	0.34	150	300	106	290
EVG [®]	560	0.34	100	200	95	368

The error margin of each data point is the standard deviation of the three height values used to calculate \tilde{h}_{avg} . Consequently, the error bars are a measure of the height variations between differently shaped structures with similar dimensions. If no external pressure is applied to the EVG[®] mold, the errors are quite small. Thus, pillars and line patterns with $w = 100$ nm are imprinted homogeneously with the same filling speed. In the experiments with externally applied pressure, the values of \tilde{h}_{avg} differ more strongly from each other. Apart from the data at 150 s, however, the errors are still comparable to those of the 100 nm patterns imprinted with $p_{\text{mag}} = 0$. This indicates that different cavity types with identical w fill with similar speed if the mold is in conformal contact with the molecular-glass film.

To summarize, both Elastosil[®] 601 and EVG[®] molds have advantages and disadvantages. The Elastosil[®] 601 molds are more flexible and, thus, the imprinted patterns are not torn off easily when the mold is released from the resist. Furthermore, they establish good conformal contact with the resist, which also compensates for rough surfaces of the resist. A major drawback is that Elastosil[®] 601 molds collapse laterally and, thus, are not suited for imprinting line-type structures as small as 100 nm. This problem can be avoided by preparing the molds from the considerably stiffer EVG[®] polymer instead. The conformal contact between azobenzene-functionalized resist and EVG[®] mold is reduced to a critical level, however, such that additional pressure is required to restore it. Also, the increased stiffness of the mold causes pillar-type structures to be ripped from the resist more easily during lift-off.

10.3.2 Influence of the Size of the Mold Cavities on the Filling Speed

In the preceding chapter it has been shown that the filling speed of the mold cavities decreases when w is reduced from 300 nm to 100 nm. This result, for the line patterns, has already been published by our group.^[79] The relevant experiment was conducted with an EVG[®] mold (type II) which was imprinted on a 625 nm thick film of molecular glass **1a** with applied pressure ($p_{\text{mag}} = 0.34$ bar). Thus, the imprinting procedure was identical to that described in the previous chapter. The build-up time constants in reference [79], however, are 48 s for the 300 nm line patterns, 103 s for the 150 nm line patterns, and 176 s for the 100 nm line patterns. They are significantly shorter than the values of τ listed in Table 10.6 for the EVG[®] molds with applied pressure but they also increase with decreasing w . Since the more recent results show less scatter and take all nine pattern types into account, they are assumed to be more accurate.

The time constants found in the different experiments are plotted in Fig. 10.17 as a function of the cavity width w . Data obtained from imprinting EVG[®] molds with $p_{\text{mag}} = 0.34$ bar are indicated by filled symbols, whereas open symbols show the time constants for Elastosil[®] 601 molds without externally applied pressure. Filled squares and open circles denote the τ values listed in Table 10.6. The data of reference [79] are marked by filled triangles. A double-logarithmic plot is used to determine, whether τ can be described by a power law. The dashed, straight lines represent a function of the type $\tau = C \cdot w^{-1}$, which has only one free parameter (the prefactor C). Since they reproduce each individual data set well, it follows that $\tau \propto w^{-1}$. The filled triangles have a slightly steeper slope, but the deviations from the inverse proportionality between τ and w are small. For comparison, the build-up time constant determined in the imprinting experiments on the micrometer scale for the 505 nm thick film of molecular glass **1a** (cf. Chapter 10.1.4) is plotted in Fig. 10.17 as well. Obviously, $\tau \propto w^{-1}$ is only valid for lateral cavity dimensions significantly below 1 μm .

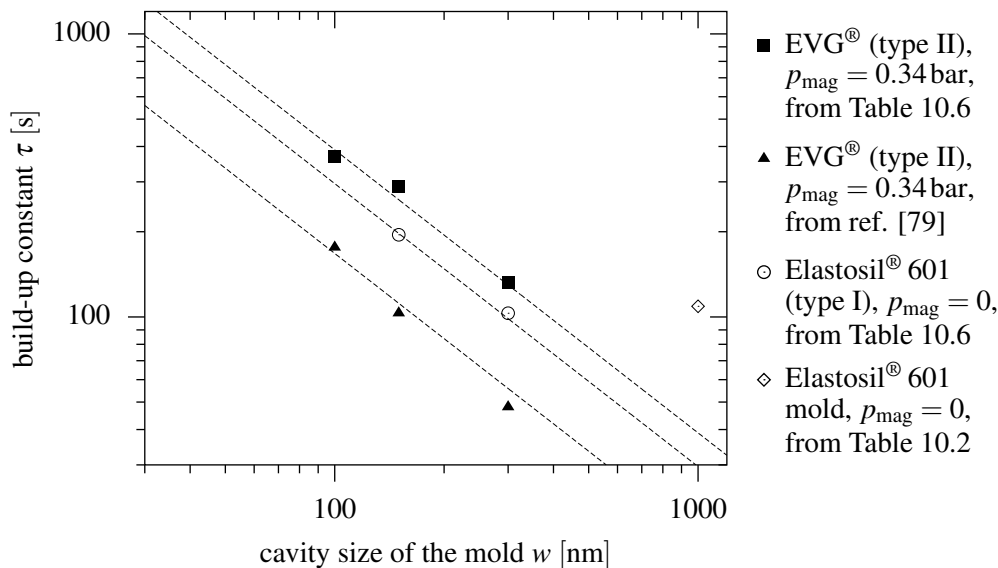


Figure 10.17: Build-up time constant τ as a function of the size of the mold cavity w under different experimental conditions. The mold material and type, the externally applied pressure, and the data source are indicated on the right side. Each dashed line represents a power law of the form $\tau \propto w^{-1}$. The plot is double-logarithmic.

For $w \leq 300$ nm, the mold material and the applied pressure affect only the relative offset of the data sets but not their slope. This indicates that the inverse proportionality of τ and w seems to be a universal property which results from the dimensions of the mold cavities. Another universal property is the exponential approach of the structure height to a maximum value. It occurs in all experiments with molecular glasses, independent of the initial film thickness, the dimensions of the mold structures, or the mold material. Both observations can be combined to explain the filling behavior of the molds in Azo-NIL experiments. The following discussion specifically applies to line patterns. The fundamental points are expected to be true for punch cavities as well, however, because they showed a similar filling behavior in the preceding experiments.

According to Chapter 10.1.4, the Stefan equation reads $t_f = (v \eta_0 s^2 h_m) / p d_0^3$ for a completely immersed mold if $h_m \ll d_0$. For short exposure times, the molds are filled only partially and the photofluid in the cavities is not affected by the presence of the roofs. Under the assumption that the imprinted pattern has a step profile, h_m can be replaced by h_{avg} in the above equation. This implies that $h_{\text{avg}}(t_f) \propto t_f / (v s^2)$ for $t \rightarrow 0$. The temporal evolution of the filling height found in the experiments is given by Eq. (10.3), which yields $h_{\text{avg}}(t) \propto (1 - \exp(-t/\tau)) \approx t/\tau$ for $t \rightarrow 0$. Thus, the initial growth of the structures is linear, as predicted by the Stefan equation. However, smaller mold protrusions or cavities do not result in reduced filling times, which follows from $t_f \propto v s^2 = w s^2 / (w + s)$ (without loss of generality w and s can be set equal so that $v s^2 = w^2 / 2 = s^2 / 2$). Heyderman et al. proposed that s^2 should be replaced by the unpatterned border area of the mold.^[169] Still, this does not account for the increased filling time of the smaller cavities. The model of Oliva and Joye (cf. Chapter 4.3), on the other hand, suggests that $h_{\text{avg}}(t)^2 \propto t w$. Here, the approximation $h_{\text{min}} \approx h_{\text{avg}}$ is made, which is roughly fulfilled as soon as the photofluid reaches a certain height in the mold cavities. Since the derivation of the above relation is based on the assumption that the same flow profile develops inside each cavity of the mold, it predicts that the filling of smaller cavities require a longer time. More precisely, for a given fill height t is inversely proportional to w and, therefore, it increases with decreasing channel size, as indicated by Fig. 10.17. However, the model also claims $h_{\text{avg}} \propto \sqrt{t}$, which is at odds with the initial linear decrease of h_{avg} experimentally found for short exposure times.

It can be concluded that characteristics of both models appear for cavity widths below 300 nm. This is not surprising since, according to the classification of Cross,^[168] the dimensions of the mold parameters h_m , w , and s are such that the flow takes the character of both lateral cavity filling and capillary filling (cf. Chapter 4.3). The above results imply that lateral cavity filling is the dominating mechanism initially. Once the photofluid reaches a certain height in the mold cavities, it begins to feel the constraints of the surrounding mold material. Hence, capillary filling superimposes the lateral filling and eventually becomes dominant at longer imprinting times. Finally, when the photofluidic resist reaches the roof of the mold, the material transport is terminated abruptly.

10.3.3 Influence of the Substituent of the Azobenzene Chromophores on the Imprint Quality

The nanostructures discussed so far have been imprinted into films of molecular glass **1a**. In Chapter 10.2.3 it was demonstrated that high-quality patterns with features on the micrometer scale can be transferred to films of molecular glasses **1b**, **1c**, and **1e** as well. To investigate their suitability as resist materials for the production of nanometer-sized structures, EVG[®] molds were imprinted on each of the three compounds with externally applied

pressure ($p_{\text{mag}} = 0.34 \text{ bar}$). The quality of the imprints is discussed for the example of the 100 nm orthogonally arranged pillars.

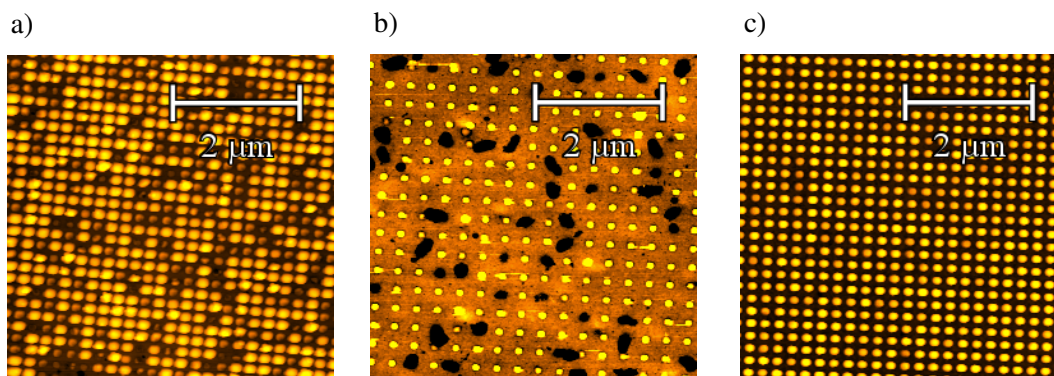


Figure 10.18: False-color AFM images of the orthogonal pillar-type patterns imprinted on molecular glasses **1b**, **1c**, and **1e** with an EVG[®] mold and externally applied pressure ($p_{\text{mag}} = 0.34 \text{ bar}$). a) Pillars imprinted with a type I mold on a 520 nm thick film of molecular glass **1b** after 1 h exposure. b) Pillars imprinted with a type II mold on a 430 nm thick film of molecular glass **1c** after 1 h exposure. c) Pillars imprinted with a type I mold on a 550 nm thick film of molecular glass **1e** after 600 s exposure. The heights of the yellow bright spots are a) $\approx 74 \text{ nm}$, b) $\approx 15 \text{ nm}$, and c) $\approx 64 \text{ nm}$.

Figure 10.18 a) shows an AFM image of the pillars imprinted into a 520 nm thick film of molecular glass **1b** with a type I mold. The pillars emerge very irregularly and an exposure time of 1 h is required to imprint protrusions with an average height of 74 nm. At several places the punch cavities of the mold remain almost unfilled, which causes the dark spaces between the pillars in the AFM image. As illustrated in Fig. 10.18 b), the imprint quality further decreases if molecular glass **1c** is used as resist material. The film thickness was 430 nm and a type II mold was used. Various defects are superimposed on the orthogonal pillar lattice and the height of the protrusions is only 15 nm after 1 h of illumination. The elliptical indentations (black areas) appear wherever the mold plane has been in contact with the resist. They do not originate from pillars which were ripped from the film surface. To avoid sticking of the resist material to the mold, the azobenzene chromophores in compounds **1b** and **1c** are functionalized with CF_3 and C_3F_7 end groups. For the same reason, the EVG[®] polymer is functionalized with fluorine. Functionalization of both the resist and the mold, however, seems to decrease the adhesion to a critical level such that the filling of the cavities is impeded. A long exposure time is required to imprint nanometer-sized structures of reasonable height, and numerous defects occur. Thus, molecular glasses **1b** and **1c** do not provide advantages as compared to **1a**.

The orthogonally arranged pillars imprinted in a 550 nm thick film of molecular glass **1e** with a type I mold after 600 s exposure are shown in Fig. 10.18 c). The depicted pillars have a height of $64 \pm 9 \text{ nm}$ and the scanned area is free from release-induced defects. As in the case of molecular glass **1a**, however, pillars were torn off sporadically when the experiment was repeated at different positions on the film. This indicates that the protrusions were not ripped off because of strong adhesion between the resist and the mold but rather due to mechanical stress during the detachment of the mold. In Chapter 10.2.3 it was shown that the L-shaped line cavities of Elastosil[®] 601 molds with $w = 1 \mu\text{m}$ fill most rapidly if molecular glass **1e** is used as resist material. Hence, **1e** is expected to fill the nanometer-sized punch and line cavities of the EVG[®] mold similarly well. To check this, the above experiment was repeated with different exposure times and the heights of the imprinted 300

and 100 nm patterns (lines and pillars) were determined by AFM. The 150 nm patterns have been omitted here. From the AFM data, \tilde{h}_{avg} was calculated as described in Chapter 10.3.1. The respective values are plotted in Fig. 10.19 as a function of the exposure time. The solid, black lines indicate an exponential approach to a maximum height. They correspond to Eq. (10.3) with the fit parameters listed in Table 10.7.

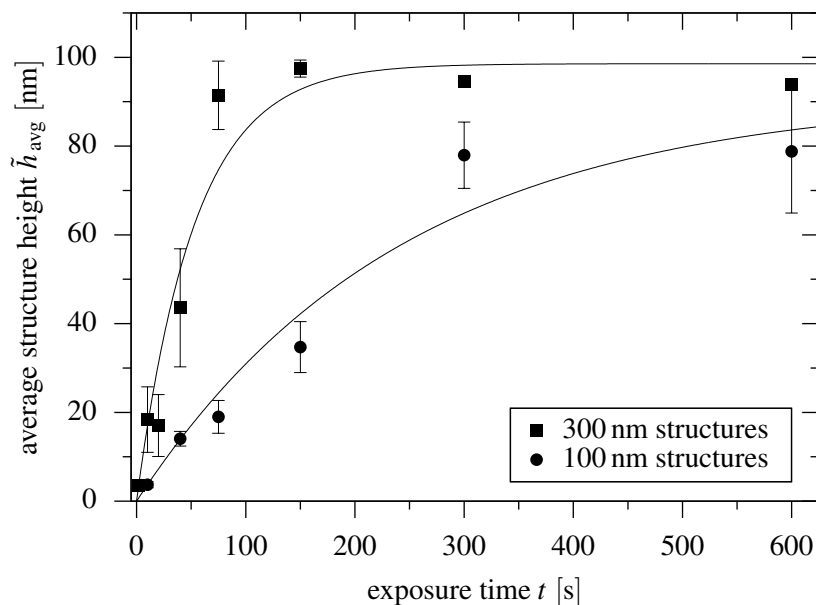


Figure 10.19: Average height \tilde{h}_{avg} of the 100 and 300 nm structures imprinted into a film of molecular glass **1e** as a function of the exposure time t . Imprinting was performed with an EVG[®] mold (type I) and $p_{\text{mag}} = 0.34$ bar.

The build-up time constant is 53 s for the 300 nm structures and 242 s for the 100 nm structures. These times are significantly shorter than for molecular glass **1a**. The comparison with Table 10.6 shows that the use of molecular glass **1e** as resist material improves the filling speed by a factor of two on average. This factor is equal to that found for the filling of the micrometer cavities in Chapter 10.2.3. The fits plotted in Fig. 10.19 predict that both the 300 nm and the 100 nm mold cavities fill almost completely (cf. Table 10.7). Furthermore, line and punch cavities of equal w fill with a similar speed. Like in Chapter 10.2.3, the error bars indicate the standard deviation of the three height values used to calculate \tilde{h}_{avg} . The filling time τ increases with decreasing w as in the case of the patterns imprinted into molecular glass **1a**.

Table 10.7: Summary of the experimental data of the nanostructures imprinted into molecular glass **1e** with an EVG[®] mold (type I). d_0 : initial film thickness, p_{mag} : externally applied pressure, w : width of the mold cavities, s : spacing between the mold cavities, h_0 : imprint height of the patterns for $t \rightarrow \infty$, τ : filling time constant of the cavities according to Eq. (10.3).

mold material	d_0 [nm]	p_{mag} [bar]	w [nm]	s [nm]	h_0 [nm]	τ [s]
EVG [®]	550	0.34	300	300	99	53
EVG [®]	550	0.34	100	100	91	242

10.4 Imprinting at Elevated Temperatures

The next approach is to heat films of compounds **1a** and **1e** to a temperature several degrees below their T_g , at which they are still amorphous when stored in the dark. To imprint a mold into the preheated azobenzene-functionalized materials, they must again be photofluidized with a suitable light source like in the previous experiments. The thermal barriers for the isomerization events of the azobenzene chromophores, however, are considerably lower than at room temperature. Hence, filling of the mold cavities is expected to occur faster at elevated temperatures.

To preclude that a thermal decrease of the viscosity causes sinking of the mold in the absence of light, the following experiment was carried out. A film of molecular glass **1a** was heated to a temperature of 88 °C, which is 20 °C below its T_g (cf. Table 5.1.2). Subsequently, an Elastosil[®] 601 mold with L-shaped protrusions was attached to it for 600 s. During this time, the film was exposed to ambient light only. After removing the mold, the contact area was investigated. AFM measurements showed that no patterns were transferred to the molecular-glass film by this procedure. The same result was obtained when the experiment was repeated at a temperature of $T = T_g = 108$ °C. When the film was heated to 128 °C, 1 μm line protrusions of 80 nm height emerged within 10 s. Cavities with $w \geq 5 \mu\text{m}$ filled only partially, as is the case for an athermally photofluidized resist (cf. Chapter 10.1.2). The important result is that the mold did not fill at resist temperatures $T \leq T_g$, since the molecular glass is not in the photofluidic state at ambient-light conditions,

Experiments at elevated temperatures were performed with the Azo-NIL setup for horizontal sample alignment. First, an Elastosil[®] 601 mold with L-shaped protrusions on the micrometer scale was imprinted into a film of molecular glass **1a**. After attaching the mold at room temperature, the film was heated on the hot stage to 98 °C. This temperature is 10 °C below the T_g of compound **1a**. Before illuminating the mold with both LEDs, the temperature of the resist was allowed to stabilize for at least 10 min. Since Elastosil[®] 601 molds make good conformal contact with spirobichromane-based derivatives, no external pressure was applied. The mold was released once the exposure was finished and the resist had cooled back to room temperature. The above procedure was repeated at different positions on the film for illumination times ranging from 1 to 150 s. In a second step, the experiment was repeated with a film of molecular glass **1e** at a processing temperature of 97 °C, which is also 10 °C below the T_g of the molecular glass. Finally, the average structure heights of the 1 μm patterns imprinted into both films were measured by AFM.

Figure 10.20 shows h_{avg} as a function of the exposure time t for both compounds. The black, solid lines indicate exponential fits (Eq. (10.3)) with the parameters listed in Table 10.8. The build-up time constants are 15.2 s for compound **1a** (filled squares) and 9.5 s for compound **1e** (filled circles), respectively. As compared to the experiments conducted at room temperature, the filling time decreases by a factor of approximately seven for both materials. After only 1 s of illumination, the structures imprinted on both molecular glasses reach a height of over 10 nm. The 1 μm cavities of the Elastosil[®] 601 mold fill completely such that $h_{\text{avg}} \sim 100$ nm for exposure times even below 75 s. The L-shaped imprints have the same quality as the ones produced at room temperature.

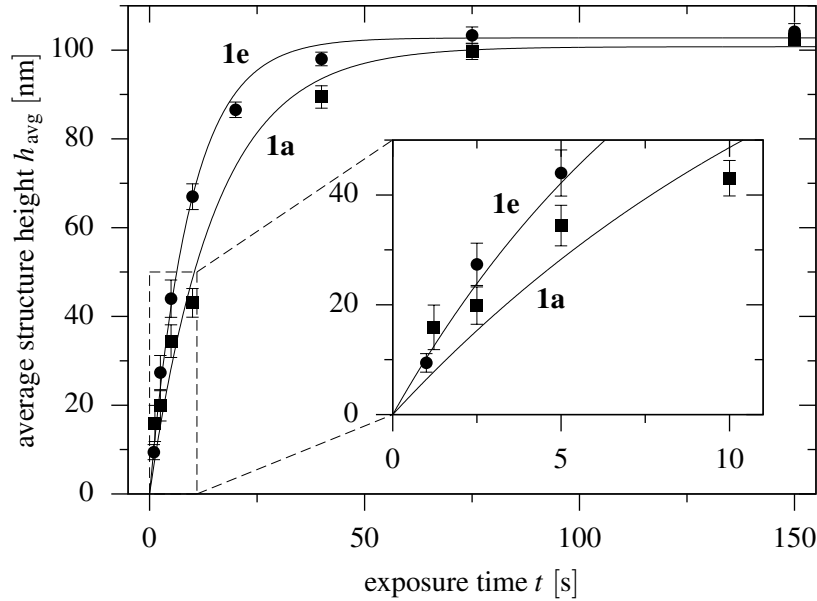


Figure 10.20: Average height h_{avg} of the $1\ \mu\text{m}$ structures imprinted into molecular glasses **1a** (filled squares) and **1e** (filled circles) as a function of the exposure time t . The molecular-glass films were preheated to a temperature of 98 and 97 °C, respectively. Imprinting was performed with an Elastosil[®] 601 mold with L-shaped protrusions. No external pressure was applied.

Nanometer-sized structures were imprinted with EVG[®] molds (type I) into films of molecular glasses **1a** and **1e** according to the same procedure as described above. Since the resist must be illuminated through the mold in the hot-stage setup, no external pressure could be applied without blocking the incident light (cf. Chapter 7.2). Hence, imprinting was performed by simply attaching the EVG[®] molds to the resists. As discussed in Chapter 10.3.1, the molds lack conformal contact in this case. Because this affects the filling behavior of the cavities, the AFM data of the imprints allow only approximate statements about the temporal evolution of the structure heights. As expected, also nanometer-sized lines or pillars can be imprinted faster into the preheated films than at room temperature. Complete filling of the 300 nm line and punch cavities requires ~ 75 s for both molecular glasses. As compared to the unheated film of molecular glass **1a** with pressure applied (cf. Chapter 10.3.1), this is an improvement by a factor of about four. Lines and pillars with $w = 150$ or 100 nm sporadically reach the maximum height of 100 nm. The required time is on the order of 600 s. As in the experiments conducted at room temperature, the filling speed decreases when the spatial dimension of the mold cavities is reduced from 300 to 100 nm.

Table 10.8: Summary of the experimental data of molecular glasses **1a** and **1e** measured at elevated temperatures. T : resist temperature, d_0 : initial film thicknesses, h_0 : imprint height of the $1\ \mu\text{m}$ line patterns for $t \rightarrow \infty$, τ : filling time constant of the $1\ \mu\text{m}$ cavities according to Eq. (10.3).

material	T [°C]	d_0 [nm]	h_0 [nm]	τ [s]
1a	98	520	101	15.2
1e	97	490	103	9.5

A selection of patterns imprinted into a preheated film ($T = 98^\circ\text{C}$) of molecular glass **1a** after 600 s of illumination are shown in Fig. 10.21. The perspective AFM images in Fig. 10.21 a) and b) depict 300 and 150 nm hexagonally arranged pillars, respectively. Areas up to $10 \times 10 \mu\text{m}^2$ were found to be reproduced homogeneously. For the sake of clarity, the figures show only a portion of the complete AFM scan. The imprint in Fig. 10.21 a) is an almost perfect replica of the master, since the 300 nm pillars have a height of 105 nm and a rectangular shape. This is also true for imprints of the 300 nm lines and orthogonal pillars (data not shown). Heating seems to soften the polymer of the mold, however. As a result, the pillars with $w \leq 150\text{ nm}$ appear more rounded than when produced at room temperature. Furthermore, the higher imprinting speed comes at the cost of an increased number of defects for both the 100 nm hexagonal and the 100 nm orthogonal patterns. This is illustrated by the perspective AFM image of Fig. 10.21 c). Two types of defects could be observed for the imprint of the 100 nm hexagonal pillars, viz. detachment of large resist areas (indicated by the hole in the left corner of Fig. 10.21 c)) and tearing off of individual pillars. The remaining pillars had a height of almost 100 nm, indicating that the mold was almost completely filled prior to its release. The higher number of defects is not surprising since heating and cooling causes additional thermal stress. Similar results have been obtained on preheated films ($T = 97^\circ\text{C}$) of molecular glass **1e** as well.

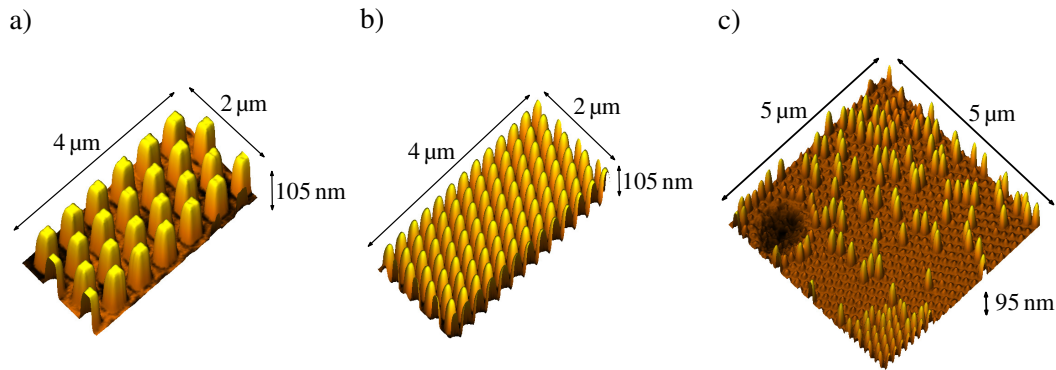


Figure 10.21: Perspective AFM images of the a) 300 nm, b) 150 nm, and c) 100 nm hexagonal pillar-type patterns imprinted into molecular glass **1a** after 600 s illumination at a resist temperature of 98°C . An EVG[®] mold (type I) was imprinted without externally applied pressure.

In sum, preheating was found to boost the photofluidization of molecular glasses, which increases the imprinting speed. Structures larger than 150 nm were imprinted with similar quality as at room temperature. For $w \leq 150\text{ nm}$, the shape of the protrusions deviates from the master; the pillars appear to be rounded. Also, 100 nm pillar-type patterns were transferred with higher defect density. The temperature-dependent measurements clearly demonstrate the advantages of Azo-NIL as compared to other NIL techniques. As long as the viscosity of the resist is reduced solely due to athermal photofluidization, thermal stress is virtually eliminated. The mold is not heated in this case and the profiles of the imprinted structures are less distorted.

Formation of Complex Superstructures in Spirobichromane-Based Molecular Glasses

In the preceding chapters, the azobenzene-functionalized molecular glasses **1a** and **1e** based on the spirobichromane core turned out to be highly suitable materials for both the inscription of SRGs and the imprinting of structures on the micro- and nanometer scale. Once the molecular glasses are in the photofluidic state, a small externally applied force, which can be exerted by a light intensity or polarization gradient, adhesion, or other mechanisms, is sufficient to allow for efficient mass transport. A surprising behavior is observed when a film of one of the above compounds is illuminated with *p*-polarized writing beams in the holographic setup. Initially, the material migrates in a direction parallel to the intensity gradient, which causes the formation of sinusoidal SRGs. For sufficiently long inscription times, however, complex zigzag-shaped structures of remarkable height emerge. The photofluid is transported preferably parallel to the grating crests in this case. A similar behavior has been reported for star-shaped molecular glasses functionalized with a single azobenzene chromophore by the group of Ishow.^[64] For azobenzene-functionalized spirobichromane derivatives, however, the formation of complex superstructures has been unknown so far.

The following chapter discusses the properties and dynamics of pattern formation on films of molecular glasses **1a** and **1e** during illumination with a *pp* intensity grating. For this purpose, the temporal evolution of the 1st-order diffraction efficiency is investigated. Further, the dependence of the formation speed of the structures on the fluence is analyzed. Since the profiles of the superstructures are not as regular as those of sinusoidal SRGs, a theoretical description of their formation is not provided. Instead, a qualitative description of the mechanism leading to their formation is given. To generate both sinusoidal SRGs and complex superstructures, the holographic setup presented in Chapter 7.1 was used. The surfaces of all illuminated spots were measured by AFM.

11.1 Fluence Dependence of the Diffraction Efficiency

In contrast to Raman-Nath gratings stored in the volume of a material, SRGs are not expected to suffer from overexposure. A widely used approach to describe the temporal evolution of the SRG amplitude is to assume that it approaches a maximum value exponentially,^[98] denoted herein by $d_{1,\max}$. The grating amplitude after a writing time t is

$$d_1(t) = d_{1,\max} \cdot [1 - \exp(-t/\tau)] \quad (11.1)$$

with τ being the buildup constant. If this expression is inserted into Eq. (2.12), the 1st-order diffraction efficiency of a sinusoidal SRG becomes

$$\eta_1 = J_1^2 \left(\frac{2\pi\Delta n}{\lambda_r \cos \theta_r} d_{1,\max} \cdot [1 - \exp(-t/\tau)] \right), \quad (11.2)$$

which implies that η_1 is constant for long writing times. The temporal evolution of η_1 in spirobichromane-based molecular glasses shows a different behavior, however, which is discussed in the following.

In a first step, a film of molecular glass **1a** with a thickness of 1.1 μm was illuminated for 2000 s with the sinusoidal interference pattern of the p -polarized writing beams. Each of them had an intensity of 1 W cm^{-2} , so their total intensity was 2 W cm^{-2} . At the same time, the temporal evolution of the 1st-order diffraction efficiency was monitored with the reading laser. Subsequently, the experiment was repeated at different positions on the sample. The diffraction efficiencies of two exemplary measurements are plotted as a function of the inscription time in the second graph on the left-hand side of Fig. 11.1 (from top to bottom). An enlarged version of the region marked by the gray-shaded box is shown on the right.

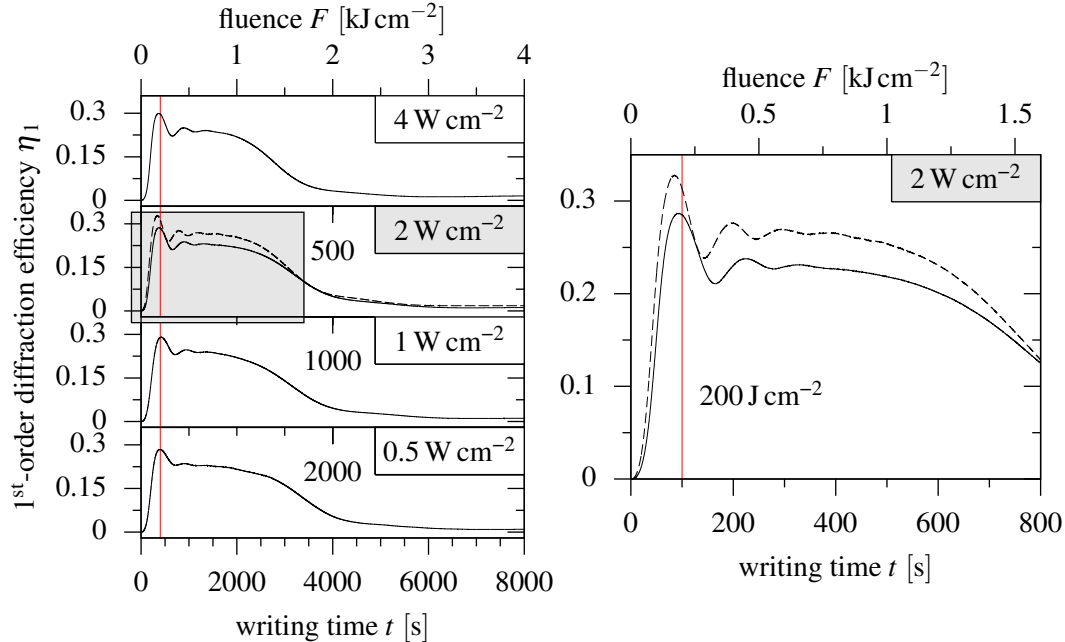


Figure 11.1: 1st-order diffraction efficiency η_1 of surface reliefs inscribed in a film of molecular glass **1a** as a function of both the writing time t and the fluence F . The total intensities of the writing beams were 0.5, 1, 2, and 4 W cm^{-2} . The scalings of the time axes on the left are chosen such that they are in the same proportion as their corresponding total intensities. Thus, all graphs have the same fluence scale (top abscissa). The solid and dashed line in the enlarged section on the right are measured at different places on the sample under the same experimental conditions.

The 1st-order diffraction efficiency of the first SRG (solid line) increases within approximately 90 s to a value of about 28.7 %. In the second measurement (dashed line), η_1 reaches a higher value of $\sim 32.8\%$, which is near the theoretical limit of scalar Raman-Nath gratings. The time required to reach the maximum does not change significantly. The solid and dashed curves represent a lower and an upper limit for η_1 . SRGs inscribed at other positions on the molecular glass film result in similar curves that lie between the depicted ones. Interestingly, the diffraction efficiencies are not constant after reaching their maximum value but decrease slightly first. Although this is plausible from the point of view that a sinusoidal grating with monotonously increasing amplitude emerges, the subsequent small oscillations and the steep decrease after ~ 600 s cannot be explained with this argumentation. For illumination times longer than 1500 s, η_1 decreases to almost zero, which implies that the SRG is destroyed.

To analyze, whether the decay at long writing times is a side effect of laser-induced heating, the dependence of the diffraction efficiency on the fluence $F = I \cdot t$ was investigated. Similar as in Chapter 10.1.1, F is defined as the product of the total intensity of the writing beams I and the inscription time t . Thus, it is a measure of the energy deposited in the molecular glass. Surface relief gratings were inscribed at a total writing intensity of 0.5, 1, and 4 W cm⁻². The temporal evolution of the 1st-order diffraction efficiencies is plotted on the left-hand side of Fig. 11.1 together with that measured at 2 W cm⁻². The scalings of the time axes are in the same proportion as the corresponding total writing intensities. In this representation, the same horizontal position belongs to the same fluence. The top abscissa is labeled with the respective values. As indicated by the red lines, the diffraction efficiency reaches a maximum at a fluence of ~ 200 J cm⁻² for each of the four writing intensities. Subsequently, η_1 decreases and slightly oscillates around a constant value ($0.2 \text{ kJ cm}^{-2} \leq F \leq 1 \text{ kJ cm}^{-2}$) until it finally decays to almost zero ($F > 1 \text{ kJ cm}^{-2}$). The five curves plotted in Fig. 11.1 are almost congruent, which demonstrates that the formation of surface structures solely depends on the fluence. Laser-induced heating can be precluded from being the underlying mechanism, since the decay of η_1 at long writing times occurs at low and high writing intensities. This is further supported by the observation that the shape of the curves does not change when the writing laser is switched off during inscription. In this case, the diffraction efficiency stays constant. As soon as the writing laser is turned on again, it continues its original course.

11.2 Formation of Sinusoidal Surface Relief Gratings at Low Fluence

The results of the preceding chapter show that the developing pattern cannot be an SRG whose amplitude approaches a maximum value exponentially. However, since the 1st-order diffraction efficiency increases continuously for fluences below 200 J cm⁻², it is plausible to assume that initially a sinusoidal grating with a steadily growing amplitude emerges. To study the SRG formation at low fluences ($F \leq 210 \text{ J cm}^{-2}$), different spots of a film of molecular glass **1a** were illuminated with the writing beams having a total intensity of 2 W cm⁻². Each grating was inscribed with a different fluence by varying the writing time within a range of 0 to 105 s. The respective 1st-order diffraction efficiencies were measured and d_1 was calculated from Eq. (2.12) following the approach described in Chapter 2.3. To determine Δn , the refractive index of molecular glass **1a** was inserted from Table 9.1 (cf. Chapter 9.3). Finally, the profiles of the inscribed gratings were measured near their center with an AFM.

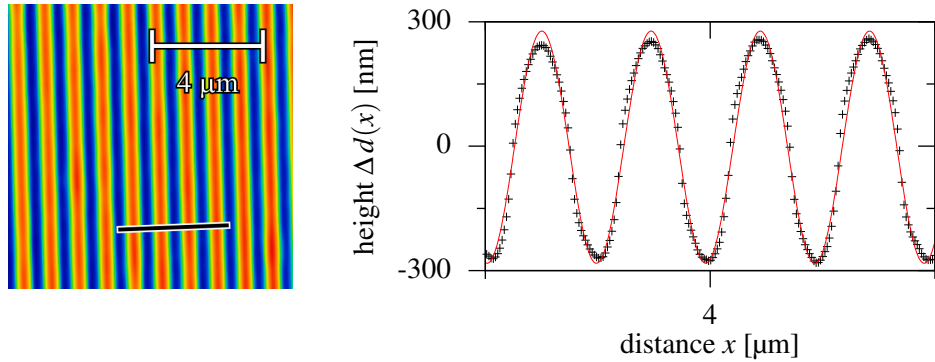


Figure 11.2: The left panel shows a false-color AFM image of a sinusoidal SRG inscribed into a film of molecular glass **1a** with a fluence of 210 J cm^{-2} . The profile measured along the black line is plotted on the right (black crosses). A sine function (red line) with an amplitude of $d_1 = 280 \text{ nm}$ and a periodicity of $\Lambda = 972 \text{ nm}$ fits the data well.

Since Eq. (2.12) applies to sinusoidal gratings only, the AFM data are discussed first. The left panel of Fig. 11.2 shows an AFM image of an SRG inscribed into a film of molecular glass **1a** after 105 s of illumination ($F = 210 \text{ J cm}^{-2}$). In addition to the fact that the produced grating is very regular, its surface is essentially sinusoidal. This becomes apparent from the graph on the right side. It depicts the profile of the grating measured along the straight line drawn in the AFM image on the left. The red line is a fit function of the form $\Delta d(x) = 280 \text{ nm} \cdot \sin(2\pi x/972 \text{ nm} + 243^\circ)$. Slight deviations from the sinusoidal profile exist, which are best visible near the grating maxima. The grating height varies across the SRG, the fluctuations are on the order of 50 nm. Considering that the average grating height is 560 nm, the variations are below 10%. Gratings inscribed with lower fluences have sinusoidal profiles of similar or higher quality. Generally speaking, the fluctuations are always below 10% of the average grating height for fluences below 210 J cm^{-2} . The grating period of $\Lambda = 972 \text{ nm}$ does not agree with the value calculated from Eq. (2.3) ($\Lambda = 1000.7 \text{ nm}$). This is an artifact of the AFM measurement, which can be attributed to the fact that the scanning direction was parallel to the grating crests.

The peak-to-peak heights $H = 2d_1$ of the sinusoidal SRGs determined from both the AFM data (filled squares) and the diffraction efficiencies (open circles) are plotted as a function of the writing time t in Fig. 11.3. Since the total intensity of the writing beams was constant during the experiment, each data point can be assigned to its corresponding fluence. The respective values are marked on the upper abscissa. As indicated by the filled squares, the grating heights determined from the AFM data increase linearly throughout the whole measurement series. The linear growth persists even until a time slightly after the 1st-order diffraction efficiency reaches its maximum (cf. Fig. 11.1). The growth rate determined from the linear fit through the origin (lower solid line) is 5.3 nm s^{-1} , where the grating reaches a height of $\sim 560 \text{ nm}$ after 105 s of illumination. For fluences below 100 J cm^{-2} the values of H are lower than predicted by the fit. A possible explanation is that the SRG heights have been measured near the edge of the grating, where the fluence decreases according to the Gaussian profile of the writing beams. This systematic error predominantly occurs for gratings of low height because their center is more difficult to locate.

The grating heights determined from the diffraction efficiencies increase linearly for fluences below 100 J cm^{-2} . This is indicated by the dashed line through the origin with a slope of 5.6 nm s^{-1} . It results from a fit which only includes the data of the SRGs inscribed with $F < 100 \text{ J cm}^{-2}$. Within this range, the grating heights calculated with Eq. (2.12) almost lie on the regression line obtained from the AFM data. When H exceeds 250 nm

($F > 100 \text{ J cm}^{-2}$), the calculated values clearly deviate from the dashed line. In addition to an increased scatter, most of the calculated values are systematically too high and the deviations from the AFM data become as large as 100 nm. In summary, grating heights calculated from η_1 are more exact for small values of H , whereas those measured by AFM are more reliable for $H > 250 \text{ nm}$.

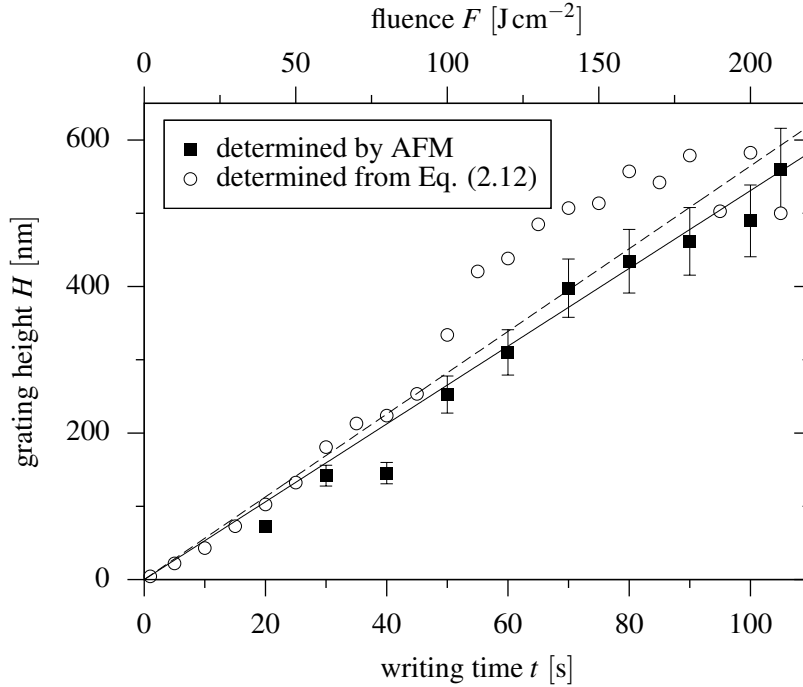


Figure 11.3: Grating heights H determined with the AFM (filled squares) and Eq. (2.12) (open circles) as a function of both the writing time t and the fluence F . The total intensity of the writing beams was 2 W cm^{-2} . The linear functions indicated by the straight lines through the origin have slopes of 5.3 nm s^{-1} and 5.6 nm s^{-1} . The slope of the dashed line was determined only from the data points with $F < 100 \text{ J cm}^{-2}$.

The initial linear growth of the SRGs can be explained with laminar-flow models which treat the photofluid as a viscous fluid.^[57,233] Apart from a constant prefactor, the functional relationship between the grating height and the writing time is similar to the one derived from the Stefan equation in Chapter 10.1.4 (cf. Eq. (10.6)). The reason is that mold filling and SRG formation are equivalent to a certain extent, if the origin of the pressure or force which causes the material flow is not closer specified. In other words, the photofluidic molecular glass does not distinguish between forces exerted by optical gradients or mold adhesion. The continuing linear growth for high grating amplitudes is unexpected, however, since the models mentioned above apply to SRGs with small amplitudes only and, moreover, neglect the surface tension of the photofluid. The deviations between the grating heights calculated from η_1 and those measured by AFM for $H > 250 \text{ nm}$ can have different reasons. Equation (2.12) follows from a transmission matrix approach which is the adaption of a model developed to describe the diffraction off scalar Raman-Nath gratings inscribed in the volume of a material. Thus, it neglects the fact that for SRGs the angle of incidence becomes a function of position. To take this effect into account, high numerical effort would be required.^[234,235] Additionally, light scattering at the corrugated SRG surface is neglected. Finally, the height fluctuations discussed before reduce the regularity of the grating, which further affects its diffraction behavior. All the above effects gain importance with increasing grating height, as it is the case in the experiments.

11.3 Formation of Complex Superstructures at High Fluence

In the previous chapter it was shown that SRGs grow linearly for fluences below 210 J cm^{-2} and that their profile is essentially sinusoidal. This applies approximately until η_1 reaches its maximum (cf. Fig. 11.1 and 11.3). The subsequent first and second decay, however, cannot be attributed to a continuously growing grating. Instead, they are caused by the beginning formation of complex superstructures, which are discussed in the following. To investigate the formation of structures at high fluences, different spots of a film of molecular glass **1a** were illuminated with the interference pattern of the writing beams. Their total intensity was 2 W cm^{-2} and the inscription time was varied from 125 to 4000 s, corresponding to fluences between 0.25 and 8 kJ cm^{-2} . Subsequently, the profiles of the inscribed structures were measured by AFM.

The beginning of the process, which eventually results in the formation of complex superstructures, is depicted in Fig. 11.4 a). It shows an AFM image of a grating which was inscribed with a fluence of 1 kJ cm^{-2} . Exposure with fluences between 0.25 kJ cm^{-2} and 1 kJ cm^{-2} resulted in the formation of similar patterns; the corresponding AFM images are not shown. The above fluences belong to the range where η_1 has passed its maximum and temporarily decays to a constant value. In Fig. 11.4 a) the average grating height is on the order of 400 nm , which is lower than that measured for fluences of about 210 J cm^{-2} ($H \approx 600 \text{ nm}$). At distinct places the crests of the grating become narrower, whereas elsewhere they begin to form bulges. As a consequence, the grating height strongly varies over the scanned area. Yet, the original SRG is clearly recognizable and still resembles the interference pattern of the writing beams. The decreased height in combination with the reduced regularity explains the first decay of η_1 . The black arrows illustrate that, unlike SRG formation at low fluences, the molecular glass begins to flow in a direction parallel to the grating crests. From the snapshot of the process, however, it cannot be distinguished whether the material still also migrates in a direction parallel to the optical gradient. The polarization of the incident laser light is indicated by the white arrow, which is parallel to the optical grating vector \vec{K} .

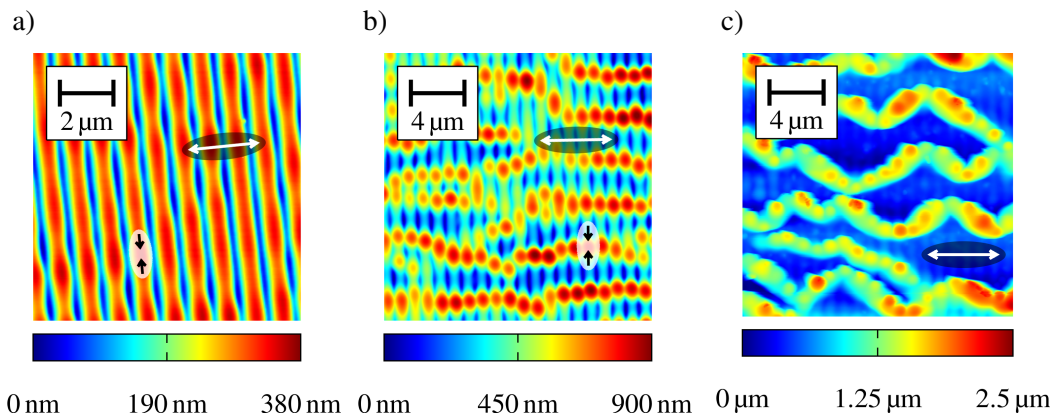


Figure 11.4: False-color AFM images of the structures generated on a film of molecular glass **1a** after exposing it to a fluence of a) 1 kJ cm^{-2} , b) 1.6 kJ cm^{-2} , and c) 8 kJ cm^{-2} . Black arrows indicate the direction of the material transport, whereas white arrows correspond to the polarization of the writing beams.

The effects of the persistent material transport along the grating crests can be seen more clearly in Fig. 11.4 b). The depicted pattern was inscribed with a fluence of $\sim 1.6 \text{ kJ cm}^{-2}$, where η_1 already decays (cf. Fig. 11.1). It becomes even more apparent that the photofluidic molecular glass flows predominantly in a direction perpendicular to the polarization or

\vec{K} . The material migrates into both the top and the bottom direction (black arrows), which causes the formation of rounded cones which appear as small droplets in the AFM image. At the same time, less molecular glass is transported into the horizontal direction. Since the previously inscribed SRG already had a reasonable height, the accumulation of molecular glass at distinct points along each grating crest causes the formation of even higher structures up to 900 nm. One can further see that hills preferably develop at the same horizontal position, where they gradually begin to merge. The above observations add further complexity to the migration behavior of azobenzene-functionalized molecular glasses in optical fields. Periodic polarization or intensity gradients do not exist along the grating crests and, thus, cannot be responsible for the formation of the complex patterns. Also effects of gravity can be neglected, otherwise the photofluid would accumulate at the edge of the substrate. (The sample was oriented vertically during the experiment.)

Figure 11.4 c) shows the final state of the process. The depicted structures formed after exposing the molecular glass film to a fluence of 8 kJ cm^{-2} . The rounded cones now have fused into complex zigzag lines with remarkable heights up to $2.5 \mu\text{m}$. The tendency of the cones to align horizontally causes the ridges of the pattern to run parallel to the polarization of the light or the grating vector. Similar structures were measured when the fluence was reduced to 4 kJ cm^{-2} . This implies that the formation process is largely completed once the 1st-order diffraction efficiency has fully decayed. Closer inspection shows that the height of the zigzag lines as well as the valleys between them are slightly modulated, reflecting the initial SRG. This indicates that the intensity gradients of the optical grating still exert a force onto the photofluidic molecular glass, which causes the material to migrate in a direction parallel to \vec{K} . As compared to the height of the zigzag lines, however, the amplitude of the surface modulation is negligible.

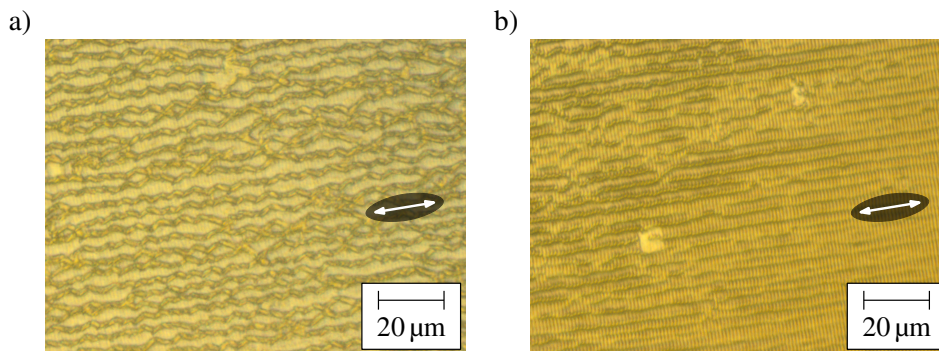


Figure 11.5: Microscope images of complex superstructures inscribed on a film of molecular glass **1a** with a *pp* intensity grating. a) Center region of the illuminated spot. b) Edge region of the illuminated spot. White arrows indicate the polarization of the optical grating.

To provide an overview of the complex superstructures at larger scales, the illuminated spot shown in Fig. 11.4 c) was further investigated with an optical microscope. Two images were recorded, one at the center of the hologram, and the other one near its edge. They are shown in Fig. 11.5 a) and b), respectively. Due to the Gaussian profile of the laser beams, the fluence reaches its highest value at the center. Thus, the pattern depicted in Fig. 11.5 a) solely consists of zigzag lines. The latter occur with a certain regularity in the direction perpendicular to the optical grating vector and form a new surface-relief grating with a periodicity of $\sim 4 \mu\text{m}$. As in the AFM image, the polarization of the writing beams is indicated by the white arrow. In the microscope images it can be seen more clearly that the zigzag lines are aligned parallel to the polarization axis. Near the edge of the illuminated region shown in Fig. 11.5 b) the fluence decreases and a transition state between the sinusoidally

modulated surface and that with zigzag lines can be observed. At high magnification one can clearly distinguish the vertical stripes of the original sinusoidal SRG, which are well preserved on the right side. On the left side, the pattern of perpendicular zigzag lines is more dominant.

11.4 Complex Superstructures in Methoxyazobenzene-Functionalized Spirobichromane-Based Molecular Glasses

So far, only the formation of SRGs and complex superstructures on films of molecular glass **1a** was discussed. As mentioned in the beginning of the chapter, a material which is expected to show a similar behavior is molecular glass **1e**. It is based on the spirobichromane core as well, but features a higher absorption near the laser wavelength since it is functionalized with methoxy-substituted azobenzene chromophores. As a consequence, it forms SRGs faster than compound **1a** (cf. Chapter 9.3). To investigate the surface reliefs formed by molecular glass **1e** after being exposed to high fluences, it was prepared as a 1.1 μm thick film which was illuminated in the holographic setup for 500 s with a *pp* intensity grating. During this time, the 1st-order diffraction efficiency was measured. The total intensity of the writing beams was 2 W cm^{-2} .

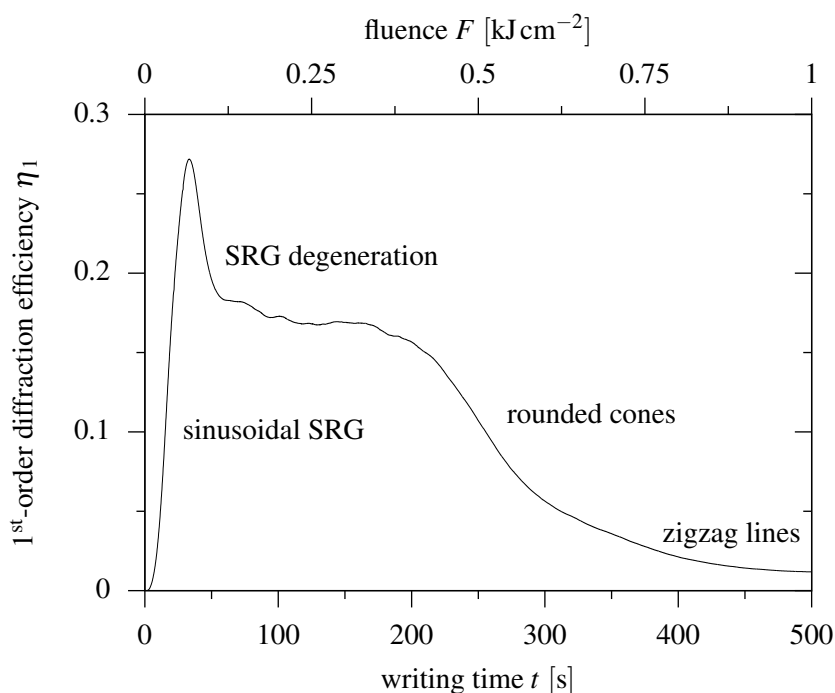


Figure 11.6: 1st-order diffraction efficiency η_1 of a surface relief inscribed on a film of molecular glass **1e** as a function of both the writing time t and the fluence F . The total intensity of the writing beams was 2 W cm^{-2} .

Figure 11.6 shows η_1 as a function of both the writing time and the fluence. Once the illumination has been started, the diffraction efficiency first reaches a maximum, then decays to a plateau, and finally approaches a value of almost zero. The behavior of η_1 is virtually identical to that of molecular glass **1a** (cf. Fig. 11.1). The diffraction efficiencies of compounds **1a** and **1e** only differ by their time or fluence scale. For relief patterns inscribed in molecular glass **1e**, η_1 progresses three times faster than for **1a**. This result indicates that complex superstructures emerge more quickly on films of **1e**. Furthermore,

molecular glass **1e** should undergo the same stages of pattern formation as **1a**. To prove this assumption, the above experiment was repeated for fluences between 0 and 1 kJ cm^{-2} at different spots on the molecular glass film. Afterward, the inscribed structures were investigated with an optical microscope. These measurements confirmed that the formation of SRGs and complex superstructures in molecular glass **1e** takes place in a way analogous to that in **1a**. Initially a sinusoidal SRG emerges. It reaches a similar height as in the case of **1a**, which follows from the 1st-order diffraction efficiencies of compound **1a** and **1e**. With increasing fluence, the SRG transforms into rounded cones and eventually into complex superstructures. As in the case of molecular glass **1a**, the complex superstructures consist of zigzag lines that are aligned parallel to the polarization of the interfering writing beams. The different stages of pattern formation are indicated in Fig. 11.6.

In the present thesis, the suitability of azobenzene-functionalized molecular glasses and polymers for different fields of application was investigated. They comprise the storage of holographic volume gratings, the lithographic manufacturing of micrometer- and nanometer-sized structures, and the optical generation of surface relief patterns. In addition, a new method for the determination of refractive indices was developed and characterized.

The large variety of research applications arises from the rich photophysics of the materials used in the experiments. They are functionalized with covalently attached azobenzene moieties which perform repeated *trans-cis-trans* isomerization cycles when exposed to UV or blue light. Depending on their molecular structure, azobenzene-functionalized compounds react differently upon illumination. In some materials, the azobenzene chromophores only perform a rotational motion. If the light is polarized, they orient and the refractive index of the material becomes anisotropic. On the contrary, a large number of azobenzene-functionalized materials becomes photofluidic. In this state, they are able to flow like a liquid without raising their macroscopic temperature. Exposure to a light intensity or polarization grating exerts a force onto the moieties, which causes a translational motion of the material over macroscopic distances. Since the migration preferably occurs in the direction of the optical gradient, sinusoidal SRGs or more complex patterns can be formed. Alternatively, the driving force of the material transport can be adhesion, which is important for lithographic applications.

The investigated materials were azobenzene-functionalized low-molecular-weight compounds, homopolymers, and block copolymers. Low-molecular-weight compounds that feature a stable amorphous phase are also known as molecular glasses. They can easily turn into the photofluidic state and efficiently form SRGs. Thus, they are ideal candidates for the optical and lithographic fabrication of a large variety of surface patterns. Homopolymers have similar properties. Due to the presence of entanglements, material migration is less efficient than in the molecular glasses. If the polarization of the incident light is chosen appropriately, homopolymers can store stable Raman-Nath refractive-index gratings in the volume. The block copolymers consist of an azobenzene-functionalized minority and a polystyrene majority phase which are microphase-separated. Since the photo-addressable part is confined by the optically inert polystyrene matrix, photoinduced material transport is completely inhibited. In addition, block copolymers feature a low optical density. Both properties are required for the inscription of Bragg-selective volume gratings and, thus, for holographic data storage.

Chapter 8 constitutes a guide on how to improve the holographic performance of azobenzene-functionalized block copolymers. In the presented approach, different polymer types were blended with an azobenzene-functionalized molecular glass and prepared as thin films. Subsequently, volume gratings were inscribed with a holographic setup. To understand the photophysical behavior of the molecular glass located in the two phases of the block copolymers, blends with a photo-orientable and an optically inert homopolymer were investigated first. From the holographic writing times measured in these systems, it was derived that cooperative interactions exist between both the chromophores of the molecular glass and those of the molecular glass and the photo-orientable polymer. Thus, the molecular glass acts as a plasticizer and speeds up the alignment of the chromophores of the surrounding polymer matrix. Increasing the content of molecular glass in photo-orientable homo- and block copolymers shortens the time required to inscribe a holographic grating significantly. A comparative analysis of the writing times in all polymer blends further revealed that the molecular glass mainly accumulates in the photo-orientable minority phase of the block copolymers. The maximum refractive-index modulation achieved in the blends is essentially a superposition of that of the neat compounds. Since the neat molecular glass features a higher refractive-index modulation than the neat block copolymers, its addition allows for the storage of more intense holograms. Blending with molecular glass also improves the homogeneity of the prepared films. Annealing enhances the microphase separation and causes the molecular glass to accumulate even more in the photo-orientable block. Both processes result in a better reproducibility of the writing times. The concentration of molecular glass, however, cannot be increased arbitrarily without affecting the post-development of the inscribed gratings and the optical density of the blend. Adding an amount of 15 wt% molecular glass to a block copolymer with stabilizing mesogenic units in its photo-addressable block results in a long-term-stable refractive-index modulation. Furthermore, the optical density of the blend is still low at this concentration and the inscription time reduces to about 10 s, which is a factor of more than 15 as compared to the neat block copolymer. In summary, blending photo-orientable block copolymers with an azobenzene-functionalized molecular glass improves their holographic performance, making them promising candidates for holographic data storage or forgery-proof security features.

In Chapter 9 a new method for the determination of the refractive index of solids was developed. When a periodic pattern exists near the surface of a material, the grating equation implies that an incident monochromatic laser beam is diffracted into various orders. They emerge at different angles inside the medium which depend on the angle of incidence. For individual orders, a critical angle of incidence exists at which the direction of propagation is parallel to the grating vector, i. e., parallel to the surface of the material. From these critical diffraction angles, the refractive index can be determined. Two different criteria were derived from the grating equation. They allow for the calculation of the refractive index either from the wavelength of the incident light, the grating constant, and the 1st-order critical diffraction angle or from the 1st- and 2nd-order critical diffraction angles exclusively. Since the grating equation is valid for periodic patterns in general, both approaches apply to surface-relief, refractive-index, or absorption gratings with arbitrary shape (sinusoidal, rectangular, etc.). Moreover, no information about the thickness of the material below the grating is required. To study the applicability of the method, the dispersion of a non-photoactive PDMS polymer was measured. For this purpose, a holographically prepared SRG was transferred to a PDMS film by molding. As reference, the PDMS dispersion was measured with an Abbe refractometer. The results of the combined experiments demonstrated that the refractive indices can be calculated from the 1st- and 2nd-order critical diffraction angles with an accuracy of about three decimal digits. Different experimental error sources were discussed in detail. Systematic errors can occur if the spectral width of the laser is too large.

They can be eliminated either by correcting the wavelength accordingly or by using the approach that involves the determination of two critical diffraction angles. Finally, the new technique was applied to determine the refractive indices of different molecular glass formers. They have similar refractive indices, which are 1.521 at a wavelength of 489.2 nm and 1.510 at a wavelength of 685 nm. In summary, a method for the determination of the refractive index of solids was developed, characterized, and tested. Since various techniques exist for the preparation of gratings (e.g., holographic inscription, embossing, imprinting), the presented approach constitutes a powerful tool for a large scope of applications such as holography, optical fibers, or thin-film optics.

A novel lithographic method for the reproduction of micrometer- and nanometer-sized structures was introduced in Chapter 10. It is denoted by Azo-NIL and uses the well-known concept of transferring patterns from a rigid master to a resist with a flexible mold. Unlike other imprint methods, the resist material is an azobenzene-functionalized molecular glass or homopolymer which can be switched to the photofluidic state with visible or UV light. Filling of the mold is driven by adhesion and, thus, the mold has to be in good conformal contact with the resist. For this reason, the properties of molds prepared from different polymers were analyzed. The roofs of PDMS molds collapse to the azobenzene-functionalized resists initially and the PDMS polymer adheres strongly. Yet, molds prepared from PDMS cannot be used to imprint defect-free line structures smaller than 150 nm since the mold protrusions collapse also laterally in this case. A solution is to prepare molds from the less flexible, so-called EVG[®] polymer. Because it is much stiffer and less adhesive than PDMS, conformal contact with the resist has to be restored by applying additional external pressure. Since Azo-NIL is a new technique, fundamental questions regarding the dynamics of the resist flow were discussed. Coherent and incoherent light sources in the UV and blue spectral range can be used to photofluidize the azobenzene-functionalized resists. The most efficient filling of the molds is achieved by exciting the $n \rightarrow \pi^*$ and the $\pi \rightarrow \pi^*$ transition of the chromophores simultaneously with two different light sources. If the initial thickness of the photofluidizable resist is thinner than 500 nm, both the filling speed of the mold and the maximum height of the imprinted structures decrease. For higher film thicknesses, the filling rate is constant and complete filling can be achieved. This behavior follows from the Stefan equation and applies to viscous fluids independent of the resist material. Different azobenzene-functionalized molecular glasses and homopolymers were investigated for their applicability in Azo-NIL. Low-molecular-weight compounds based on a triphenylamine core crystallize upon illumination and, thus, produce imprints of poor quality. In contrast, imprints of high quality can be obtained from azobenzene-functionalized homopolymers, trisamide-based molecular glasses, and spirobichromane-based molecular glasses, since all compounds return to the amorphous state after illumination. Among these compounds, the spirobichromane-based derivatives turned out to be the most efficient resist materials with the shortest filling times. Also, the influence of the substituent of the azobenzene chromophores was investigated. The introduction of perfluorinated groups reduces both the filling speed and the imprint quality. Substitution with methoxy groups, on the other hand, changes the absorption of the azobenzene chromophores, so imprinting requires less time. At short exposure times, the height of the imprints is proportional to the fluence. Thus, higher intensities increase the imprinting speed. After sufficiently long exposure, complete filling of the cavities is achieved and the profile of the master is reproduced with high quality. For approximately 500 nm thick films prepared from a spirobichromane derivative featuring hydrogen-substituted azobenzene moieties, the time required to fill 63 % of 100 nm deep mold cavities with a width of 1000 or 100 nm is 112 or 368 s, respectively, when illuminated at room temperature. In smaller mold cavities, the photofluidic resist requires a longer time to rise. This is due to the fact that capillary flow becomes the dominating mechanism

once the photofluid reaches a certain height inside the mold cavities. Finally, the influence of preheating azobenzene-functionalized resists on the imprinting speed was investigated. Since the thermal barriers for azobenzene isomerization attempts are lowered, photofluidization is enhanced. If molecular glass resists are stored 10 °C below their glass transition temperature during imprinting, the processing time decreases by a factor of up to seven but, also, the number of defects upon mold release increases. In summary, Azo-NIL allows for the precise replication of micrometer- and nanometer-sized patterns. Because it is based on the athermal photofluidization of azobenzene-functionalized materials, its advantage as compared to common imprint methods is that it can be performed without thermal treatment or crosslinking reactions, so it is not affected by issues associated with material shrinkage. Azo-NIL holds the potential to be applied as a technique for the fabrication of functional optical materials, microlens arrays, photonic elements, or complex patterns with feature sizes down to 10 nm.

The surface-relief patterns formed by two different spirobichromane-based molecular glasses upon illumination with a *p*-polarized optical grating were the subject of further investigations in Chapter 11. As long as the fluence stays below a critical value, the developing surface relief resembles the interference pattern, so its profile is essentially sinusoidal. The critical fluence roughly corresponds to the time at which the 1st-order diffraction efficiency reaches its maximum. At that moment, the height of the grating is about 600 nm. When the holographic illumination continues, the sinusoidal SRG decays. For higher fluences, rounded cones develop which finally fuse into complex superstructures. The latter consist of irregular zigzag-shaped lines which run perpendicular to the diffraction fringes of the optical grating. The zigzag-shaped lines reach heights up to several micrometers and are significantly higher than the initial, sinusoidal SRG. The resulting pattern resembles a grating with a periodicity of $\sim 4\ \mu\text{m}$ and represents the final state of pattern formation. Surprisingly, at high fluences the material transport occurs predominantly in a direction with negligible optical gradients. The formation of gratings or complex superstructures is accelerated if the azobenzene-functionalized moieties feature methoxy substituents. The reason is that the absorption of the chromophores shifts towards the wavelength of the writing laser. In summary, the temporal evolution of the surface relief patterns emerging on azobenzene-functionalized molecular glasses based on a spirobichromane core was analyzed and characterized. For this material class, the formation of complex superstructures is reported for the first time. Their existence is relevant for the correct interpretation of the diffraction efficiencies of holographically prepared SRGs and, thus, for the fabrication of homogeneous gratings.

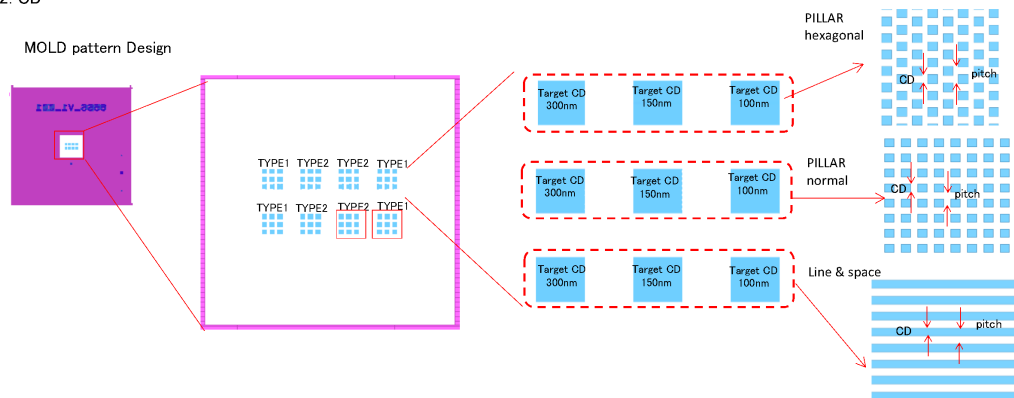
Appendices

NIL-Technology Master Data Sheet

1. Qz depth

MASK NAME	Target depth(nm)	Result (nm)
65SS V1.002	100	103.14

2. CD



DataTYPE	Pattern	Target CD (nm)	Pitch(nm)	CD(nm)
				65SS V1.002
TYPE1	Line & space	100	200	92.5
	Line & space	150	300	139.4
	Line & space	300	600	286.2
	PILLAR normal	100	200	97.3
	PILLAR normal	150	300	141.4
	PILLAR normal	300	600	289.3
	PILLAR hexagonal	100	200	100.2
	PILLAR hexagonal	150	300	142.9
	PILLAR hexagonal	300	600	290.8
TYPE2	Line & space	100	300	88.4
	Line & space	150	450	136.1
	Line & space	300	900	284.1
	PILLAR normal	100	300	91.6
	PILLAR normal	150	450	135.2
	PILLAR normal	300	900	292.4
	PILLAR hexagonal	100	300	93.2
	PILLAR hexagonal	150	450	136
	PILLAR hexagonal	300	900	291.1

Figure A.1: Technical data of the NIL-Technology master. The data sheet illustrates the arrangement of the different pattern types and lists the heights of the available structures as well as their target widths and their actual widths.



List of Publications

- 1. Improving Holographic Writing Performance of Photo-Orientable Azobenzene Polymers by Molecular Glasses**
C. Probst, C. Meichner, H. Audorff, R. Walker, K. Kreger, L. Kador, and H.-W. Schmidt
published in *Journal of Polymer Science Part B: Polymer Physics* **54**, 2110–2117 (2016)
- 2. Refractive-Index Determination of Solids from First- and Second-Order Critical Diffraction Angles of Periodic Surface Patterns**
C. Meichner, A. E. Schedl, C. Neuber, K. Kreger, H.-W. Schmidt, and L. Kador
published in *AIP Advances* **5**, 87135 (2015)
- 3. Athermal Azobenzene-Based Nanoimprint Lithography**
C. Probst, C. Meichner, K. Kreger, L. Kador, C. Neuber and H.-W. Schmidt
published in *Advanced Materials Communications* **28**, 2624–2628 (2016)
- 4. Measuring Cumulative Exposure to Oxygen with a Diphenylphosphine–Alkyl Naphthaleneimide Luminescence Turn-On Dyad**
R. Shritz, R. Shapira, E. Borzin, B. Tumanskii, W. Reichstein, C. Meichner, F. Schwaiger, P. M. Reichstein, J. Kreyenschmidt, D. Haarer, L. Kador and Y. Eichen
published in *Chemistry A European Journal* **21**, 11531–11537 (2015).

List of References

- [1] M. Hilbert and P. López, “The world’s technological capacity to store, communicate, and compute information”, *Science* **332**, 60 (2011).
- [2] Cisco® Visual Networking Index™ (Cisco VNI™), “The zettabyte era — Trends and analysis”, Web 03 Jan. 2017, URL: <http://www.cisco.com/c/en/us/solutions/collateral/service-provider/visual-networking-index-vni/vni-hyperconnectivity-wp.pdf>.
- [3] IDC, “The digital universe of opportunities: Rich data and the increasing Value of the internet of things — Executive summary”, *EMC Digital Universe with Research & Analysis* on April 2014, Web 03 Jan. 2017, URL: <https://www.emc.com/leadership/digital-universe/2014iview/executive-summary.htm>.
- [4] G. E. Moore, “Cramming more components onto integrated circuits”, *Proceedings of the IEEE* **86**, 82 (1998).
- [5] W. Arden, M. Brillouët, P. Coge, M. Graef, B. Huizing and R. Mahnkopf (editors), “More than Moore white paper”, *International Technology Roadmap for Semiconductors (ITRS)*, Web 11 Nov. 2016, URL: www.itrs2.net/uploads/4/9/7/7/49775221/irc-itrs-mtm-v2_3.pdf.
- [6] P. A. Packan, “Pushing the limits”, *Science* **285**, 2079 (1999).
- [7] Samsung, “Exploring the key Samsung technologies that enabled 10nm-class DRAM”, *Samsung Newsroom* on April 2016, Web 10 Jan. 2017, URL: <https://news.samsung.com/global/exploring-the-key-samsung-technologies-that-enabled-10nm-class-dram>.
- [8] R. Borkar, M. Bohr, S. Jourdan, “Advancing Moore’s law — The road to 14 nm”, *Intel* on August 2014, Web 09 Jan. 2017, URL: <http://www.intel.com/content/www/us/en/silicon-innovations/advancing-moores-law-in-2014-presentation.html>.
- [9] Samsung, “3D technology has taken microchips into another dimension”, *Samsung Newsroom* on May 2016, Web 10 Jan. 2017, URL: <https://news.samsung.com/global/3d-technology-has-taken-microchips-into-another-dimension>.

- [10] “Over 6 decades of continued transistor shrinkage, innovation — Intel’s 22 nm technology moves transistor into the 3rd dimension”, *Intel* on May 2011, Web 10 Jan. 2017, URL: <http://www.intel.com/content/www/us/en/silicon-innovations/standards-22-nanometers-technology-background.html>.
- [11] “International Technology Roadmap for Semiconductors 2013 Edition Lithography”, *International Technology Roadmap for Semiconductors (ITRS)*, Web 13 Jan. 2017, URL: <http://www.itrs2.net/2013-itrs.html>.
- [12] UserBenchmark, “February 2017 SSD Rankings”, Web 16 Feb. 2017, URL: <http://ssd.userbenchmark.com/Explore/Fastest-SSD/8>.
- [13] T. Yamaguchi, “Modelling and control of a disk file head-positioning system”, *J. Syst. Cont. Eng.* **215**, 549 (2001).
- [14] M. Re (presenter), “HDD Areal Density”, *Seagate Tech Talks* on August 2015, Web 16 Dez. 2016, URL: http://www.seagate.com/www-content/investors/_shared/docs/tech-talk-mark-re-20150825.pdf.
- [15] UserBenchmark, “February 2017 HDD Rankings”, Web 16 Feb. 2017, URL: <http://hdd.userbenchmark.com/Explore/Fastest/13>.
- [16] M. Emmelius, G. Pawlowski, and H. W. Vollmann, “Materials for optical data storage”, *Angew. Chem. Int. Ed* **28**, 1445 (1989).
- [17] R. Waser (editor), *Nanoelectronics and Information Technology* (Wiley, 2007), second edition.
- [18] Blu-ray Disc Association, “Blu-ray Disc Format — General 4th Edition (August 2015)”, *Blu-ray Disc Technical White Papers* on August 2015, Web 16 Feb. 2017, URL: <http://blu-raydisc.com/en/Technical/TechnicalWhitePapers/General.aspx>.
- [19] H. Coufal and L. Dhar, “Materials for optical data storage”, *MRS Bull.* **31**, 294 (2006).
- [20] K. Curtis, L. Dhar, A. J. Hill, W. L. Wilson, and M. R. Ayres (editors), *Holographic Data Storage* (John Wiley & Sons, Ltd, 2010).
- [21] F.-K. Bruder, R. Hagen, T. Rölle, M.-S. Weiser, and T. Fäcke, “From the surface to volume: Concepts for the next generation of optical-holographic data-storage materials”, *Angew. Chem. Int. Edit.* **50**, 4552 (2011).
- [22] L. Hesselink, S. S. Orlov, and M. C. Bashaw, “Holographic data storage systems”, *Proc. IEEE* **92**, 1231 (2004).
- [23] K.-i. Shimada, T. Ishii, T. Ide, S. Hughes, A. Hoskins, and K. Curtis, “High density recording using monocular architecture for 500gb consumer system”, in “2009 Optical Data Storage Topical Meeting”, p. 61 (2009).
- [24] J. Freijlich, *Photorefractive materials* (Wiley-Interscience, 2007).
- [25] L. Solymar, *The physics and applications of photorefractive materials* (Clarendon Press, 1996).

- [26] P. Günter and H. J.-P., *Photorefractive materials and their applications*, volume 1–3 (Springer, Berlin, 2006).
- [27] K. Buse, S. Breer, K. Peithmann, S. Kapphan, M. Gao, and E. Krätzig, “Origin of thermal fixing in photorefractive lithium niobate crystals”, *Phys. Rev. B* **56**, 1225 (1997).
- [28] L. Dhar, K. Curtis, M. Tackitt, M. Schilling, S. Campbell, W. Wilson, A. Hill, C. Boyd, N. Levinos, and A. Harris, “Holographic storage of multiple high-capacity digital data pages in thick photopolymer systems”, *Opt. Lett.* **23**, 1710 (1998).
- [29] V. L. Colvin, R. G. Larson, A. L. Harris, and M. L. Schilling, “Quantitative model of volume hologram formation in photopolymers”, *J. Appl. Phys.* **81**, 5913 (1997).
- [30] R. M. Shelby, D. A. Waldman, and R. T. Ingwall, “Distortions in pixel-matched holographic data storage due to lateral dimensional change of photopolymer storage media”, *Opt. Lett.* **25**, 713 (2000).
- [31] M. Eich and J. H. Wendorff, “Erasable holograms in polymeric liquid crystals”, *Makromol. Chem. Rap. Comm.* **8**, 467 (1987).
- [32] M. Eich, J. H. Wendorff, B. Reck, and H. Ringsdorf, “Reversible digital and holographic optical storage in polymeric liquid crystals”, *Makromol. Chem. Rap. Comm.* **8**, 59 (1987).
- [33] A. Natansohn and P. Rochon, “Photoinduced motions in azo-containing polymers”, *Chem. Rev.* **102**, 4139 (2002).
- [34] P. Rochon, J. Gosselin, A. Natansohn, and S. Xie, “Optically induced and erased birefringence and dichroism in azoaromatic polymers”, *Appl. Phys. Lett.* **60**, 4 (1992).
- [35] A. Natansohn, P. Rochon, J. Gosselin, and S. Xie, “Azo polymers for reversible optical storage. 1. Poly[4'-[[2-(acryloyloxy)ethyl]ethylamino]-4-nitroazobenzene]”, *Macromolecules* **25**, 2268 (1992).
- [36] P. Rochon, D. Bissonnette, A. Natansohn, and S. Xie, “Azo polymers for reversible optical storage. III. Effect of film thickness on net phase retardation and writing speed”, *Appl. Opt.* **32**, 7277 (1993).
- [37] M. Häckel, L. Kador, D. Kropp, and H.-W. Schmidt, “Polymer blends with azobenzene-containing block copolymers as stable rewritable volume holographic media”, *Adv. Mater.* **19**, 227 (2007).
- [38] K. Kreger, C. Löffler, R. Walker, N. Wirth, D. Bingemann, H. Audorff, E. A. Rössler, L. Kador, and H.-W. Schmidt, “Dynamic behavior of the minority phase of photoaddressable block copolymers”, *Macromol. Chem. Phys.* **208**, 1530 (2007).
- [39] A. S. Matharu, S. Jeeva, and P. S. Ramanujam, “Liquid crystals for holographic optical data storage”, *Chem. Soc. Rev.* **36**, 1868 (2007).
- [40] C. Frenz, A. Fuchs, H.-W. Schmidt, U. Theissen, and D. Haarer, “Diblock copolymers with azobenzene side-groups and polystyrene matrix: Synthesis, characterization and photoaddressing”, *Macromol. Chem. Phys.* **205**, 1246 (2004).

- [41] M. Häckel, L. Kador, D. Kropp, C. Frenz, and H.-W. Schmidt, "Holographic gratings in diblock copolymers with azobenzene and mesogenic side groups in the photoaddressable dispersed phase", *Adv. Funct. Mat.* **15**, 1722 (2005).
- [42] S. Lee, H. S. Kang, and J.-K. Park, "Directional photofluidization lithography: Micro/Nanostructural evolution by photofluidic motions of azobenzene materials", *Adv. Mater.* **24**, 2069 (2012).
- [43] A. Priimagi and A. Shevchenko, "Azopolymer-based micro- and nanopatterning for photonic applications", *Polym. Sci. Pol. Phys.* **52**, 163 (2014).
- [44] P. Karageorgiev, D. Neher, B. Schulz, B. Stiller, U. Pietsch, M. Giersig, and L. Brehmer, "From anisotropic photo-fluidity towards nanomanipulation in the optical near-field", *Nat. Mater.* **4**, 699 (2005).
- [45] J. Vapaavuori, A. Laventure, C. G. Bazuin, O. Lebel, and C. Pellerin, "Submolecular plasticization induced by photons in azobenzene materials", *J. Am. Chem. Soc.* **137**, 13510 (2015).
- [46] N. Hurduc, B. C. Donose, L. Rocha, C. Ibanescu, and D. Scutaru, "Azo-polymers photofluidisation — a transient state of matter emulated by molecular motors", *RSC Adv.* **6**, 27087 (2016).
- [47] P. Rochon, E. Batalla, and A. Natansohn, "Optically induced surface gratings on azoaromatic polymer films", *Appl. Phys. Lett.* **66**, 136 (1995).
- [48] E. Kim, Y. Xia, and G. M. Whitesides, "Polymer microstructures formed by moulding in capillaries", *Nature* **376**, 581 (1995).
- [49] N. K. Viswanathan, D. Y. Kim, S. Bian, J. Williams, W. Liu, L. Li, L. Samuelson, J. Kumar, and S. K. Tripathy, "Surface relief structures on azo polymer films", *J. Mater. Chem.* **9**, 1941 (1999).
- [50] H. Audorff, R. Walker, L. Kador, and H.-W. Schmidt, "Polarization dependence of the formation of surface relief gratings in azobenzene-containing molecular glasses", *J. Phys. Chem. B* **113**, 3379 (2009).
- [51] N. S. Yadavalli and S. Santer, "In-situ atomic force microscopy study of the mechanism of surface relief grating formation in photosensitive polymer films", *J. Appl. Phys.* **113**, 224304 (2013).
- [52] N. S. Yadavalli, M. Saphiannikova, and S. Santer, "Photosensitive response of azobenzene containing films towards pure intensity or polarization interference patterns", *Appl. Phys. Lett.* **105**, 051601 (2014).
- [53] Y. Zhao and T. Ikeda (editors), *Smart Light-Responsive Materials* (John Wiley & Sons, Inc., Hoboken, New Jersey, 2009).
- [54] K. G. Yager and C. J. Barrett, "Temperature modeling of laser-irradiated azo-polymer thin films", *J. Chem. Phys.* **120**, 1089 (2004).
- [55] C. J. Barrett, A. L. Natansohn, and P. L. Rochon, "Mechanism of optically inscribed high-efficiency diffraction gratings in azo polymer films", *J. Phys. Chem.* **100**, 8836 (1996).

- [56] J. Kumar, L. Li, X. L. Jiang, D.-Y. Kim, T. S. Lee, and S. Tripathy, "Gradient force: The mechanism for surface relief grating formation in azobenzene functionalized polymers", *Appl. Phys. Lett.* **72**, 2096 (1998).
- [57] S. Bian, W. Liu, J. Williams, L. Samuelson, J. Kumar, and S. Tripathy, "Photoinduced surface relief grating on amorphous poly(4-phenylazophenol) films", *Chem. Mater.* **12**, 1585 (2000).
- [58] T. G. Pedersen, P. M. Johansen, N. C. R. Holme, P. S. Ramanujam, and S. Hvilsted, "Mean-field theory of photoinduced formation of surface reliefs in side-chain azobenzene polymers", *Phys. Rev. Lett.* **80**, 89 (1998).
- [59] P. Lefin, C. Fiorini, and J.-M. Nunzi, "Anisotropy of the photo-induced translation diffusion of azobenzene dyes in polymer matrices", *Pure Appl. Opt.* **7**, 71 (1998).
- [60] M. L. Juan, J. Plain, R. Bachelot, P. Royer, S. K. Gray, and G. P. Wiederrecht, "Multi-scale model for photoinduced molecular motion in azo polymers", *ACS Nano* **3**, 1573 (2009).
- [61] F. You, M. Paik, M. Häckel, L. Kador, D. Kropp, H.-W. Schmidt, and C. Ober, "Control and suppression of surface relief gratings in liquid-crystalline perfluoroalkyl-azobenzene polymers", *Adv. Funct. Mat.* **16**, 1577 (2006).
- [62] N. K. Viswanathan, S. Balasubramanian, L. Li, S. K. Tripathy, and J. Kumar, "A detailed investigation of the polarization-dependent surface-relief-grating formation process on azo polymer films", *Jpn. J. Appl. Phys.* **38**, 5928 (1999).
- [63] H. Nakano, T. Takahashi, T. Kadota, and Y. Shirota, "Formation of a surface relief grating using a novel azobenzene-based photochromic amorphous molecular material", *Adv. Mat.* **14**, 1157 (2002).
- [64] E. Ishow, R. Camacho-Aguilera, J. Guérin, A. Brosseau, and K. Nakatani, "Spontaneous formation of complex periodic superstructures under high interferential illumination of small-molecule-based photochromic materials", *Adv. Funct. Mat.* **19**, 796 (2009).
- [65] M. Guo, Z. Xu, and X. Wang, "Photofabrication of two-dimensional quasi-crystal patterns on UV-curable molecular azo glass films", *Langmuir* **24**, 2740 (2008).
- [66] X. Wang, J. Yin, and X. Wang, "Photoinduced self-structured surface pattern on a molecular azo glass film: Structure-property relationship and wavelength correlation", *Langmuir* **27**, 12666 (2011).
- [67] R. Walker, H. Audorff, L. Kador, and H.-W. Schmidt, "Synthesis and structure-property relations of a series of photochromic molecular glasses for controlled and efficient formation of surface relief nanostructures", *Adv. Funct. Mat.* **19**, 2630 (2009).
- [68] J. H. Yang, C. K. Ullal, M. Maldovan, T. Gorishnyy, S. Kool, C. Koh, and E. L. Thomas, "3D micro- and nanostructures via interference lithography", *Adv. Funct. Mater.* **17**, 3027 (2007).
- [69] R. F. Pease and S. Y. Chou, "Lithography and other patterning techniques for future electronics", *Proc. IEEE* **96**, 248 (2008).

- [70] T. M. de Jong, D. K. G. de Boer, and C. W. M. Bastiaansen, "Surface-relief and polarization gratings for solar concentrators", *Opt. Express* **19**, 15127 (2011).
- [71] S.-I. Na, S.-S. Kim, and J. Jo, "Efficient polymer solar cells with surface relief gratings fabricated by simple soft lithography", *Adv. Funct. Mater.* **18**, 3956 (2008).
- [72] K. D. Renuka, C. L. Lekshmi, K. Joseph, and S. Mahesh, "Sustainable electronic materials: Reversible phototuning of conductance in a noncovalent assembly of MWCNT and bioresource-derived photochromic molecule", *ACS Appl. Mater. Interfaces* **9**, 1167 (2017).
- [73] S. Yang, K. Yang, L. Niu, R. Nagarajan, S. Bian, A. K. Jain, and J. Kumar, "Patterning of substrates using surface relief structures on an azobenzene-functionalized polymer film", *Adv. Funct. Mater.* **16**, 693 (2004).
- [74] A. Kravchenko, A. Shevchenko, V. Ovchinnikov, A. Priimagi, and M. Kaivola, "Optical interference lithography using azobenzene-functionalized polymers for micro- and nanopatterning of silicon", *Adv. Funct. Mater.* **23**, 4174 (2011).
- [75] A. De Silva, N. M. Felix, and C. K. Ober, "Molecular glass resists as high-resolution patterning materials", *Adv. Mat.* **20**, 3355 (2008).
- [76] S. Lee, Y.-C. Jeong, and J.-K. Park, "Facile fabrication of close-packed microlens arrays using photoinduced surface relief structures as templates", *Opt. Express* **15**, 14550 (2007).
- [77] R. H. Lambeth, J. Park, H. Liao, D. J. Shir, S. Jeon, J. A. Rogers, and J. S. Moore, "Proximity field nanopatterning of azopolymer thin films", *Nanotechnology* **21**, 165301 (2010).
- [78] J. Choi, W. Cho, Y. S. Jung, H. S. Kang, and H.-T. Kim, "Direct fabrication of micronano-patterned surfaces by vertical-directional photofluidization of azobenzene materials", *ACS Nano* **11**, 1320 (2017).
- [79] C. Probst, C. Meichner, K. Kreger, L. Kador, C. Neuber, and H.-W. Schmidt, "Athermal azobenzene-based nanoimprint lithography", *Adv. Mat.* **28**, 2624 (2016).
- [80] C. Meichner, A. E. Schedl, C. Neuber, K. Kreger, H.-W. Schmidt, and L. Kador, "Refractive-index determination of solids from first- and second-order critical diffraction angles of periodic surface patterns", *AIP Adv.* **5**, 087135 (2015).
- [81] D. Gabor, "A new microscopic principle", *Nature* **161**, 777 (1948).
- [82] E. N. Leith and J. Upatnieks, "New techniques in wavefront reconstruction", *J. Opt. Soc. Am.* **51**, 1469 (1961).
- [83] "Dennis Gabor - Facts", *Nobelprize.org*, Nobel Media AB 2014, Web 11 Nov. 2016, URL: http://www.nobelprize.org/nobel_prizes/physics/laureates/1971/gabor-facts.html.
- [84] L. Nikolova and P. S. Ramanujam, *Polarization Holography* (Cambridge University Press, 2009), first edition.
- [85] H. Audorff, *Holographic Investigation of Azobenzene-Containing Low-Molecular-Weight Compounds*, PhD Thesis, Universität Bayreuth (2011).

- [86] T. Huang and K. H. Wagner, "Coupled mode analysis of polarization volume hologram", *IEEE J. Quantum Elect.* **31**, 372 (1995).
- [87] F. Bloch, "Über die Quantenmechanik der Elektronen in Kristallgittern", *Z. Phys.* **52**, 555 (1929).
- [88] R. Petit (editor), *Electromagnetic Theory of Gratings*, volume 22 of *Topics in Current Physics* (Springer, Berlin Heidelberg, 1980), first edition.
- [89] R. Magnusson and T. K. Gaylord, "Diffraction regimes of transmission gratings", *J. Opt. Soc. Am.* **68**, 809 (1978).
- [90] R. Magnusson and T. K. Gaylord, "Diffraction efficiencies of thin phase gratings with arbitrary grating shape", *J. Opt. Soc. Am.* **68**, 806 (1978).
- [91] M. G. Moharam, T. K. Gaylord, and R. Magnusson, "Criteria for bragg regime diffraction by phase gratings", *Opt. Commun.* **32**, 14 (1980).
- [92] H. Kogelnik, "Coupled wave theory for thick hologram gratings", *Bell Syst. Tech. J.* **48**, 2909 (1969).
- [93] W. R. Klein and B. D. Cook, "Unified approach to ultrasonic light diffraction", *IEEE T. Son. Ultrason.* **14**, 123 (1967).
- [94] M. A. Golub and A. A. Friesem, "Effective grating theory for resonance domain surface-relief diffraction gratings", *J. Opt. Soc. Am. A* **22**, 1115 (2005).
- [95] N. C. R. Holme, L. Nikolova, P. S. Ramanujam, and S. Hvilsted, "An analysis of the anisotropic and topographic gratings in a side-chain liquid crystalline azobenzene polyester", *Appl. Phys. Lett.* **70**, 1518 (1997).
- [96] L. Nikolova and T. Todorov, "Diffraction efficiency and selectivity of polarization holographic recording", *Opt. Acta* **31**, 579 (1984).
- [97] N. Reinke, A. Draude, T. Fuhrmann, H. Franke, and R. A. Lessard, "Electric field assisted holographic recording of surface relief gratings in an azo-glass", *Appl. Phys. B* **78**, 205 (2004).
- [98] A. Sobolewska and A. Miniewicz, "Analysis of the kinetics of diffraction efficiency during the holographic grating recording in azobenzene functionalized polymers", *J. Phys. Chem. B* **111**, 1536 (2007).
- [99] F. L. Labarthe, P. Rochon, and A. Natansohn, "Polarization analysis of diffracted orders from a birefringence grating recorded on azobenzene containing polymer", *Appl. Phys. Lett.* **75**, 1377 (1999).
- [100] R. C. Jones, "A new calculus for the treatment of optical systems I. Description and discussion of the calculus", *J. Opt. Soc. Am.* **31**, 488 (1941).
- [101] R. M. A. Azzam and N. M. Bashara, *Ellipsometry and Polarized Light* (Elsevier Science B.V., Amsterdam, North-Holland, 1977).
- [102] U. Ruiz, P. Pagliusi, C. Provenzano, K. Volke-Sepúlveda, and G. Cipparrone, "Polarization holograms allow highly efficient generation of complex light beams", *Opt. Express* **21**, 7505 (2013).

- [103] T. Huang and K. H. Wagner, "Holographic diffraction in photoanisotropic organic materials", *J. Opt. Soc. Am. A* **10**, 306 (1993).
- [104] R. Magnusson and T. K. Gaylord, "Analysis of multiwave diffraction of thick gratings", *J. Opt. Soc. Am.* **67**, 1165 (1977).
- [105] A. E. Crecca, C. R. and Roitberg, "Theoretical study of the isomerization mechanism of azobenzene and disubstituted azobenzene derivatives", *J. Phys. Chem. A* **110**, 8188 (2006).
- [106] L. Gagliardi, G. Orlandi, F. Bernardi, A. Cembran, and M. Garavelli, "A theoretical study of the lowest electronic states of azobenzene: The role of torsion coordinate in the cis-trans photoisomerization", *Theor. Chem. Acc.* **111**, 363 (2004).
- [107] G. S. Hartley and R. J. W. Le Fevre, "119. The dipole moments of cis- and trans-azobenzenes and of some related compounds", *J. Chem. Soc.* p. 531 (1939).
- [108] F. W. Schulze, H. J. Petrick, H. K. Cammenga, and H. Klinge, "Thermodynamic properties of the structural analogues benzo[c]cinnoline, trans-azobenzene, and cis-azobenzene", *Z. Phys. Chem.* **107**, 1 (1977).
- [109] S. Monti, G. Orlandi, and P. Palmieri, "Features of the photochemically active state surfaces of azobenzene", *Chem. Phys.* **71**, 87 (1982).
- [110] H. M. D. Bandara and S. C. Burdette, "Photoisomerization in different classes of azobenzene", *Chem. Soc. Rev.* **41**, 1809 (2012).
- [111] E. V. Brown and G. R. Granneman, "Cis-trans isomerism in the pyridyl analogs of azobenzene. Kinetic and molecular orbital analysis", *J. Am. Chem. Soc.* **97**, 621 (1975).
- [112] P. Hamm, S. M. Ohline, and W. Zinth, "Vibrational cooling after ultrafast photoisomerization of azobenzene measured by femtosecond infrared spectroscopy", *J. Chem. Phys.* **106**, 519 (1997).
- [113] P. P. Birnbaum, J. H. Linford, and D. W. G. Style, "The absorption spectra of azobenzene and some derivatives", *Trans. Faraday Soc.* **49**, 735 (1953).
- [114] T. Cusati, G. Granucci, M. Persico, and G. Spighi, "Oscillator strength and polarization of the forbidden $n \rightarrow \pi^*$ band of trans-azobenzene: A computational study", *J. Chem. Phys.* **128**, 194312 (2008).
- [115] D. Gegiou, K. A. Muszkat, and E. Fischer, "Temperature dependence of photoisomerization. V. Effect of substituents on the photoisomerization of stilbenes and azobenzenes", *J. Am. Chem. Soc.* **90**, 3907 (1968).
- [116] H. Rau and E. Lueddecke, "On the rotation-inversion controversy on photoisomerization of azobenzenes. Experimental proof of inversion", *J. Am. Chem. Soc.* **104**, 1616 (1982).
- [117] S. Xie, A. Natansohn, and P. Rochon, "Recent developments in aromatic azo polymers research", *Chem. Mater.* **5**, 403 (1993).
- [118] M. Granucci, G. and Persico, "Excited state dynamics with the direct trajectory surface hopping method: Azobenzene and its derivatives as a case study", *Theor. Chem. Acc.* **117**, 1131 (2007).

- [119] C. M. Stuart, R. R. Frontiera, and R. A. Mathies, "Excited-state structure and dynamics of cis- and trans-azobenzene from resonance raman intensity analysis", *J. Phys. Chem. A* **111**, 12072 (2007).
- [120] T. Ikeda and O. Tsutsumi, "Optical switching and image storage by means of azobenzene liquid-crystal films", *Science* **268**, 1873 (1995).
- [121] I. Mita, K. Horie, and K. Hirao, "Photochemistry in polymer solids. 9. Photoisomerization of azobenzene in a polycarbonate film", *Macromolecules* **22**, 558 (1989).
- [122] T. Fujino, S. Y. Arzhantsev, and T. Tahara, "Femtosecond time-resolved fluorescence study of photoisomerization of trans-azobenzene", *J. Phys. Chem. A* **105**, 8123 (2001).
- [123] M. Fischer, A. E. Osman, P.-A. Blanche, and M. Dumont, "Photoinduce dichroism as a tool for understanding orientational mobility of photoisomerizable dyes in amorphous matrices", *Synt. Met.* **115**, 139 (2000).
- [124] L. Lamarre and C. S. P. Sung, "Studies of physical aging and molecular motion by azochromophoric labels attached to the main chains of amorphous polymers", *Macromolecules* **16**, 1729 (1983).
- [125] M. Shahinpoor and H.-J. Schneider (editors), *Intelligent Materials* (The Royal Society of Chemistry, 2007).
- [126] T. Ikeda, "Photomodulation of liquid crystal orientations for photonic applications", *J. Mater. Chem.* **13**, 2037 (2003).
- [127] K. Kreger, P. Wolfer, H. Audorff, L. Kador, N. Stingelin-Stutzmann, P. Smith, and H.-W. Schmidt, "Stable holographic gratings with small-molecular trisazobenzene derivatives", *J. Am. Chem. Soc.* **132**, 509 (2010).
- [128] J. F. Rabek (editor), *Photochemistry and Photophysics*, volume II (CRC Press Taylor & Francis Group, Boca Raton, Florida, 1990).
- [129] C. J. Barrett, J.-I. Mamiya, K. G. Yager, and T. Ikeda, "Photo-mechanical effects in azobenzene-containing soft materials", *Soft Matter* **3**, 1249 (2007).
- [130] T. Ubukata, K. Takahashi, and Y. Yokoyama, "Photoinduced surface relief structures formed on polymer films doped with photochromic spiropyrans", *J. Phys. Org. Chem.* **20**, 981 (2007).
- [131] Y. Shirota, "Photo- and electroactive amorphous molecular materials-molecular design, syntheses, reactions, properties, and applications", *J. Mater. Chem.* **15**, 75 (2005).
- [132] X. L. Jiang, L. Li, J. Kumar, D. Y. Kim, and S. K. Tripathy, "Unusual polarization dependent optical erasure of surface relief gratings on azobenzene polymer films", *Appl. Phys. Lett.* **72**, 2502 (1998).
- [133] C. J. Yager, K. G. and Barrett, "Photomechanical surface patterning in azo-polymer materials", *Macromolecules* **39**, 9320 (2006).
- [134] S. Bian, L. Li, J. Kumar, D. Y. Kim, J. Williams, and S. K. Tripathy, "Single laser beam-induced surface deformation on azobenzene polymer films", *Appl. Phys. Lett.* **73**, 1817 (1998).

- [135] S. Bian, J. M. Williams, D. Y. Kim, L. Li, S. Balasubramanian, J. Kumar, and S. Tripathy, "Photoinduced surface deformations on azobenzene polymer films", *J. Appl. Phys.* **86**, 4498 (1999).
- [136] M. Saphiannikova, T. M. Geue, O. Henneberg, K. Morawetz, and U. Pietsch, "Linear viscoelastic analysis of formation and relaxation of azobenzene polymer gratings", *J. Chem. Phys.* **120**, 4039 (2004).
- [137] N. C. R. Holme, L. Nikolova, S. Hvilsted, P. H. Rasmussen, R. H. Berg, and P. S. Ramanujam, "Optically induced surface relief phenomena in azobenzene polymers", *Appl. Phys. Lett.* **74**, 519 (1999).
- [138] M. Helgert, L. Wenke, S. Hvilsted, and P. S. Ramanujam, "Surface relief measurements in side-chain azobenzene polyesters with different substituents", *Appl. Phys. B* **72**, 429 (2001).
- [139] K. Sumaru, T. Fukuda, T. Kimura, H. Matsuda, and T. Yamanaka, "Photoinduced surface relief formation on azopolymer films: A driving force and formed relief profile", *J. Appl. Phys.* **91**, 3421 (2002).
- [140] C. J. Barrett, P. L. Rochon, and A. L. Natansohn, "Model of laser-driven mass transport in thin films of dye-functionalized polymers", *J. Chem. Phys.* **109**, 1505 (1998).
- [141] S. Bauer-Gogonea, S. Bauer, W. Wirges, and R. Gerhard-Multhaupt, "Pyroelectrical investigation of the dipole orientation in nonlinear optical polymers during and after photoinduced poling", *J. Appl. Phys.* **76**, 2627 (1994).
- [142] G. J. Fang, J. E. MacLennan, Y. Yi, M. A. Glaser, M. Farrow, E. Korblova, D. M. Walba, T. E. Furtak, and N. A. Clark, "Athermal photofluidization of glasses", *Nat. Commun.* **4** (2013).
- [143] N. Hurduc, B. C. Donose, A. Macovei, C. Paius, C. Ibanescu, D. Scutaru, M. Hamel, N. Branza-Nichita, and L. Rocha, "Direct observation of athermal photofluidisation in azo-polymer films", *Soft Matter* **10**, 4640 (2014).
- [144] D. P. Hoffman and R. A. Mathies, "Photoexcited structural dynamics of an azobenzene analog 4-nitro-4'-dimethylamino-azobenzene from femtosecond stimulated Raman", *Phys. Chem. Chem. Phys.* **14**, 6298 (2012).
- [145] M. Baroncini, S. d'Agostino, G. Bergamini, P. Ceroni, A. Comotti, P. Sozzani, I. Basanetti, F. Grepioni, T. M. Hernandez, S. Silvi, M. Venturi, and A. Credi, "Photoinduced reversible switching of porosity in molecular crystals based on star-shaped azobenzene tetramers", *Nat. Chem.* **7**, 634 (2015).
- [146] J. Taniguchi, H. Ito, J. Mizuno, and T. Saito (editors), *Nanoimprint Technology* (Wiley, 2013), first edition.
- [147] K. Tawarayama, H. Aoyama, S. Magoshi, Y. Tanaka, S. Shirai, and H. Tanaka, "Recent progress of EUV full-field exposure tool in selete", *Proc. SPIE* **7271**, 727118 (2009).
- [148] H. I. Smith, D. J. D. Carter, J. Ferrera, D. Gil, J. Goodberlet, J. T. Hastings, M. H. Lim, M. Meinhold, R. Menon, E. E. Moon, C. A. Ross, T. Savas, M. Walsh, and F. Zhang, "Soft X-rays for deep sub-100 nm lithography, with and without masks", *Proc. Mater. Res. Soc. Symp.* **584**, 11 (1999).

- [149] W. Banqiu and K. Ajay, "Extreme ultraviolet lithography: A review", *J. Vac. Sci. Technol. B* **25**, 1743 (2007).
- [150] L. J. Guo, "Recent progress in nanoimprint technology and its applications", *J. Phys. D Appl. Phys.* **37**, R123 (2004).
- [151] T. Balla, S. M. Spearing, and S. M. Monk, "An assessment of the process capabilities of nanoimprint lithography", *J. Phys. D Appl. Phys.* **41**, 174001 (2008).
- [152] S. Fujimori, "Fine pattern fabrication by the molded mask method (nanoimprint lithography) in the 1970s", *Jpn. J. Appl. Phys.* **48**, 1 (2009).
- [153] B. Bhushan (editor), *Handbook of Nanotechnology* (Springer, 2007), second edition.
- [154] H. P. Herzig (editor), *Micro-Optics* (Taylor & Francis, 1997), first edition.
- [155] S. Y. Chou, P. R. Krauss, and P. J. Renstrom, "Imprint of sub-25 nm vias and trenches in polymers", *Appl. Phys. Lett.* **67**, 3114 (1995).
- [156] S. Y. Chou, P. R. Krauss, and P. J. Renstrom, "Nanoimprint lithography", *J. Vac. Sci. Technol. B* **14**, 4129 (1996).
- [157] Y. Chen, "Applications of nanoimprint lithography/hot embossing: A review", *Appl. Phys. A* **121**, 451 (2015).
- [158] H. D. Rowland and W. P. King, "Polymer deformation and filling modes during microembossing", *J. Micromech. Microeng.* **14**, 1625 (2004).
- [159] V. C. Sundar, H.-J. Eisler, T. Deng, Y. Chan, E. L. Thomas, and M. G. Bawendi, "Soft-lithographically embossed, multilayered distributed-feedback nanocrystal lasers", *Adv. Mat.* **16**, 2137 (2004).
- [160] H. Tan, A. Gilbertson, and S. Y. Chou, "Roller nanoimprint lithography", *J. Vac. Sci. Technol. B* **16**, 3926 (1998).
- [161] N. Kooy, K. Mohamed, L. Pin, and O. Guan, "A review of roll-to-roll nanoimprint lithography", *Nanoscale Res. Lett.* **9**, 320 (2014).
- [162] S. C. Colburn, M. and Johnson, M. D. Stewart, S. Damle, T. C. Bailey, B. Choi, M. Wedlake, T. B. Michaelson, S. V. Sreenivasan, J. G. Ekerdt, and C. G. Willson, "Step and flash imprint lithography: a new approach to high-resolution patterning", *Proc. SPIE* **3676**, 379 (1999).
- [163] L. M. Campos, I. Meinel, R. G. Guino, M. Schierhorn, N. Gupta, G. D. Stucky, and C. J. Hawker, "Highly versatile and robust materials for soft imprint lithography based on thiol-ene click chemistry", *Adv. Mat.* **20**, 3728 (2008).
- [164] D. Myers, *Surfaces, Interfaces and Colloids* (WILEY-VCH Verlag GmbH, 1999), second edition.
- [165] C. S. Torres (editor), *Alternative Lithography* (Kluwer Academic, Plenum Publ., New York, 2003), second edition.
- [166] H. Li, W. Yu, J. Xu, C. Yang, Y. Wang, and H. Bu, "Hierarchical structure formation and pattern replication by capillary force lithography", *RSC Adv.* **4**, 39684 (2014).

- [167] K. Y. Suh, Y. S. Kim, and H. H. Lee, "Capillary force lithography", *Adv. Mat.* **13**, 1386 (2001).
- [168] G. L. W. Cross, "The production of nanostructures by mechanical forming", *J. Phys. D Appl. Phys.* **39**, R363 (2006).
- [169] L. J. Heyderman, H. Schiff, C. David, J. Gobrecht, and T. Schweizer, "Flow behaviour of thin polymer films used for hot embossing lithography", *Microelectron. Eng.* **54**, 229 (2000).
- [170] H.-C. Scheer and H. Schulz, "A contribution to the flow behaviour of thin polymer films during hot embossing lithography", *Microelectronic Engineering* **56**, 311 (2001).
- [171] C. Y. Hui, Y. Y. Lin, J. M. Baney, and E. J. Kramer, "The mechanics of contact and adhesion of periodically rough surfaces", *J. Polym. Sci. Pol. Phys.* **39**, 1195 (2001).
- [172] K. L. Johnson, "The adhesion of two elastic bodies with slightly wavy surfaces", *Int. J. Solids Struct.* **32**, 423 (1995).
- [173] E. W. Washburn, "The dynamics of capillary flow", *Phys. Rev.* **17**, 273 (1921).
- [174] L. R. Fisher and P. D. Lark, "An experimental study of the Washburn equation for liquid flow in very fine capillaries", *J. Colloid Interf. Sci.* **69**, 486 (1979).
- [175] M. A. Oliva and D. D. Joye, "Determination of viscosity of Newtonian liquids in a capillary flow between horizontal, parallel flat plates", *J. Colloid Interf. Sci.* **51**, 509 (1975).
- [176] Y. Shirota, K. Moriwaki, S. Yoshikawa, T. Ujike, and H. Nakano, "4-[di(biphenyl-4-yl)amino]azobenzene and 4,4'-bis[bis(4'-tert-butylbiphenyl-4-yl)amino]azobenzene as a novel family of photochromic amorphous molecular materials", *J. Mater. Chem.* **8**, 2579 (1998).
- [177] Y. Shirota, "Organic materials for electronic and optoelectronic devices", *J. Mater. Chem.* **10**, 1 (2000).
- [178] P. Strohriegl and J. V. Grazulevicius, "Charge-transporting molecular glasses", *Adv. Mat.* **14**, 1439 (2002).
- [179] H. Audorff, R. Walker, L. Kador, and H.-W. Schmidt, "Holographic investigations of azobenzene-containing low-molecular-weight compounds in pure materials and binary blends with polystyrene", *Chem. Eur. J.* **17**, 12722 (2011).
- [180] P. Wolfer, H. Audorff, K. Kreger, L. Kador, H.-W. Schmidt, N. Stingelin, and P. Smith, "Photo-induced molecular alignment of trisazobenzene derivatives", *J. Mater. Chem.* **21**, 4339 (2011).
- [181] H. Audorff, K. Kreger, R. Walker, D. Haarer, L. Kador, and H.-W. Schmidt, "Holographic gratings and data storage in azobenzene-containing block copolymers and molecular glasses", in "Complex Macromolecular Systems II", (A. Müller and H.-W. Schmidt, editors), volume 228 of *Adv. Polym. Sci.*, p. 59 (Springer, Berlin Heidelberg, 2010).

- [182] H. Nakano, T. Takahashi, and Y. Shiota, "Photoinduced surface relief grating formation using a photochromic amorphous molecular material, n,n'-bis(9,9-dimethylfluoren-2-yl)-4-(4-pyridylazo)aniline", *J. Photopolym. Sci. Technol.* **22**, 253 (2009).
- [183] C. Probst, C. Meichner, H. Audorff, R. Walker, K. Kreger, L. Kador, and H.-W. Schmidt, "Improving holographic writing performance of photo-orientable azobenzene polymers by molecular glasses", *J. Polym. Sci., Part B: Polym. Phys.* **54**, 2110 (2016).
- [184] M. Häckel, *Holographische Datenspeicherung in nanostrukturierten azobenzolhaltigen Polymeren*, PhD Thesis, Universität Bayreuth (2006).
- [185] O. Lebel, T. Maris, M.-È. Perron, E. Demers, and J. D. Wuest, "The dark side of crystal engineering: Creating glasses from small symmetric molecules that form multiple hydrogen bonds", *J. Am. Chem. Soc.* **128**, 10372 (2006).
- [186] C. Probst, *Azobenzene-Functionalized Materials for Holographic Applications and Nanoimprint Lithography*, PhD Thesis (unpublished), Universität Bayreuth (submitted 2016).
- [187] R. Walker, *Azobenzene-Functionalized Molecular Glasses for Holographic Applications*, PhD Thesis, Universität Bayreuth (2010).
- [188] T. Breiner, K. Kreger, R. Hagen, M. Häckel, L. Kador, A. H. E. Müller, E. J. Kramer, and H.-W. Schmidt, "Blends of poly(methacrylate) block copolymers with photoaddressable segments", *Macromolecules* **40**, 2100 (2007).
- [189] M. M. J. Decré, P. H. M. Timmermans, O. van der Sluis, and R. Schroeders, "Numerical and experimental study of critical roof collapse conditions in soft lithography", *Langmuir* **21**, 7971 (2005).
- [190] K. J. Hsia, Y. Huang, E. Menard, J.-U. Park, W. Zhou, J. Rogers, and J. M. Fulton, "Collapse of stamps for soft lithography due to interfacial adhesion", *Appl. Phys. Lett.* **86**, 154106 (2005).
- [191] Y. Y. Huang, W. Zhou, K. J. Hsia, E. Menard, J.-U. Park, J. A. Rogers, and A. G. Alleyne, "Stamp collapse in soft lithography", *Langmuir* **21**, 8058 (2005).
- [192] W. Zhou, Y. Huang, E. Menard, N. R. Aluru, J. A. Rogers, and A. G. Alleyne, "Mechanism for stamp collapse in soft lithography", *Appl. Phys. Lett.* **87**, 251925 (2005).
- [193] I. D. Johnston, D. K. McCluskey, C. K. L. Tan, and M. C. Tracey, "Mechanical characterization of bulk Sylgard 184 for microfluidics and microengineering", *J. Microelectromech. Microeng.* **24**, 035017 (2014).
- [194] J. Hoffmann, *Charakterisierung faserverstärkter Elastomere für formvariable Strukturflächen*, PhD Thesis, Technische Universität München (2012).
- [195] T. Farrell, C. I. Smith, A. L. Schofield, R. L. Williams, and P. Weightman, "Reflection anisotropy spectra of polydimethylsiloxane under a range of mechanically applied stress", *J. Phys. D Appl. Phys.* **43**, 245301 (2010).
- [196] M. K. Chaudhury and G. M. Whitesides, "Direct measurement of interfacial interactions between semispherical lenses and flat sheets of poly(dimethylsiloxane) and their chemical derivatives", *Langmuir* **7**, 1013 (1991).

- [197] C. Y. Hui, A. Jagota, Y. Y. Lin, and E. J. Kramer, "Constraints on microcontact printing imposed by stamp deformation", *Langmuir* **18**, 1394 (2002).
- [198] S. Wu, *Polymer Handbook*, volume IV (Wiley-Interscience, New York, 1989), third edition.
- [199] F. Schneider, J. Draheim, R. Kamberger, and U. Wallrabe, "Process and material properties of polydimethylsiloxane (PDMS) for Optical MEMS", *Sensor. Actuat. A-Phys.* **151**, 95 (2009).
- [200] M. Huber, *Oberflächengitter Photoadressierbarer Polymere*, PhD Thesis, Universität Bayreuth (2001).
- [201] U. Theißen, *Photoadressierbare Blockcopolymere als Material für die holographische Datenspeicherung*, PhD Thesis, Universität Bayreuth (2002).
- [202] C. A. Walsh and W. E. Moerner, "Two-beam coupling measurements of grating phase in a photorefractive polymer", *J. Opt. Soc. Am. B* **9**, 1642 (1992).
- [203] Y. Kawabe, K. Fukuzawa, T. Uemura, K. Matsuura, T. Yoshikawa, J.-I. Nishide, and H. Sasabe, "Photoinduced grating formation in a polymer containing azo-carbazole dyes", *Appl. Opt.* **51**, 6653 (2012).
- [204] G. Haugstad, *Atomic Force Microscopy* (John Wiley & Sons, Inc., Hoboken, New Jersey, 2012), first edition.
- [205] R. F. Egerton, *Physical Principles of Electron Microscopy* (Springer US, 2005), first edition.
- [206] P. Forcén, L. Oriol, C. Sánchez, R. Alcalá, S. Hvilsted, K. Jankova, and J. Loos, "Synthesis, characterization and photoinduction of optical anisotropy in liquid crystalline diblock azo-copolymers", *J. Polym. Sci., Part A: Polym. Chem.* **45**, 1899 (2007).
- [207] H. Yu, Y. Naka, A. Shishido, and T. Ikeda, "Well-defined liquid-crystalline diblock copolymers with an azobenzene moiety: Synthesis, photoinduced alignment and their holographic properties", *Macromolecules* **41**, 7959 (2008).
- [208] S. Gimeno, P. Forcén, L. Oriol, M. Piñol, C. Sánchez, F. J. Rodríguez, R. Alcalá, K. Jankova, and S. Hvilsted, "Photoinduced optical anisotropy in azobenzene methacrylate block copolymers: Influence of molecular weight and irradiation conditions", *Eur. Polym. J.* **45**, 262 (2009).
- [209] X. Tong, L. Cui, and Y. Zhao, "Confinement effects on photoalignment, photochemical phase transition, and thermochromic behavior of liquid crystalline azobenzene-containing diblock copolymers", *Macromolecules* **37**, 3101 (2004).
- [210] C. Berges, I. Javakhishvili, S. Hvilsted, C. Sánchez-Somolinos, and R. Alcalá, "Holographic storage and multiplexing in azopolyester blends using low energy pulses down to 2 ms", *Appl. Phys. Lett.* **102**, 193303 (2013).
- [211] J. del Barrio, E. Blasco, L. Oriol, R. Alcalá, and C. Sánchez-Somolinos, "Diblock copolymer-azobenzene complexes through hydrogen bonding: Self-assembly and stable photoinduced optical anisotropy", *J. Polym. Sci. Pol. Chem.* **51**, 1716 (2013).
- [212] M.-J. Kim, E.-M. Seo, D. Vak, and D.-Y. Kim, "Photodynamic properties of azobenzene molecular films with triphenylamines", *Chem. Mater.* **15**, 4021 (2003).

- [213] A. Stracke, J. H. Wendorff, D. Goldmann, and D. Janietz, "Optical storage in a smectic mesophase: Thermal amplification of light-induced chromophore orientations and surface relief gratings", *Liq. Cryst.* **27**, 1049 (2000).
- [214] T. Sasaki, T. Shoho, K. Kawai, K. Noda, N. Kawatsuki, and H. Ono, "Effects of plasticizer on the transient diffraction properties of polarization holographic gratings made from polarization-sensitive polymeric films", *Jpn. J. Appl. Phys.* **53**, 062601 (2014).
- [215] A. Martin, C. Tefehne, and W. Gronski, "A deuteron NMR study on order and phase behaviour of liquid-crystalline copolymers", *Macromol. Rapid Comm.* **17**, 305 (1996).
- [216] H. A. Macleod, *Thin Film Optical Filters*, Series in Optics and Optoelectronics (CRC Press Taylor & Francis Group, 2001), third edition.
- [217] F. Mitschke, *Fiber Optics Physics and Technology* (Springer, Berlin Heidelberg, 2010), first edition.
- [218] S. Singh, "Refractive index measurement and its applications", *Phys. Scripta* **65**, 167 (2002).
- [219] R. J. Nussbaumer, M. Halter, T. Tervoort, W. R. Caseri, and P. Smith, "A simple method for the determination of refractive indices of (rough) transparent solids", *J. Mater. Sci.* **40**, 575 (2005).
- [220] B. Šantić, "Measurement of the refractive index and thickness of a transparent film from the shift of the interference pattern due to the sample rotation", *Thin Solid Films* **518**, 3619 (2010).
- [221] G. E. Jellison, "Data analysis for spectroscopic ellipsometry", *Thin Solid Films* **234**, 416 (1993).
- [222] L. A. Smith, X. Liu, and P. X. Ma, "Tissue engineering with nano-fibrous scaffolds", *Soft Matter* **4**, 2144 (2008).
- [223] A. Naeemi and J. D. Meindl, "Carbon nanotube interconnects", *Ann. Rev. Mater. Res.* **39**, 255 (2009).
- [224] Z. Z. Bandić, D. Litvinov, and M. Rooks, "Nanostructured materials in information storage", *MRS Bull.* **33**, 831 (2008).
- [225] Y. Zhang, J. Lu, Q. Wang, M. Takahashi, T. Itoh, and M. Ryutaro, "Nanoimprint of polymer electrolyte membrane for micro direct methanol fuel cell application", *ECS Transactions* **16**, 11 (2009).
- [226] M. Aizawa and H. Gyoten, "Effect of micro-patterned membranes on the cathode performances for PEM fuel cells under low humidity", *J. Electrochem. Soc.* **160**, F417 (2013).
- [227] Y. Zhang, J. Lu, S. Shimano, H. Zhou, and R. Maeda, "Nanoimprint of proton exchange membrane for MEMS-based fuel cell application", in "Polymers and Adhesives in Microelectronics and Photonics, 2007. Polytronic 2007. 6th International Conference on", p. 91 (2007).

- [228] K.-S. Han, S.-H. Hong, K.-I. Kim, J.-Y. Cho, K.-w. Choi, and H. Lee, "Fabrication of 3d nano-structures using reverse imprint lithography", *Nanotechnology* **24**, 045304 (2013).
- [229] H. Schiff, "Nanoimprint lithography: 2d or not 2d? A review", *Appl. Phys. A* **121**, 415 (2015).
- [230] X.-J. Shen, L.-W. Pan, and L. Lin, "Microplastic embossing process: Experimental and theoretical characterizations", *Sens. Actuators, A* **97–98**, 428 (2002).
- [231] G. Strobl, *The Physics of Polymers* (Springer-Verlag, Berlin Heidelberg, 1996), first edition.
- [232] M. Doi and S. F. Edwards, *The Theory of Polymer Dynamics* (Oxford University Press, Oxford, 1986), first edition.
- [233] C. J. Barrett, P. L. Rochon, and A. L. Natansohn, "Model of laser-driven mass transport in thin films of dye-functionalized polymers", *J. Chem. Phys.* **109**, 1505 (1998).
- [234] M. G. Moharam and T. K. Gaylord, "Diffraction analysis of dielectric surface-relief gratings", *J. Opt. Soc. Am.* **72**, 1385 (1982).
- [235] M. G. Moharam, T. K. Gaylord, D. A. Pommet, and E. B. Grann, "Stable implementation of the rigorous coupled-wave analysis for surface-relief gratings: Enhanced transmittance matrix approach", *J. Opt. Soc. Am. A* **12**, 1077 (1995).

Danksagung

Das Verfassen der vorliegenden Dissertation wäre ohne die Unterstützung und das Mitwirken verschiedener Personen nicht möglich gewesen. Aus diesem Grund danke ich aufrichtig

meinem Doktorvater **Lothar Kador** für die Möglichkeit, meine Dissertationsschrift in seiner Arbeitsgruppe zu verfassen. Er hat sein breit gefächertes physikalisches Wissen, seine Kenntnisse und Fähigkeiten als Experimentator und seine Erfahrung im Bereich der Optik und Holographie stets dazu eingesetzt, mich bei der Umsetzung und Weiterentwicklung meiner Ideen zu unterstützen. Lothars Begeisterung für die Physik und seine wissenschaftliche Expertise dienten mir dabei stets als Vorbild.

Hans-Werner Schmidt für die Beschäftigung als wissenschaftlicher Mitarbeiter an der Universität Bayreuth während eines Großteils meiner Promotion. Als Inhaber des Lehrstuhls Makromolekulare Chemie I hat er die für die Probensynthese und -präparation benötigte Infrastruktur zur Verfügung gestellt und seine Mitarbeiter in die gemeinsamen Forschungsprojekte eingebunden.

Christian Probst für die Synthese und die Präparation eines Großteils der untersuchten Materialien. Ich danke ihm weiterhin für die Unterstützung bei der Fertigung zahlreicher Stempel und für seine anhaltende Motivation während der AFM Vermessung unserer Proben.

Andreas Schedl für die Präparation von Filmen für die optische Oberflächenstrukturierung und von deren PDMS Replika.

Christian Neuber für das Einbringen neuartiger Konzepte in Bezug auf die Anwendungsmöglichkeiten der untersuchten Materialien. Im Rahmen des European Union's Seventh Framework Programme FP7/2007-2013 (SNM: Single Nanometer Manufacturing for beyond CMOS devices) hat Christian es mir ermöglicht, praxisrelevante Einblicke in das Themengebiet der Lithographie zu gewinnen.

Klaus Kreger für die intensiven wissenschaftlichen Diskussionen und die detaillierte Erläuterung chemischer Prozesse. Durch seine kritischen aber ebenso konstruktiven Anmerkungen konnte er die Qualität unserer Veröffentlichungen stets aufwerten.

Jürgen Köhler für die Nutzung der Ressourcen des Lehrstuhls EP IV. Durch seine Unterstützung war es mir möglich, direkten Zugang zu einem gut ausgestatteten Labor zu erhalten, Spektrometermessungen durchzuführen und meinen Aufbau um diverse ungenutzte optische Komponenten zu erweitern.

Werner Köhler für die Bereitstellung eines Abbe Refraktometers und die anregenden Gespräche beim Mittagessen.

Uwe Gerken für das Aufspüren und den Verleih eines Multicolor He-Ne Lasers.

Markus Hund für eine ausführliche AFM Einweisung und seine Genehmigung, die AFMs des Lehrstuhls Physikalische Chemie II (Prof. Fery) zu verwenden.

Petra Weiss, Christina Wunderlich und **Evelyn Hülsmann** für die tatkräftige Unterstützung bei administrativen und bürokratischen Verwaltungsaufgaben.

allen festen und vorübergehenden Mitarbeitern der Arbeitsgruppen **Werner Köhler, Jürgen Köhler, Braun** und **Kador** für die gemeinsamen Stunden in der Kaffeepause und beim Mittagessen, die angeregten Fachdiskussionen und die unterhaltsamen Gespräche neben der Arbeit.

Werner Reichstein und **Dietrich Haarer** für die Übertragung spannender Aufgaben in einem Projekt, das der Entwicklung eines chemischen Detektors zur Bestimmung des Sauerstoffgehalts in Schutzatmosphären diene.

den **Mitarbeitern der Werkstatt** für die Herstellung und Reparatur diverser mechanischer Komponenten.

meinen Eltern **Anja Brigl** und **Uwe Meichner**, sowie meinen Großeltern **Rosemarie** und **Franz Brigl-Rath** und **Gertraud** und **Rudolf Meichner**, für die finanzielle und moralische Unterstützung der letzten 30 Jahre.

meiner Schwester **Gianna Queijo Garcia** für ihren Zuspruch während des Zusammenschreibens, sowie **Jürgen Brigl-Veitz**, dem Mann meiner Mutter, für seine Unterstützung.

den Radsportextremisten sowie meinen guten Freunden aus dem Freitagmittagsstammtisch **Matthias Dauth, Tobias Schmidt, Stephan Blaha, Daniel Reck** und **Stefan Hain** für die vielen unterhaltsamen und geselligen Stunden.

Silvia Tumino für ihre Unterstützung, Fürsorge und aufrichtige Liebe.

Eidesstattliche Versicherung

Hiermit bestätige ich an Eides statt, dass ich die vorliegende Arbeit selbstständig verfasst und keine anderen als die von mir angegebenen Quellen und Hilfsmittel verwendet habe.

Weiterhin erkläre ich, dass ich die Hilfe von gewerblichen Promotionsberatern bzw. -vermittlern oder ähnlichen Dienstleistern weder bisher in Anspruch genommen habe, noch zukünftig in Anspruch nehmen werde.

Zusätzlich erkläre ich hiermit, dass ich keinerlei frühere Promotionsversuche unternommen habe.

Bayreuth, den 21. Dezember 2017

Unterschrift